

Physics-based turbulence models for large-eddy simulation

Theory and application to rotating turbulent flows



Maurits H. Silvis

Propositions

accompanying the thesis

Physics-based turbulence models for large-eddy simulation

Theory and application to rotating turbulent flows

by

Maurits H. Silvis

1. The physical and mathematical properties of turbulent flows can be used to form an extensive framework of constraints for the analysis of existing and the construction of new turbulence models. (Chapters 3 & 4)
2. Existing turbulence models do not respect all the physical and mathematical properties of turbulent flows. (Chapter 5)
3. Physics-based turbulence models that respect most of the properties of flows can be created systematically. (Chapter 6)
4. The proposed physics-based turbulence model for rotating flows respects most of the properties of flows, is suitable for simulations of laminar, transitional and turbulent flows, and is easy to implement. (Chapter 9)
5. The proposed physics-based turbulence model provides outstanding predictions of incompressible rotating turbulent flows. (Chapter 10)
6. The proposed physics-based turbulence model performs as well as, or much better than, several existing turbulence models, without requiring (dynamic) adaptation or near-wall damping of the model constants. (Chapter 10)
7. Successfully *postdicting* the behavior of idealized turbulent flows is so complicated already that predictions of real-life flows should be taken with a grain of salt.
8. Large-eddy simulation will not become obsolete, for, as computational power grows, so will the complexity of the flows we would like to predict.
9. All scientists should follow a course in popular science writing.
10. Society will make a great step forward when scientists stop investing their creativity, energy and time in supporting the military-industrial complex.

Stellingen

behorende bij het proefschrift

Op natuurkunde gebaseerde turbulentiemodellen voor large-eddy-simulatie

Theorie en toepassing op roterende turbulente stromingen

door

Maurits H. Silvis

1. De wis- en natuurkundige eigenschappen van turbulente stromingen kunnen gebruikt worden om een uitgebreid stelsel van eisen voor het analyseren van bestaande en het maken van nieuwe turbulentiemodellen te vormen. (Hoofdstukken 3 & 4)
2. Bestaande turbulentiemodellen respecteren niet alle wis- en natuurkundige eigenschappen van turbulente stromingen. (Hoofdstuk 5)
3. Op natuurkunde gebaseerde turbulentiemodellen die de meeste eigenschappen van stromingen respecteren, kunnen systematisch gecreëerd worden. (Hoofdstuk 6)
4. Het voorgestelde op natuurkunde gebaseerde turbulentiemodel voor roterende stromingen respecteert de meeste eigenschappen van stromingen, is geschikt voor simulaties van laminaire, transitionele en turbulente stromingen, en is eenvoudig te implementeren. (Hoofdstuk 9)
5. Het voorgestelde turbulentiemodel geeft uitstekende voorspellingen van incompressibele roterende turbulente stromingen. (Hoofdstuk 10)
6. Het voorgestelde turbulentiemodel presteert zo goed als, of veel beter dan, verscheidene bestaande modellen, zonder (dynamische) aanpassing of demping van de modelconstanten nodig te hebben. (Hoofdstuk 10)
7. Het succesvol achteraf voorspellen van het gedrag van geïdealiseerde turbulente stromingen is reeds zo ingewikkeld dat voorspellingen van realistische stromingen met een korreltje zout genomen moeten worden.
8. *Large-eddy*-simulatie zal niet overbodig worden, want naarmate de rekenkracht van computers groeit, zal ook de complexiteit van de stromingen die we willen voorspellen, toenemen.
9. Alle wetenschappers zouden een cursus populair-wetenschappelijk schrijven moeten volgen.
10. De maatschappij zal een grote stap voorwaarts zetten zodra wetenschappers ermee ophouden hun creativiteit, energie en tijd te investeren in het ondersteunen van het militair-industrieel complex.

Physics-based turbulence models for large-eddy simulation

Theory and application to
rotating turbulent flows

Maurits H. Silvis

Cover: An invitation to ponder the question: How well do models reflect reality?

Cover design: Mathijs de Haan

This research project was carried out in the research group Computational Mechanics & Numerical Mathematics of the Bernoulli Institute for Mathematics, Computer Science and Artificial Intelligence of the University of Groningen, The Netherlands.



This work is part of the research programme Free Competition in the Physical Sciences with project number 613.001.212, which is (partly) financed by the Dutch Research Council (NWO).

This thesis was created using the $\text{\LaTeX} 2_{\epsilon}$ typesetting system, the `memoir` class, and the `amsmath` and `biblatex` packages. The body text is set in Latin Modern with a 10pt font set and a 12pt leading on a 12 cm measure. Graphs were created using MATLAB, *MATLAB2TikZ*, *TikZ* and PGFPLOTS.

Printed by: Gildeprint – The Netherlands



A digital version of this thesis can be found at www.mauritssilvis.nl/thesis.

Copyright © 2020 Maurits H. Silvis. All rights reserved.



university of
 groningen

Physics-based turbulence models for large-eddy simulation

Theory and application to rotating turbulent flows

PhD thesis

to obtain the degree of PhD at the
 University of Groningen
 on the authority of the
 Rector Magnificus Prof. C. Wijmenga
 and in accordance with
 the decision by the College of Deans.

This thesis will be defended in public on

Friday 9 October 2020 at 14:30 hours

by

Maurits Henri Silvis

born on 8 February 1989
 in Zwolle, The Netherlands

Supervisor

Prof. R.W.C.P. Verstappen

Co-supervisor

Prof. A.E.P. Veldman

Assessment committee

Prof. M.K. Camlibel

Prof. A.W. Vreman

Prof. B.J. Geurts

Contents

1	Introduction	1
1.1	Turbulence in fluid flows	1
1.2	The incompressible Navier–Stokes equations	7
1.3	The Reynolds-averaged Navier–Stokes equations	23
1.4	Large-eddy simulation	25
1.5	Thesis overview	30
I	Theory: Model constraints for large-eddy simulation	33
	Abstract	33
2	Introduction	35
	Large-eddy simulation	35
	Constraints on subgrid-scale models	36
	Outline	37
3	Model constraints	39
3.1	Introduction	39
3.2	Dimensional requirements	39
3.3	Symmetry requirements	39
3.4	Symmetry breaking requirements	42
3.5	Conservation requirements	45
3.6	Dissipation requirements	48
3.7	Realizability requirements	59
3.8	Near-wall scaling requirements	61
3.9	Conclusions	62
4	Subgrid-scale models based on the local velocity gradient	63
4.1	Introduction	63
4.2	Assumptions	63
4.3	Eddy viscosity models	64
4.4	A general class of subgrid-scale models	65
4.5	Constructing new subgrid-scale models	72
4.6	Constraints	73
4.7	Conclusions	83
5	Analysis of existing subgrid-scale models	85
5.1	Introduction	85
5.2	Examples of existing subgrid-scale models	85
5.3	Properties of existing subgrid-scale models	87

5.4	Conclusions	94
6	Constructing new subgrid-scale models	95
6.1	Introduction	95
6.2	Systematic procedure	95
6.3	Examples of new subgrid-scale models	98
6.4	Properties of new subgrid-scale models	103
6.5	Conclusions	105
7	Conclusions and outlook	107
	Conclusions	107
	Outlook	108
II	Application: Large-eddy simulations of rotating turbulent flows	111
	Abstract	111
8	Introduction	113
	Rotating turbulent flows	113
	Large-eddy simulation and subgrid-scale models	114
	A new subgrid-scale model	116
	Outline	116
9	A new nonlinear subgrid-scale model	117
9.1	Introduction	117
9.2	Selecting the model terms	117
9.3	Defining the model coefficients	119
9.4	The new nonlinear subgrid-scale model	122
9.5	Implementing the new subgrid-scale model	123
9.6	Conclusions	126
10	Numerical results	127
10.1	Introduction	127
10.2	Numerical method	127
10.3	Rotating decaying turbulence	128
10.4	Spanwise-rotating plane-channel flow	142
11	Conclusions and outlook	169
	Conclusions	169
	Outlook	170
	Appendices	173
A	Independence of the basis tensors	175
A.1	The generalized Cayley–Hamilton theorem	175

A.2	The Gram–Schmidt orthogonalization process	175
A.3	Basis tensor projections	176
A.4	Orthogonalized basis tensors	177
A.5	Independence of the basis tensors	179
B	Convergence of numerical results	181
B.1	Rotating decaying turbulence	181
B.2	Spanwise-rotating plane-channel flow	183
C	Turbulent bursts and other flow instabilities	189
C.1	Turbulent bursts	189
C.2	Quasi-periodic collapse of the mean velocity	189
C.3	Impact on flow statistics	191
	List of acronyms	193
	List of symbols	195
	List of publications	201
	List of presentations	203
	Bibliography	207
	Summary	219
	Inleiding	221
	Turbulentie in vloeistofstromingen	221
	Overzicht van dit proefschrift	226
	Samenvatting	229
	Acknowledgments	231
	Biography	237



Chapter 1

Introduction

Imagine walking along a small mountain stream. You hear the steady rustling of the water, inviting you to come closer. On the surface of the stream, you see complex patterns of ripples and waves; and where the water flows past stones, vortices form. You also notice how quiet the stream is in some places and then plunges into a rapid further on. As you study the flow, you begin to wonder what happens underneath the surface. Which phenomena take place within the clear water? How can they be described? In this thesis, we study these questions. In particular, we focus on describing and predicting turbulence in fluid flows.

1.1 Turbulence in fluid flows*

Fluid dynamics

Fluid flows are everywhere. Apart from small streams of water, consider, for example, rivers, ocean currents and the blood that is flowing through our veins. Using the term *fluid* for both liquids and gases, we can additionally think of the flow of air in the atmosphere and the air that moves through our lungs as we breathe in and out. Engineering examples are given by the flow of water through pipes, the flow of air around an airplane and the mixing of fuel and oxygen in the engine of a car.

As these examples show, there is a large variety of fluid flows. We can, for instance, observe flows of a single fluid that is in either the liquid or the gas phase, but also flows of multiple fluids in different phases exist. Additionally, we may encounter different types of fluids. Some fluids, including air, are *compressible*. That is, they will change in volume when pressure is applied to them. Other fluids, like water, are (practically) *incompressible*. Fluids also vary in their thickness or *viscosity*. Some fluids are highly *viscous*, such as honey, whereas other fluids are nearly *inviscid*, like superfluid helium. We may, furthermore, see that fluid flows interact with various objects, from blood cells to airplanes.

Consequently, the behavior of flows has many different aspects. For example, waves can be observed where two different fluids like water and air meet, as on the surface of a stream. Different fluids may also mix. In addition, fluid flows can transport small particles like sediment, salt, blood cells, nutrients and

* A Dutch version of this introduction starts on page [221](#) of this thesis.

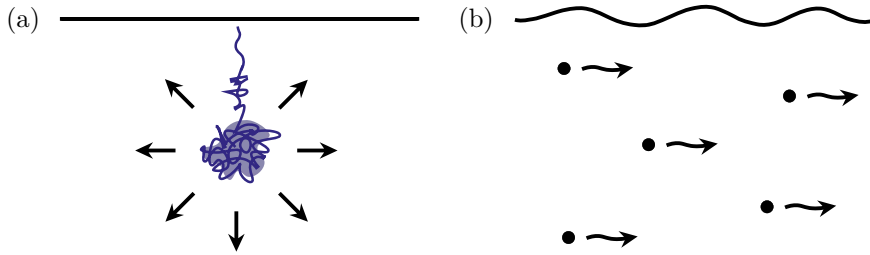


Figure 1.1: Schematic illustration of two transport processes that take place in fluid flows, namely, (a) diffusion and (b) convection.

pollutants. Flows may also transfer heat, as is clear when hot air is circulated in a room. When a fluid flows along or past a solid body, like air flowing around an airplane, friction may play an important role. We may also distinguish fluid flows that are smooth from very chaotic flows. This distinction, to which we will turn shortly, plays a key role in this thesis.

As the above shows, fluid flows appear in many different situations and show very diverse behavior. Their study, therefore, is very interesting, both from a fundamental point of view and from the perspective of industrial and engineering applications. The study of fluid flows is called *fluid dynamics* or *fluid mechanics* and aims to understand, describe and predict the behavior of fluids and all flow-related phenomena.

Transport

The study of fluid flows has revealed two fundamentally different transport processes. On the one hand, we have *diffusion*. Diffusion spreads out particles that are immersed in a fluid by evening out concentration differences. A prime example of this process is the spreading of a dye in calm water, which is schematically illustrated in Fig. 1.1(a).

On the other hand, we have *convection*. Convection, which is also called *advection*, is the process that takes particles along with the flow. This type of transport can, for example, be observed in a blood flow, which distributes blood cells and nutrients. See Fig. 1.1(b) for a schematic illustration of convection.

In addition to affecting particles in flows, the processes of diffusion and convection influence flows themselves. Specifically, they transport physical quantities, such as the *momentum* and *kinetic energy* of flows. The momentum is a measure of the speed of a flow, given by the product of the fluid mass and velocity. The kinetic energy is the energy associated with the fluid movement.

Diffusion has the following effects on flows. Due to diffusion of momentum, regions of a flow in which a fluid moves fast will spread out into regions where the fluid moves slower. Similarly, slow-moving fluid will diffuse to areas where the fluid is moving faster. As a consequence, fast-moving regions of a flow slow down, while slow-moving fluid accelerates. Diffusion also levels off the

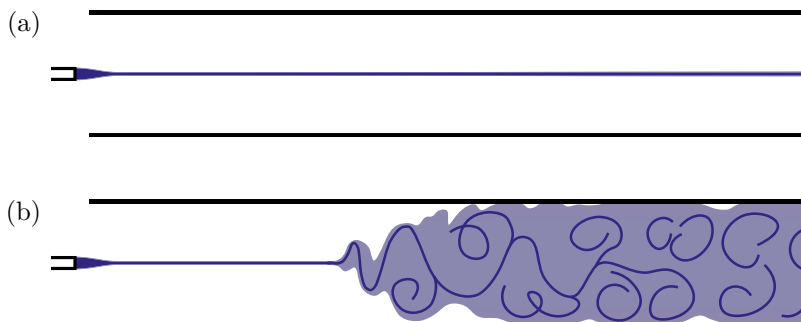


Figure 1.2: Schematic illustration of the experimental observations of Reynolds of a dye in (a) a regular, smooth or *laminar* flow and in (b) an irregular, chaotic or *turbulent* flow.

kinetic energy of flows. Moreover, diffusion leads to friction, which *dissipates* the kinetic energy of flows. That is, friction turns this energy into heat.

Convection causes entirely different effects. Both convection and momentum depend on the velocity of a flow. The convection of momentum, therefore, is a *nonlinear* process, in which a flow interacts with itself. Consequently, flow patterns like vortices, which are also called *eddies*, can merge or split to form eddies of a different size. Similarly, kinetic energy can be exchanged between different eddies. Whereas diffusion smooths out flows, convection, thus, creates more intricate flow patterns. In other words, diffusion and convection are competing processes.

Competition

Osborne Reynolds (1842–1912) showed that the competition between diffusion and convection plays an important role in determining the behavior of flows. In his seminal 1883 paper,¹ he described a set of experiments in which he injected a dye in water that was flowing through a glass tube. Reynolds observed a number of different flow states with two clear extremes.

On the one hand, he saw that the dye could be drawn out into a thin long band (see Fig. 1.2(a)). On the other hand, the dye could suddenly mix with the water and fill up the entire tube (see Fig. 1.2(b)). In the former case, Reynolds concluded that the fluid moved in a very regular, smooth way. In the latter case, the dye revealed a very irregular, chaotic flow.

Reynolds hypothesized the existence of a *critical flow velocity*, which marks the transition between the two flow states. Using dimensional analysis, he additionally argued that this critical velocity would depend on the diameter of the glass tube and on the viscosity of the fluid of interest. Reynolds confirmed

¹ See the reference to the paper of Reynolds (1883) in the bibliography that starts on page 207 of this thesis.

this hypothesis with experiments in which he took special care to reduce disturbances at the inlet of the flow.

Reynolds, thereby, showed that he could characterize the flow states he observed using one number, based on the flow velocity, tube diameter and fluid viscosity. If the value of this number, which we now call the *Reynolds number*, was below a critical value, Reynolds observed a smooth flow. With a Reynolds number above the critical value, the flow would be irregular and chaotic. The Reynolds number forms a measure of the relative strength of convection with respect to diffusion. Reynolds, thus, showed that the competition between these processes plays an important role in flows.²

Turbulence

We call smooth, regular flows *laminar* or layered, whereas chaotic, irregular flows are called *turbulent*. In laminar flows, the process of diffusion dominates convection and the fluid velocity only shows minor variations. On the other hand, turbulent flows are dominated by convection and are characterized by large fluctuations in the fluid velocity.

Because of the dominance of convection, turbulent flows contain eddies of many different sizes (see, e.g., Fig. 1.3(a)), which constantly exchange momentum and kinetic energy. Compared to laminar flows, turbulent flows, therefore, enhance mixing. Kinetic energy exchanges lead to energy transfer from large to small eddies and vice versa. These processes are, respectively, called the *direct* and *inverse cascade* of energy. The kinetic energy of the smallest eddies is dissipated by diffusion. This dissipation is larger in turbulent than in laminar flows. Hence, turbulent flows experience more friction than laminar flows.

Another important feature of turbulent flows is that they are very unstable. More specifically, they are extremely sensitive to variations in the initial flow state, to irregularities in the flow domain and to changes in the properties of the fluid. As a consequence, exactly producing the same turbulent flow twice is practically impossible. In the field of fluid dynamics, the behavior of turbulent flows is referred to as *turbulence*.

Turbulent flows are not only interesting from a fundamental point of view. As most fluid flows are turbulent, their properties are also relevant for many applications. The mixing that occurs in turbulent flows can, for example, be used to optimize combustion processes. Reducing the friction experienced by turbulent flows is important for the design of cars, boats and airplanes. In this work, we will, therefore, focus on describing and predicting the behavior of turbulent flows.

Computational fluid dynamics

The behavior of many fluid flows, both laminar and turbulent, can be described by the *Navier–Stokes equations*. These equations were named after the French

² For more details about these and other findings of Reynolds, see, for example, the popular science article of Silvis (2015).

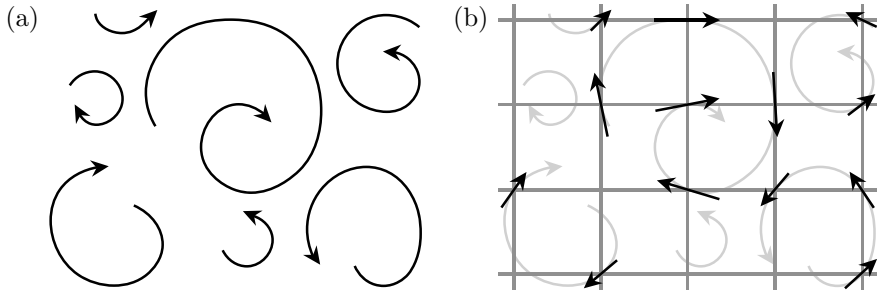


Figure 1.3: Schematic illustration of (a) a flow containing eddies of different sizes and (b) the numerical representation of the velocity of these eddies on a coarse grid. Note that the smallest eddies cannot be represented.

engineer and physicist Claude-Louis Navier (1785–1836), and the Irish mathematician and physicist George Stokes (1819–1903), who both contributed to the mathematical description of fluids in the first half of the nineteenth century (Navier 1827; Stokes 1845).

The Navier–Stokes equations describe the processes of diffusion and convection of momentum, as well as the effects of pressure on flows. The term describing the convection of momentum is nonlinear in the flow velocity. On the other hand, the diffusion of momentum is described using a linear term. As such, the Navier–Stokes equations are valid for *Newtonian fluids*. Newtonian fluids are fluids for which the diffusion depends linearly on the rate at which the fluid deforms. Despite having greatly varying properties, many fluids can be assumed to be Newtonian. Moreover, the Navier–Stokes equations have been shown to provide very accurate predictions of the behavior of such fluids.

Because of the nonlinear convective term, few analytical solutions of the Navier–Stokes equations have been found. Additionally, most discovered solutions represent simple, laminar flows. Studies of flows, therefore, are often based on numerical computations performed using computers. The numerical study of fluid flows is called *computational fluid dynamics* (commonly abbreviated as CFD³). Computations in which the Navier–Stokes equations are solved numerically are called *direct numerical simulations* (DNSs).

Turbulence modeling

Most turbulent flows contain both very large and small eddies (see, e.g., Fig. 1.3(a)). These differently sized eddies play distinct, but important roles. The large eddies carry the largest share of the kinetic energy of a flow, while the energy of the small eddies is dissipated by diffusion.

Because of limits to the available computer memory, the smallest eddies can, however, usually not be represented on the grids used in numerical simulations (see Fig. 1.3(b)). As a consequence, the behavior of many flows cannot

³ A list of the acronyms used in this work can be found on page 193 of this thesis.

be predicted accurately by numerically solving the Navier–Stokes equations. Alternative descriptions of turbulent flows have, therefore, been developed.

A well-known approach, which is based on the work of Reynolds (1895), seeks to predict the average behavior of turbulent flows. This approach employs a variant of the Navier–Stokes equations called the *Reynolds-averaged Navier–Stokes* (RANS) *equations*. Because of the nonlinearity of the convective term, these equations do, however, not have a closed form and cannot be solved without additional information. We, thus, encounter a *closure problem*.

This closure problem is addressed by prescribing, or *modeling*, the deviations of the fluid velocity from the average value. Different *closure* or *turbulence models* have been proposed to predict the average behavior of different flows. The Reynolds-averaged Navier–Stokes approach provides little information about the temporal behavior of flows, however.

Another popular approach, which is called *large-eddy simulation* (LES), therefore, aims to predict the time evolution of the large eddies in flows. As is the case for the Reynolds-averaged Navier–Stokes equations, the equations describing the large eddies do not have a closed form. The behavior of small eddies and their effect on the large eddies, therefore, have to be modeled.

The eddies that cannot be represented on the grids used in numerical simulations (see Fig. 1.3(b)) are generally seen as the small eddies. Models for the small eddies are, therefore, often called *subgrid-scale* (SGS) *models*. Like closure models for the Reynolds-averaged Navier–Stokes equations, subgrid-scale models are also referred to as *turbulence models*. The aim of subgrid-scale models is to reduce the computational cost of numerically solving the Navier–Stokes equations, while ensuring reliable and accurate predictions of the behavior of the large eddies in flows.

Outline

In this thesis, we aim to improve the numerical prediction of incompressible turbulent flows using large-eddy simulation. The question, however, is: how to create turbulence models for such flows? Several answers to this question can be given. One could, for example, select one of the many turbulence models that have been proposed since the advent of computational fluid dynamics. The question remains, however: what defines a well-designed turbulence model?

We will, therefore, focus on the construction of *physics-based turbulence models*, which are turbulence models that respect the physical and mathematical properties of flows. The main question we consider is:

How to create physics-based turbulence models for large-eddy simulations of incompressible turbulent flows?

In the next sections, we discuss the necessary mathematical background to answer this question. In particular, in Section 1.2, we derive the Navier–Stokes equations for incompressible turbulent flows. Then, in Section 1.3, we discuss the Reynolds-averaged Navier–Stokes equations. Finally, in Section 1.4, we

introduce the equations underlying large-eddy simulation. An overview of the work that is presented in the remainder of this thesis is provided in Section 1.5.

1.2 The incompressible Navier–Stokes equations

In this thesis, we study the behavior of incompressible turbulent fluid flows. We focus, in particular, on modeling turbulence in flows of constant-density Newtonian fluids at a constant temperature. The behavior of such flows is governed by the incompressible Navier–Stokes equations. We will derive these equations below.

1.2.1 The continuum hypothesis

The derivation of the incompressible Navier–Stokes equations relies on the *continuum hypothesis*. The continuum hypothesis is the assumption that, on the macroscopic scales we are interested in, fluids and their properties can accurately be described using continuous fields. That is, all the quantities of interest, including the density of fluids, and the velocity and pressure in flows, are assumed to be defined at each time instance and in every point of space. The fact that fluids consist of discrete molecules on microscopic scales is assumed to have a negligible effect on the scales of interest. The macroscopic variables we work with can be seen as averages of microscopic properties.

1.2.2 Conservation of mass

The incompressible Navier–Stokes equations essentially are a statement of conservation of fluid mass and momentum. We first focus on the conservation of mass of fluids.

Integral formulation

To derive an equation for the flow of mass of a fluid, we follow a fluid having a (mass) density denoted by ρ that is flowing through the closed boundary S of a fixed control volume V .⁴ A schematic illustration of this control volume is provided in Fig. 1.4. The total mass contained in the control volume V is governed by the equation

$$\frac{d}{dt} \int_V \rho \, dV = \int_V \frac{\partial \rho}{\partial t} \, dV = - \oint_S \rho u_i n_i \, dS. \quad (1.1)$$

Here, the vector u_i represents the velocity field of the flow, which has components in each of the three spatial directions (as labeled by the index $i = 1, 2, 3$). The density and velocity are, in general, functions of time t and the three spatial coordinates x_i . We will make use of *Cartesian*, or rectangular, *coordinates* x_i in this thesis. The vector n_i is the outward-pointing unit normal of the surface S that encloses the control volume V .

⁴ A list of the symbols used in this work starts on page 195 of this thesis.

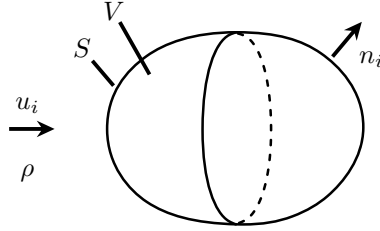


Figure 1.4: Schematic illustration of the control volume used to derive an equation for the mass flow of a fluid.

We employ the *Einstein summation convention* for repeated indices throughout, unless otherwise indicated. Therefore, expressions involving doubly occurring *dummy indices* are to be read as a sum of terms in which those indices take their three possible values, corresponding to the three spatial directions. The quantity $u_i n_i$, thus, represents the inner product of the velocity field vector u_i with the outward-pointing unit normal n_i .

The first term of Eq. (1.1) represents the rate of change of mass of the fluid contained in the control volume V . We give V a fixed shape and position. According to the Reynolds transport theorem (Reynolds 1903), we can, therefore, swap differentiation with respect to time and integration over the control volume. As such, we obtain the first equality of Eq. (1.1).

The term on the right-hand side of Eq. (1.1) indicates the cause of a change in mass contained by the volume V : the velocity field *convects*, or transports, mass through the bounding surface S . Equation (1.1) thus is a statement of conservation of mass. In the fluid mechanics literature, the equation describing mass conservation is often referred to as the *continuity equation*. Equation (1.1) provides an *integral formulation* of the continuity equation.

Differential formulation

When the density and velocity fields are sufficiently smooth (i.e., if no shock waves occur) and if certain conditions on the smoothness of the volume V are fulfilled, we may invoke the divergence theorem to rewrite the continuity equation, Eq. (1.1). Specifically, we can turn the integral over the bounding surface S of the right-hand side of Eq. (1.1) into an integral over the volume V . We, thereby, obtain the equation

$$\frac{d}{dt} \int_V \rho \, dV = \int_V \frac{\partial \rho}{\partial t} \, dV = - \int_V \frac{\partial}{\partial x_i} (\rho u_i) \, dV. \quad (1.2)$$

Since the control volume V can be chosen arbitrarily, the integral formulation of conservation of mass of Eq. (1.2) is equivalent to the *differential formulation*

$$\frac{\partial \rho}{\partial t} + \frac{\partial}{\partial x_i} (\rho u_i) = 0. \quad (1.3)$$

As we will see in Chapter 10, we will use a finite-volume method to numerically solve the equations describing fluid flows. This method is based on the original integral formulation of conservation of mass of Eq. (1.1) and the integral formulation of conservation of momentum we will encounter in Section 1.2.4. In what follows, we will, therefore, use differential formulations as a shorthand for integral formulations, without being concerned with the occurrence of shock waves or with the conditions of the divergence theorem.

Equation (1.3) is written in the *conservation form*. That is, Eq. (1.3) attributes the rate of change of a physical quantity, in this case the density ρ , to a flux. We focus on the situation in which there are no sources or sinks of mass. Therefore, the right-hand side of Eq. (1.3) is zero.

Moreover, Eq. (1.3), provides an *Eulerian description* of the density, i.e., the density is described as a function of position within a nonaccelerating, or *inertial*, frame of reference. A different description, called the *Lagrangian description*, is obtained when we express the continuity equation in the *convective form*,

$$\frac{\partial \rho}{\partial t} + u_i \frac{\partial \rho}{\partial x_i} = -\rho \frac{\partial u_i}{\partial x_i}. \quad (1.4)$$

Here, the operator appearing on the left-hand side,

$$\frac{\partial}{\partial t} + u_i \frac{\partial}{\partial x_i}, \quad (1.5)$$

is called the *material derivative*. In Eq. (1.4), this derivative specifies the rate of change of the density of a so-called *fluid particle*, that is, the rate of change of density of a small volume of fluid that is taken along by the flow.

Since we see the differential equation provided by Eq. (1.3) as a shorthand for the integral equation of Eq. (1.1), Eqs. (1.1) to (1.4) are equivalent statements of conservation of mass in fluids. In these statements, the fluid density ρ is fully general. That is, ρ can vary in both time and space.

1.2.3 The incompressibility condition

In this work, we are interested in the turbulent behavior of constant-property Newtonian fluids. We will, therefore, take the density ρ to be constant in time and uniform in space. As a consequence, the statements of conservation of mass of Section 1.2.2 reduce to the *incompressibility condition* for the flow,

$$\frac{\partial u_i}{\partial x_i} = 0. \quad (1.6)$$

Mass in a constant-density fluid, thus, is conserved if the velocity field of the flow is divergence free.

Note that there is a difference between an *incompressible fluid* and an *incompressible flow* (or *velocity field*). In an incompressible fluid, pressure does not change the fluid density. As a consequence of this constant density, Eq. (1.4) reduces to Eq. (1.6), indicating that the velocity field has to be incompressible. Thus, an incompressible fluid always has an incompressible velocity field.

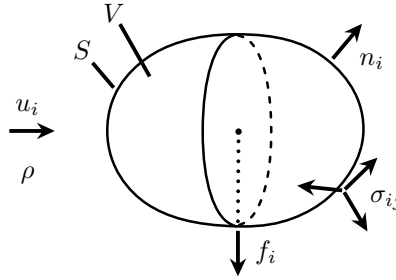


Figure 1.5: Schematic illustration of the control volume used to derive an equation for the momentum of a fluid.

The reverse of this statement is not true. As the convective form of the continuity equation, Eq. (1.4), shows, incompressibility of the velocity field means that the material derivative of the density becomes zero. Such a vanishing material derivative implies that the density of fluid particles has to be constant, while no other conditions on the variability of the fluid density itself arise. We can, therefore, have an incompressible flow of a compressible fluid.

For the constant-density fluids we consider in this work, Eq. (1.6) forms the final statement of conservation of mass.

1.2.4 Conservation of momentum

Integral formulation

To derive an evolution equation for the momentum of a fluid, we again follow a fluid with density ρ that is flowing through the closed boundary S of a fixed control volume V (see Fig. 1.5). Both sources and sinks of momentum may be present in fluids. Therefore, an evolution equation for momentum will be more complicated than the continuity equation for fluid mass, Eq. (1.1).

Indeed, the total momentum of the fluid contained in the volume V develops according to

$$\begin{aligned} \frac{d}{dt} \int_V \rho u_i \, dV &= \int_V \frac{\partial}{\partial t} (\rho u_i) \, dV \\ &= - \oint_S (\rho u_i) u_j n_j \, dS + \oint_S \sigma_{ij} n_j \, dS + \int_V f_i \, dV. \end{aligned} \quad (1.7)$$

Here, the index i is a *free index*. Therefore, Eq. (1.7) contains three equations, one for each value of $i = 1, 2, 3$. These equations relate the rate of change of momentum in the x_i -direction as contained in the control volume V to convection through the bounding surface S and to contributions from two types of forces.

The first type of forces arises due to *stresses* that act only on the surface S that is enclosing the control volume of fluid V . These stresses are described by the *stress tensor* σ_{ij} , which has nine components. The other forces are *body*

forces, which work throughout the volume of fluid and are described by the force density f_i . For simplicity, we will mostly refer to f_i as a body force rather than as a force density in what follows.

Differential formulation

We can invoke the divergence theorem to obtain a differential formulation of the integral statement of conservation of momentum of Eq. (1.7), namely,

$$\frac{\partial}{\partial t}(\rho u_i) + \frac{\partial}{\partial x_j}(\rho u_i u_j) = \frac{\partial \sigma_{ij}}{\partial x_j} + f_i. \quad (1.8)$$

As mentioned in Section 1.2.2, we will employ a finite-volume method to numerically solve the equations of fluid flow. This method is based on the original integral formulations of conservation of mass, Eq. (1.1), and momentum, Eq. (1.7). We will, therefore, regard Eq. (1.8) and the differential formulations that follow as being equivalent to and as a shorthand for the integral formulation of conservation of momentum provided in Eq. (1.7).

Equation (1.8) is known as the *Cauchy momentum equation*. This equation essentially is an expression of Newton’s second law that relates the rate of change of momentum in a fluid, given by the first term on the left-hand side of Eq. (1.8), to forces acting on the fluid. More precisely, Eq. (1.8) relates changes in the momentum density ρu_i of a fluid to a force density. For incompressible flows, for which the incompressibility condition, Eq. (1.6), holds, the left-hand side of Eq. (1.8) equals the material derivative of the momentum density.

The stress tensor

The stresses σ_{ij} that work on the bounding surface S of a volume of fluid V come in two types. One can distinguish *normal stresses* from *shear stresses*. Normal stresses work perpendicularly to the plane they are acting on, while shear stresses are directed in the plane of the surface they are acting on. If we choose a coordinate system that is aligned with the plane of interest, the normal stresses correspond to the diagonal components $\sigma_{(i)(i)}$ of the stress tensor. Here, brackets indicate that the repeated index is not to be summed over. The shear stresses correspond to the off-diagonal components of σ_{ij} , for which $i \neq j$.

The distinction between normal and shear stresses allows for the following decomposition of the stress tensor:

$$\sigma_{ij} = \frac{1}{3} \sigma_{kk} \delta_{ij} + \sigma_{ij}^{\text{dev}}. \quad (1.9)$$

Here, the first term on the right-hand side is the *isotropic part* of the stress tensor. This term involves the *Kronecker delta*, which is defined as

$$\delta_{ij} = \begin{cases} 1 & \text{if } i = j, \\ 0 & \text{if } i \neq j. \end{cases} \quad (1.10)$$

The second term on the right-hand side of Eq. (1.9) represents the *anisotropic* or *deviatoric part* of the stress tensor,

$$\sigma_{ij}^{\text{dev}} = \sigma_{ij} - \frac{1}{3}\sigma_{kk}\delta_{ij}. \quad (1.11)$$

The isotropic part of the stress tensor relates to changes in the volume of a fluid, while the deviatoric stresses relate to changes in shape.

1.2.5 The incompressible Euler equations

The stress tensor of inviscid fluids

To specify the stress tensor σ_{ij} , we first focus on inviscid or *ideal fluids*. Inviscid fluids are frictionless and, therefore, do not experience any shear stresses. As before, we consider only fluids with a constant density ρ . The stress tensor is then given by

$$\sigma_{ij} = -p\delta_{ij}, \quad (1.12)$$

where p represents the pressure (Euler 1757). As is the case with the velocity field u_i , the pressure is a function of both time t and the three spatial coordinates x_i . Note that, due to the assumption of constant density, the pressure p is a mechanical and not a thermodynamic pressure.

The incompressible Euler equations

We can substitute the above expression for the stresses σ_{ij} into the Cauchy momentum equation, Eq. (1.8). Combining the resulting equation with the incompressibility condition, Eq. (1.6), we obtain the *incompressible Euler equations* for a constant-density ideal fluid,

$$\frac{\partial u_i}{\partial x_i} = 0, \quad (1.13a)$$

$$\frac{\partial u_i}{\partial t} + \frac{\partial}{\partial x_j}(u_i u_j) = -\frac{1}{\rho} \frac{\partial p}{\partial x_i} + \frac{1}{\rho} f_i. \quad (1.13b)$$

As is commonly done, each term has been divided by the density ρ .

As explained in Section 1.2.3, Eq. (1.13a) is the statement of conservation of mass of a constant-density fluid. This equation says that the velocity field of the flow u_i has to be divergence free, or incompressible. Equation (1.13b) is the statement of conservation of momentum of a constant-density ideal fluid. This equation relates changes in the momentum (or rather the velocity field) of a fluid to several forces. Specifically, the second term on the left-hand side of this equation represents convection of the velocity field under its own influence. The terms on the right-hand side of Eq. (1.13b) represent the effects of the pressure and body forces on the velocity field, respectively.

Body forces

The body forces f_i may be conservative. In that case, they can be expressed as the gradient of a scalar potential F ,

$$f_i = -\frac{\partial F}{\partial x_i}. \quad (1.14)$$

Conservative body forces may be absorbed in a modified pressure

$$p \rightarrow p + F. \quad (1.15)$$

An example of a conservative force is gravity, for which the potential is $F = \rho g x_3$. Here, the gravitational acceleration is given by g and x_3 denotes the direction antiparallel to the gravitational force. The centrifugal force, which we will encounter in Section 1.2.7, also is a conservative force. On the other hand, the Coriolis force, which we will also discuss in Section 1.2.7, is not in general a conservative force.

General remarks

Unless additional dependent variables are introduced through the body forces f_i , the incompressible Euler equations, Eq. (1.13), form a consistent system of equations for the unknown velocity u_i and (modified) pressure p . That is, we have as many equations as unknowns. Therefore, constant-density ideal fluids are fully described by the statements of conservation of mass and momentum provided by Eq. (1.13). Conservation of energy need not be considered, nor is it necessary to use additional equations to describe the internal state of the fluid.

If the incompressible Euler equations, Eq. (1.13), are to be solved, initial and boundary conditions have to be specified. As for the latter, the *impermeability condition* is usually imposed at solid boundaries, meaning that there can be no normal velocity there. A tangential velocity is allowed at solid boundaries, which is called a *slip condition*.

The dimensionless incompressible Euler equations

We may obtain a dimensionless form of the incompressible Euler equations, Eq. (1.13), by introducing reference length and velocity scales L_{ref} and u_{ref} , along with the associated time scale $L_{\text{ref}}/u_{\text{ref}}$. To that end, we first define the dimensionless variables

$$x_i^* = \frac{x_i}{L_{\text{ref}}}, \quad t^* = \frac{t}{L_{\text{ref}}/u_{\text{ref}}}, \quad u_i^* = \frac{u_i}{u_{\text{ref}}}, \quad p^* = \frac{p}{\rho u_{\text{ref}}^2}. \quad (1.16)$$

Here, the pressure is made dimensionless through division by (twice) the *dynamic pressure*.

In terms of the dimensionless variables of Eq. (1.16), the incompressible Euler equations, Eq. (1.13), take the form

$$\frac{\partial u_i^*}{\partial x_i^*} = 0, \quad (1.17a)$$

$$\frac{\partial u_i^*}{\partial t^*} + \frac{\partial}{\partial x_j^*} (u_i^* u_j^*) = -\frac{\partial p^*}{\partial x_i^*} + \frac{L_{\text{ref}}}{\rho u_{\text{ref}}} f_i. \quad (1.17b)$$

Equation (1.17) shows that, in the absence of body forces, the incompressible Euler equations exhibit *scale similarity*. That is, the equations do not depend on the choice or magnitude of the characteristic length and velocity scales. Different flows that have the same dimensionless initial and boundary conditions can, therefore, be described by the same dimensionless solution. As we will see in Section 3.4.1, the powerful concept of scale similarity is a consequence of the symmetry properties of the incompressible Euler equations.

1.2.6 The incompressible Navier–Stokes equations

The viscous stress tensor

In many practical applications fluids are not frictionless, because, in general, fluids are not inviscid, but viscous. We, therefore, need a model for the viscous stresses experienced by fluids. The first model for the viscous stresses in fluids is due to Navier (1827), Poisson (1831), Barré de Saint-Venant (1843) and Stokes (1845) (also refer to the book by Tietjens et al. 1934). Their model can be expressed in the form of a *constitutive relation*, which relates the stresses experienced by a fluid to the properties and state of that fluid. We can derive this model as follows.

We first assume that the viscous stresses $\sigma_{ij}^{\text{visc}}$ are a function of the velocity gradient of the flow, which is given by

$$G_{ij}(u) = \frac{\partial u_i}{\partial x_j}. \quad (1.18)$$

Dependence of the viscous stresses on the velocity gradient rather than on the velocity field itself ensures Galilean invariance of the momentum equation, Eq. (1.7), a property which we will discuss in Section 3.3.1.

In the next step, we assume that the fluid is Newtonian, i.e., the constitutive relation between the viscous stresses and velocity gradient is linear. The viscous stresses can then be expressed as

$$\sigma_{ij}^{\text{visc}} = \mu_{ijkl} G_{kl}(u). \quad (1.19)$$

Here, μ_{ijkl} is called the *viscosity coefficient*. The viscosity coefficient is, by definition, a *material property*. That is, μ_{ijkl} is independent of the stress state and the velocity of the flow.

We subsequently assume that the fluid under consideration is *isotropic* and, thus, has no preferred orientation in space. The viscosity coefficient can then be written as (Hodge 1961)

$$\mu_{ijkl} = \mu_1 \delta_{ij} \delta_{kl} + \mu_2 \delta_{ik} \delta_{jl} + \mu_3 \delta_{il} \delta_{jk}, \quad (1.20)$$

where μ_1 , μ_2 and μ_3 are scalars. By substituting Eq. (1.20) in Eq. (1.19) and taking into account the incompressibility condition, Eq. (1.6), we find that the expression for the viscous stresses reduces to

$$\sigma_{ij}^{\text{visc}} = \mu_2 G_{ij}(u) + \mu_3 G_{ji}(u). \quad (1.21)$$

Finally, to ensure conservation of angular momentum (see Section 3.5.1) the viscous stresses have to be symmetric,

$$\sigma_{ij}^{\text{visc}} = \sigma_{ji}^{\text{visc}}. \quad (1.22)$$

The viscous stresses experienced by a Newtonian fluid, therefore, have to be written as

$$\sigma_{ij}^{\text{visc}} = 2\mu S_{ij}(u). \quad (1.23)$$

Here, the scalar μ is given by

$$\mu = \frac{\mu_2 + \mu_3}{2} \quad (1.24)$$

and is called the *dynamic viscosity* of the fluid. The quantity $S_{ij}(u)$ represents the *rate-of-strain tensor*, or the *deformation rate*, of the fluid. This tensor is given by the symmetric part of the velocity gradient,

$$S_{ij}(u) = \frac{1}{2} \left(\frac{\partial u_i}{\partial x_j} + \frac{\partial u_j}{\partial x_i} \right). \quad (1.25)$$

As per conservation of angular momentum, the skew-symmetric part of the velocity gradient, called the *rate-of-rotation tensor*,

$$W_{ij}(u) = \frac{1}{2} \left(\frac{\partial u_i}{\partial x_j} - \frac{\partial u_j}{\partial x_i} \right), \quad (1.26)$$

does not occur in the linear constitutive relation between the viscous stresses and the velocity gradient. We will assume that the fluid temperature is constant, so that also the dynamic viscosity μ is constant.

The stress tensor of viscous fluids

By combining the expression for the stresses experienced by inviscid fluids, Eq. (1.12), with the expression for the viscous stresses, Eq. (1.23), we can write the full stress tensor of a constant-density Newtonian fluid as

$$\sigma_{ij} = -p \delta_{ij} + 2\mu S_{ij}(u). \quad (1.27)$$

Note that Eq. (1.27) lays bare the main difference between the descriptions of solids and fluids. In solids, strain (or deformation) directly causes stresses, while fluids only experience a (shear) stress upon changes in the strain. Also note that the rate-of-strain tensor of an incompressible flow is traceless, i.e., $S_{ii}(u) = 0$. The isotropic and deviatoric parts of the stress tensor of Eq. (1.27), thus, are given by

$$\frac{1}{3}\sigma_{kk}\delta_{ij} = -p\delta_{ij}, \quad (1.28a)$$

$$\sigma_{ij}^{\text{dev}} = 2\mu S_{ij}(u). \quad (1.28b)$$

In an incompressible flow, the isotropic part of the stresses, therefore, is entirely due to the pressure, while the deviatoric part is a consequence of viscous stresses alone.

The incompressible Navier–Stokes equations

Substitution of the stress tensor of Eq. (1.27) in the Cauchy momentum equation, Eq. (1.8), and combination with the incompressibility condition, Eq. (1.6), provides us with the *incompressible Navier–Stokes equations* for a constant-density Newtonian fluid at constant temperature,

$$\frac{\partial u_i}{\partial x_i} = 0, \quad (1.29a)$$

$$\frac{\partial u_i}{\partial t} + \frac{\partial}{\partial x_j}(u_i u_j) = -\frac{1}{\rho} \frac{\partial p}{\partial x_i} + 2\nu \frac{\partial S_{ij}(u)}{\partial x_j} + \frac{1}{\rho} f_i. \quad (1.29b)$$

Here, each term has been divided by the density ρ and the (*kinematic*) *viscosity* is defined as

$$\nu = \frac{\mu}{\rho}. \quad (1.30)$$

As explained in Section 1.2.3, Eq. (1.29a) is the statement of conservation of mass of a constant-density fluid. This equation says that the velocity field u_i has to be divergence free, or incompressible. Equation (1.29b) is the statement of conservation of momentum of a constant-density Newtonian fluid at constant temperature. This equation relates changes in the momentum (or rather the velocity field) of a fluid to several forces. Specifically, the second term on the left-hand side of this equation describes convection of the velocity field under its own influence. The terms on the right-hand side of Eq. (1.29b) represent the effects of the pressure, diffusion and body forces on the velocity field, respectively.

General remarks

Since we assume a constant fluid temperature, the dynamic viscosity μ is constant. Then, with a constant density ρ , also the kinematic viscosity ν has to be constant. Therefore, we do not need any additional equations to describe the internal (stress) state of the fluid.

Moreover, we will assume that no additional dependent variables are introduced through the body forces f_i . Equation (1.29), therefore, forms a consistent system of equations for the velocity u_i and pressure p . That is, constant-density Newtonian fluids at constant temperature are described fully by the statements of conservation of mass and momentum provided by Eq. (1.29). Conservation of energy does not have to be considered to obtain a closed system of equations. Conservation of angular momentum was invoked when defining the viscous stress tensor (see Eq. (1.22)).

By substituting the rate-of-strain tensor, Eq. (1.25), in Eq. (1.29b) and applying the incompressibility condition, Eq. (1.6), we may rewrite the diffusive term in terms of the Laplacian of the velocity field:

$$2\nu \frac{\partial S_{ij}(u)}{\partial x_j} = \nu \frac{\partial^2 u_i}{\partial x_j \partial x_j}. \quad (1.31)$$

Although this step is commonly taken, we will keep the original formulation of the incompressible Navier–Stokes equations provided in Eq. (1.29) to facilitate the derivation of evolution equations in Sections 3.5 and 3.6.

Despite their similarity in the limit of vanishing viscosity, $\nu \rightarrow 0$, the incompressible Navier–Stokes equations, Eq. (1.29), have a different nature than the incompressible Euler equations, Eq. (1.13). This difference is due to the presence of second-order spatial derivatives in the diffusive term in the former set of equations. As a consequence, the incompressible Navier–Stokes equations need a different set of boundary conditions than the incompressible Euler equations. For Eq. (1.29), the velocity field is usually set to zero at solid boundaries to satisfy the *no-slip condition* (no tangential velocity) in addition to the impermeability condition (no normal velocity).

The dimensionless incompressible Navier–Stokes equations

The dimensionless variables of Eq. (1.16) can be used to obtain a dimensionless form of the incompressible Navier–Stokes equations,

$$\frac{\partial u_i^*}{\partial x_j^*} = 0, \quad (1.32a)$$

$$\frac{\partial u_i^*}{\partial t^*} + \frac{\partial}{\partial x_j^*} (u_i^* u_j^*) = -\frac{\partial p^*}{\partial x_i^*} + \frac{2}{Re} \frac{\partial S_{ij}^*(u)}{\partial x_j^*} + \frac{L_{\text{ref}}}{\rho u_{\text{ref}}} f_i. \quad (1.32b)$$

Here, the dimensionless rate-of-strain tensor is defined as

$$S_{ij}^*(u) = \frac{1}{2} \left(\frac{\partial u_i^*}{\partial x_j^*} + \frac{\partial u_j^*}{\partial x_i^*} \right). \quad (1.33)$$

The Reynolds number

In Eq. (1.32), the Reynolds number Re is given by

$$Re = \frac{u_{\text{ref}} L_{\text{ref}}}{\nu}. \quad (1.34)$$

In the absence of body forces f_i , the Reynolds number is the only dimensionless parameter of the incompressible Navier–Stokes equations. Flows that have the same dimensionless initial and boundary conditions, and the same Reynolds number, can, therefore, be described using the same dimensionless solution. This powerful principle is called *Reynolds number similarity*.

As was alluded to in Section 1.1, the Reynolds number quantifies the importance of inertial (convective) forces with respect to viscous (diffusive) forces. A small Reynolds number indicates dominance of viscous over inertial forces. The incompressible Navier–Stokes equations will then (likely) produce smooth solutions, corresponding to laminar flow. For a large Reynolds number, convective processes will dominate the flow behavior and the incompressible Navier–Stokes equations will (likely) lead to chaotic solutions, which contain a large range of scales of motion. These solutions correspond to the turbulent behavior that flows commonly exhibit. For intermediate values of the Reynolds number a *transitional* state may occur, in which laminar and turbulent behavior may alternate.

Since the value of the Reynolds number depends on the choice of the reference length and velocity scales L_{ref} and u_{ref} , this number is not uniquely defined. Therefore, a direct comparison between Reynolds numbers is only possible if the choice of these length and velocity scales is explained and if this choice is similar. If the reference scales are not defined in a similar way, as may be the case for flows having a different geometry, the Reynolds number provides at most a general idea of the dominance of convective over diffusive forces.

The incompressible Navier–Stokes equations for a constant-density Newtonian fluid at constant temperature provided by Eq. (1.29) form the basis for the research presented in this thesis.

1.2.7 The incompressible Navier–Stokes equations in a rotating frame

The incompressible Navier–Stokes equations, Eq. (1.29), describe the behavior of constant-density Newtonian fluids as seen from a nonaccelerating, inertial frame of reference. The rotating flows considered in Part II of this thesis are, however, more easily studied from a rotating frame of reference. In this section, we will, therefore, discuss the incompressible Navier–Stokes equations in a rotating frame of reference.

Transformation rules

To obtain the incompressible Navier–Stokes equations in a rotating frame of reference, we first consider the effect of frame rotation on each physical quantity appearing in the incompressible Navier–Stokes equations, Eq. (1.29).

First of all, time t and pressure p are scalar quantities, which are, by definition, invariant under rotations of the frame of reference. Indicating a quantity in the rotating frame of reference with a hat, we can, thus, write the

transformation rules of these quantities as

$$t \rightarrow \hat{t} = t, \quad (1.35a)$$

$$p \rightarrow \hat{p} = p. \quad (1.35b)$$

The density ρ and viscosity ν are also scalar quantities that have to be independent of frame rotation. More importantly, however, these quantities are material properties that we will see as flow parameters. We will, therefore, take ρ and ν as constants with respect to any coordinate transformation, disregarding *equivalence transformations*.

Vector quantities like the spatial coordinates x_i and velocity field u_i are not invariant under frame rotation. The transformation from coordinates x_i in the nonrotating, inertial frame of reference to coordinates \hat{x}_i in the rotating frame is given by

$$x_i \rightarrow \hat{x}_i = Q_{ij}(t) x_j. \quad (1.36)$$

Here, $Q_{ij}(t)$ is a possibly time-dependent rotation matrix that is orthogonal, i.e., $Q_{ik}(t) Q_{jk}(t) = \delta_{ij}$. Derivation of Eq. (1.36) with respect to time provides us with the transformation rule for the velocity,

$$u_i \rightarrow \hat{u}_i = Q_{ij}(t) u_j + \dot{Q}_{ij}(t) x_j. \quad (1.37)$$

Here, the dot over $Q_{ij}(t)$ indicates derivation with respect to time.

Transforming the incompressible Navier–Stokes equations

We may now obtain the incompressible Navier–Stokes equations in a rotating frame of reference in two ways. We can either consider the forward transformation, from coordinates in the nonrotating, inertial frame of reference to coordinates in the rotating frame, or the backward (inverse) transformation.

For the forward transformation, one takes the incompressible Navier–Stokes equations in a nonrotating reference frame, Eq. (1.29), as starting point and tries to obtain the equations in a rotating frame of reference. This approach requires expressions of the original dependent variables in terms of the transformed variables. That is, we need to invert the transformation rule for the velocity field, Eq. (1.37). The transformation rule for the coordinates, Eq. (1.36), does not have to be inverted, because the coordinates only occur through derivatives. They can, therefore, be rewritten in terms of transformed coordinates using the chain rule.

To perform the backward transformation, one assumes that the original equations, Eq. (1.29), hold in a rotating frame. These equations should, thus, be read with hats appearing on each quantity. In this case, the transformation rule for the velocity field, Eq. (1.37), can simply be substituted. The transformation rule for the coordinates, Eq. (1.36), has to be inverted, however.

The forward and backward transformations only differ in the sense of the imposed frame rotation. We are, therefore, free to choose either approach. Since inverting the transformation rule for the coordinates, Eq. (1.36), is simpler than inversion of the velocity field transformation, Eq. (1.37), we employ the backward transformation.

The incompressible Navier–Stokes equations in a constantly rotating frame

For simplicity, we first assume the special case in which we have a constant-in-time rotation, also called a *solid body rotation*. We will take the x_3 -axis as the axis of rotation. The rotation matrix of Eqs. (1.36) and (1.37) then reduces to $Q_{ij}(t) = Q_{ij}^{2D}(t)$, which satisfies the relation $\dot{Q}_{ik}^{2D}(t) Q_{jk}^{2D}(t) = \epsilon_{3ij} \Omega_3$. Here, the superscript ‘2D’ indicates the rotation only takes place in planes perpendicular to the rotation axis. The *Levi-Civita symbol* or *alternating tensor* is given by

$$\epsilon_{ijk} = \begin{cases} +1 & \text{if } (i, j, k) = (1, 2, 3), (2, 3, 1) \text{ or } (3, 1, 2), \\ -1 & \text{if } (i, j, k) = (3, 2, 1), (1, 3, 2) \text{ or } (2, 1, 3), \\ 0 & \text{if } i = j \text{ or } j = k \text{ or } k = i \end{cases} \quad (1.38)$$

and the quantity Ω_3 is used to denote the constant rate of rotation about the x_3 -axis.

We supply each physical quantity in the incompressible Navier–Stokes equations, Eq. (1.29), with a hat and we apply the transformation rules of Eqs. (1.35) to (1.37). We assume that no body forces f_i are present. The resulting incompressible Navier–Stokes equations in a frame that is rotating with a constant rate Ω_3 are given by

$$\frac{\partial u_i}{\partial x_i} = 0, \quad (1.39a)$$

$$\begin{aligned} \frac{\partial u_i}{\partial t} + \frac{\partial}{\partial x_j} (u_i u_j) &= -\frac{1}{\rho} \frac{\partial p}{\partial x_i} + 2\nu \frac{\partial S_{ij}(u)}{\partial x_j} \\ &\quad - 2\Omega_3 (\delta_{i2} u_1 - \delta_{i1} u_2) + \Omega_3^2 (\delta_{i1} x_1 + \delta_{i2} x_2). \end{aligned} \quad (1.39b)$$

Here, for simplicity of notation, all quantities are written without hats. They should, however, be interpreted as quantities in the rotating frame of reference. That is, u_i and p are, respectively, used to denote the velocity field and pressure in the rotating frame of reference.

Comparison of Eq. (1.39) with the incompressible Navier–Stokes equations in a nonrotating, inertial frame of reference, Eq. (1.29), shows that the flow in a frame that is steadily rotating about the x_3 -axis can be said to experience a body force

$$f_i = -2\rho \Omega_3 (\delta_{i2} u_1 - \delta_{i1} u_2) + \rho \Omega_3^2 (\delta_{i1} x_1 + \delta_{i2} x_2), \quad (1.40)$$

comprising the Coriolis and centrifugal forces.

As we will see in Section 3.3.1, the body force of Eq. (1.40) can be absorbed in the pressure and, thus, is conservative. The potential corresponding to the Coriolis force is nonlocal, however. Here, we will, therefore, only absorb the centrifugal force in the pressure term. Defining the centrifugal force potential

$$F^{\text{centr}} = -\frac{1}{2} \rho \Omega_3^2 (x_1^2 + x_2^2), \quad (1.41)$$

we can rewrite Eq. (1.39) as

$$\frac{\partial u_i}{\partial x_i} = 0, \quad (1.42a)$$

$$\begin{aligned} \frac{\partial u_i}{\partial t} + \frac{\partial}{\partial x_j}(u_i u_j) = & -\frac{1}{\rho} \frac{\partial(p + F^{\text{centr}})}{\partial x_i} + 2\nu \frac{\partial S_{ij}(u)}{\partial x_j} \\ & - 2\Omega_3(\delta_{i2}u_1 - \delta_{i1}u_2). \end{aligned} \quad (1.42b)$$

The dimensionless incompressible Navier–Stokes equations in a constantly rotating frame

We can use the dimensionless variables of Eq. (1.16) to write the incompressible Navier–Stokes equations in a constantly rotating frame, Eq. (1.42), in a dimensionless form:

$$\frac{\partial u_i^*}{\partial x_i^*} = 0, \quad (1.43a)$$

$$\begin{aligned} \frac{\partial u_i^*}{\partial t^*} + \frac{\partial}{\partial x_j^*}(u_i^* u_j^*) = & -\frac{\partial(p^* + F^{\text{centr},*})}{\partial x_i^*} + \frac{2}{Re} \frac{\partial S_{ij}^*(u)}{\partial x_j^*} \\ & - Ro(\delta_{i2}u_1^* - \delta_{i1}u_2^*). \end{aligned} \quad (1.43b)$$

Here, the dimensionless centrifugal force potential $F^{\text{centr},*}$ is defined by dividing Eq. (1.41) by twice the dynamic pressure ρu_{ref}^2 and the dimensionless rate-of-strain tensor $S_{ij}^*(u)$ is defined in Eq. (1.33).

The rotation number

In Eq. (1.43), the *rotation number* is given by

$$Ro = \frac{2\Omega_3 L_{\text{ref}}}{u_{\text{ref}}}. \quad (1.44)$$

Flows in a constantly rotating frame that are not exposed to any other body forces than those originating from the frame rotation can be fully characterized using the Reynolds number Re of Eq. (1.34) and the rotation number Ro .

Other sets of two dimensionless numbers may, however, also be used to characterize such rotating flows. For example, the *Rossby number*, which is inversely proportional to the rotation number of Eq. (1.44), is also often employed in combination with the Reynolds number. In addition, one may replace the time scale $L_{\text{ref}}/u_{\text{ref}}$ that we implicitly used to derive Eq. (1.43) by a time scale involving Ω_3 .

The incompressible Navier–Stokes equations in an arbitrary rotating frame

Equation (1.39) may be generalized to the incompressible Navier–Stokes equations in a frame with a time-dependent rotation about an arbitrary axis. These

equations are given by (Pope 2011)

$$\frac{\partial u_i}{\partial x_i} = 0, \quad (1.45a)$$

$$\begin{aligned} \frac{\partial u_i}{\partial t} + \frac{\partial}{\partial x_j}(u_i u_j) = & -\frac{1}{\rho} \frac{\partial p}{\partial x_i} + 2\nu \frac{\partial S_{ij}(u)}{\partial x_j} \\ & - 2\epsilon_{ijk}\Omega_j u_k - \epsilon_{ijk}\Omega_j(\epsilon_{klm}\Omega_l x_m) - \epsilon_{ijk} \frac{\partial \Omega_j}{\partial t} x_k. \end{aligned} \quad (1.45b)$$

Here, Ω_i denotes the rotation rate about the x_i -axis. In an arbitrary rotating frame, the fluid, thus, experiences the body force

$$f_i = -2\rho \epsilon_{ijk}\Omega_j u_k - \rho \epsilon_{ijk}\Omega_j(\epsilon_{klm}\Omega_l x_m) - \rho \epsilon_{ijk} \frac{\partial \Omega_j}{\partial t} x_k, \quad (1.46)$$

comprising the Coriolis force, the centrifugal force and the *Euler* or *angular acceleration force*.

The centrifugal force is a conservative force with potential

$$F^{\text{centr}} = \frac{1}{2}\rho(x_j\Omega_j x_k\Omega_k - x_j x_j \Omega_k \Omega_k) \quad (1.47)$$

and may be absorbed in a modified pressure. Contrary to the Coriolis force resulting from a constant rotation about a single rotation axis, as contained in Eq. (1.39), the general Coriolis force is not a conservative force. This force may, however, be absorbed in the convective term of the momentum equation (Beddhu et al. 1996). If we ignore the Euler force, we can, therefore, write the incompressible Navier–Stokes equations in a rotating frame as

$$\frac{\partial u_i}{\partial x_i} = 0, \quad (1.48a)$$

$$\frac{\partial u_i}{\partial t} + \frac{\partial}{\partial x_i}[(u_i + 2u_i^{\text{Cor}})u_i] = -\frac{1}{\rho} \frac{\partial(p + F^{\text{centr}})}{\partial x_i} + 2\nu \frac{\partial S_{ij}(u)}{\partial x_j}, \quad (1.48b)$$

where the convected velocity is modified by the Coriolis force through

$$u_i^{\text{Cor}} = \epsilon_{ijk}\Omega_j x_k. \quad (1.49)$$

From Eq. (1.48) it is clear that both the Coriolis force and the centrifugal force conserve mass and momentum.

In the remainder of this thesis, we will only consider two types of body forces, namely, constant driving forces and forces originating from rotation. In the latter category, we will mostly focus on the forces originating from a solid body rotation. Unless otherwise indicated, we will not consider the effects of time-dependent rotations and the Euler or angular acceleration force. For simplicity, we will absorb the centrifugal force in the pressure throughout.

1.2.8 Derived quantities

Apart from the velocity field u_i , several other physical quantities play an important role in flows. We will consider the *vorticity*, which is defined as the curl of the velocity field,

$$\omega_i(u) = \epsilon_{ijk} \frac{\partial}{\partial x_j} u_k = -\epsilon_{ijk} W_{jk}(u), \quad (1.50)$$

as well as the kinetic energy, *enstrophy* and *helicity*.

The kinetic energy density of a flow is given by $\frac{1}{2}\rho u_i u_i$. We can, therefore, define the kinetic energy per unit mass by

$$k(u) = \frac{1}{2} u_i u_i. \quad (1.51)$$

We additionally define the enstrophy density as

$$e(u) = \frac{1}{2} \omega_i(u) \omega_i(u). \quad (1.52)$$

Finally, the helicity density is given by (Moreau 1961; Moffatt 1969)

$$h(u) = u_i \omega_i(u). \quad (1.53)$$

1.3 The Reynolds-averaged Navier–Stokes equations

The incompressible Navier–Stokes equations, Eq. (1.29), form a very accurate description of turbulent flows. As explained in Section 1.1, the behavior of most turbulent flows can, however, not yet accurately be predicted using these equations. This is because many turbulent flows contain a large range of physically relevant scales of motion, which cannot be resolved using the currently available computational power.

Therefore, several methods have been developed that aim to provide a description of turbulent flows that requires fewer degrees of freedom. We first discuss the method based on Reynolds averaging of the Navier–Stokes equations, which aims to obtain information about the average behavior of turbulent flows.

1.3.1 The Reynolds decomposition and Reynolds averaging

The Reynolds decomposition

In his seminal paper, Reynolds (1895) introduced a decomposition of the velocity field u_i of flows,

$$u_i = \langle u_i \rangle + u'_i, \quad (1.54)$$

into a mean velocity $\langle u_i \rangle$ and a relative velocity u'_i . This decomposition is called the *Reynolds decomposition*. Reynolds (1895) defined the mean velocity according to a spatial average, similar to the filtering operation which we discuss in Section 1.4.2. Nowadays, the mean velocity is usually defined through a statistical averaging procedure called *Reynolds averaging*.

Reynolds averaging

The *Reynolds* or *statistical average* of any random variable u can be expressed as (Pope 2011)

$$\langle u \rangle = \int_{u=-\infty}^{\infty} u P(u) \, du. \quad (1.55)$$

Here, the *probability density function* $P(u)$, which is assumed known, has to be nonnegative, $P(u) \geq 0$, and normalized,

$$\int_{u=-\infty}^{\infty} P(u) \, du = 1. \quad (1.56)$$

More generally, the statistical average of an arbitrary function $f(u)$ is given by

$$\langle f(u) \rangle = \int_{u=-\infty}^{\infty} f(u) P(u) \, du. \quad (1.57)$$

The averaging procedure defined by Eqs. (1.55) to (1.57) is a linear operation that satisfies

$$\langle u \langle v \rangle \rangle = \langle u \rangle \langle v \rangle \quad (1.58)$$

for any two random variables u and v . As a consequence, the *fluctuation* of u , which is defined as

$$u' = u - \langle u \rangle, \quad (1.59)$$

has a vanishing average. That is, we have

$$\langle u' \rangle = 0. \quad (1.60)$$

In addition, averaging commutes with differentiation with respect to time and space.

Alternative averaging procedures

In practice, the statistical average of u is often approximated using a time average,

$$\langle u \rangle \approx \frac{1}{T} \int_{t=0}^T u \, dt, \quad (1.61)$$

an average over a (homogeneous) flow direction,

$$\langle u \rangle \approx \frac{1}{L} \int_{x_i=0}^L u \, dx_i \quad (1.62)$$

and/or an average over an ensemble of different realizations of the random variable. Here, T and L have to represent sufficiently long intervals of time and space, respectively.

1.3.2 The Reynolds-averaged Navier–Stokes equations

The Reynolds-averaged Navier–Stokes equations

Applying the averaging procedure of Eqs. (1.55) to (1.57) to the incompressible Navier–Stokes equations, Eq. (1.29), and assuming no body forces are present, we obtain the Reynolds-averaged Navier–Stokes equations,

$$\frac{\partial \langle u_i \rangle}{\partial x_i} = 0, \quad (1.63a)$$

$$\frac{\partial \langle u_i \rangle}{\partial t} + \frac{\partial}{\partial x_j} (\langle u_i \rangle \langle u_j \rangle) = -\frac{1}{\rho} \frac{\partial \langle p \rangle}{\partial x_i} + 2\nu \frac{\partial S_{ij}(\langle u \rangle)}{\partial x_j} - \frac{\partial R_{ij}(u)}{\partial x_j}. \quad (1.63b)$$

Here, $\langle u_i \rangle$ and $\langle p \rangle$ represent the average velocity and pressure fields, respectively, and the average rate-of-strain tensor is given by

$$S_{ij}(\langle u \rangle) = \frac{1}{2} \left(\frac{\partial \langle u_i \rangle}{\partial x_j} + \frac{\partial \langle u_j \rangle}{\partial x_i} \right). \quad (1.64)$$

We have decomposed the average nonlinear term in such a way that a new term appears, namely, the divergence of the *Reynolds stresses*,

$$R_{ij}(u) = \langle u_i u_j \rangle - \langle u_i \rangle \langle u_j \rangle. \quad (1.65)$$

The Reynolds stresses are the one-point one-time autocovariance of the velocity field. Using the Reynolds decomposition, Eq. (1.54), and the properties of averaging given by Eqs. (1.58) and (1.60), we can also write the Reynolds stresses as

$$R_{ij}(u) = \langle u'_i u'_j \rangle. \quad (1.66)$$

Closure problem

The Reynolds stresses cannot be expressed in terms of the mean velocity $\langle u_i \rangle$. Therefore, the Reynolds-averaged Navier–Stokes equations, Eq. (1.63), contain fewer equations than unknowns and cannot be solved. Solutions, or rather approximate solutions, of the average velocity and pressure of turbulent flows can only be obtained if the Reynolds stresses are modeled.

In the current work, we will not pursue modeling of the Reynolds stresses. Rather, we will focus on large-eddy simulation, which is based on a mathematical description similar to that of the Reynolds-averaged Navier–Stokes equations but which allows for a more detailed description of turbulent flows.

1.4 Large-eddy simulation

Large-eddy simulation provides a description of turbulent flows with a level of detail lying between that of direct numerical simulations and the Reynolds-averaged Navier–Stokes approach. Specifically, large-eddy simulation is aimed at predicting the large-scale behavior of turbulent flows. To that end, the behavior of the large scales of motion in a flow is explicitly computed, whereas small-scale effects have to be modeled.

1.4.1 Assumptions

One of the primary assumptions underlying large-eddy simulation is the assumption that small-scale turbulent motions exhibit a certain universal behavior that is independent of the large-scale flow structure (Kolmogorov 1941). According to this assumption of *universality*, the small scales of motion in a turbulent flow and their effects on the large-scale motions are amenable to modeling.

Large-eddy simulation is additionally based on the related assumption of *scale separation*. That is, one assumes that the coupling between large and small scales of motion in turbulent flows is not very strong. Since all scales of motion in a turbulent flow are, in principle, coupled through the convective, nonlinear term appearing in the incompressible Navier–Stokes equations, Eq. (1.29), it is also often assumed that any coupling is dominated by the large-scale motions.

1.4.2 Filtering

In large-eddy simulation, large and small scales of motion are generally distinguished using a spatial *filtering* or *coarse-graining operation* (Leonard 1975; Sagaut 2006). Given a function u of the spatial coordinates x_i and time t , we can express this filtering operation as

$$\bar{u}(\vec{x}, t) = \int_{V'} u(\vec{x}', t) G(\vec{x}, \vec{x}') dV'. \quad (1.67)$$

Here, integration ranges over a spatial domain of interest V' , which may be as large as the full three-dimensional space. The function $G(\vec{x}, \vec{x}')$ represents a *filter kernel* that has to be normalized, i.e.,

$$\int_{V'} G(\vec{x}, \vec{x}') dV' = 1. \quad (1.68)$$

Contrary to what holds for the temporal and spatial averaging procedures introduced in Eqs. (1.61) and (1.62), the output \bar{u} of the spatial filtering operation of Eq. (1.67) is a function of the same independent variables as the input u .

If we assume the use of a *homogeneous filter*, which has the same form regardless of the position in space, Eq. (1.67) reduces to the convolution integral

$$\bar{u}(\vec{x}, t) = \int_{V'} u(\vec{x}', t) G(\vec{x} - \vec{x}') dV'. \quad (1.69)$$

An example of a homogeneous filter is the *top-hat* or *box filter*, which has the kernel

$$G(\vec{x} - \vec{x}') = \begin{cases} 1/\bar{\delta} & \text{if } |\vec{x} - \vec{x}'| \leq \bar{\delta}/2, \\ 0 & \text{otherwise.} \end{cases} \quad (1.70)$$

Here, $\bar{\delta}$ represents the *filter length* that is associated with filtering. For each point in the space of interest, the box-filtered quantity \bar{u} contains the spatial

average of the function u over a cube of side $\bar{\delta}$ centered around that point. The box filter, thus, removes details of a scale smaller than size $\bar{\delta}$ from a given input function.

Given a spatial filtering operation that removes small-scale details, we may introduce a decomposition of a function u ,

$$u = \bar{u} + u', \quad (1.71)$$

into a *filtered* component \bar{u} and a *subfilter-scale* (SFS) component u' . The subfilter-scale component u' can also be called the *fluctuation*. Unlike the averaging procedures introduced in Section 1.3.1, spatial filtering is not, in general, a projective operation, that is,

$$\overline{\bar{u}} \neq \bar{u}. \quad (1.72)$$

As a consequence, the filtered fluctuation is not generally zero,

$$\overline{u'} \neq 0. \quad (1.73)$$

1.4.3 The filtered incompressible Navier–Stokes equations

The filtered incompressible Navier–Stokes equations

To filter the incompressible Navier–Stokes equations, Eq. (1.29), we will assume the use of a filtering operation that commutes with differentiation. Assuming in addition that no body forces are present, we see that the evolution of incompressible filtered velocity fields can formally be described by the filtered incompressible Navier–Stokes equations given by

$$\frac{\partial \bar{u}_i}{\partial x_i} = 0, \quad (1.74a)$$

$$\frac{\partial \bar{u}_i}{\partial t} + \frac{\partial}{\partial x_j} (\bar{u}_i \bar{u}_j) = -\frac{1}{\rho} \frac{\partial \bar{p}}{\partial x_i} + 2\nu \frac{\partial S_{ij}(\bar{u})}{\partial x_j} - \frac{\partial \tau_{ij}(u)}{\partial x_j}. \quad (1.74b)$$

Here, \bar{u}_i and \bar{p} , respectively, represent the filtered velocity and pressure fields. The filtered rate-of-strain tensor is denoted by $S_{ij}(\bar{u})$.

We have decomposed the filtered convective term in such a way that a new term appears, namely, the divergence of the *turbulent* or *subfilter-scale stress tensor*,

$$\tau_{ij}(u) = \overline{u_i u_j} - \bar{u}_i \bar{u}_j. \quad (1.75)$$

The turbulent stress tensor represents the interactions between large (filtered) and small (subfilter) scales of motion.

The closure problem of large-eddy simulation

Since the turbulent stress tensor is not solely expressed in terms of the filtered velocity field \bar{u}_i , Eq. (1.74) is not closed and cannot be solved. We have to model $\tau_{ij}(u)$ to solve this closure problem.

1.4.4 Large-eddy simulation without explicit filtering

The equations of large-eddy simulation

We will consider modeling of the turbulent stresses within the context of *large-eddy simulation without explicit filtering*. That is, we look for closure models $\tau_{ij}^{\text{mod}}(v)$ for the turbulent stress tensor $\tau_{ij}(u)$ of Eq. (1.75), such that the set of equations given by

$$\frac{\partial v_i}{\partial x_i} = 0, \quad (1.76a)$$

$$\frac{\partial v_i}{\partial t} + \frac{\partial}{\partial x_j}(v_i v_j) = -\frac{1}{\rho} \frac{\partial q}{\partial x_i} + 2\nu \frac{\partial S_{ij}(v)}{\partial x_j} - \frac{\partial \tau_{ij}^{\text{mod}}(v)}{\partial x_j} \quad (1.76b)$$

provides accurate approximations of the filtered velocity and pressure. In other words, we aim to choose the closure model $\tau_{ij}^{\text{mod}}(v)$ in such a way that $v_i \approx \bar{u}_i$ and $q \approx \bar{p}$.

We will refer to Eq. (1.76) as the *equations of large-eddy simulation*. Since we focus on large-eddy simulation without explicit filtering, no overbars appear in these equations. The resemblance between Eq. (1.29) and Eq. (1.76) reveals that a practical large-eddy simulation without explicit filtering consist in numerically solving the Navier–Stokes equations, Eq. (1.29), on a coarse grid, with the addition of a forcing term that is meant to represent the effects of the unresolved, subgrid-scale motions on the large-scale flow behavior.

We will accordingly call v_i , q and $S_{ij}(v)$ the *resolved* or *large-scale* velocity field, pressure and rate-of-strain tensor, and we will refer to the closure model $\tau_{ij}^{\text{mod}}(v)$ as a subgrid-scale (stress) model. We will also refer to subgrid-scale models as turbulence models.

1.4.5 Large-eddy simulation of rotating turbulent flows

The filtered incompressible Navier–Stokes equations in a rotating frame

We obtained the filtered incompressible Navier–Stokes equations in an inertial frame of reference, Eq. (1.74), by filtering the incompressible Navier–Stokes equations, Eq. (1.29). In a similar way, we may filter Eq. (1.45) to obtain the filtered incompressible Navier–Stokes equations in a rotating frame of reference,

$$\frac{\partial \bar{u}_i}{\partial x_i} = 0, \quad (1.77a)$$

$$\frac{\partial \bar{u}_i}{\partial t} + \frac{\partial}{\partial x_j}(\bar{u}_i \bar{u}_j) = -\frac{1}{\rho} \frac{\partial \bar{p}}{\partial x_i} + 2\nu \frac{\partial S_{ij}(\bar{u})}{\partial x_j} - 2\epsilon_{ijk} \Omega_j \bar{u}_k - \frac{\partial \tau_{ij}(u)}{\partial x_j}. \quad (1.77b)$$

Here, \bar{u}_i and \bar{p} , respectively, represent the filtered velocity and pressure fields in the rotating frame of reference. The filtered rate-of-strain tensor $S_{ij}(\bar{u})$ and the turbulent stress tensor $\tau_{ij}(u)$ are also defined in the rotating frame. The

centrifugal force is absorbed in the pressure and the rates of rotation Ω_i are assumed to be constant in time.

The equations of large-eddy simulation in a rotating frame

We define the corresponding equations of large-eddy simulation in a rotating frame of reference as

$$\frac{\partial v_i}{\partial x_i} = 0, \quad (1.78a)$$

$$\frac{\partial v_i}{\partial t} + \frac{\partial}{\partial x_j}(v_i v_j) = -\frac{1}{\rho} \frac{\partial q}{\partial x_i} + 2\nu \frac{\partial S_{ij}(v)}{\partial x_j} - 2\epsilon_{ijk} \Omega_j v_k - \frac{\partial \tau_{ij}^{\text{mod}}(v)}{\partial x_j}. \quad (1.78b)$$

Here, the large-scale velocity v_i , pressure q , rate-of-strain tensor $S_{ij}(v)$ and subgrid-scale model $\tau_{ij}^{\text{mod}}(v)$ are all defined in the rotating frame of reference. The pressure again includes the centrifugal force and the rates of rotation Ω_i are assumed to be constant in time.

1.4.6 Notation

For brevity, we will write the (true) turbulent stress tensor of Eq. (1.75) as

$$\tau_{ij} = \tau_{ij}(u) \quad (1.79)$$

in what follows. In addition, we will employ the short-hand notation

$$\tau_{ij}^{\text{mod}} = \tau_{ij}^{\text{mod}}(v), \quad G_{ij} = G_{ij}(v), \quad S_{ij} = S_{ij}(v), \quad W_{ij} = W_{ij}(v) \quad (1.80)$$

for subgrid-scale models, and the large-scale velocity gradient, rate-of-strain and rate-of-rotation tensors. Where convenient we will employ matrix notation for these quantities, dropping all indices. Finally, we will write the vorticity, the kinetic energy per unit mass, the enstrophy and helicity densities, and the Reynolds stresses corresponding to the large-scale velocity field v_i as

$$\omega_i = \omega_i(v), \quad k = k(v), \quad e = e(v), \quad h = h(v), \quad R_{ij} = R_{ij}(v). \quad (1.81)$$

In Part I of this thesis, we will focus on the description of flows in an inertial frame of reference, as provided by the incompressible Navier–Stokes equations, Eq. (1.29), and the equations of large-eddy simulation, Eq. (1.76). The quantities of Eqs. (1.79) to (1.81) are then defined with respect to this inertial frame. In Part II, we study turbulent flows from a constantly rotating frame of reference by using the incompressible Navier–Stokes equations and equations of large-eddy simulation in a rotating frame, Eqs. (1.42) and (1.78). The quantities of Eqs. (1.79) to (1.81) are then defined relative to the rotating frame.

1.5 Thesis overview

Fluid flows are everywhere. Think, for example, of rivers, the flow of air in the atmosphere and the blood that is flowing through our veins. Most flows are turbulent and the prediction of their behavior is essential for many applications, including the design of cars, boats and airplanes. However, accurately predicting turbulent flows is very challenging, as computers do not have enough memory to store all flow details.

With the aim to improve the numerical prediction of incompressible turbulent flows, we will, therefore, make use of large-eddy simulation. In large-eddy simulation, only the large eddies in flows are computed directly, while small eddies have to be described using turbulence models. The question, however, is: how to create such models? Several answers to this question can be given. One could, for example, select one of the many turbulence models that have been developed since the advent of computational fluid dynamics. The question remains, however: what defines a well-designed turbulence model?

In this thesis, we will, therefore, focus on the construction of physics-based turbulence models, which are turbulence models that respect the physical and mathematical properties of flows. The main question that we consider is:

How to create physics-based turbulence models for large-eddy simulations of incompressible turbulent flows?

In Part I of this thesis, we aim to answer this question by following a systematic approach. In particular, we first discuss in detail several fundamental physical and mathematical properties of flows. We then outline existing and propose new requirements that turbulence models have to satisfy in order to preserve these properties. In this fashion, we obtain a framework of constraints for the construction of physics-based turbulence models. We use this framework to analyze the properties of several existing turbulence models. We also illustrate how new physics-based turbulence models can be created systematically and we provide examples of such models.

In Part II, we apply the framework of model constraints to improve the numerical prediction of rotating turbulent flows. Specifically, we first propose a new physics-based turbulence model for large-eddy simulations of such flows. We subsequently study and validate this model using detailed computations of rotating flows. Finally, we determine how the proposed model performs in comparison to a number of existing turbulence models.

As we will see, the framework of model constraints allows us to systematically create physics-based turbulence models that respect most of the properties of flows. These models can be used in arbitrary flow domains, without requiring so-called near-wall damping functions or dynamic procedures. Moreover, they are suitable for simulations of laminar, transitional and turbulent flows. We study in detail one such a physics-based turbulence model and we show that this model provides outstanding predictions of rotating flows. We also demonstrate that these predictions are either as good as or much better than predictions from

existing turbulence models. Our work can, thus, aid in improving predictions of both rotating and nonrotating turbulent flows.

We provide a detailed discussion of our findings and conclusions in Part [I](#) and Part [II](#) of this thesis. Both parts contain their own abstracts, introductions and conclusion chapters. An overarching summary of the current work is provided on page [219](#). An overview of the publications and presentations that led up to this thesis starts on page [201](#).



Part I

Theory:

Model constraints for large-eddy simulation

Abstract We study the construction of subgrid-scale models for large-eddy simulations of incompressible turbulent flows. In particular, we aim to consolidate a systematic approach of constructing subgrid-scale models, based on the idea that it is desirable that subgrid-scale models are consistent with the fundamental physical and mathematical properties of the Navier–Stokes equations and the turbulent stresses. To that end, we first discuss in detail the symmetries and conservation laws of the Navier–Stokes equations. We also discuss the dissipation properties, realizability and near-wall scaling behavior of the turbulent stresses. We then outline existing and propose new requirements that subgrid-scale models have to satisfy in order to preserve these important physical and mathematical properties.

In this fashion, we obtain a framework of constraints for the construction of physics-based subgrid-scale models, which can be used to analyze existing and to create new subgrid-scale models. We first apply this framework to a general class of subgrid-scale models based on the local velocity gradient. We then analyze the behavior of a number of existing models from this class and show that these models do not satisfy all the desired properties. This conclusion can partly be understood from incompatibilities between model constraints and limitations of the considered class of subgrid-scale models. However, we also reason that there is room for improvement in the properties and, hence, the behavior of existing subgrid-scale models. Finally, we use the developed framework of model constraints to propose a systematic procedure for the construction of physics-based subgrid-scale models that have built-in desirable properties. We also provide a few examples of such models.

Partly published as

Silvis, M. H., Remmerswaal, R. A., and Verstappen, R. (2017). “Physical consistency of subgrid-scale models for large-eddy simulation of incompressible turbulent flows”. *Phys. Fluids* 29, 015105. DOI: [10.1063/1.4974093](https://doi.org/10.1063/1.4974093).

Chapter 2

Introduction

Large-eddy simulation

As explained in Section 1.3, the incompressible Navier–Stokes equations, given by Eq. (1.29), form a very accurate description of turbulent flows. The behavior of most turbulent flows can, however, not yet accurately be predicted using these equations, because the current computational power does not suffice to resolve all physically relevant scales of motion in such flows. We, therefore, turn to large-eddy simulation to predict the large-scale behavior of incompressible turbulent flows.

Challenges of subgrid-scale modeling

In large-eddy simulation, the large scales of motion in a flow are explicitly computed, whereas effects of small-scale motions have to be modeled. Here, the question is:

How to model the effects of small-scale motions on the large scales of motion in turbulent flows?

Several answers to this question can be found in the literature. For example, since the advent of computational fluid dynamics many subgrid-scale models have been proposed and successfully applied to the simulation of a wide range of turbulent flows (see, e.g., the encyclopedic work of Sagaut 2006). Given the variety of models present in the literature, the question remains, however:

What defines a well-designed subgrid-scale model?

Systematic approach

Some authors have, therefore, taken a systematic approach of finding constraints for the construction of subgrid-scale models (Speziale 1985a; Vreman et al. 1994b; Oberlack 1997; Vreman 2004; Razafindralandy et al. 2007; Rebholz 2007; Nicoud et al. 2011; Verstappen 2011) (also refer to the extensive review by Ghosal 1999). Most of these constraints are based on the idea that it is desirable that subgrid-scale models are consistent with important physical and mathematical properties of the Navier–Stokes equations and the turbulent stresses. In this part of this thesis, we aim to consolidate this systematic approach. We specifically aim to obtain a framework for the assessment of existing and the creation of new physics-based subgrid-scale models for large-eddy simulation.

Constraints on subgrid-scale models

Properties of the Navier–Stokes equations

Constraints on the properties of subgrid-scale models come in several forms. For example, it is well known that the incompressible Navier–Stokes equations are invariant under certain transformations, such as instantaneous rotations of the coordinate system and the Galilean transformation (Pope 2011). Such transformations, also referred to as *symmetries*, play an important physical role because they make sure that the description of fluids is the same in all inertial frames of reference. Furthermore, they relate to scaling laws, such as the log law of wall-bounded flows (Oberlack 1997; Razafindralandy et al. 2007).

To ensure physical consistency, one could, therefore, argue that it is desirable that subgrid-scale models preserve the symmetries of the incompressible Navier–Stokes equations. Speziale (1985a) was the first to emphasize the importance of Galilean invariance of subgrid-scale models for large-eddy simulation. Later, Oberlack (1997) formulated requirements to make subgrid-scale models compatible with all the known symmetries of the incompressible Navier–Stokes equations. An example of a class of models that was designed to preserve the symmetries of the incompressible Navier–Stokes equations can be found in the work of Razafindralandy et al. (2007).

The conservation laws of the Navier–Stokes equations (Cheviakov and Oberlack 2014) form another fundamental property of turbulent flows. Rebholz (2007), therefore, argues that subgrid-scale models should respect these laws. Thus, it seems desirable that subgrid-scale models satisfy both the symmetry and conservation properties of the incompressible Navier–Stokes equations.

Properties of the turbulent stresses

Using large-eddy simulation, we hope to obtain a good approximation of the large-scale behavior of turbulent flows. Therefore, one could also argue that it is desirable that subgrid-scale models share some basic properties with the true turbulent stresses that appear in the filtered incompressible Navier–Stokes equations, Eq. (1.74). The true turbulent stresses, for example, have certain dissipation properties, they exhibit realizability (Vreman et al. 1994b) and they were observed to have a certain near-wall scaling behavior (Chapman and Kuhn 1986).

Examples of subgrid-scale models that exhibit the same near-wall scaling behavior as the turbulent stresses are given by the WALE model (Nicoud and Ducros 1999), the σ model (Nicoud et al. 2011) and the S3PQR models (Trias et al. 2015). The dissipation behavior of the turbulent stresses was studied by Vreman (2004), who proposed a model that has a vanishing subgrid dissipation whenever the true turbulent stresses are not causing energy transfer to subgrid scales. The QR model (Verstappen et al. 2010; Verstappen 2011; Verstappen et al. 2014), the anisotropic minimum-dissipation model (Rozema et al. 2015) and the recently developed scaled anisotropic minimum-dissipation model (Ver-

stappen 2018) were designed to exhibit a particular dissipation behavior that leads to scale separation between large and small scales of motion.

The property of realizability of the turbulent stresses pertains to subgrid-scale models that, unlike the eddy viscosity models mentioned so far, include a model for the generalized subfilter-scale kinetic energy. Examples of realizable models are the gradient model (Leonard 1975; Clark et al. 1979) and the explicit algebraic subgrid-scale stress model (Marstorp et al. 2009). We will shortly discuss in more detail the properties of the turbulent stress tensor and the corresponding constraints for subgrid-scale models.

Additional properties

A feature of interest of the gradient and explicit algebraic subgrid-scale stress models is that they contain terms that are nonlinear in the local velocity gradient. As a consequence, they can describe nondissipative processes, allowing us to go beyond the dissipative description of turbulent flows that is provided by eddy viscosity models.

Other studies of subgrid-scale models that are nonlinear in the velocity gradient were, for instance, conducted by Lund and Novikov (1992), Kosović (1997), Wang and Bergstrom (2005), and Wendling and Oberlack (2007). For an extensive review of the use of nonlinear models in the context of the Reynolds-averaged Navier–Stokes equations, see Gatski and Jongen (2000). The reader that seeks detailed background information about nonlinear constitutive equations and their role in describing fluid flows in general is referred to the book by Deville and Gatski (2012).

Apart from the requirements on the near-wall scaling behavior of subgrid-scale models, all model constraints discussed in this part of this thesis arise from analytical, deterministic considerations. For information about conditions on the statistical properties of subgrid-scale models, see, e.g., Langford and Moser (1999). Also refer to the work by Meneveau and Marusic (2013), and Stevens et al. (2014).

Outline

In Chapter 3, we provide a detailed discussion of the aforementioned physical and mathematical properties of the Navier–Stokes equations and the turbulent stresses. We also outline the requirements that subgrid-scale models have to satisfy in order to preserve these properties. In Chapter 4, we apply the framework of model constraints that so arises to a general class of subgrid-scale models based on the velocity gradient. We subsequently perform a systematic analysis of the properties of a number of existing subgrid-scale models that are based on velocity gradient in Chapter 5. In Chapter 6, we illustrate how new physics-based subgrid-scale models, which have desired built-in properties, can be designed. We also provide examples of such new models. Finally, in Chapter 7, we discuss the conclusions of this part of this thesis.

Chapter 3

Model constraints

3.1 Introduction

As was alluded to in Chapter 2, the incompressible Navier–Stokes equations, Eq. (1.29), and the turbulent stress tensor τ_{ij} , defined in Eq. (1.75), have several fundamental physical and mathematical properties. One could argue that, to ensure physical consistency, it is desirable that these properties are also exhibited by the equations of large-eddy simulation, Eq. (1.76), and are not lost when modeling the turbulent stresses. In what follows, we will, therefore, provide a detailed discussion of several properties of the Navier–Stokes equations and the turbulent stresses. We also discuss the constraints that subgrid-scale models have to satisfy in order to preserve these properties.

In Section 3.2, we briefly discuss the desired physical dimensions of subgrid-scale models. Then, in Sections 3.3 to 3.5, we consider the symmetries and conservation laws of the incompressible Navier–Stokes equations, as well as their consequences for subgrid-scale modeling. We discuss existing and propose new constraints on the dissipation caused by subgrid-scale models in Section 3.6, whereas considerations relating to realizability are treated in Section 3.7. In Section 3.8, we discuss the desired near-wall scaling behavior of subgrid-scale models. A brief summary of this chapter is provided in Section 3.9.

3.2 Dimensional requirements

The turbulent stress tensor τ_{ij} of Eq. (1.75) has the physical dimensions of a squared velocity. To ensure dimensional consistency of the equations of large-eddy simulation, Eq. (1.76), a subgrid-scale model should have these same units. Any subgrid-scale model, therefore, has to satisfy the requirement

$$U: [\tau_{ij}^{\text{mod}}] = \text{m}^2 \text{s}^{-2}. \quad (3.1)$$

Here, U is the label that we will use to refer to this requirement.

3.3 Symmetry requirements

The Navier–Stokes equations are invariant under several transformations of the coordinate system (see, e.g., Pope 2011). As mentioned in Chapter 2, these transformations, or symmetries, play an important physical role because they ensure that the description of fluids is the same in all inertial frames of reference.

They furthermore relate to scaling laws (Razafindralandy et al. 2007). Speziale (1985a), Oberlack (1997, 2002) and Razafindralandy et al. (2007), therefore, argue that it is desirable that the equations of large-eddy simulation, Eq. (1.76), admit the same symmetries as the Navier–Stokes equations, Eq. (1.29).

3.3.1 Symmetries of the incompressible Navier–Stokes equations

The incompressible Navier–Stokes equations, Eq. (1.29), are invariant under the following coordinate transformations (Pope 2011; Oberlack 1997, 2002; Razafindralandy et al. 2007):

- the time translation,

$$(t, x_i, u_i, p) \rightarrow (t + T, x_i, u_i, p); \quad (3.2)$$

- the pressure translation,

$$(t, x_i, u_i, p) \rightarrow (t, x_i, u_i, p + P(t)); \quad (3.3)$$

- the generalized Galilean transformation,

$$(t, x_i, u_i, p) \rightarrow (t, x_i + X_i(t), u_i + \dot{X}_i(t), p - \rho x_i \ddot{X}_i(t)); \quad (3.4)$$

- orthogonal transformations,

$$(t, x_i, u_i, p) \rightarrow (t, Q_{ij}x_j, Q_{ij}u_j, p); \quad (3.5)$$

- a scaling transformation,

$$(t, x_i, u_i, p) \rightarrow (e^{2a}t, e^a x_i, e^{-a}u_i, e^{-2a}p); \quad (3.6)$$

- and a solid body rotation of a two-component flow,

$$(t, x_i, u_i, p) \rightarrow (t, Q_{ij}^{2D}(t)x_j, Q_{ij}^{2D}(t)u_j + \dot{Q}_{ij}^{2D}(t)x_j, \quad (3.7) \\ p + \frac{1}{2}\rho\Omega_3^2(x_1^2 + x_2^2) + 2\rho\Omega_3\psi).$$

In the time and pressure translations, Eqs. (3.2) and (3.3), T and $P(t)$ indicate an arbitrary time shift and a time variation of the (background) pressure, respectively. The generalized Galilean transformation, Eq. (3.4), represents arbitrary time-dependent translations of the frame of reference. This transformation encompasses the space translation for a constant $X_i(t)$ and the classical Galilean transformation for $X_i(t)$ linear in time. Orthogonal transformations of the coordinate frame, Eq. (3.5), are represented by a time-independent matrix Q_{ij} that is orthogonal, i.e., $Q_{ik}Q_{jk} = \delta_{ij}$. These transformations correspond to instantaneous rotations and reflections of the coordinate system, and include parity or spatial inversion (Frisch 1995).

The scaling transformation of Eq. (3.6) is parametrized by a real a . This transformation, in which time and space are scaled simultaneously, forms the mathematical basis of the principle of Reynolds number similarity, which we discussed after defining the Reynolds number in Eq. (1.34). In addition, this scaling transformation relates to the appearance of scaling laws like the log law of wall-bounded flows (Oberlack 1997; Razafindralandy et al. 2007).

The transformation of Eq. (3.7) represents a solid body rotation of the coordinate system about the x_3 -axis. As discussed in the context of the incompressible Navier–Stokes equations in a constantly rotating frame, Eq. (1.39), this transformation is characterized by a time-dependent rotation matrix that we denote by $Q_{ij}^{2D}(t)$. This matrix satisfies $\dot{Q}_{ik}^{2D}(t) Q_{jk}^{2D}(t) = \epsilon_{3ij} \Omega_3$, where Ω_3 represents the constant rate of rotation about the x_3 -axis. For the purposes of this transformation, the flow is assumed to depend only on the x_1 - and x_2 -directions, for which ψ represents the two-dimensional stream function.

Invariance under the transformation of Eq. (3.7) is called *two-dimensional material frame indifference* (2DMFI) or, more precisely, *material frame indifference in the limit of a two-component flow* (Speziale 1998). Refer to Oberlack (2002) for more information about the interpretation of two-dimensional material frame indifference as an invariance (and not a material) property. To avoid confusion, we remark that not all references provide the same expression for the pressure in the rotating frame (Oberlack 1997, 2002; Razafindralandy et al. 2007). To the best of our knowledge, the expression we provide in Eq. (3.7), which matches that of Oberlack (2002), is correct.

3.3.2 Symmetry requirements

To ensure physical consistency with the Navier–Stokes equations, Eq. (1.29), we require that the equations of large-eddy simulation, Eq. (1.76), are invariant under the symmetry transformations of Eqs. (3.2) to (3.7). Because of the notation used in Eq. (1.76), we have to read v_i instead of u_i and q instead of p in these symmetry transformations. The resulting symmetry requirements on the transformation behavior of the modeled subgrid-scale stresses are (Oberlack 1997)

$$\text{S1-3: } \hat{\tau}_{ij}^{\text{mod}} = \tau_{ij}^{\text{mod}}, \quad (3.8)$$

$$\text{S4: } \hat{\tau}_{ij}^{\text{mod}} = Q_{im} Q_{jn} \tau_{mn}^{\text{mod}}, \quad (3.9)$$

$$\text{S5: } \hat{\tau}_{ij}^{\text{mod}} = e^{-2a} \tau_{ij}^{\text{mod}}, \quad (3.10)$$

$$\text{S6: } \hat{\tau}_{ij}^{\text{mod}} = Q_{im}^{2D}(t) Q_{jn}^{2D}(t) \tau_{mn}^{\text{mod}}. \quad (3.11)$$

In symmetry requirements S1 to S3, Eq. (3.8), the hat indicates application of the time or pressure translations, or the generalized Galilean transformation (see Eqs. (3.2) to (3.4)). Symmetry requirements S4 and S5 ensure invariance under instantaneous rotations and reflections, Eq. (3.5), and the scaling transformation of Eq. (3.6), respectively. Material frame indifference in the limit of a two-component flow, i.e., invariance under Eq. (3.7), holds when Eq. (3.11) is

satisfied. In the case of explicitly filtered large-eddy simulations, also the filtering operation needs to satisfy certain requirements to ensure that the above symmetry properties are not destroyed (Oberlack 1997; Razafindralandy et al. 2007).

3.4 Symmetry breaking requirements

The coordinate transformations of Eqs. (3.2) to (3.7) form the complete set of known symmetries of the incompressible Navier–Stokes equations, Eq. (1.29). Several more coordinate transformations that are not symmetries of the Navier–Stokes equations play an important role in mechanics, however. In this section, we will argue that subgrid-scale models should not be invariant under these coordinate transformations.

3.4.1 Symmetries of the incompressible Euler equations

The incompressible Euler equations, Eq. (1.13), are invariant under two more coordinate transformations than the incompressible Navier–Stokes equations, namely, (Oberlack 2002)

- time reversal,

$$(t, x_i, u_i, p) \rightarrow (-t, x_i, -u_i, p); \quad (3.12)$$

- and a spatial scaling transformation,

$$(t, x_i, u_i, p) \rightarrow (t, e^b x_i, e^b u_i, e^{2b} p). \quad (3.13)$$

Here, the scaling transformation is parametrized by a real b .

Combining the scaling transformations of Eqs. (3.6) and (3.13), we see that the incompressible Euler equations can be scaled independently in time and space. These transformations originate from the fact that, in inviscid mechanics, arbitrary units can be used to measure space and time (Oberlack 2002). They underlie the scale similarity of the incompressible Euler equations, which we discussed in Section 1.2.5 after introducing the dimensionless incompressible Euler equations, Eq. (1.17).

3.4.2 The Euclidean transformation and three-dimensional material frame indifference

Another coordinate transformation that does not form a symmetry of the Navier–Stokes equations and that is mostly considered in solid mechanics is

- the Euclidean transformation,

$$\begin{aligned} (t, x_i, u_i, p) \rightarrow & (t, Q_{ij}^{3D}(t) x_j + X_i(t), \\ & Q_{ij}^{3D}(t) u_j + \dot{Q}_{ij}^{3D}(t) x_j + \dot{X}_i(t), p). \end{aligned} \quad (3.14)$$

This transformation combines an arbitrary time-dependent rotation of the coordinate system, characterized by the rotation matrix $Q_{ij}^{3D}(t)$, with an arbitrary time-dependent translation characterized by $X_i(t)$. The superscript ‘3D’ is used to distinguish arbitrary rotations from the solid body rotations of Eq. (3.7).

The constitutive equation for the viscous stresses experienced by a Newtonian fluid, Eq. (1.23), forms an example of an equation that is invariant under the Euclidean transformation. Invariance under the Euclidean transformation is also called *three-dimensional material frame indifference* (3DMFI), which is not to be confused with the notion of two-dimensional material frame indifference discussed in Section 3.3.1.

3.4.3 Symmetry breaking requirements

Time reversal invariance and invariance under the spatial scaling transformation of Eq. (3.13) form fundamental properties of the incompressible Euler equations, Eq. (1.13). Similarly, invariance under the Euclidean transformation, Eq. (3.14), forms an important property of the viscous stress tensor of Newtonian fluids, Eq. (1.23).

However, the incompressible Navier–Stokes equations are not invariant under the coordinate transformations of Eqs. (3.12) to (3.14). Indeed, the diffusive term of the incompressible Navier–Stokes equations breaks time reversibility as well as spatial scaling invariance. Furthermore, Eq. (1.45) shows that additional forces such as the Coriolis force appear in a frame undergoing an arbitrary time-dependent rotation. Therefore, we can wonder whether the description of turbulence provided by subgrid-scale models should be invariant under the transformations of Eqs. (3.12) to (3.14) or not. In what follows, we discuss each transformation separately.

First, the turbulent stress tensor τ_{ij} of Eq. (1.75) is invariant under time reversal, Eq. (3.12) (Berselli et al. 2006). Time reversibility should, however, not be regarded as a desirable property of subgrid-scale models. Carati et al. (2001) and Winkelmann et al. (2001) argue that, in practical large-eddy simulations, subgrid-scale models have to cause an irreversible loss of information. Therefore, at least one of the terms comprising a subgrid-scale model has to break time reversal invariance.

Secondly, the turbulent stress tensor transforms as a squared length scale under the spatial scaling transformation of Eq. (3.13). The divergence of the turbulence stresses, thus, has the same transformation behavior as the convective term in the filtered incompressible Navier–Stokes equations, Eq. (1.74). This behavior should, however, not be reflected by subgrid-scale models. As we will explain in Section 3.6, subgrid-scale models need to contribute to the dissipation of kinetic energy. Subgrid-scale models should, therefore, have a component that is similar to the diffusive term of the incompressible Navier–Stokes equations, Eq. (1.29). This diffusive term breaks spatial scaling invariance, which is a property that should, thus, also hold for subgrid-scale models.

Finally, the definition of the turbulent stress tensor τ_{ij} of Eq. (1.75) is not invariant under the Euclidean transformation, Eq. (3.14) (Speziale 1985b). That

is, this definition will contain terms that depend on the frame rotation when transformed to a frame of reference undergoing rotation. On the other hand, the divergence of the turbulent stresses transforms in the same way as the coordinate vector x_i , if an isotropic filter is employed (Speziale 1985b). With this specific filter, the force exerted by the turbulent stresses, thus, does not depend on the choice of (rotating) reference frame. The question, therefore, is whether turbulence should in general be modeled using a subgrid-scale model that is three-dimensional material frame indifferent or not.

One could answer this question by arguing that the description of turbulence has to be the same for all observers, regardless of their choice of coordinate system. As Frewer (2009) explains, however, only inertial frames of reference are equivalent in the sense that they cannot be distinguished from each other experimentally. There is no equivalence principle for noninertial frames of reference. Therefore, one cannot argue a priori that the description of turbulence should be the same for all observers. Only analysis of the behavior of turbulence can shed light on this issue.

In this context, Speziale (1985b) found that the evolution equation for the small-scale component of a turbulent velocity field contains a Coriolis term. Turbulent motions, thus, are not independent of rotation. The effects of the Coriolis force on the small-scale velocity field decrease as the ratio between the characteristic time scales of the small- and large-scale motions becomes smaller. If this ratio is small in actual turbulent flows, turbulence can be said to be three-dimensional material frame indifferent in an approximate sense.

Speziale (1985b) first argued that one can reasonably assume that the effect of the Coriolis force on turbulence is negligibly small. Later, he discussed evidence from numerical experiments, which shows that turbulence is sensitive to frame rotation (Speziale 1998). Concurring with Lumley (1970), he, therefore, concluded that material frame indifference breaks down for three-dimensional turbulence (Speziale 1998). Subgrid-scale models should, therefore, break three-dimensional material frame indifference by being sensitive to frame rotation.

Weis and Hutter (2003) use arguments of invariance to reason that such frame dependence of subgrid-scale models may only be introduced through the *absolute rate-of-rotation tensor*. This tensor can be obtained by adding the frame rotation to the rate-of-rotation tensor computed in a rotating frame. However, as mentioned above, there is no equivalence principle that requires turbulence models to have the same form in all noninertial frames of reference (Frewer 2009). Experimental observations should, therefore, be used to determine in which way subgrid-scale models have to be rotation dependent.

In summary, subgrid-scale models should break time reversal invariance, spatial scaling invariance and Euclidean invariance. We, therefore, present the symmetry breaking requirements

$$\text{B1: } \hat{\tau}_{ij}^{\text{mod}} \neq \tau_{ij}^{\text{mod}}, \quad (3.15)$$

$$\text{B2: } \hat{\tau}_{ij}^{\text{mod}} \neq e^{2b} \tau_{ij}^{\text{mod}}, \quad (3.16)$$

$$\text{B3: } \hat{\tau}_{ij}^{\text{mod}} \neq Q_{im}^{\text{3D}}(t) Q_{jn}^{\text{3D}}(t) \tau_{mn}^{\text{mod}} \quad (3.17)$$

for subgrid-scale models. In these equations, the hat, respectively, indicates application of time reversal, Eq. (3.12), the spatial scaling transformation of Eq. (3.13) and the Euclidean transformation, Eq. (3.14).

3.5 Conservation requirements

As we saw in Section 1.2, the incompressible Navier–Stokes equations, Eq. (1.29), are based on the conservation laws of mass, momentum and angular momentum. Several more conservation laws can be derived from the Navier–Stokes equations (Cheviakov and Oberlack 2014). Since conservation laws are important physical statements, it is desirable that the equations of large-eddy simulation, Eq. (1.76), respect these laws (Rebholz 2007). We discuss the resulting requirements for subgrid-scale models after presenting in more detail the conservation laws of the incompressible Navier–Stokes equations.

3.5.1 Conservation laws of the incompressible Navier–Stokes equations

Conservation of mass

In Section 1.2.2, we discussed the statement of conservation of mass in fluid flows. In Section 1.2.3, we saw that this statement reduces to the incompressibility condition,

$$\frac{\partial u_i}{\partial x_i} = 0, \quad (3.18)$$

for fluids with a constant density ρ . A generalized form of this continuity equation can be obtained by multiplication by an arbitrary differentiable function of time (Cheviakov and Oberlack 2014).

Conservation of momentum

In Sections 1.2.4 to 1.2.6, we discussed conservation of momentum (and the momentum density ρu_i) in fluids. There, we obtained the statement of conservation of momentum of Eq. (1.29b) that is part of the incompressible Navier–Stokes equations, Eq. (1.29). In the absence of external forces, this statement reduces to

$$\frac{\partial u_i}{\partial t} + \frac{\partial}{\partial x_j}(u_i u_j) = -\frac{1}{\rho} \frac{\partial p}{\partial x_i} + 2\nu \frac{\partial S_{ij}(u)}{\partial x_j}. \quad (3.19)$$

As explained in Section 1.2.6, this equation relates changes in the momentum (or rather the velocity field) of a fluid to several forces. Specifically, the second term on the left-hand side of this equation describes the effects of convection. The terms on the right-hand side of Eq. (3.19) represent transport effects of the pressure and diffusion on the velocity field, respectively.

We can use the definition of the rate-of-strain tensor, Eq. (1.25), and the incompressibility condition, Eq. (3.18), to express the diffusive term using the Laplacian of the velocity field (see Eq. (1.31)). We purposely keep the statement

of conservation of momentum of Eq. (3.19) involving the rate-of-strain tensor, however, to facilitate the derivation of conservation constraints for subgrid-scale models. Multiplying Eq. (3.19) by the density ρ and an arbitrary differentiable function of time $f(t)$, we can also obtain the conservation law of a generalized momentum density $\rho f(t) u_i$ (Cheviakov and Oberlack 2014).

Conservation of angular momentum

In Section 1.2.6, we invoked the law of conservation of angular momentum to define the stress tensor of a viscous fluid. Defining the angular momentum density as $\rho \epsilon_{ijk} x_j u_k$, we can derive this conservation law from Eq. (3.19) by replacing the indices i and j by k and l , and by multiplying by $\rho \epsilon_{ijk} x_j$. Simplifying the resulting equation, we obtain

$$\begin{aligned} \frac{\partial}{\partial t}(\epsilon_{ijk} x_j u_k) + \frac{\partial}{\partial x_l}(\epsilon_{ijk} x_j u_k u_l) \\ = -\frac{1}{\rho} \frac{\partial}{\partial x_k}(\epsilon_{ijk} x_j p) + 2\nu \frac{\partial}{\partial x_l}[\epsilon_{ijk} x_j S_{kl}(u)]. \end{aligned} \quad (3.20)$$

The second term on the left-hand side of this equation represents convection of angular momentum, while the terms on the right-hand side represent transport effects of the pressure and diffusion on the evolution of the angular momentum, respectively.

Conservation of vorticity

Another quantity that is conserved in constant-property Newtonian fluids is the vorticity (Cheviakov and Oberlack 2014), which is given by the curl of the velocity field (see Eq. (1.50)). We can derive the conservation law of vorticity from Eq. (3.19) by replacing the indices i and j by k and l , and by applying the curl operator $\epsilon_{ijk} \frac{\partial}{\partial x_j}$. Rearranging the terms, we obtain

$$\frac{\partial \omega_i(u)}{\partial t} + \frac{\partial}{\partial x_l}[\omega_i(u) u_l] = \frac{\partial}{\partial x_l}[u_i \omega_l(u)] + 2\nu \frac{\partial}{\partial x_l} \left[\epsilon_{ijk} \frac{\partial S_{kl}(u)}{\partial x_j} \right]. \quad (3.21)$$

The second term on the left-hand side of this equation represents convection of vorticity, while the first term on the right-hand side is called the *vortex stretching*. The second term on the right-hand side of Eq. (3.21) represents viscous transport effects on the vorticity. The pressure does not affect the vorticity.

Note that the conservation law of vorticity, Eq. (3.21), is *locally trivial* as a volume and as a surface conservation law (Anco and Cheviakov 2020). That is, integration of Eq. (3.21) over a volume or over a surface does not provide any local information about the flow.

Conservation of vorticity-related quantities

Finally, an infinite family of vorticity conservation laws may be obtained from the conservation law of vorticity, Eq. (3.21), by repeated differentiation and/or

by multiplication with the gradient of an arbitrary scalar function f of time t and the spatial coordinates x_i (Cheviakov and Oberlack 2014). The latter operation results in the class of conservation laws given by

$$\begin{aligned} \frac{\partial}{\partial t} \left[\frac{\partial f}{\partial x_i} \omega_i(u) \right] + \frac{\partial}{\partial x_l} \left[\frac{\partial f}{\partial x_i} \omega_i(u) u_l \right] \\ = \frac{\partial}{\partial x_l} \left[\frac{\partial f}{\partial x_i} u_i \omega_l(u) \right] + 2\nu \frac{\partial}{\partial x_j} \left[\frac{\partial f}{\partial x_i} \epsilon_{ijk} \frac{\partial S_{kl}(u)}{\partial x_l} \right] \\ + \frac{\partial}{\partial x_i} \left[\frac{\partial f}{\partial t} \omega_i(u) \right]. \end{aligned} \quad (3.22)$$

This class of conservation laws describes the evolution of the scalar $\frac{\partial f}{\partial x_i} \omega_i(u)$ under transport effects of convection, vortex stretching, diffusion and the time derivative of the scalar function f . The class of conservation laws of Eq. (3.22) is locally trivial when integrated over a volume, but leads to a nontrivial result when integrated over a surface (Anco and Cheviakov 2020).

3.5.2 Conservation requirements

To ensure physical consistency, it is desirable that the equations of large-eddy simulation, Eq. (1.76), respect the conservation laws of Eqs. (3.18) to (3.22).

Conservation of mass

To start with, we see that the incompressibility condition that is part of the equations of large-eddy simulation, Eq. (1.76), takes on the same form as the statement of conservation of mass of Eq. (3.18). Specifically, the former equation does not contain the subgrid-scale model τ_{ij}^{mod} . Therefore, the requirement of conservation of mass, which we will label as C1, is automatically satisfied by subgrid-scale models.

Conservation of momentum

Comparing the statement of conservation of momentum of Eq. (3.19) with the evolution equation of the large-scale velocity field, Eq. (1.76b), we see that momentum is conserved by the latter equation if subgrid-scale effects are included in a conservative way. That is, the subgrid-scale model needs to appear in Eq. (1.76b) through a term that can be written in the form of a divergence,

$$- \frac{\partial \tau_{ij}^{\text{mod}}}{\partial x_j}. \quad (3.23)$$

We will label this requirement of conservation of momentum, in which the minus sign is a matter of convention, as C2.

Any subgrid-scale model introduced in the equations of large-eddy simulation, Eq. (1.76), satisfies C2. Alternative formulations of large-eddy simulation are possible, however, for which this statement does not hold (Sagaut 2006).

Conservation of angular momentum, vorticity and vorticity-related quantities

If requirement C2 is satisfied, equations for the evolution of angular momentum, vorticity and vorticity-related quantities in a large-eddy simulation can easily be derived from Eq. (3.19). We first apply the substitutions

$$\begin{aligned} u_i &\rightarrow v_i, \\ p &\rightarrow q + \frac{1}{3}\rho\tau_{jj}^{\text{mod}}, \\ 2\nu S_{ij}(u) &\rightarrow 2\nu S_{ij} - \tau_{ij}^{\text{mod,dev}}, \end{aligned} \quad (3.24)$$

where the right-hand sides employ the short-hand notation of Section 1.4.6, and $\frac{1}{3}\tau_{jj}^{\text{mod}}$ and $\tau_{ij}^{\text{mod,dev}}$, respectively, denote the isotropic and deviatoric parts of the subgrid-scale model (see Eqs. (1.9) and (1.11)). Then we apply the same operations that led to Eqs. (3.20) to (3.22).

The resulting equations make clear that conservation of angular momentum, vorticity and vorticity-related quantities are, respectively, satisfied by the equations of large-eddy simulation, Eq. (1.76), if

$$\text{C3: } \epsilon_{ijk}x_j \frac{\partial \tau_{kl}^{\text{mod,dev}}}{\partial x_l} = \frac{\partial}{\partial x_l} (\epsilon_{ijk}x_j \tau_{kl}^{\text{mod,dev}}), \quad (3.25)$$

$$\text{C4: } \epsilon_{ijk} \frac{\partial}{\partial x_j} \frac{\partial \tau_{kl}^{\text{mod,dev}}}{\partial x_l} = \frac{\partial}{\partial x_l} \left(\epsilon_{ijk} \frac{\partial \tau_{kl}^{\text{mod,dev}}}{\partial x_j} \right), \quad (3.26)$$

$$\text{C5: } \frac{\partial f}{\partial x_i} \epsilon_{ijk} \frac{\partial}{\partial x_j} \frac{\partial \tau_{kl}^{\text{mod,dev}}}{\partial x_l} = \frac{\partial}{\partial x_j} \left(\frac{\partial f}{\partial x_i} \epsilon_{ijk} \frac{\partial \tau_{kl}^{\text{mod,dev}}}{\partial x_l} \right). \quad (3.27)$$

The requirement of conservation of angular momentum (requirement C3 of Eq. (3.25)) is satisfied if the subgrid-scale model is symmetric. Equation (3.25) can, thus, be rewritten as

$$\text{C3: } \tau_{ij}^{\text{mod}} = \tau_{ji}^{\text{mod}}. \quad (3.28)$$

The requirements of conservation of vorticity and the class of vorticity-related quantities (requirements C4–5 of Eqs. (3.26) and (3.27)) are identically satisfied by any subgrid-scale model τ_{ij}^{mod} that satisfies requirement C2.

Note that the requirements of Eqs. (3.25) to (3.27) are only valid if requirement C2 is satisfied. Different conservation requirements may be applicable for subgrid-scale models that have a different form and do not satisfy C2.

3.6 Dissipation requirements

The list of quantities that are conserved by the incompressible Navier–Stokes equations provided in Section 3.5 may not be exhaustive (see, e.g., Anco and Webb 2020). Most physical quantities are, however, dissipated in viscous flows. Often, the kinetic energy, enstrophy and helicity (Moreau 1961; Moffatt

1969; Cheviakov and Oberlack 2014) are discussed because these quantities are dissipated by the incompressible Navier–Stokes equations, Eq. (1.29), but are conserved by the incompressible Euler equations, Eq. (1.13), or their two-dimensional equivalent.

In the current section, we discuss several existing requirements for the dissipation of kinetic energy by subgrid-scale models. We also present new requirements for the dissipation of enstrophy and helicity. To that end, we first discuss the evolution equations of kinetic energy, enstrophy and helicity corresponding to the incompressible Navier–Stokes equations, Eq. (1.29).

3.6.1 Dissipation by the incompressible Navier–Stokes equations

Dissipation of kinetic energy

In Eq. (1.51), we defined the kinetic energy per unit mass as $k(u) = \frac{1}{2}u_i u_i$. Multiplying the momentum equation of Eq. (3.19) by u_i and simplifying the result, we can obtain the evolution equation for this quantity in the form

$$\begin{aligned} \frac{\partial k(u)}{\partial t} + \frac{\partial}{\partial x_j} [k(u) u_j] \\ = -\frac{1}{\rho} \frac{\partial}{\partial x_i} (u_i p) + 2\nu \frac{\partial}{\partial x_j} [u_i S_{ij}(u)] - 2\nu S_{ij}(u) S_{ij}(u). \end{aligned} \quad (3.29)$$

The second term on the left-hand side of this equation represents convection of kinetic energy, while the terms on the right-hand side represent transport effects due to the pressure and diffusion, as well as the viscous dissipation of kinetic energy. The kinetic energy is conserved in all inviscid flows.

Dissipation of enstrophy

The evolution equation of the enstrophy, whose density we defined as $e(u) = \frac{1}{2}\omega_i(u) \omega_i(u)$ in Eq. (1.52), can be obtained by multiplying the vorticity equation of Eq. (3.21) by $\omega_i(u)$. Rearranging the different terms, we obtain

$$\begin{aligned} \frac{\partial e(u)}{\partial t} + \frac{\partial}{\partial x_l} [e(u) u_l] \\ = \frac{\partial}{\partial x_l} [h(u) \omega_l(u)] - \frac{\partial \omega_i(u)}{\partial x_l} u_i \omega_l(u) \\ + 2\nu \frac{\partial}{\partial x_l} \left[\omega_i(u) \epsilon_{ijk} \frac{\partial S_{kl}(u)}{\partial x_j} \right] - 2\nu \frac{\partial \omega_i(u)}{\partial x_l} \epsilon_{ijk} \frac{\partial S_{kl}(u)}{\partial x_j}. \end{aligned} \quad (3.30)$$

The second term on the left-hand side of this equation represents convection of enstrophy. The terms on the right-hand side, respectively, represent transport effects due to and production of enstrophy by the vortex stretching, as well as viscous transport and dissipation of enstrophy. The definition of the helicity

density was provided in Eq. (1.53): $h(u) = u_i \omega_i(u)$. As per the definition of the rate-of-strain tensor, given in Eq. (1.25),

$$2\nu \frac{\partial \omega_i(u)}{\partial x_l} \epsilon_{ijk} \frac{\partial S_{kl}(u)}{\partial x_j} = \nu \frac{\partial \omega_i(u)}{\partial x_l} \frac{\partial \omega_i(u)}{\partial x_l}, \quad (3.31)$$

which shows that the viscous dissipation of enstrophy is nonnegative. The pressure has no effect on the enstrophy. The enstrophy is conserved in two-dimensional inviscid flows, in which all vortex stretching and viscous terms are zero.

Dissipation of helicity

The evolution equation of the helicity (whose density we defined as $h(u) = u_i \omega_i(u)$ in Eq. (1.53)) can be obtained by multiplying the momentum equation of Eq. (3.19) by $\omega_i(u)$, the vorticity equation of Eq. (3.21) by u_i and by summing the results. The resulting equation can be expressed as

$$\begin{aligned} \frac{\partial h(u)}{\partial t} + \frac{\partial}{\partial x_l} [h(u) u_l] &= \frac{\partial}{\partial x_l} [k(u) \omega_l(u)] - \frac{1}{\rho} \frac{\partial}{\partial x_i} [\omega_i(u) p] \\ &+ 2\nu \frac{\partial}{\partial x_l} \left[u_i \epsilon_{ijk} \frac{\partial S_{kl}(u)}{\partial x_j} + \omega_i(u) S_{il}(u) \right] \\ &- 2\nu \left[\frac{\partial u_i}{\partial x_l} \epsilon_{ijk} \frac{\partial S_{kl}(u)}{\partial x_j} + \frac{\partial \omega_i(u)}{\partial x_l} S_{il}(u) \right]. \end{aligned} \quad (3.32)$$

The second term on the left-hand side of this equation represents convection of helicity, while the first two terms on the right-hand side describe transport effects due to vortex stretching and the pressure. The last two terms represent the effects of viscous transport and dissipation on the helicity. Note that, like the helicity, the viscous dissipation of helicity does not have a definite sign. The helicity is conserved in inviscid flows.

3.6.2 Preliminary discussion

Since kinetic energy and helicity are conserved in inviscid flows, these quantities are also conserved in the *inertial range* of a turbulent flow, which is the range of scales of motion on which viscosity has a negligible effect. Similarly, the enstrophy is conserved in the inertial range of an inviscid two-dimensional flow. The inertial-range conservation of kinetic energy, enstrophy and helicity plays an important role in the behavior of turbulent flows (see, e.g., Alexakis and Biferale 2018). Rebholz (2007), therefore, argues that turbulence models should respect this conservation behavior.

Although we would like to underline the physical importance of conserved quantities, we remark that inertial-range conservation by subgrid-scale models is difficult to evaluate analytically. In practical coarse-grid large-eddy simulations,

the small-scale motions that are affected by dissipation are not (well) resolved. As a consequence, the kinetic energy is dissipated at a smaller rate than in direct numerical simulations. One of the primary tasks of subgrid-scale models, therefore, is to increase the rate of dissipation of kinetic energy. This dissipation will invariably affect the properties of the inertial range, but the exact effects are not readily quantified analytically.

Distinguishing different parts or terms of subgrid-scale models to determine their respective conservation properties is possible (Rebholz 2007). The velocity-gradient-based subgrid-scale models we consider in Chapter 4, for example, are easily decomposed into parts that, respectively, conserve and dissipate kinetic energy. Such a decomposition is not possible for subgrid-scale models like the scale similarity model of Bardina et al. (1983), however. Moreover, the effects of the (necessary) dissipative terms on the properties of the inertial range remain unclear.

A proper analysis of the effects of subgrid-scale models on the inertial-range properties of turbulent flows, thus, likely has to be based on numerical simulations. Such an analysis is out of the scope of the current study. Given the practical importance of dissipation of kinetic energy in large-eddy simulations, we will, therefore, discuss dissipation of this quantity, enstrophy and helicity by subgrid-scale models in what follows, rather than focusing on the inertial-range conservation of these quantities.

3.6.3 Dissipation of kinetic energy in large-eddy simulations

To discuss the dissipation of kinetic energy in large-eddy simulations, it is useful to consider the evolution equations of this quantity as derived from both the filtered incompressible Navier–Stokes equations, Eq. (1.74), and the equations of large-eddy simulation, Eq. (1.76). The evolution equation for the kinetic energy of the filtered velocity field can easily be obtained from the evolution equation Eq. (3.29) using the substitutions

$$\begin{aligned} u_i &\rightarrow \bar{u}_i, \\ p &\rightarrow \bar{p} + \frac{1}{3}\rho \tau_{jj}, \\ 2\nu S_{ij}(u) &\rightarrow 2\nu S_{ij}(\bar{u}) - \tau_{ij}^{\text{dev}}. \end{aligned} \tag{3.33}$$

The substitutions listed in Eq. (3.24) lead to a corresponding equation for the kinetic energy of the large-scale velocity field v_i . Given the nature of the substitutions of Eqs. (3.24) and (3.33), both resulting equations contain new terms.

In the equation for the kinetic energy of the filtered velocity field, we can specifically distinguish the *subfilter dissipation of kinetic energy*,

$$D^k = -\tau_{ij}^{\text{dev}} S_{ij}(\bar{u}). \tag{3.34}$$

This quantity, which measures the alignment between the deviatoric part of the turbulent stress tensor and the filtered rate-of-strain tensor, describes the rate

of energy transfer from the filtered to the subfilter scales of motion as caused by the turbulent stresses.

In turbulent flows, energy can be transported from large to small scales of motion (*forward scatter*) and vice versa (*backscatter*). Therefore, D^k can be both positive and negative. Moreover, if an invertible filter is used, the energy transfer between filtered and subfilter scales of motion is reversible. Rather than subfilter dissipation, the quantity D^k , therefore, is sometimes called the *production of subfilter-scale kinetic energy*. For simplicity, we will mostly employ the former nomenclature. The quantity D^k represents the reference dissipation rate for large-eddy simulations. We will, therefore, also refer to this quantity as the *true dissipation of kinetic energy*.

Using the evolution equation of the kinetic energy corresponding to Eq. (1.76), we can define the *subgrid dissipation of kinetic energy* as

$$D^{k,\text{mod}} = -\tau_{ij}^{\text{mod,dev}} S_{ij}. \quad (3.35)$$

This quantity, which measures the alignment of the deviatoric part of a subgrid-scale model and the large-scale rate-of-strain tensor, describes the rate of energy transfer to subgrid-scale motions due to a subgrid-scale model. In a practical large-eddy simulation, the subgrid-scale motions are not (well) resolved. In contrast to what holds for the subfilter dissipation, a positive subgrid dissipation, therefore, leads to an irreversible loss of information. We will also refer to $D^{k,\text{mod}}$ as the *modeled dissipation of kinetic energy*.

3.6.4 Vreman's dissipation requirements

Subgrid-scale models should not cause unphysical transitions from laminar to turbulent flow or vice versa in a large-eddy simulation. Vreman (2004), therefore, argues that the turbulent stresses should be modeled in such a way that the corresponding subgrid dissipation of kinetic energy is small in laminar and transitional regions of a flow. On the other hand, the modeled dissipation should not be small where turbulence occurs.

To realize the above situation, Vreman (2004) requires that the modeled dissipation of kinetic energy vanishes for flows for which the true dissipation is known to be zero. On the other hand, if it is known that there is energy transport to subfilter scales for a certain flow, the modeled dissipation should be nonzero. These requirements for the modeled dissipation of kinetic energy can be summarized as

$$\text{D1: } D^{k,\text{mod}} = 0 \text{ when } D^k = 0, \quad (3.36)$$

$$\text{D2: } D^{k,\text{mod}} \neq 0 \text{ when } D^k \neq 0. \quad (3.37)$$

3.6.5 Nicoud et al. zero-dissipation requirements

On the basis of physical grounds, Nicoud et al. (2011) argue that certain flows cannot be maintained if energy is transported to subgrid scales. They,

therefore, see it as a desirable property that the modeled dissipation of kinetic energy vanishes for these flows. In particular, they require that a subgrid-scale model is constructed in such a way that the subgrid dissipation is zero for all two-component flows (a requirement that we label D3) and for the pure axisymmetric strain (D4). We will provide a characterization of these flows in Section 4.4.2.

3.6.6 Consistency with the second law of thermodynamics

As can be concluded from Section 3.6.3, the subfilter dissipation of kinetic energy, described by Eq. (3.34), is not a (fully) dissipative process. On the other hand, transfer of energy to subgrid-scale motions in a practical large-eddy simulation leads to an irreversible loss of information. One can, therefore, argue that the subgrid dissipation, Eq. (3.35), is a dissipative process.

The second law of thermodynamics requires that the total dissipation in flows is nonnegative (Razafindralandy et al. 2007). Assuming that only the subgrid and viscous dissipation of kinetic energy play a role in large-eddy simulation, we, thus, need

$$\text{D5: } D^{k,\text{mod}} + 2\nu S_{ij}S_{ij} \geq 0. \quad (3.38)$$

The viscous dissipation of the kinetic energy of the large-scale velocity field, $2\nu S_{ij}S_{ij}$, is a positive quantity. Therefore, the subgrid dissipation $D^{k,\text{mod}}$ is allowed to become negative. The viscous dissipation of kinetic energy can, however, be small in practical coarse-grid large-eddy simulations. The second law, thus, implies that dissipative subgrid-scale models are well suited to parametrize the net transport of energy from large to small scales of motion, but other means than negative dissipation have to be sought to model backscatter of energy. Additional model terms, such as nondissipative tensor terms that are nonlinear in the velocity gradient, can be used for that purpose (see, e.g., Chapter 4).

Precluding negative dissipation in a practical simulation by satisfying requirement D5 of Eq. (3.38) does not only ensure consistency with the second law of thermodynamics, but also prevents small- and subgrid-scale errors from growing to the size of large-scale motions through a backward-heat-equation-type instability.

3.6.7 Verstappen's minimum-dissipation requirement

When the filtered incompressible Navier–Stokes equations, Eq. (1.74), are supplied with a turbulence model, one obtains the closed set of equations of large-eddy simulation, given by Eq. (1.76). Solutions of Eq. (1.76), however, are not necessarily independent of scales of motion smaller than the filter length $\bar{\delta}$. Indeed, due to the convective nonlinearity, energy transport takes place between large and small scales of motion.

This energy transport is troublesome when the small scales of motion are not well resolved, as is commonly the case in large-eddy simulations. Verstappen

(2011, 2018), therefore, argues that subgrid-scale models should be constructed in such a way that the equations of large-eddy simulation, Eq. (1.76), provide a solution of the large-scale dynamics of flows that is independent of small-scale motions. Stated otherwise, subgrid-scale models have to cause scale separation (Verstappen et al. 2014; Verstappen 2018).

Scale separation can be achieved by ensuring that subgrid-scale models counterbalance the convective production of small-scale kinetic energy and dissipate any kinetic energy (initially) contained in the small scales of motion. From the filtered incompressible Navier–Stokes equations, Eq. (1.74), it can be shown that the kinetic energy of subfilter-scale motions is influenced by both filtered and subfilter scales of motion. Similarly, the kinetic energy of subgrid-scale motions, as corresponding to Eq. (1.76), depends on both large and small scales of motion. Because the behavior of the small scales of motion is not (fully) known in a large-eddy simulation, subgrid-scale models cannot directly target their kinetic energy.

We can, however, apply the *Poincaré inequality* to bound the kinetic energy of small-scale motions in terms of the magnitude of the large-scale velocity gradient (Verstappen 2011, 2018). Subgrid-scale models can, thus, be constructed to quench the kinetic energy of small-scale motions by reducing the velocity gradient magnitude.

Anticipating discretization using a finite-volume method, we divide the flow domain into a number of small nonoverlapping (control) volumes $V_{\tilde{\delta}}$. These volumes are characterized by a length scale $\tilde{\delta}$ that has to satisfy $\tilde{\delta} \geq \delta$. Here, δ is the *subgrid characteristic length scale*, which is commonly associated with the grid resolution or the large-eddy simulation filter length $\tilde{\delta}$.

Denoting the average over a (control) volume $V_{\tilde{\delta}}$ using $\tilde{\cdot}$, we can write the Poincaré inequality for the small-scale kinetic energy contained in this volume as follows:

$$\int_{V_{\tilde{\delta}}} \frac{1}{2} \rho (v_i - \tilde{v}_i)(v_i - \tilde{v}_i) dV \leq C_{\tilde{\delta}} \int_{V_{\tilde{\delta}}} \frac{\rho}{2} \frac{\partial v_i}{\partial x_k} \frac{\partial v_i}{\partial x_k} dV. \quad (3.39)$$

Here, $C_{\tilde{\delta}}$ is called the *Poincaré constant*, which is positive, has units of a squared length scale and depends only on the geometry of the volume $V_{\tilde{\delta}}$.

According to Eq. (3.39), the kinetic energy of motions of a scale smaller than the length scale $\tilde{\delta}$ is bounded by the squared magnitude of the large-scale velocity gradient at that same scale. We can, therefore, render motions that are smaller than the length scale $\tilde{\delta}$ inactive by forcing the right-hand side of Eq. (3.39) to zero. That is, we need

$$\text{D6: } \frac{d}{dt} \int_{V_{\tilde{\delta}}} \frac{1}{2} \frac{\partial v_i}{\partial x_k} \frac{\partial v_i}{\partial x_k} dV \leq 0. \quad (3.40)$$

Here, the evolution equation of half the squared magnitude of the large-scale velocity gradient follows from using the substitutions of Eq. (3.24) in the momentum equation of Eq. (3.19) and applying the operator $\frac{\partial v_i}{\partial x_k} \frac{\partial}{\partial x_k}$.

The resulting equation can be expressed as

$$\begin{aligned}
\frac{\partial}{\partial t} \left(\frac{1}{2} \frac{\partial v_i}{\partial x_k} \frac{\partial v_i}{\partial x_k} \right) + \frac{\partial}{\partial x_j} \left(\frac{1}{2} \frac{\partial v_i}{\partial x_k} \frac{\partial v_i}{\partial x_k} v_j \right) + \frac{\partial v_i}{\partial x_k} \frac{\partial v_j}{\partial x_k} \frac{\partial v_i}{\partial x_j} \\
= -\frac{1}{\rho} \frac{\partial}{\partial x_i} \left[\frac{\partial v_i}{\partial x_k} \frac{\partial}{\partial x_k} \left(q + \frac{1}{3} \rho \tau_{jj}^{\text{mod}} \right) \right] \\
+ 2\nu \frac{\partial}{\partial x_j} \left(\frac{\partial v_i}{\partial x_k} \frac{\partial S_{ij}}{\partial x_k} \right) - 2\nu \frac{\partial S_{ij}}{\partial x_k} \frac{\partial S_{ij}}{\partial x_k} \\
- \frac{\partial}{\partial x_j} \left(\frac{\partial v_i}{\partial x_k} \frac{\partial \tau_{ij}^{\text{mod,dev}}}{\partial x_k} \right) + \frac{\partial S_{ij}}{\partial x_k} \frac{\partial \tau_{ij}^{\text{mod,dev}}}{\partial x_k}.
\end{aligned} \tag{3.41}$$

The second and third terms on the left-hand side of this equation, respectively, represent the convection and the convective production of (half the squared) magnitude of the large-scale velocity gradient. The first terms on the right-hand side of Eq. (3.41) describe transport effects due to the pressure and the isotropic part of the subgrid-scale model, and the effects of viscous transport and dissipation. The last two terms represent transport effects due to the subgrid-scale model and the subgrid dissipation of the velocity gradient magnitude.

To satisfy requirement D6 of Eq. (3.40), the viscous and subgrid dissipation terms at least have to dissipate the convective production of the large-scale velocity gradient magnitude, as well as all contributions to the velocity gradient magnitude from transport into the volume V_{δ} . Requirement D6 is, therefore, called a *minimum-dissipation condition* for scale separation (Verstappen et al. 2010; Verstappen 2011; Verstappen et al. 2014; Verstappen 2018).

3.6.8 Dissipation of enstrophy in large-eddy simulations

Equations for the evolution of the enstrophy corresponding to the filtered incompressible Navier–Stokes equations, Eq. (1.74), and the equations of large-eddy simulation, Eq. (1.76), can easily be derived from the evolution equation Eq. (3.30) using the substitutions of Eqs. (3.24) and (3.33). Using these equations, we can define the *true* (or *subfilter*) and *modeled* (or *subgrid*) *dissipation of enstrophy* as

$$D^e = -\frac{\partial \omega_i(\bar{u})}{\partial x_l} \epsilon_{ijk} \frac{\partial \tau_{kl}^{\text{dev}}}{\partial x_j}, \tag{3.42}$$

$$D^{e,\text{mod}} = -\frac{\partial \omega_i}{\partial x_l} \epsilon_{ijk} \frac{\partial \tau_{kl}^{\text{mod,dev}}}{\partial x_j}, \tag{3.43}$$

respectively. Here, $\omega_i(\bar{u})$ and $\omega_i = \omega_i(v)$, respectively, represent the filtered and large-scale vorticity (see Eqs. (1.50) and (1.81)).

3.6.9 Enstrophy dissipation requirements

One can argue that the lines of reasoning concerning the modeled dissipation of kinetic energy, presented in Sections 3.6.4 to 3.6.7, also apply to the dissipation

of enstrophy caused by subgrid-scale models. The argumentation of Vreman (2004) then leads to two requirements for the dissipation of enstrophy by subgrid-scale models, namely,

$$\text{D7: } D^{e,\text{mod}} = 0 \text{ when } D^e = 0, \quad (3.44)$$

$$\text{D8: } D^{e,\text{mod}} \neq 0 \text{ when } D^e \neq 0. \quad (3.45)$$

These requirements imply that subgrid-scale models should (not) dissipate enstrophy when the turbulent stresses do (not do) so.

Similarly, following the reasoning of Nicoud et al. (2011) for the dissipation of kinetic energy, we can require that the subgrid dissipation of enstrophy is zero for all two-component flows (a requirement which we label as D9) and for the pure axisymmetric strain (D10). Consistency with the second law of thermodynamics is ensured if the dissipation of enstrophy satisfies

$$\text{D11: } D^{e,\text{mod}} + 2\nu \frac{\partial \omega_i}{\partial x_l} \epsilon_{ijk} \frac{\partial S_{kl}}{\partial x_j} \geq 0. \quad (3.46)$$

Finally, employing the Poincaré inequality for the enstrophy of scales of motion smaller than the volume $V_{\bar{\delta}}$, we can derive the new *minimum-enstrophy-dissipation requirement*

$$\text{D12: } \frac{d}{dt} \int_{V_{\bar{\delta}}} \frac{1}{2} \frac{\partial \omega_i}{\partial x_m} \frac{\partial \omega_i}{\partial x_m} dV \leq 0. \quad (3.47)$$

Here, the evolution equation of half the squared magnitude of the large-scale vorticity gradient can be obtained by using the substitutions of Eq. (3.24) in Eq. (3.21) and applying the operator $\frac{\partial \omega_i}{\partial x_m} \frac{\partial}{\partial x_m}$.

The resulting equation can be expressed as

$$\begin{aligned} & \frac{\partial}{\partial t} \left(\frac{1}{2} \frac{\partial \omega_i}{\partial x_m} \frac{\partial \omega_i}{\partial x_m} \right) + \frac{\partial}{\partial x_l} \left(\frac{1}{2} \frac{\partial \omega_i}{\partial x_m} \frac{\partial \omega_i}{\partial x_m} v_l \right) + \frac{\partial \omega_i}{\partial x_m} \frac{\partial v_l}{\partial x_m} \frac{\partial \omega_i}{\partial x_l} \\ &= \frac{\partial}{\partial x_l} \left(\frac{\partial v_i}{\partial x_m} \frac{\partial \omega_i}{\partial x_m} \omega_l \right) \\ &+ \frac{\partial \omega_i}{\partial x_m} \frac{\partial \omega_l}{\partial x_m} \frac{\partial v_i}{\partial x_l} - \frac{\partial v_i}{\partial x_m} \frac{\partial^2 \omega_i}{\partial x_m \partial x_l} \omega_l \\ &+ 2\nu \frac{\partial}{\partial x_l} \left[\frac{\partial \omega_i}{\partial x_m} \frac{\partial}{\partial x_m} \left(\epsilon_{ijk} \frac{\partial S_{kl}}{\partial x_j} \right) \right] \\ &- 2\nu \frac{\partial^2 \omega_i}{\partial x_l \partial x_m} \frac{\partial}{\partial x_m} \left(\epsilon_{ijk} \frac{\partial S_{kl}}{\partial x_j} \right) \\ &- \frac{\partial}{\partial x_l} \left[\frac{\partial \omega_i}{\partial x_m} \frac{\partial}{\partial x_m} \left(\epsilon_{ijk} \frac{\partial \tau_{kl}^{\text{mod,dev}}}{\partial x_j} \right) \right] \\ &+ \frac{\partial^2 \omega_i}{\partial x_l \partial x_m} \frac{\partial}{\partial x_m} \left(\epsilon_{ijk} \frac{\partial \tau_{kl}^{\text{mod,dev}}}{\partial x_j} \right). \end{aligned} \quad (3.48)$$

The second and third terms on the left-hand side of this equation describe the convection and the convective production of (half the squared) magnitude of the large-scale vorticity gradient. The first two lines of terms on the right-hand side describe transport effects as well as production of the vorticity gradient magnitude due to the vortex stretching. The other terms describe transport effects and dissipation as caused by diffusion and the subgrid-scale model.

To satisfy the minimum-ensrophy-dissipation condition (requirement D12 of Eq. (3.47)), the viscous and subgrid dissipation have to balance the production of the large-scale vorticity gradient magnitude caused by the convection and the vortex stretching, and have to dissipate all contributions to the vorticity gradient magnitude from transport into the volume V_{δ} .

3.6.10 Dissipation of helicity in large-eddy simulations

Equations for the evolution of the helicity corresponding to the filtered incompressible Navier–Stokes equations, Eq. (1.74), and the equations of large-eddy simulation, Eq. (1.76), can be derived from the evolution equation Eq. (3.32) using the substitutions of Eqs. (3.24) and (3.33). In these equations, we can distinguish the *true* (or *subfilter*) and *modeled* (or *subgrid*) *dissipation rates of helicity*, which are, respectively, given by

$$D^h = -\frac{\partial \bar{u}_i}{\partial x_l} \epsilon_{ijk} \frac{\partial \tau_{kl}^{\text{dev}}}{\partial x_j} - \frac{\partial \omega_i(\bar{u})}{\partial x_l} \tau_{il}^{\text{dev}}, \quad (3.49)$$

$$D^{h,\text{mod}} = -\frac{\partial v_i}{\partial x_l} \epsilon_{ijk} \frac{\partial \tau_{kl}^{\text{mod,dev}}}{\partial x_j} - \frac{\partial \omega_i}{\partial x_l} \tau_{il}^{\text{mod,dev}}. \quad (3.50)$$

3.6.11 Helicity dissipation requirements

Extending the requirements for the subgrid dissipation of kinetic energy of Vreman (2004), given by Eqs. (3.36) and (3.37), to dissipation of helicity, we have

$$\text{D13: } D^{h,\text{mod}} = 0 \text{ when } D^h = 0, \quad (3.51)$$

$$\text{D14: } D^{h,\text{mod}} \neq 0 \text{ when } D^h \neq 0. \quad (3.52)$$

That is, a subgrid-scale model should not dissipate helicity when the turbulent stresses do not cause subfilter dissipation of this quantity. On the other hand, a subgrid-scale model should cause subgrid dissipation of helicity when the subfilter dissipation of this quantity is nonzero.

We can generalize the reasoning of Nicoud et al. (2011) to require that the modeled dissipation of helicity is zero in all two-component flows (a requirement which we label using D15) and for the pure axisymmetric strain (D16). The subgrid dissipation of helicity satisfies the second law of thermodynamics if

$$\text{D17: } D^{h,\text{mod}} + 2\nu \left(\frac{\partial v_i}{\partial x_l} \epsilon_{ijk} \frac{\partial S_{kl}}{\partial x_j} + \frac{\partial \omega_i}{\partial x_l} S_{il} \right) \geq 0. \quad (3.53)$$

Being a sign-indefinite quantity, the helicity cannot be expressed as a square. As such, we cannot directly apply the Poincaré inequality to derive a minimum-dissipation condition for this quantity. The kinetic energy of scales of motion smaller than the length scale δ , given by the left-hand side of Eq. (3.39), can, however, also be seen as the squared deviation of the large-scale velocity field from the average velocity over the volume V_δ . Similarly, the enstrophy of motions contained in the volume V_δ can be seen as the squared deviation from the average vorticity over this volume.

We, therefore, apply the Poincaré inequality to (half) the squared deviation of the helicity from the average helicity (as corresponding to the large-scale velocity field) over the volume V_δ . The resulting new *minimum-helicity-dissipation requirement* is given by

$$\text{D18: } \frac{d}{dt} \int_{V_\delta} \frac{1}{2} \frac{\partial h}{\partial x_m} \frac{\partial h}{\partial x_m} dV \leq 0, \quad (3.54)$$

where h is the helicity corresponding to the large-scale velocity v_i . The evolution equation of half the squared helicity gradient magnitude can be obtained from the evolution equation of the helicity, Eq. (3.32), by using the substitutions of Eq. (3.24) and applying the operator $\frac{\partial h}{\partial x_m} \frac{\partial}{\partial x_m}$.

The resulting equation can be expressed as

$$\begin{aligned} & \frac{\partial}{\partial t} \left(\frac{1}{2} \frac{\partial h}{\partial x_m} \frac{\partial h}{\partial x_m} \right) + \frac{\partial}{\partial x_l} \left(\frac{1}{2} \frac{\partial h}{\partial x_m} \frac{\partial h}{\partial x_m} v_l \right) + \frac{\partial h}{\partial x_m} \frac{\partial v_l}{\partial x_m} \frac{\partial h}{\partial x_l} \\ &= \frac{\partial}{\partial x_l} \left(\frac{\partial k}{\partial x_m} \frac{\partial h}{\partial x_m} \omega_l \right) \\ &+ \frac{\partial h}{\partial x_m} \frac{\partial \omega_l}{\partial x_m} \frac{\partial k}{\partial x_l} - \frac{\partial k}{\partial x_m} \frac{\partial^2 h}{\partial x_m \partial x_l} \omega_l \\ &- \frac{1}{\rho} \frac{\partial}{\partial x_i} \left(\frac{\partial q}{\partial x_m} \frac{\partial h}{\partial x_m} \omega_i \right) \\ &- \frac{1}{\rho} \frac{\partial h}{\partial x_m} \frac{\partial \omega_i}{\partial x_m} \frac{\partial q}{\partial x_i} + \frac{1}{\rho} \frac{\partial q}{\partial x_m} \frac{\partial^2 h}{\partial x_m \partial x_i} \omega_i \\ &+ 2\nu \frac{\partial}{\partial x_l} \left[\frac{\partial h}{\partial x_m} \frac{\partial}{\partial x_m} \left(v_i \epsilon_{ijk} \frac{\partial S_{kl}}{\partial x_j} + \omega_i S_{il} \right) \right] \\ &- 2\nu \frac{\partial^2 h}{\partial x_l \partial x_m} \frac{\partial}{\partial x_m} \left(v_i \epsilon_{ijk} \frac{\partial S_{kl}}{\partial x_j} + \omega_i S_{il} \right) \\ &- 2\nu \frac{\partial h}{\partial x_m} \frac{\partial}{\partial x_m} \left(\frac{\partial v_i}{\partial x_l} \epsilon_{ijk} \frac{\partial S_{kl}}{\partial x_j} + \frac{\partial \omega_i}{\partial x_l} S_{il} \right) \\ &- \frac{\partial}{\partial x_l} \left[\frac{\partial h}{\partial x_m} \frac{\partial}{\partial x_m} \left(v_i \epsilon_{ijk} \frac{\partial \tau_{kl}^{\text{mod,dev}}}{\partial x_j} + \omega_i \tau_{il}^{\text{mod,dev}} \right) \right] \\ &+ \frac{\partial^2 h}{\partial x_l \partial x_m} \frac{\partial}{\partial x_m} \left(v_i \epsilon_{ijk} \frac{\partial \tau_{kl}^{\text{mod,dev}}}{\partial x_j} + \omega_i \tau_{il}^{\text{mod,dev}} \right) + \end{aligned} \quad (3.55a)$$

$$+ \frac{\partial h}{\partial x_m} \frac{\partial}{\partial x_m} \left(\frac{\partial v_i}{\partial x_l} \epsilon_{ijk} \frac{\partial \tau_{kl}^{\text{mod,dev}}}{\partial x_j} + \frac{\partial \omega_i}{\partial x_l} \tau_{il}^{\text{mod,dev}} \right). \quad (3.55b)$$

The second and third terms on the left-hand side of this equation describe the convection and the convective production of (half the squared) helicity gradient magnitude (as corresponding to the large-scale velocity field). The first two lines of terms on the right-hand side describe transport effects as well as the production of the helicity gradient magnitude due to the vortex stretching. In these terms, we used the abbreviation $k = k(v)$ for the kinetic energy per unit mass of the large-scale velocity field v_i (see Section 1.4.6). The third and fourth lines of terms on the right-hand side of Eq. (3.55) represent transport effects as well as the production of the helicity gradient magnitude due to the pressure. The remaining terms describe transport effects and dissipation as caused by diffusion and the subgrid-scale model.

To satisfy the minimum-helicity-dissipation condition (requirement D18 of Eq. (3.54)), the viscous and subgrid dissipation have to balance the production of the helicity gradient magnitude corresponding to the large-scale velocity field, as caused by the convection, the vortex stretching and the pressure. Moreover, these terms have to dissipate all contributions to the helicity gradient magnitude from transport into the volume $V_{\bar{s}}$.

3.7 Realizability requirements

In the Reynolds-averaged Navier–Stokes approach, which we discussed in Section 1.3, a statistical average is employed to study the behavior of turbulent flows. The Reynolds-averaged Navier–Stokes equations, Eq. (1.63), therefore, contain the Reynolds stress tensor $R_{ij}(u)$ of Eq. (1.65).

As the Reynolds stress tensor represents a statistical average, this tensor is symmetric positive semidefinite, also called *realizable* (Du Vachat 1977; Schumann 1977). Vreman et al. (1994b) showed that, for positive spatial filters, the turbulent stress tensor τ_{ij} of large-eddy simulation, given by Eq. (1.75), is also realizable. They, therefore, argue that, from a theoretical point of view, it is desirable that subgrid-scale models exhibit realizability as well.

3.7.1 Realizability of the turbulent stresses

Realizability of the turbulent stress tensor can be expressed in several equivalent ways (Ghosal 1999). For instance, realizability implies that the three eigenvalues of τ_{ij} , denoted by k_i here, are nonnegative. Equivalently, the principal invariants of the turbulent stress tensor,

$$\begin{aligned} P_\tau &= \text{tr}(\tau) = k_1 + k_2 + k_3, \\ Q_\tau &= \frac{1}{2}[\text{tr}(\tau)^2 - \text{tr}(\tau^2)] = k_1 k_2 + k_2 k_3 + k_3 k_1, \\ R_\tau &= \det(\tau) = k_1 k_2 k_3, \end{aligned} \quad (3.56)$$

have to be nonnegative. Here, we employ matrix notation for the turbulent stress tensor τ_{ij} .

The first principal invariant of the turbulent stress tensor, P_τ , equals twice the *generalized subfilter-scale kinetic energy*, (Sagaut 2006)

$$k_t = \frac{1}{2} \text{tr}(\tau). \quad (3.57)$$

Each k_i can, therefore, be seen as a partial energy. Since energy should not become negative, we obtain a physical argument for the realizability of subgrid-scale models.

3.7.2 Realizability requirements

To study the realizability of subgrid-scale models, it is convenient to introduce the decomposition

$$\tau^{\text{mod}} = \frac{2}{3}(k_t^{\text{mod}})I + \tau^{\text{mod,dev}}. \quad (3.58)$$

The first term on the right-hand side of this equation is the isotropic part of the subgrid-scale model, which models the generalized subfilter-scale kinetic energy. The second term is the deviatoric part of the subgrid-scale model. The quantity I represents the identity matrix, which has elements given by the Kronecker delta δ_{ij} of Eq. (1.10).

A subgrid-scale model satisfies realizability if

$$0 \leq P_{\tau^{\text{mod}}} = 2k_t^{\text{mod}}, \quad (3.59)$$

$$0 \leq Q_{\tau^{\text{mod}}} = \frac{4}{3}(k_t^{\text{mod}})^2 + Q_{\tau^{\text{mod,dev}}}, \quad (3.60)$$

$$0 \leq R_{\tau^{\text{mod}}} = \frac{8}{27}(k_t^{\text{mod}})^3 + \frac{2}{3}k_t^{\text{mod}}Q_{\tau^{\text{mod,dev}}} + R_{\tau^{\text{mod,dev}}}, \quad (3.61)$$

$$0 \leq 4(-Q_{\tau^{\text{mod,dev}}})^3 - 27(R_{\tau^{\text{mod,dev}}})^2. \quad (3.62)$$

The last inequality, Eq. (3.62), ensures that the eigenvalues of the subgrid-scale model are real. This inequality is satisfied for all real symmetric $\tau_{ij}^{\text{mod,dev}}$.

Ordering the partial energies according to $k_1 \geq k_2 = r k_1 \geq k_3 = s k_2 \geq 0$, with real r and s that satisfy $0 \leq r, s \leq 1$, and maximizing the ratios R_τ^2/Q_τ^3 and Q_τ/P_τ^2 with respect to s and r , we can additionally obtain the chain of inequalities (Vreman 2004)

$$0 \leq R_{\tau^{\text{mod}}} \leq \frac{1}{3\sqrt{3}}(Q_{\tau^{\text{mod}}})^{3/2} \leq \frac{1}{27}(P_{\tau^{\text{mod}}})^3. \quad (3.63)$$

Equations (3.59) to (3.63) will be referred to as realizability conditions (labeled using R) for the modeled subgrid-scale stresses. The requirements of Eqs. (3.61) and (3.62) correspond to Lumley's triangle in the invariant map of the Reynolds stress anisotropy (Lumley and Newman 1977; Lumley 1979).

No conclusions can be drawn regarding the realizability of subgrid-scale models that do not contain a model k_t^{mod} for the generalized subfilter-scale kinetic energy, as is the case for eddy viscosity models (see Section 4.3). The above inequalities then lead to useful bounds for k_t^{mod} (Vreman et al. 1994b).

3.8 Near-wall scaling requirements

Using numerical simulations, Chapman and Kuhn (1986) revealed the limiting power-law behavior of incompressible turbulence near a solid wall. Among other findings, they determined the scaling behavior of the Reynolds stresses in terms of the wall-normal distance. To ensure that, for example, the dissipation of kinetic energy near solid walls is properly captured, subgrid-scale models for the turbulent stresses should exhibit the same asymptotic near-wall behavior as the Reynolds stresses (Nicoud et al. 2011; Trias et al. 2015).

3.8.1 Near-wall scaling behavior of the Reynolds stresses

Chapman and Kuhn (1986) specifically observed that the Reynolds stresses, defined in Eq. (1.65), exhibit a near-wall scaling behavior in terms of a wall-normal coordinate x_2 given by

$$\begin{aligned} R_{11}(u), R_{33}(u) &= \mathcal{O}(x_2^2), \\ R_{12}(u) &= \mathcal{O}(x_2^3), \\ R_{22}(u) &= \mathcal{O}(x_2^4). \end{aligned} \quad (3.64)$$

They also proposed a simple model for their observations that is based on expanding the fluctuating velocities u'_i , which can be computed from the velocity field u_i using Eq. (1.59), in terms of the wall-normal coordinate.

In particular, they suggested a linear scaling for the fluctuating velocities parallel to the wall:

$$\begin{aligned} u'_1 &= f(x_1, x_3) x_2 + \mathcal{O}(x_2^2), \\ u'_3 &= g(x_1, x_3) x_2 + \mathcal{O}(x_2^2). \end{aligned} \quad (3.65)$$

Here, f and g are arbitrary functions of the coordinates x_1 and x_3 . The incompressibility condition, Eq. (1.6), then leads to a second-order scaling for the fluctuating velocity in the wall-normal direction,

$$u'_2 = -\frac{1}{2} \left(\frac{\partial f}{\partial x_1} + \frac{\partial g}{\partial x_3} \right) x_2^2 + \mathcal{O}(x_2^3). \quad (3.66)$$

The observed scaling behavior of Eq. (3.64), as well as the scaling relations $R_{13}(u) = \mathcal{O}(x_2^2)$ and $R_{23}(u) = \mathcal{O}(x_2^3)$, can subsequently be obtained using the expression for the Reynolds stresses given by Eq. (1.66).

3.8.2 Near-wall scaling requirements

Focusing on wall-resolved large-eddy simulations, we would like to make sure that the modeled stresses exhibit the same asymptotic behavior as the Reynolds stresses. Such behavior would, for instance, ensure that dissipative effects due to the model fall off quickly enough near solid boundaries. In what follows, we will, therefore, require that subgrid-scale models show the same near-wall

behavior as the Reynolds stresses, but then instantaneously. We can express the corresponding near-wall scaling requirements (labeled with N) as

$$\begin{aligned}\tau_{11}^{\text{mod}}, \tau_{13}^{\text{mod}}, \tau_{33}^{\text{mod}} &= \mathcal{O}(x_2^2), \\ \tau_{12}^{\text{mod}}, \tau_{23}^{\text{mod}} &= \mathcal{O}(x_2^3), \\ \tau_{22}^{\text{mod}} &= \mathcal{O}(x_2^4).\end{aligned}\tag{3.67}$$

3.9 Conclusions

In this chapter, we described in detail several fundamental physical and mathematical properties of the Navier–Stokes equations and the turbulent stresses. We also outlined the constraints that subgrid-scale models have to satisfy in order to preserve these properties.

First, we briefly discussed the desired physical dimensions of subgrid-scale models. Then, we discussed the symmetries and conservation laws of the Navier–Stokes equations, and we described the corresponding symmetry and conservation requirements for subgrid-scale models. We also argued that subgrid-scale models should break certain symmetries and we proposed corresponding symmetry breaking requirements.

We subsequently focused on the dissipative behavior of turbulent flows. We discussed several existing requirements for the dissipation of kinetic energy by subgrid-scale models and we extended these requirements to the dissipation of enstrophy and helicity. We thereby obtained new minimum-dissipation requirements for the dissipation of enstrophy and helicity by subgrid-scale models. Finally, we discussed realizability and the desired near-wall scaling behavior of subgrid-scale models.

The discussed model constraints form a framework that can be used to systematically analyze the properties of existing subgrid-scale models and to construct new physics-based subgrid-scale models for large-eddy simulation. In the remainder of this thesis, we will apply this framework of model constraints to subgrid-scale models that are based on the local velocity gradient.

Chapter 4

Subgrid-scale models based on the local velocity gradient

4.1 Introduction

As mentioned in Chapter 2, many different subgrid-scale models have been developed for large-eddy simulation. In this thesis, we focus on the analysis and construction of subgrid-scale models that are based on the local velocity gradient. We introduce such subgrid-scale models in this chapter.

In Section 4.2, we briefly discuss the assumptions underlying subgrid-scale models that are based on the local velocity gradient. We then discuss subgrid-scale models of eddy viscosity type, including their limitations, in Section 4.3. Aiming to go beyond these limitations, we discuss in detail a general class of subgrid-scale models based on the local velocity gradient in Section 4.4.

In Section 4.5, we discuss which steps have to be taken to construct new subgrid-scale models from this general class. To facilitate these steps, we subsequently apply the framework of model constraints of Chapter 3 to this general class of subgrid-scale models in Section 4.6. Conclusions are provided in Section 4.7.

4.2 Assumptions

As explained in Section 1.4, large-eddy simulation is based on the assumption that small-scale turbulent motions exhibit a certain universal behavior that is independent of the large-scale flow structure (Kolmogorov 1941). According to this assumption, the small scales of motion in a turbulent flow and their effects on the large-scale motions are amenable to modeling. One of the principal effects of small-scale turbulent motions is the viscous dissipation of kinetic energy, which is intimately related to the inertial range of a turbulent flow (Obukhov 1941a,b). This relation motivates modeling of the small-scale turbulent motions in terms of inertial-range quantities.

In large-eddy simulation, it is also often assumed that transport of the turbulent stresses τ_{ij} can be neglected. Subgrid-scale models for the turbulent stress tensor can then be formulated based on local physical quantities, rather than in terms of (separate) transport equations.

In a practical large-eddy simulation, one aims to resolve scales of motion down to the inertial range. Physical quantities directly derived from the resolved,

large-scale velocity field, then, are local inertial-range quantities. In this context, the large-scale velocity gradient is of particular interest. Apart from being defined locally and being based on inertial-range information, this quantity can be said to characterize the fluctuations, i.e., the small-scale details, of the velocity field of a flow. In addition, the velocity gradient is Galilean invariant and transforms in a proper way under several other transformations discussed in Section 3.3.2.

As is commonly done in the context of large-eddy simulation, we will, therefore, assume that turbulence can be fully characterized using the local large-scale velocity gradient. For brevity, we will refer to the local large-scale velocity gradient as the velocity gradient in what follows. All other discussed physical quantities are defined with respect to this large-scale velocity field unless otherwise indicated.

4.3 Eddy viscosity models

A commonly used class of subgrid-scale models that is based on the velocity gradient is the class of *eddy viscosity models*.

4.3.1 The Boussinesq hypothesis

Eddy viscosity models originate in the *Boussinesq hypothesis* (Boussinesq 1877), which is the assumption that small-scale turbulent motions effectively cause diffusion of the large scales of motion. This diffusion can be expressed via a (local) increase in the viscosity. The Boussinesq hypothesis, thus, implies that the turbulent stresses τ_{ij} can be modeled as being proportional to the rate-of-strain tensor S_{ij} .

4.3.2 Formulation

In incompressible flows, the rate-of-strain tensor is traceless, i.e., $S_{ii} = 0$. Eddy viscosity models can, therefore, be expressed using a linear relation between the deviatoric part of the subgrid-scale stresses and the rate-of-strain tensor. That is,

$$\tau_e^{\text{mod,dev}} = -2\nu_e S. \quad (4.1)$$

Here, we employed matrix notation and the quantity ν_e is called the *eddy* or *turbulent viscosity*.

As we will see in Chapter 5, the eddy viscosity is commonly defined as a nonlinear function of the velocity gradient. Nonetheless, eddy viscosity models are often called linear models because the eddy viscosity ν_e can be seen as the proportionality constant in the linear relation between the subgrid-scale stresses and the rate-of-strain tensor. We will follow this naming convention here and contrast (linear) eddy viscosity models with nonlinear subgrid-scale models.

4.3.3 Limitations

Given their basis in the Boussinesq hypothesis, eddy viscosity models are dissipative subgrid-scale models. They are often used in large-eddy simulations to prescribe the net dissipation of kinetic energy that is characteristic of turbulence. The dissipative description of turbulent flows that is provided by eddy viscosity models is known to work well for certain canonical turbulent flows, such as decaying homogeneous isotropic turbulence (Lund and Novikov 1992).

The Boussinesq hypothesis is, however, known to be invalid in general. Indeed, the turbulent stress tensor τ_{ij} is usually not aligned with the rate-of-strain tensor S_{ij} (Clark et al. 1979; Bardina et al. 1983; Liu et al. 1994; Tao et al. 2002; Horiuti 2003). Therefore, the small-scale motions in a turbulent flow must also have a nondissipative effect on the large scales of motion.

As a consequence, we can expect that eddy viscosity models do not provide accurate predictions of all turbulent flows. With their associated energy transfer processes, especially rotating turbulent flows, which we consider in Part II of this thesis, can be expected to form a challenging test case for eddy viscosity models.

4.4 A general class of subgrid-scale models

To allow for the description of nondissipative processes in turbulent flows, we consider subgrid-scale models that contain tensor terms that are nonlinear in the local velocity gradient. The classical derivation of a general class of such subgrid-scale models is as follows.

4.4.1 Derivation

The assumption that turbulence can fully be characterized using the local velocity gradient naturally leads to the general form for subgrid-scale models given by (Lund and Novikov 1992; Pope 1975)

$$\tau^{\text{mod}} = f(S, W). \quad (4.2)$$

Here, f represents a local function of the rate-of-strain and rate-of-rotation tensors S and W . To ensure rotational invariance of the equations of large-eddy simulation, Eq. (1.76), τ^{mod} has to satisfy symmetry requirement S4 of Eq. (3.9) (Oberlack 1997). As a consequence, f should be an isotropic function of the elements of S and W .

Assuming that the function f is well behaved, we can employ a Taylor series expansion to express the subgrid-scale model τ^{mod} as a polynomial of the rate-of-strain and rate-of-rotation tensors. That is, we can write τ^{mod} as a (possibly infinite) sum of terms of the form $I, S, S^2, SW, WS, W^2, \dots$. Using a generalized form of the Cayley–Hamilton theorem of matrix algebra,¹ we can

¹ Refer to Appendix A.1 for more information about the generalized Cayley–Hamilton theorem.

reduce this sum to a finite number of terms (Rivlin 1955; Spencer and Rivlin 1958, 1962).

Moreover, to ensure conservation of angular momentum (requirement C3 of Eq. (3.28)), the subgrid-scale model has to be a symmetric tensor. Therefore, only symmetric tensor terms involving S and W are of interest to us. These terms are given by (Pope 1975; Lund and Novikov 1992)

$$\begin{aligned}
 T^{(0)} &= I, & T^{(6)} &= SW^2 + W^2S, \\
 T^{(1)} &= S, & T^{(7)} &= WSW^2 - W^2SW, \\
 T^{(2)} &= S^2, & T^{(8)} &= SW^2S - S^2WS, \\
 T^{(3)} &= W^2, & T^{(9)} &= S^2W^2 + W^2S^2, \\
 T^{(4)} &= SW - WS, & T^{(10)} &= WS^2W^2 - W^2S^2W. \\
 T^{(5)} &= S^2W - WS^2, & &
 \end{aligned} \tag{4.3}$$

The general form for subgrid-scale models given by Eq. (4.2) can, thus, also be written as the finite sum

$$\tau^{\text{mod}} = \sum_{i=0}^{10} \alpha_{(i)} T^{(i)}. \tag{4.4}$$

Here, the $\alpha_{(i)}$ are model coefficients that are generally defined as

$$\alpha_{(i)} = C_{(i)} \delta_{(i)}^2 f_{(i)}(I_1, I_2, \dots, I_6), \tag{4.5}$$

where no summation is implied over indices in brackets. Each of the model coefficients consists of three factors: a dimensionless constant $C_{(i)}$; the square of a subgrid characteristic length scale $\delta_{(i)}$, which is usually associated with the grid resolution or the large-eddy simulation filter length $\bar{\delta}$; and a function $f_{(i)}$ of the local velocity gradient.

By the requirement of rotational invariance of the subgrid-scale model (requirement S4 of Eq. (3.9)), each function $f_{(i)}$ can depend only on the *combined invariants of the rate-of-strain and rate-of-rotation tensors* (Spencer and Rivlin 1962; Pope 1975; Lund and Novikov 1992),

$$\begin{aligned}
 I_1 &= \text{tr}(S^2), & I_3 &= \text{tr}(S^3), & I_5 &= \text{tr}(S^2W^2), \\
 I_2 &= \text{tr}(W^2), & I_4 &= \text{tr}(SW^2), & I_6 &= \text{tr}(S^2W^2SW).
 \end{aligned} \tag{4.6}$$

4.4.2 Physical significance of the invariants

Relation to known flow quantities

In addition to providing information about the rate-of-strain and rate-of-rotation tensors, the invariants of Eq. (4.6) contain important flow details. The principal invariants of the velocity gradient can, for example, be expressed as

$$P_G = 0, \quad Q_G = -\frac{1}{2}(I_1 + I_2), \quad R_G = \frac{1}{3}I_3 + I_4. \tag{4.7}$$

More information about flows can be obtained when we express the rate-of-rotation tensor in terms of the vorticity,

$$W_{ij} = -\frac{1}{2}\epsilon_{ijk}\omega_k, \quad (4.8)$$

and rewrite the invariants of Eq. (4.6) as

$$\begin{aligned} I_1 &= S_{ij}S_{ji} = S_{ij}S_{ij} = |S|^2, \\ I_2 &= W_{ij}W_{ji} = -\frac{1}{2}\omega_i\omega_i = -\frac{1}{2}|\vec{\omega}|^2, \\ I_3 &= S_{ij}S_{jk}S_{ki}, \\ I_4 &= S_{ij}W_{jk}W_{ki} = \frac{1}{4}\omega_i S_{ij}\omega_j = \frac{1}{4}\vec{\omega} \cdot (S\vec{\omega}), \\ I_5 &= S_{ij}S_{jk}W_{kl}W_{li} = \frac{1}{4}(\omega_i S_{ij}S_{jk}\omega_k - S_{ij}S_{ij}\omega_k\omega_k) \\ &= \frac{1}{4}(|S\vec{\omega}|^2 - |S|^2|\vec{\omega}|^2), \\ I_6 &= S_{ij}S_{jk}W_{kl}W_{lm}S_{mn}W_{ni} = -\frac{1}{4}\omega_k S_{kj}S_{ji}W_{in}S_{nm}\omega_m \\ &= -\frac{1}{8}(SS\vec{\omega}) \cdot (\vec{\omega} \times S\vec{\omega}). \end{aligned} \quad (4.9)$$

Here, we implicitly defined the squared magnitudes of the rate-of-strain tensor, the vorticity and the vector $S_{ij}\omega_j$ as

$$\begin{aligned} |S|^2 &= S_{ij}S_{ij}, \\ |\vec{\omega}|^2 &= \omega_i\omega_i, \\ |S\vec{\omega}|^2 &= \omega_i S_{ij}S_{jk}\omega_k. \end{aligned} \quad (4.10)$$

Furthermore, the operations \cdot and \times , respectively, indicate the inner (dot) and outer (cross) product of vectors.

Comparison of Eq. (4.9) with the evolution equation of the kinetic energy of Eq. (3.29) and the definition of the enstrophy of Eq. (1.52) shows that the invariants I_1 and I_2 correspond to the viscous dissipation of kinetic energy and the enstrophy density through the relations

$$\begin{aligned} 2\nu I_1 &= 2\nu S_{ij}S_{ij}, \\ I_2 &= -e. \end{aligned} \quad (4.11)$$

These two invariants additionally relate to the squared magnitude of the velocity gradient through

$$I_1 - I_2 = \frac{\partial v_i}{\partial x_k} \frac{\partial v_i}{\partial x_k}. \quad (4.12)$$

Using the invariants I_3 and I_4 , we can express the convective production of half the squared velocity gradient magnitude (see Eq. (3.41)) as

$$I_3 - I_4 = \frac{\partial v_i}{\partial x_k} \frac{\partial v_j}{\partial x_k} \frac{\partial v_i}{\partial x_j}. \quad (4.13)$$

Finally, we focus on the vortex stretching term in the evolution equation for the (large-scale) vorticity, which can be obtained from the evolution equation Eq. (3.21) using the substitutions of Eq. (3.24). This vortex stretching term can be written as

$$\frac{\partial}{\partial x_l}(v_i \omega_l) = S_{ij} \omega_j. \quad (4.14)$$

The quantity

$$4I_4 = \omega_i S_{ij} \omega_j, \quad (4.15)$$

therefore, represents the effects of the vortex stretching on the enstrophy and

$$4(I_5 - \frac{1}{2}I_1 I_2) = \omega_i S_{ij} S_{jk} \omega_k = |S\vec{\omega}|^2 \quad (4.16)$$

is the squared vortex stretching magnitude (Trias et al. 2015).

Bounds on the invariants

As will be clear from Eq. (4.9), the invariant I_1 is nonnegative, while I_2 is at most zero. By application of the Cauchy–Schwarz inequality, one can, furthermore, show that I_5 is at most zero. On the other hand, the rate-of-strain tensor is a symmetric, but not a positive-(semi)definite matrix. Therefore, the invariant I_4 does not have a definite sign. I_3 and I_6 can also take on both positive and negative values. None of the invariants of Eq. (4.6) can take on arbitrary values, however.

By finding the extreme values of (dimensionless combinations of) the invariants, we can show that

$$\begin{aligned} 0 &\leq I_1, \\ I_2 &\leq 0, \\ |I_3| &\leq \frac{1}{6}\sqrt{6}|S|^3 = \frac{1}{6}\sqrt{6I_1}I_1, \\ |I_4| &\leq \frac{1}{4}|S\vec{\omega}||\vec{\omega}| = \frac{1}{2}\sqrt{2(I_5 - \frac{1}{2}I_1 I_2)(-I_2)} \\ &\leq \frac{1}{12}\sqrt{6}|S||\vec{\omega}|^2 = \frac{1}{6}\sqrt{6I_1}(-I_2), \\ 0 &\leq I_5 - \frac{1}{2}I_1 I_2 \\ &\leq \frac{1}{6}|S|^2|\vec{\omega}|^2 = \frac{1}{3}I_1(-I_2). \end{aligned} \quad (4.17)$$

The first inequalities for the invariants I_4 and $I_5 - \frac{1}{2}I_1 I_2$ can also be obtained from the Cauchy–Schwarz inequality, whereas the second inequalities for these invariants provide sharper bounds than the Cauchy–Schwarz inequality.

Several inequalities can be derived for I_6 . For example,

$$\begin{aligned}
 |I_6| &\leq \frac{1}{8} |SS\vec{\omega}||\vec{\omega} \times S\vec{\omega}| \\
 &= \frac{1}{2} \sqrt{I_1(I_5 - \frac{1}{2}I_1I_2) + \frac{2}{3}I_3I_4} \sqrt{(-I_2)(I_5 - \frac{1}{2}I_1I_2) - 2I_4^2} \\
 &\leq \frac{1}{8} |SS\vec{\omega}||\vec{\omega}||S\vec{\omega}| \\
 &= \frac{1}{2} \sqrt{I_1(I_5 - \frac{1}{2}I_1I_2) + \frac{2}{3}I_3I_4} \sqrt{(-I_2)(I_5 - \frac{1}{2}I_1I_2)}.
 \end{aligned} \tag{4.18}$$

In addition, we obtained the inequalities

$$\begin{aligned}
 |I_6| &\leq \frac{1}{32} \sqrt{2} |SS\vec{\omega}||S||\vec{\omega}|^2 \\
 &= \frac{1}{8} \sqrt{I_1(I_5 - \frac{1}{2}I_1I_2) + \frac{2}{3}I_3I_4} \sqrt{I_1(-I_2)}, \\
 |I_6| &\leq \frac{1}{16} \sqrt{2} |S||S\vec{\omega}|^2 |\vec{\omega}| \\
 &= \frac{1}{2} \sqrt{I_1(I_5 - \frac{1}{2}I_1I_2)} \sqrt{-I_2}, \\
 |I_6| &\leq \frac{1}{32} |S|^2 |S\vec{\omega}||\vec{\omega}|^2 \\
 &= \frac{1}{8} I_1 \sqrt{I_5 - \frac{1}{2}I_1I_2} (-I_2), \\
 |I_6| &\leq \frac{1}{144} \sqrt{6} |S|^3 |\vec{\omega}|^3 \\
 &= \frac{1}{36} \sqrt{-3I_1I_2} (-I_1I_2).
 \end{aligned} \tag{4.19}$$

Special flows

Special flows (or flow regions) occur when one or more of the invariants of Eq. (4.6) are identically zero or when they attain the bounds of Eqs. (4.17) to (4.19). In particular, vanishing of I_1 (or, equivalently, of S) indicates the absence of shear. We then have a *purely rotational flow* (region), for which

$$I_1 = I_3 = I_4 = I_5 = I_6 = 0. \tag{4.20}$$

When I_2 (or, equivalently, W) is zero, we have a *pure shear flow*, which is characterized by

$$I_2 = I_4 = I_5 = I_6 = 0. \tag{4.21}$$

The invariant I_3 vanishes when the rate-of-strain tensor has a zero eigenvalue. The strain then acts in a plane and can be called a *plane strain*. In general, no other invariants vanish in a plane strain, so that such flows are characterized by

$$I_3 = 0. \tag{4.22}$$

The invariant I_3 attains the bound of Eq. (4.17) in case of an *axisymmetric strain*, i.e., when the rate-of-strain tensor has two equal eigenvalues. In this case,

$$I_3^2 = \frac{1}{6}I_1^3, \quad I_6 = 0. \quad (4.23)$$

Equation (4.9) shows that I_4 becomes zero when the vorticity and vortex stretching vectors are perpendicular to each other. The invariant I_4 assumes the first bound of Eq. (4.17) for two special flows. Either the vorticity is aligned with one of the directions of principal strain, for which

$$I_4^2 = \frac{1}{2}(I_5 - \frac{1}{2}I_1I_2)(-I_2), \quad I_6 = 0, \quad (4.24)$$

or the vorticity is perpendicular to the direction of the largest strain of an axisymmetric strain. In the latter case,

$$I_3^2 = \frac{1}{6}I_1^3, \quad I_4^2 = \frac{1}{24}I_1I_2^2, \quad I_5 - \frac{1}{2}I_1I_2 = \frac{1}{12}I_1(-I_2), \quad I_6 = 0. \quad (4.25)$$

The invariant I_4 attains the second bound of Eq. (4.17) in case of an axisymmetric strain in which the vorticity is aligned with the direction of the largest principal strain. For such a flow

$$I_3^2 = \frac{1}{6}I_1^3, \quad I_4^2 = \frac{1}{6}I_1I_2^2, \quad I_5 - \frac{1}{2}I_1I_2 = \frac{1}{3}I_1(-I_2), \quad I_6 = 0. \quad (4.26)$$

The invariant I_5 only vanishes in purely rotational (Eq. (4.20)) and pure shear flows (Eq. (4.21)). More interestingly, the vortex stretching magnitude of Eq. (4.16) is also zero in case the strain is planar and the vorticity vector is directed perpendicular to the plane in which the strain acts. Such *two-component flows* are characterized by

$$I_3 = I_4 = I_5 - \frac{1}{2}I_1I_2 = I_6 = 0. \quad (4.27)$$

Just like I_4 , the invariant $I_5 - \frac{1}{2}I_1I_2$ attains the upper bound of Eq. (4.17) in case of an axisymmetric strain in which the vorticity is aligned with the direction of the largest principal strain (see Eq. (4.26)).

Finally, Eq. (4.9) shows that I_6 becomes zero when the vorticity and vortex stretching are collinear or when the two vectors of which an inner product is taken are perpendicular. The former occurs when the strain is axisymmetric and the vorticity vector is perpendicular to the direction of the largest strain (see Eq. (4.25)). The latter happens in case of an axisymmetric strain (see Eq. (4.23)) or when the vorticity vector is perpendicular to any of the principal straining directions. The bounds of Eqs. (4.18) and (4.19) are attained for one or more of the special flows of Eqs. (4.20), (4.21), (4.25) and (4.27).

4.4.3 Independence of the invariants

Equations (4.20), (4.21) and (4.23) to (4.26) show that certain relations exist among the invariants of Eq. (4.6) for special flows. Since we are studying incompressible flows, for which the velocity gradient has five degrees of freedom, there should be one relation that is valid for all flows and that shows that there are (at most) five independent invariants.

As far as we are aware, none of the invariants of Eq. (4.6) can in general be expressed as a (rational) polynomial of the other invariants. The invariants do, however, implicitly depend on each other through the nonlinear relation (Lund and Novikov 1992)

$$\begin{aligned} I_6^2 - \frac{1}{16}I_1^3I_2^3 + \frac{1}{8}I_1^2I_2I_4^2 + \frac{1}{2}I_1^2I_2^2I_5 - \frac{1}{6}I_1I_2^2I_3I_4 - \frac{1}{2}I_1I_4^2I_5 \\ - \frac{5}{4}I_1I_2I_5^2 - \frac{1}{72}I_2^3I_3^2 + \frac{1}{3}I_3I_4^3 + \frac{1}{2}I_2I_3I_4I_5 + I_5^3 = 0 \end{aligned} \quad (4.28)$$

Thus, there are indeed at most five independent invariants. The relation of Eq. (4.28) is rather complex, however. We will, therefore, keep the definition of the model coefficients $\alpha_{(i)}$ of Eq. (4.5) in terms of all six invariants I_1 to I_6 , rather than making a selection of five invariants.

4.4.4 Independence of the basis tensors

In Section 4.4.1, we discussed that a generalized form of the Cayley–Hamilton theorem can be used to express all symmetric tensors based on the rate-of-strain and rate-of-rotation tensors in terms of the eleven tensors of Eq. (4.3). This theorem cannot be used to further reduce the number of tensors. However, since the tensors of Eq. (4.3) are symmetric 3×3 matrices, no more than six of them can simultaneously be linearly independent (Rivlin and Ericksen 1955; Lund and Novikov 1992). Therefore, not all the $T^{(i)}$ provide an independent contribution to the sum of Eq. (4.4).

As we show in Appendix A, the six tensors $T^{(0)}$ to $T^{(5)}$ in general suffice to form a linearly independent basis for the subgrid-scale stresses. Only for certain special flow cases will a few of these tensors become linearly dependent. We can specifically distinguish a purely rotational flow (see Eq. (4.20)) and a pure strain (see Eq. (4.21)). Also in case of an axisymmetric strain (see Eq. (4.23)) or for flows in which the vorticity vector is aligned with one of the principal directions of strain (see Eq. (4.24)), will some of the tensors $T^{(0)}$ to $T^{(5)}$ become linearly dependent (Lund and Novikov 1992). In case of an axisymmetric strain in which the vorticity vector is not perpendicular to the direction of the largest strain, $T^{(6)}$ and $T^{(7)}$ can be added to again obtain six linearly independent basis tensors. Tensors $T^{(8)}$ to $T^{(10)}$ never contain additional independent information.²

² Refer to Appendix A or the work by Silvis and Verstappen (2015, n.d. a) for more information about the independence of the tensors of Eq. (4.3).

4.4.5 A general class of subgrid-scale models

Expression

Disregarding the exceptional case of an axisymmetric strain (Lund and Novikov 1992), we can, thus, reduce Eq. (4.4) to

$$\tau^{\text{mod}} = \sum_{i=0}^5 \alpha_{(i)} T^{(i)}. \quad (4.29)$$

This general class of subgrid-scale models has a basis of six tensors, out of which four are nonlinear in the rate-of-strain and rate-of-rotation tensors. If one is only interested in modeling the deviatoric part of the subgrid-scale stresses, as is commonly done for incompressible turbulent flows, one can consider the traceless version of Eq. (4.29) (Lund and Novikov 1992).

Properties

The general class of subgrid-scale models of Eq. (4.29) has several appealing properties. First of all, as we will see in Section 4.6, Eq. (4.29) is consistent with several symmetries and the known conservation laws of the Navier–Stokes equations.

Secondly, one can obtain different existing subgrid-scale models from the class of models of Eq. (4.29) for specific choices of the model coefficients $\alpha_{(i)}$. For example, one recovers the class of eddy viscosity models, Eq. (4.1), by setting $\alpha_1 = -2\nu_e$ and taking $\alpha_{(i)} = 0$ for $i \neq 1$. Also the gradient model of Leonard (1975) and Clark et al. (1979), the general nonlinear model of Lund and Novikov (1992), the subgrid-scale model of Kosović (1997), and the explicit algebraic subgrid-scale stress model of Marstorp et al. (2009) form specific cases of Eq. (4.29) (see, e.g., Section 5.2).

Finally, the class of subgrid-scale models of Eq. (4.29) can describe dissipative as well as nondissipative processes. Indeed, some terms of Eq. (4.29) provide a nonzero contribution to the subgrid dissipation of kinetic energy, Eq. (3.35), while other terms are perpendicular to the rate-of-strain tensor. These latter terms, thus, do not directly contribute to the subgrid dissipation and have to describe nondissipative processes.

4.5 Constructing new subgrid-scale models

Given the above properties, the general class of subgrid-scale models of Eq. (4.29) forms a very useful starting point for the construction of new subgrid-scale models. Specifically, this class of models can potentially take us beyond the limitations of eddy viscosity models discussed in Section 4.3.3. To obtain new practical subgrid-scale models from Eq. (4.29), however, we have to overcome three challenges.

First, six terms are too much for a practical and tractable subgrid-scale model, as such a subgrid-scale model would have a large computational cost. In addition,

one would have to determine the effects of six separate terms and, possibly, of different combinations of these terms on predictions of turbulent flows (Wendling and Oberlack 2007). Most importantly, however, single-term eddy viscosity models perform well in large-eddy simulations of decaying homogeneous isotropic turbulence (Lund and Novikov 1992). It seems unlikely that five additional terms are needed for the simulation of other flows. We, therefore, have to make a selection of model terms from the general formulation of Eq. (4.29).

Secondly, we need to specify a model coefficient $\alpha_{(i)}$ for each model term. The model coefficients can, however, depend in many dimensionally consistent ways on the combined invariants of the rate-of-strain and rate-of-rotation tensors given in Eq. (4.6). We, therefore, need a procedure to define the model coefficient of each term. Finally, we need to determine the model constant $C_{(i)}$ and define the subgrid characteristic length scale $\delta_{(i)}$ that are part of each model coefficient.

We will now address the second challenge, of specifying the model coefficients of the general class of subgrid-scale models of Eq. (4.29). In particular, we propose to define these model coefficients using the framework of model constraints of Chapter 3.

4.6 Constraints

We aim to facilitate the analysis of existing subgrid-scale models as well as the construction of new physics-based subgrid-scale models that are based on the velocity gradient. We will, therefore, apply the framework of model requirements of Chapter 3 to the general class of subgrid-scale models of Eq. (4.29). The model requirements lead to constraints on the model coefficients $\alpha_{(i)}$, which we discuss in what follows.

A summary of the constraints on the model coefficients is provided in Table 4.1. This table also shows for which flows the constraints are valid and reports the (transformation) behavior of the invariants of Eq. (4.6). Subgrid-scale models with fewer terms than the general class of Eq. (4.29) can be considered by setting certain model constants to zero. In this case, only constraints that apply to nonzero model coefficients have to be taken into account.

4.6.1 Dimensional requirements

The dimensional requirements (requirement U of Eq. (3.1)), straightforwardly lead to constraints on the coefficients $\alpha_{(i)}$ of the general class of subgrid-scale models of Eq. (4.29). To see this, we note that the velocity gradient has units of inverse time, i.e., $[G_{ij}] = \text{s}^{-1}$. As a consequence, the rate-of-strain and rate-of-rotation tensors, the tensors of Eq. (4.3) and the invariants of Eq. (4.6) also have units that depend only on time.

The general class of subgrid-scale models of Eq. (4.29) can, thus, be given the proper time units by selecting the dependence of the model coefficients $\alpha_{(i)}$ of Eq. (4.5) on the invariants of Eq. (4.6). As indicated by Eq. (4.5), the

Table 4.1: Summary of the constraints on the model coefficients $\alpha_{(i)}$ of the general class of subgrid-scale models of Eq. (4.29) as resulting from the model requirements of Chapter 3. For each set of constraints, we provide a reference to the corresponding requirement in Chapter 3, we indicate for which subset of flows the constraints are applicable and we report the behavior of some selected quantities. The constraints only apply to model coefficients $\alpha_{(i)}$ with a nonzero model constant $C_{(i)}$.

Req.	Ref.	Flow	Constraints	Selected quantities
U	Eq. (3.1)		$[\alpha_0] = m^2 s^{-2}$ $[\alpha_1] = m^2 s^{-1}$ $[\alpha_2] = m^2$ $[\alpha_3] = m^2$ $[\alpha_4] = m^2$ $[\alpha_5] = m^2 s$	$[I_1] = s^{-2}$ $[I_2] = s^{-2}$ $[I_3] = s^{-3}$ $[I_4] = s^{-3}$ $[I_5] = s^{-4}$ $[I_6] = s^{-6}$ $[\delta_{(i)}] = m$
S1-3	Eq. (3.8)		$\hat{\alpha}_{(i)} = \alpha_{(i)}$ $\hat{C}_{(i)} \hat{\delta}_{(i)}^2 = C_{(i)} \delta_{(i)}^2$	$\hat{I}_{(i)} = I_{(i)}$
S4	Eq. (3.9)		$\hat{\alpha}_{(i)} = \alpha_{(i)}$ $\hat{C}_{(i)} \hat{\delta}_{(i)}^2 = C_{(i)} \delta_{(i)}^2$	$\hat{I}_{(i)} = I_{(i)}$
S5	Eq. (3.10)		$\hat{\alpha}_0 = e^{-2a} \alpha_0$ $\hat{\alpha}_1 = \alpha_1$ $\hat{\alpha}_2 = e^{2a} \alpha_2$ $\hat{\alpha}_3 = e^{2a} \alpha_3$ $\hat{\alpha}_4 = e^{2a} \alpha_4$ $\hat{\alpha}_5 = e^{4a} \alpha_5$ $\hat{C}_{(i)} \hat{\delta}_{(i)}^2 = e^{2a} C_{(i)} \delta_{(i)}^2$	$\hat{I}_1 = e^{-4a} I_1$ $\hat{I}_2 = e^{-4a} I_2$ $\hat{I}_3 = e^{-6a} I_3$ $\hat{I}_4 = e^{-6a} I_4$ $\hat{I}_5 = e^{-8a} I_5$ $\hat{I}_6 = e^{-12a} I_6$
S6	Eq. (3.11)	Eq. (4.27)	$\hat{\alpha}_0 = \alpha_0$ $\hat{\alpha}_1 = \alpha_1$ $\hat{\alpha}_2 = \alpha_2$ $\hat{\alpha}_3 = \alpha_3 = 0$ $\hat{\alpha}_4 = \alpha_4 = 0$	$\hat{I}_1 = I_1$ $\hat{I}_2 \neq I_2$ $\hat{I}_3 = I_3 = 0$ $\hat{I}_4 = I_4 = 0$ $\hat{I}_5 \neq I_5$ $\hat{I}_5 - \frac{1}{2} \hat{I}_1 \hat{I}_2 =$ $I_5 - \frac{1}{2} I_1 I_2 = 0$ $\hat{I}_6 = I_6 = 0$
B1	Eq. (3.15)		$\hat{\alpha}_0 \neq \alpha_0$ $\hat{\alpha}_1 \neq -\alpha_1$ $\hat{\alpha}_2 \neq \alpha_2$ $\hat{\alpha}_3 \neq \alpha_3$ $\hat{\alpha}_4 \neq \alpha_4$ and/or $\hat{\alpha}_5 \neq -\alpha_5$	$\hat{I}_1 = I_1$ $\hat{I}_2 = I_2$ $\hat{I}_3 = -I_3$ $\hat{I}_4 = -I_4$ $\hat{I}_5 = I_5$ $\hat{I}_6 = I_6$

Req.	Ref.	Flow	Constraints	Selected quantities
B2	Eq. (3.16)		$\hat{\alpha}_0 \neq e^{2b}\alpha_0$ $\hat{\alpha}_1 \neq e^{2b}\alpha_1$ $\hat{\alpha}_2 \neq e^{2b}\alpha_2$ $\hat{\alpha}_3 \neq e^{2b}\alpha_3$ $\hat{\alpha}_4 \neq e^{2b}\alpha_4$ $\hat{\alpha}_5 \neq e^{2b}\alpha_5$ $\hat{C}_{(i)}\hat{\delta}_{(i)}^2 \neq e^{2b}C_{(i)}\delta_{(i)}^2$	$\hat{I}_1 = I_1$ $\hat{I}_2 = I_2$ $\hat{I}_3 = I_3$ $\hat{I}_4 = I_4$ $\hat{I}_5 = I_5$ $\hat{I}_6 = I_6$
B3	Eq. (3.17)		$\hat{\alpha}_0 \neq \alpha_0$ $\hat{\alpha}_1 \neq \alpha_1$ $\hat{\alpha}_2 \neq \alpha_2$ $\hat{\alpha}_3 \neq 0$ $\hat{\alpha}_4 \neq 0$ and/or $\hat{\alpha}_5 \neq 0$	$\hat{I}_1 = I_1$ $\hat{I}_2 \neq I_2$ $\hat{I}_3 = I_3$ $\hat{I}_4 \neq I_4$ $\hat{I}_5 \neq I_5$ $\hat{I}_5 - \frac{1}{2}\hat{I}_1\hat{I}_2 \neq$ $I_5 - \frac{1}{2}I_1I_2$ $\hat{I}_6 \neq I_6$
D1	Eq. (3.36)	Sec. 4.6.5	$\alpha_1 I_1 = 0$	Table 5.2
D2	Eq. (3.37)	Sec. 4.6.5	$\alpha_1 I_1 + \alpha_2 I_3 +$ $\alpha_3 I_4 \neq 0$	Table 5.2
D3	Sec. 3.6.5	Eq. (4.27)	$\alpha_1 I_1 = 0$	
D4	Sec. 3.6.5	Eq. (4.21) Eq. (4.23)	$\alpha_1 \pm \frac{1}{6}\sqrt{6I_1}\alpha_2 = 0$	
D5	Eq. (3.38)		$(2\nu - \alpha_1)I_1 +$ $-\alpha_2 I_3 - \alpha_3 I_4 \geq 0$	
D6	Eq. (4.34)	Eq. (4.35) Eq. (4.36)	$\nu_e \geq 0$ $\nu_e > 0$	
R	Eq. (3.59) Eq. (3.60) Eq. (3.61) Eq. (3.63)		Eq. (4.37) Eq. (4.38) Eq. (4.39) Eq. (3.63)	
N	Eq. (3.67)		$\alpha_0 = \mathcal{O}(x_2^4)$ $\alpha_1 = \mathcal{O}(x_2^3)$ $\alpha_2 = \mathcal{O}(x_2^4)$ $\alpha_3 = \mathcal{O}(x_2^4)$ $\alpha_4 = \mathcal{O}(x_2^4)$ $\alpha_5 = \mathcal{O}(x_2^3)$	$I_1 = \mathcal{O}(1)$ $I_2 = \mathcal{O}(1)$ $I_3 = \mathcal{O}(x_2)$ $I_4 = \mathcal{O}(x_2)$ $I_5 = \mathcal{O}(1)$ $I_6 = \mathcal{O}(x_2^2)$ $I_1 + I_2 = \mathcal{O}(x_2^2)$ $I_3 + 3I_4 = \mathcal{O}(x_2^3)$ $I_5 - \frac{1}{2}I_1I_2 = \mathcal{O}(x_2^2)$

correct units of length should be provided by a squared length scale. The exact dimensional requirements on the model coefficients are listed in Table 4.1, along with information on the units of the invariants of Eq. (4.6).

4.6.2 Symmetry requirements

To determine the consequences of symmetry requirements S1–4, Eqs. (3.8) and (3.9), for the general class of subgrid-scale models of Eq. (4.29), we note that the velocity gradient is invariant under the time and pressure translations, and the generalized Galilean transformation, Eqs. (3.2) to (3.4). In addition, the velocity gradient properly transforms as a tensor under orthogonal transformations of the coordinate system, Eq. (3.5). The tensors of Eq. (4.3) show the same transformation behavior. In order to satisfy model requirements S1–4, the model coefficients $\alpha_{(i)}$ of the general class of subgrid-scale models, therefore, have to be invariant under the transformations of Eqs. (3.2) to (3.4).

The invariants of the rate-of-strain and rate-of-rotation tensors do not change under these transformations. Furthermore, these invariants are (by definition) invariant under the orthogonal transformations of Eq. (3.5). The constraints of time translation, pressure translation, generalized Galilean, rotation and reflection invariance (requirements S1–4 of Eqs. (3.8) and (3.9)), therefore, directly transfer to the products $C_{(i)}\delta_{(i)}^2$, involving the dimensionless model constants $C_{(i)}$ and the subgrid characteristic length scales $\delta_{(i)}$.

These constraints are, for example, satisfied when the model constants are given fixed numerical values and the $\delta_{(i)}$ are defined in terms of the local grid size. Alternatively, the dynamic procedure (Germano et al. 1991; Lilly 1992) may be used to determine the model constants. Do note that the dynamic procedure relies on an explicit filtering operation. This procedure may, therefore, destroy some symmetry properties of subgrid-scale models unless certain restrictions on the filter are fulfilled (Oberlack 1997; Razafindralandy et al. 2007).

Symmetry requirement S5 of Eq. (3.10), which requires invariance of subgrid-scale models under the scaling transformation of Eq. (3.6), also directly transfers to the products $C_{(i)}\delta_{(i)}^2$. This requirement can, however, only be satisfied if the subgrid characteristic length scales $\delta_{(i)}$ are intrinsic length scales (Oberlack 1997; Razafindralandy et al. 2007). That is, the $\delta_{(i)}$ have to be length scales that are directly related to the properties of a flow.

A length scale that is based on the grid size in a numerical simulation is an externally imposed rather than an intrinsic length scale and, therefore, breaks scale invariance. Subgrid-scale models that break scale invariance can in principle not capture certain scaling laws, like the well-known log law of wall-bounded flows, or certain self-similar solutions (Oberlack 1997; Razafindralandy et al. 2007). If the model constants $C_{(i)}$ are determined dynamically (Germano et al. 1991; Lilly 1992), scale invariance is known to hold also with externally imposed length scales (Oberlack 1997; Razafindralandy et al. 2007).

The general class of subgrid-scale models of Eq. (4.29) satisfies material frame indifference in the limit of a two-component flow (requirement S6 of Eq. (3.11)) if the model coefficients α_0 , α_1 and α_2 are invariant under the transformation

of Eq. (3.7) for two-component flows (see Eq. (4.27)). In addition, α_3 and α_4 should both vanish for such flows, whereas no restrictions apply to α_5 . Tensor terms that involve the rate-of-rotation tensor, thus, do not have to be discarded to satisfy two-dimensional material frame indifference.

4.6.3 Symmetry breaking requirements

As explained in Section 3.4.3, at least one of the terms comprising a subgrid-scale model has to break time reversal invariance. The general class of subgrid-scale models of Eq. (4.29), thus, satisfies time irreversibility (requirement B1 of Eq. (3.15)) if at least one of the corresponding constraints on the coefficients shown in Table 4.1 is satisfied. In these constraints, the unequal sign means ‘not in general equal’. The original and transformed model coefficients may be equal for particular flows.

The dynamic procedure (Germano et al. 1991; Lilly 1992) can restore time reversal invariance of the modeled subgrid-scale stresses when used without clipping (Carati et al. 2001; Oberlack 1997; Razafindralandy et al. 2007). In the light of the discussion in Section 3.4.3, this behavior should be seen as an artifact of this procedure (Carati et al. 2001).

The requirement of breaking of spatial scaling invariance (requirement B2 of Eq. (3.16)) provides an identical constraint for each coefficient $\alpha_{(i)}$ of the general class of subgrid-scale models of Eq. (4.29). As was the case with scaling requirement S5 of Eq. (3.10), these constraints directly lead to restrictions on the products $C_{(i)}\delta_{(i)}^2$.

In contrast to what holds for requirement S5, however, symmetry breaking requirement B2 demands that the subgrid characteristic length scales $\delta_{(i)}$ are not intrinsic length scales. Given the methods discussed so far to determine the model constants and subgrid characteristic length scales, requirements S5 and B2 can, thus, not simultaneously be satisfied using subgrid-scale models of the form of Eq. (4.29).

The general class of subgrid-scale models of Eq. (4.29) satisfies symmetry breaking requirement B3 of Eq. (3.17) if at least one term breaks three-dimensional material frame indifference. Proper sensitivity to rotation is ensured if all model terms break this symmetry. To break three-dimensional material frame indifference, a model term needs to contain the rate-of-rotation tensor. The dynamic procedure (Germano et al. 1991; Lilly 1992) breaks three-dimensional material frame indifference for all practical filters (Razafindralandy et al. 2007).

4.6.4 Conservation requirements

As explained in Section 3.5.2, all subgrid-scale models used in conjunction with the equations of large-eddy simulation, Eq. (1.76), satisfy conservation of mass, momentum, vorticity and vorticity-related quantities (requirements C1–2 and C4–5 of Section 3.5.2). These conservation laws are, therefore, also respected by the general class of subgrid-scale models of Eq. (4.29). In addition, this class of

subgrid-scale models is symmetric and, therefore, conserves angular momentum (requirement C3 of Eq. (3.28)). The conservation requirements of Section 3.5.2, thus, do not lead to any restrictions on the model coefficients of the class of subgrid-scale models of Eq. (4.29).

4.6.5 Dissipation requirements

Using Eq. (3.35), we can determine that the subgrid dissipation of kinetic energy caused by the general class of subgrid-scale models of Eq. (4.29) is given by

$$D^{k,\text{mod}} = -\alpha_1 I_1 - \alpha_2 I_3 - \alpha_3 I_4. \quad (4.30)$$

Vreman's dissipation requirements

To study the behavior of both the true dissipation of kinetic energy, Eq. (3.34), and the modeled dissipation of kinetic energy of Eq. (4.30), Vreman (2004) developed a classification of flows based on the number and position of zero elements in the unfiltered velocity gradient tensor $G_{ij}(u)$. He distinguishes a total of 320 flow types, corresponding to all unfiltered incompressible velocity gradients having zero to nine vanishing elements. Nonzero elements are left unspecified.

Vreman (2004) showed that, for general filters, there are only thirteen flow types for which the true dissipation of kinetic energy D^k always vanishes. He calls such flow types *locally laminar* and refers to their collection as the *flow algebra* of D^k . Since we are interested in constructing subgrid-scale models that comply with the symmetry properties of the Navier–Stokes equations, we assume the use of an isotropic filter. The three flow classes that correspond to a pure plane strain, which can be characterized using Eqs. (4.21) and (4.22), then also belong to the flow algebra of D^k . The subfilter dissipation is not generally zero for any of the remaining 304 flow classes (Vreman 2004).

Given requirement D1 of Eq. (3.36), we, thus, obtain sixteen laminar flow types for which we would like the modeled dissipation of kinetic energy $D^{k,\text{mod}}$ to vanish. These flow types form a subset of the two-component flows, which can be characterized using Eq. (4.27). We also have 304 flow classes, containing both two-component and three-dimensional flows, for which $D^{k,\text{mod}}$, preferably, is not generally zero (requirement D2 of Eq. (3.37)).

Although specific flows may exist that behave differently, we will consider D1 to be fulfilled when $D^{k,\text{mod}}$ vanishes for the sixteen laminar flow types. Moreover, we will see D2 as satisfied when the modeled dissipation is nonzero for the remaining flow types, which are in general nonlaminar. Both requirements are contained in Table 4.1. Table 5.2, which we discuss in Section 5.3.5, includes an analysis of the flow algebra of the invariants of Eq. (4.6).

Nicoud et al. zero-dissipation requirements

The above flow algebra analysis shows that the requirement that the modeled dissipation of kinetic energy vanishes in all two-component flows (requirement D3

of Section 3.6.5) is not compatible with requirement D2 of Eq. (3.37). Moreover, the pure axisymmetric strain is a three-dimensional flow. The requirement that the modeled dissipation should vanish for such a flow (requirement D4 of Section 3.6.5), therefore, is also incompatible with requirement D2. Apparently, the physical reasoning employed by Nicoud et al. (2011) to arrive at requirements D3–4 is not consistent with the mathematical properties of the turbulent stress tensor discovered by Vreman (2004).

Consistency with the second law of thermodynamics

The general class of subgrid-scale models of Eq. (4.29) is consistent with the second law of thermodynamics if the subgrid dissipation of Eq. (4.30) satisfies requirement D5 of Eq. (3.38). Substituting Eq. (4.30) into Eq. (3.38), we readily obtain the constraint on the coefficients $\alpha_{(i)}$ provided in Table 4.1.

Verstappen’s minimum-dissipation requirement

To test if Verstappen’s minimum-dissipation condition for scale separation (requirement D6 of Eq. (3.40)) is satisfied, we will make a few simplifying assumptions. We first assume that the viscous terms of Eq. (3.41) dissipate the initial magnitude of the velocity gradient as well as all contributions to the velocity gradient magnitude from transport into the volume V_{δ} . The requirement of Eq. (3.40) then reduces to

$$-\int_{V_{\delta}} \frac{\partial S_{ij}}{\partial x_k} \frac{\partial \tau_{ij}^{\text{mod,dev}}}{\partial x_k} dV \geq -\int_{V_{\delta}} \frac{\partial v_i}{\partial x_k} \frac{\partial v_j}{\partial x_k} \frac{\partial v_i}{\partial x_j} dV. \quad (4.31)$$

In other words, a subgrid-scale model should at least quench the convective production of the velocity gradient magnitude.

Secondly, given the complexity of the inequality of Eq. (4.31) for the general class of subgrid-scale models of Eq. (4.29), we focus on eddy viscosity models. As discussed in Section 4.4.5, eddy viscosity models can be obtained from Eq. (4.29) by setting $\alpha_1 = -2\nu_e$ and $\alpha_{(i)} = 0$ for $i \neq 1$. Assuming the use of an eddy viscosity model with an eddy viscosity ν_e that is (approximately) constant over the integration volume V_{δ} , we can express Eq. (4.31) as

$$2\nu_e \int_{V_{\delta}} \frac{\partial S_{ij}}{\partial x_k} \frac{\partial S_{ij}}{\partial x_k} dV \geq -\int_{V_{\delta}} \frac{\partial v_i}{\partial x_k} \frac{\partial v_j}{\partial x_k} \frac{\partial v_i}{\partial x_j} dV. \quad (4.32)$$

If we additionally assume that the average strain over the volume V_{δ} is zero, the integral on the left-hand side of Eq. (4.32) satisfies the Poincaré inequality

$$2\nu_e \int_{V_{\delta}} \frac{\partial S_{ij}}{\partial x_k} \frac{\partial S_{ij}}{\partial x_k} dV \geq \frac{2\nu_e}{C_{\delta}} \int_{V_{\delta}} S_{ij} S_{ij} dV. \quad (4.33)$$

We can subsequently rewrite the right-hand sides of Eqs. (4.32) and (4.33) using the invariants of Eq. (4.6) (see Eqs. (4.11) and (4.13)).

Finally, combining the resulting equations and assuming the invariants are constant over the integration volume $V_{\bar{\delta}}$, we obtain the minimum-dissipation condition on the eddy viscosity,

$$\nu_e \geq -C_{\bar{\delta}} \frac{I_3 - I_4}{2I_1}. \quad (4.34)$$

The value of the Poincaré constant $C_{\bar{\delta}}$ is not known in general. Analytically, we can, therefore, at best determine if the form of the eddy viscosity is such that Eq. (4.34) can be satisfied for some value of $C_{\bar{\delta}}$. That is, we have to check whether ν_e is nonnegative whenever the right-hand side of Eq. (4.34) is zero, i.e., when

$$-(I_3 - I_4) = 0 \quad (4.35)$$

and whether ν_e is positive when the right-hand side of Eq. (4.34) is positive,

$$-(I_3 - I_4) > 0. \quad (4.36)$$

Note that the condition of Eq. (4.34) cannot be satisfied if the eddy viscosity complies with requirement D4 of Section 3.6.5, because $-(I_3 - I_4)$ does not vanish for the pure axisymmetric strain.

Enstrophy and helicity dissipation requirements

The requirements on the dissipation of enstrophy and helicity by subgrid-scale models, which we presented in Sections 3.6.9 and 3.6.11, all rely on second- and higher-order derivatives of the velocity field. As most methods discussed in this chapter rely on the use of the first-order derivatives of the velocity field, testing the satisfaction of these requirements for the general class of subgrid-scale models of Eq. (4.29) is beyond the scope of this thesis. The development of practical tests for the presented enstrophy and helicity dissipation requirements is left for future work.

4.6.6 Realizability requirements

We can specify the realizability requirements R, Eqs. (3.59) to (3.63), for the general class of subgrid-scale models of Eq. (4.29) by substituting this class of models into the definitions of the principal invariants of Eq. (3.56). The realizability constraint for the first principal invariant of the general class of subgrid-scale models can be expressed as

$$0 \leq P_{\tau\text{-mod}} = 3\alpha_0 + \alpha_2 I_1 + \alpha_3 I_2, \quad (4.37)$$

whereas we obtained the inequality

$$\begin{aligned} 0 \leq Q_{\tau\text{-mod}} = & 3\alpha_0^2 + 2\alpha_0\alpha_2 I_1 + 2\alpha_0\alpha_3 I_2 - \frac{1}{2}\alpha_1^2 I_1 - \alpha_1\alpha_2 I_3 - \alpha_1\alpha_3 I_4 \\ & + \frac{1}{4}\alpha_2^2 I_1^2 + \alpha_2\alpha_3(I_1 I_2 - I_5) + \frac{1}{4}\alpha_3^2 I_2^2 - \frac{1}{2}\alpha_4^2(I_1 I_2 - 6I_5) \\ & + \alpha_4\alpha_5(I_1 I_4 + I_2 I_3) + \frac{1}{4}\alpha_5^2(I_1^2 I_2 - 2I_1 I_5 + 4I_3 I_4) \end{aligned} \quad (4.38)$$

for the second principal invariant. The requirement on the third principal invariant of the class of subgrid-scale models can be expressed as

$$\begin{aligned}
0 \leq R_{\tau\text{-mod}} = & \alpha_0^3 + \alpha_0^2\alpha_2I_1 + \alpha_0^2\alpha_3I_2 - \frac{1}{2}\alpha_0\alpha_1^2I_1 - \alpha_0\alpha_1\alpha_2I_3 \\
& - \alpha_0\alpha_1\alpha_3I_4 + \frac{1}{4}\alpha_0\alpha_2^2I_1^2 + \alpha_0\alpha_2\alpha_3(I_1I_2 - I_5) + \frac{1}{4}\alpha_0\alpha_3^2I_2^2 \\
& - \frac{1}{2}\alpha_0\alpha_4^2(I_1I_2 - 6I_5) + \alpha_0\alpha_4\alpha_5(I_1I_4 + I_2I_3) \\
& + \frac{1}{4}\alpha_0\alpha_5^2(I_1^2I_2 - 2I_1I_5 + 4I_3I_4) + \frac{1}{3}\alpha_1^3I_3 \\
& - \frac{1}{2}\alpha_1^2\alpha_3(I_1I_2 - 2I_5) - \frac{1}{6}\alpha_1\alpha_2^2I_1I_3 - \frac{1}{3}\alpha_1\alpha_2\alpha_3I_2I_3 \\
& - \frac{1}{2}\alpha_1\alpha_3^2I_2I_4 - 2\alpha_1\alpha_3\alpha_5I_6 - \frac{1}{2}\alpha_1\alpha_4^2(I_1I_4 + I_2I_3) \\
& - \frac{1}{2}\alpha_1\alpha_4\alpha_5(I_1^2I_2 - 2I_1I_5 + 4I_3I_4) \\
& - \frac{1}{12}\alpha_1\alpha_5^2(3I_1^2I_4 + 5I_1I_2I_3 - 12I_3I_5) + \frac{1}{9}\alpha_2^3I_3^2 \\
& + \frac{1}{12}\alpha_2^2\alpha_3(3I_1^2I_2 - 6I_1I_5 + 4I_3I_4) + \frac{1}{4}\alpha_2\alpha_3^2(I_1I_2^2 - 2I_2I_5) \\
& + 2\alpha_2\alpha_3\alpha_4I_6 + \frac{1}{4}\alpha_2\alpha_4^2(I_1^2I_2 - 2I_1I_5 + 4I_3I_4) \\
& + \frac{1}{6}\alpha_2\alpha_4\alpha_5(3I_1^2I_4 + 5I_1I_2I_3 - 12I_3I_5) \\
& + \frac{1}{24}\alpha_2\alpha_5^2(3I_1^3I_2 - 6I_1^2I_5 + 8I_1I_3I_4 - 4I_2I_3^2) \\
& + \frac{1}{4}\alpha_3\alpha_4^2(I_1I_2^2 - 2I_2I_5 - 4I_4^2) \\
& + \frac{1}{6}\alpha_3\alpha_4\alpha_5(3I_1I_2I_4 + I_2^2I_3 - 12I_4I_5) \\
& - \frac{1}{24}\alpha_3\alpha_5^2(3I_1^2I_2^2 - 18I_1I_2I_5 + 4I_2I_3I_4 + 24I_5^2) \\
& + 2\alpha_4^3I_6 - \alpha_4\alpha_5^2I_1I_6 - \frac{2}{3}\alpha_5^3I_3I_6.
\end{aligned} \tag{4.39}$$

In addition, these three principal invariants should satisfy the chain of inequalities given by Eq. (3.63). As the general class of subgrid-scale models is both real and symmetric, the requirement of Eq. (3.62) is automatically satisfied.

4.6.7 Near-wall scaling requirements

As per the no-slip and incompressibility conditions, scaling relations similar to that shown for the fluctuating velocities in Eqs. (3.65) and (3.66) can be argued to hold for the large-scale velocity components (Sagaut 2006; Trias et al. 2015). We can, therefore, expand the wall-parallel components of the large-scale

velocity as

$$\begin{aligned} v_1 &= f(x_1, x_3) x_2 + \mathcal{O}(x_2^2), \\ v_3 &= g(x_1, x_3) x_2 + \mathcal{O}(x_2^2), \end{aligned} \quad (4.40)$$

where f and g are arbitrary functions of the coordinates x_1 and x_3 , and x_2 denotes the wall-normal coordinate. The wall-normal velocity can correspondingly be expressed as

$$v_2 = -\frac{1}{2} \left(\frac{\partial f}{\partial x_1} + \frac{\partial g}{\partial x_3} \right) x_2^2 + \mathcal{O}(x_2^3). \quad (4.41)$$

These three scaling relations can be used to analyze the near-wall scaling behavior of subgrid-scale models that are based on the velocity field. A set of scripts that can perform this analysis has been made freely available.³

Table 4.1 includes the constraints on the model coefficients of the general class of subgrid-scale models of Eq. (4.29), as resulting from a near-wall scaling analysis and the near-wall scaling requirements of Eq. (3.67). Table 4.1 also shows the near-wall scaling behavior of the invariants of Eq. (4.6) and of special combinations of these invariants.

In addition to the relations shown in Table 4.1, we found that

$$I_5 + c_1 I_1^2 + c_2 I_1 I_2 + c_3 I_2^2 = \mathcal{O}(x_2^2), \quad (4.42)$$

where the dimensionless constants $c_{(i)}$ have to satisfy

$$c_1 - c_2 + c_3 = \frac{1}{2}. \quad (4.43)$$

We also obtained the scaling relation

$$\begin{aligned} I_6 + c_1 I_1^3 + c_2 I_1^2 I_2 + c_3 I_1 I_2^2 + c_4 I_2^3 \\ + c_5 I_1 I_5 + c_6 I_2 I_5 + c_7 I_3^2 + c_8 I_3 I_4 + c_9 I_4^2 = \mathcal{O}(x_2^4), \end{aligned} \quad (4.44)$$

where the dimensionless constants $c_{(i)}$ are solutions of the underdetermined system of equations given by

$$\begin{aligned} -1 &= 4c_1 - 4c_2 + 4c_3 - 4c_4, \\ c_5 &= 4c_1 - 2c_2 + 2c_4, \\ c_6 &= 2c_1 - 2c_3 + 4c_4, \\ c_9 &= 1 - 9c_7 + 3c_8. \end{aligned} \quad (4.45)$$

Application of the dynamic procedure (Germano et al. 1991; Lilly 1992) to a subgrid-scale model of the form of Eq. (4.29) may ensure the proper near-wall scaling behavior regardless of the model coefficients $\alpha_{(i)}$.

³ See <https://github.com/mauritssilvis/lesTools> for a set of scripts that can be used to study the near-wall scaling behavior of subgrid-scale models and other physical quantities that are based on the velocity field of flows.

4.7 Conclusions

In summary, in this chapter, we discussed subgrid-scale models based on the local velocity gradient. We first outlined the assumptions underlying such subgrid-scale models, after which we discussed the class of eddy viscosity models. Aiming to go beyond the limitations of eddy viscosity models, we introduced a general class of subgrid-scale models based on the local velocity gradient.

This general class of subgrid-scale models forms a very useful starting point for the construction of new subgrid-scale models. Practical subgrid-scale models can, however, only be obtained from this class when a selection of model terms is made, when a procedure is found to define the corresponding model coefficients, and when the model constants and subgrid characteristic length scales are determined. A procedure to define the model coefficients can be based on the framework of model constraints of Chapter 3.

By application of this framework, we obtained several constraints on the coefficients of the general class of subgrid-scale models. We also observed that this general class of models by construction satisfies the discussed conservation laws. Moreover, certain symmetries of the incompressible Navier–Stokes equations are preserved if some restrictions on the determination of the model constants and the subgrid characteristic length scales are fulfilled. We did not find a situation in which the discussed scaling requirements are satisfied simultaneously. The general class of subgrid-scale models, thus, seems to have some inherent limitations.

Finally, we found that some constraints on the dissipation of subgrid-scale models are not compatible with each other. The (compatible) constraints on the general class of subgrid-scale models can, however, be used to analyze the properties of existing subgrid-scale models and to construct new physics-based subgrid-scale models that are based on the local velocity gradient.

Chapter 5

Analysis of existing subgrid-scale models

5.1 Introduction

We now apply the framework of model constraints of Chapter 3 to analyze the properties of existing subgrid-scale models for large-eddy simulation. We focus in particular on subgrid-scale models that are based on the local velocity gradient, which we introduced in Chapter 4 and for which we summarized the model constraints in Table 4.1. We first provide examples of existing subgrid-scale models in Section 5.2. We discuss the properties of these models in Section 5.3. We conclude this chapter in Section 5.4.

5.2 Examples of existing subgrid-scale models

Several well-known existing subgrid-scale models are based on the local velocity gradient. We consider both eddy viscosity and nonlinear models.

5.2.1 Eddy viscosity models

We introduced subgrid-scale models of eddy viscosity type in Section 4.3. Some selected eddy viscosity models and their corresponding eddy viscosities are:

- the Smagorinsky model (Smagorinsky 1963),

$$\nu_e^S = (C_S \delta)^2 \sqrt{2I_1}; \quad (5.1)$$

- the WALE model (Nicoud and Ducros 1999),

$$\nu_e^W = (C_W \delta)^2 \frac{J^{3/2}}{I_1^{5/2} + J^{5/4}}, \quad (5.2)$$

$$\text{where } J = \frac{1}{6}(I_1 + I_2)^2 + 2(I_5 - \frac{1}{2}I_1 I_2);$$

- Vreman's model (Vreman 2004),

$$\nu_e^V = (C_V \delta)^2 \sqrt{\frac{Q_{GGT}}{P_{GGT}}}; \quad (5.3)$$

- the σ model (Nicoud et al. 2011),

$$\nu_e^\sigma = (C_\sigma \delta)^2 \frac{\sigma_3(\sigma_1 - \sigma_2)(\sigma_2 - \sigma_3)}{\sigma_1^2}; \quad (5.4)$$

- the QR model (Verstappen et al. 2010; Verstappen 2011; Verstappen et al. 2014),

$$\nu_e^{\text{QR}} = (C_{\text{QR}} \delta)^2 \frac{2}{3} \frac{\max\{0, -I_3\}}{I_1}; \quad (5.5)$$

- the S3PQR models (Trias et al. 2015),

$$\nu_e^{\text{S3}} = (C_{\text{S3}} \delta)^2 P_{GG^T}^p Q_{GG^T}^{-(p+1)} R_{GG^T}^{(p+5/2)/3}; \quad (5.6)$$

- and the anisotropic minimum-dissipation (AMD) model (Rozema et al. 2015),

$$\nu_e^{\text{A}} = (C_{\text{A}} \delta)^2 \frac{\max\{0, -(I_3 - I_4)\}}{I_1 - I_2}. \quad (5.7)$$

Here, C_S, C_W, \dots, C_A are used to denote model constants and δ represents the subgrid characteristic length scale.

In Eqs. (5.3) and (5.6), the quantities

$$\begin{aligned} P_{GG^T} &= I_1 - I_2, \\ Q_{GG^T} &= \frac{1}{4}(I_1 + I_2)^2 + 4(I_5 - \frac{1}{2}I_1 I_2), \\ R_{GG^T} &= \frac{1}{9}(I_3 + 3I_4)^2 \end{aligned} \quad (5.8)$$

are the principal invariants of the tensor

$$GG^T = S^2 - W^2 - (SW - WS). \quad (5.9)$$

The σ_i in Eq. (5.4) represent the square roots of the eigenvalues of this same tensor or, equivalently, the singular values of the velocity gradient G , where $\sigma_1 \geq \sigma_2 \geq \sigma_3 \geq 0$. Nicoud et al. (2011) provide expressions of these singular values in terms of the principal invariants of Eq. (5.8).

To avoid confusion, note that the Q and R in the name of the QR model refer to the second and third principal invariants of the rate-of-strain tensor, which are, respectively, given by

$$Q_S = -\frac{1}{2}I_1, \quad R_S = \frac{1}{3}I_3. \quad (5.10)$$

The P, Q and R of the S3PQR models refer to the invariants of Eq. (5.8). The S3PQR models form a class of subgrid-scale models, one for each value of the parameter p . Following Trias et al. (2015), we consider the S3PQ ($p = -5/2$), S3PR ($p = -1$) and S3QR ($p = 0$) models.

Finally, note that Eqs. (5.3) and (5.7) provide isotropized expressions of Vreman's model (Vreman 2004) and the anisotropic minimum-dissipation (Rozema et al. 2015), respectively. These expressions are meant to analyze the properties of these subgrid-scale models. Numerical implementations should rely on the original anisotropic expressions provided by Vreman (2004) and Rozema et al. (2015).

5.2.2 Nonlinear models

A specific example of a nonlinear model that is part of the general class of subgrid-scale models of Eq. (4.29) is given by the *gradient model* of Leonard (1975) and Clark et al. (1979),

$$\tau_G^{\text{mod}} = C_G \delta^2 [S^2 - W^2 - (SW - WS)]. \quad (5.11)$$

The gradient model forms the lowest-order Taylor approximation of the turbulent stress tensor τ_{ij} of Eq. (1.75) in terms of the filter length $\bar{\delta}$. For a number of commonly used filters $C_G = 1/12$ (Berselli et al. 2006).

A different nonlinear model is the *explicit algebraic subgrid-scale stress model* (EASSM) of Marstorp et al. (2009). The nondynamic version of this model can be expressed as

$$\tau_E^{\text{mod}} = C_E \delta^2 \frac{f}{f^2 - I_2/I_1} * \left[\frac{80}{99} I_1 I - \sqrt{2I_1} \frac{f}{f^2 - I_2/I_1} S - \frac{1}{f^2 - I_2/I_1} (SW - WS) \right]. \quad (5.12)$$

Here, $f = f(I_2/I_1)$ is a dimensionless function that tends to 1 as I_2/I_1 goes to 0 and that corresponds to $9c_1/(4c_3)$ in the notation of Marstorp et al. (2009). This function involves several (empirical) constants.

5.3 Properties of existing subgrid-scale models

The behavior of the subgrid-scale models of Section 5.2 with respect to the model requirements of Chapter 3 can be analyzed using Table 4.1. We discuss the results of this analysis, which are summarized in Table 5.1, in what follows.

For the analysis, we assumed that the subgrid characteristic length scale δ is defined in terms of the grid size and that model constants are determined using a nondynamic method. We discuss the effects of the dynamic procedure (Germano et al. 1991; Lilly 1992) in Section 5.3.9.

5.3.1 Dimensional properties

According to the dimensional constraints of Table 4.1, all existing subgrid-scale models discussed in Section 5.2 have the proper physical units.

Table 5.1: Summary of the properties of several subgrid-scale models. The properties considered are U: dimensional consistency (Eq. (3.1)); S1–3: time translation, pressure translation and generalized Galilean invariance (Eq. (3.8)); S4: rotation and reflection invariance (Eq. (3.9)); S5: scaling invariance (Eq. (3.10)); S6: two-dimensional material frame indifference (Eq. (3.11)); B1: breaking of time reversal invariance (Eq. (3.15)); B2: breaking of spatial scaling invariance (Eq. (3.16)); B3: breaking of three-dimensional material frame indifference (Eq. (3.17)); C1–5: conservation of mass, momentum, angular momentum, vorticity and vorticity-related quantities (Section 3.5.2); D1: zero subgrid dissipation for laminar flows (Eq. (3.36)); D2: nonzero subgrid dissipation for nonlaminar flows (Eq. (3.37)); D3: zero subgrid dissipation for two-component flows (Section 3.6.5); D4: zero subgrid dissipation for the pure axisymmetric strain (Section 3.6.5); D5: consistency with the second law of thermodynamics (Eq. (3.38)); D6: sufficient eddy viscosity for scale separation (Eq. (4.34)); R: realizability (Eqs. (3.59) to (3.63)); and N: the proper near-wall scaling behavior (Eq. (3.67)). The horizontal rule separates eddy viscosity models from models that are nonlinear in the velocity gradient. Y: The property is satisfied. N: The property is not satisfied. C: The property may be satisfied for certain values of the model constants.

Model	Eq.	U	S1–3	S4	S5	S6	B1	B2	B3	C1–5	D1	D2	D3	D4	D5	D6	R	N
Smagorinsky	(5.1)	Y	Y	Y	N	Y	Y	Y	N	Y	N	Y	N	N	Y	Y		N
WALE	(5.2)	Y	Y	Y	N	N	Y	Y	Y	Y	N	Y	N	N	Y	Y		Y
Vreman	(5.3)	Y	Y	Y	N	N	Y	Y	Y	Y	N	Y	N	N	Y	Y		N
σ	(5.4)	Y	Y	Y	N	Y	Y	Y	Y	Y	Y	N	Y	Y	Y	N		Y
QR	(5.5)	Y	Y	Y	N	Y	Y	Y	N	Y	Y	N	Y	N	Y	N		N
S3PQR	(5.6)	Y	Y	Y	N	Y ^a	Y ^a	Y	Y	Y	Y ^a	Y ^a	Y ^a	N	Y ^a	Y ^a		Y
- S3PQ		Y	Y	Y	N	N	Y	Y	Y	Y	N	Y	N	N	Y	Y		Y
- S3PR		Y	Y	Y	N	Y	Y ^a	Y	Y	Y	Y	N	Y	N	Y ^a	N		Y
- S3QR		Y	Y	Y	N	Y	Y ^a	Y	Y	Y	Y	N	Y	N	Y ^a	N		Y
AMD	(5.7)	Y	Y	Y	N	Y	Y	Y	Y	Y	Y	N	Y	N	Y	Y		N
Gradient	(5.11)	Y	Y	Y	N	N	N	Y	Y	Y	Y	N	Y	N	N		Y	N
EASSM	(5.12)	Y	Y	Y	N	N	Y	Y	Y	Y	N	Y	N	N	C		Y	N

^a Depending on the value of the model parameter p and/or the implementation.

5.3.2 Symmetry properties

All subgrid-scale models of Section 5.2 are based on the rate-of-strain and rate-of-rotation tensors as well as their combined invariants. In addition, we assume the use of subgrid characteristic length scales δ defined in terms of the grid size and a nondynamic determination of model constants. Time translation, pressure translation, generalized Galilean, rotation and reflection invariance (requirements S1–4 of Eqs. (3.8) and (3.9)) are, therefore, satisfied by all considered subgrid-scale models.

On the other hand, with such an externally imposed length scale δ , scale invariance (requirement S5 of Eq. (3.10)) is not satisfied. As a consequence, the subgrid-scale models discussed in Section 5.2 can in principle not capture scaling laws like the well-known log law of wall-bounded flows or certain self-similar flows (Oberlack 1997; Razafindralandy et al. 2007).

All eddy viscosity models that can be expressed using the invariants characterizing two-component flows (see Eq. (4.27)) or that turn off for these flows satisfy two-dimensional material frame indifference (requirement S6 of Eq. (3.11)). The eddy viscosity may also contain I_1 . Not all eddy viscosity models have this property. The gradient and explicit algebraic subgrid-scale stress models do not satisfy requirement S6, since they contain nonlinear terms involving the rate-of-rotation tensor that do not vanish in two-component flows.

5.3.3 Symmetry breaking properties

Most eddy viscosities listed in Eqs. (5.1) to (5.7) are positive for all possible flows. Therefore, time irreversibility (requirement B1 of Eq. (3.15)) is ensured. In contrast, the gradient model is time reversal invariant. The explicit algebraic subgrid-scale stress model has the interesting property that the term that is linear in S is not time reversal invariant, whereas both other terms are. Therefore, only the gradient model does not lead to the desired breaking of time reversal invariance.

With a grid-dependent subgrid characteristic length scale, each subgrid-scale model breaks spatial scaling invariance (requirement B2 of Eq. (3.16)). Three-dimensional material frame difference is not broken by subgrid-scale models that only depend on the rate-of-strain tensor, such as the Smagorinsky and QR models, Eqs. (5.1) and (5.5). These subgrid-scale models, therefore, are not directly sensitive to rotation and may not give proper predictions of rotating turbulent flows. The other considered subgrid-scale models do break three-dimensional material frame indifference and are sensitive to rotation.

5.3.4 Conservation properties

All the subgrid-scale models of Section 5.2 are specific examples of the general class of Eq. (4.29). According to Section 4.6.4, these models, therefore, automatically satisfy the laws of conservation of mass, momentum, angular momentum, vorticity and vorticity-related quantities (requirements C1–5 of Section 3.5.2).

Table 5.2: Summary of the size of the flow algebra of the true subgrid dissipation D^k , Eq. (3.34), and of several quantities based on the tensor invariants of Eq. (4.6). Here, $Q_{(n)}$ represents the set of flow types for which the velocity gradient contains n zero elements. The total number of (three-dimensional) flows (3D) and the number of two-component (2C) flows (see Eq. (4.27)) in Vreman's classification are listed for reference. Results provided here differ from those of Vreman (2004) because we assumed the use of an isotropic filter to compute D^k .

	Q_0	Q_1	Q_2	Q_3	Q_4	Q_5	Q_6	Q_7	Q_8	Q_9	Q_{0-9}
3D flows	1	9	33	66	81	66	39	18	6	1	320
2C flows						3	6	12	6	1	28
D^k								9	6	1	16
$I_1, I_1 - I_2, P_{GG^T}, \nu_e^S, D_E^{k,\text{mod}}$										1	1
$Q_{GG^T}, \nu_e^W, \nu_e^V, \nu_e^{\text{S3PQ}}$								6	6	1	13
I_2, I_5							1	3		1	5
$I_1 + I_2, Q_G$							8	12	6	1	27
$I_5 - \frac{1}{2}I_1I_2$						3	7	12	6	1	29
I_3, ν_e^{QR}						6	18	18	6	1	49
I_4						6	19	18	6	1	50
$I_3 - I_4, \nu_e^A, D_G^{k,\text{mod}}$						6	20	18	6	1	51
I_6					3	15	19	12	6	1	56
$I_3 + 3I_4, R_G, R_{GG^T}, \nu_e^\sigma, \nu_e^{\text{S3PR}}, \nu_e^{\text{S3QR}}$				6	30	48	36	18	6	1	145

5.3.5 Dissipation properties

The dissipation of kinetic energy due to subgrid-scale models is given by Eq. (3.35), while eddy viscosity models were defined in Eq. (4.1). We can, thus, express the subgrid dissipation of kinetic energy due to eddy viscosity models as

$$D_e^{k,\text{mod}} = 2\nu_e I_1. \quad (5.13)$$

As I_1 is nonnegative and only vanishes in purely rotational flows (Eq. (4.20)), the subgrid dissipation of Eq. (5.13) is mostly determined by the eddy viscosity ν_e .

For the gradient model, Eq. (5.11), we have

$$D_G^{k,\text{mod}} = C_G \delta^2 (I_3 - I_4). \quad (5.14)$$

This quantity does not have a definite sign. The subgrid dissipation of the explicit algebraic subgrid-scale stress model, Eq. (5.12), is due to the term linear in the rate-of-strain tensor. Therefore, $D_E^{k,\text{mod}}$ has an expression similar to Eq. (5.13).

As discussed in Section 4.6.5, the dissipation behavior of subgrid-scale models can be studied using the flow classification of Vreman (2004). In particular, we can determine the flow algebra of the modeled dissipation of kinetic energy. That is, we can determine the set of flows for which this dissipation vanishes. This set of flows can then be compared to the set of laminar flows, which constitutes the flow algebra of the true dissipation. Subgrid-scale models that are constructed using quantities that have a smaller flow algebra than the true subgrid dissipation can be expected to be too dissipative. On the other hand, a model based on a quantity that is zero more often than D^k , can be expected to be underly dissipative.

Table 5.2 provides a summary of the size of the flow algebra of several quantities, including the subgrid dissipation of kinetic energy due to the subgrid-scale models discussed in Section 5.2. As this table shows, none of the discussed subgrid-scale models has exactly the same dissipation behavior as the true turbulent stresses. This result contrasts with the findings of Vreman (2004), which is due to the fact that we assumed the use of an isotropic filter to compute the true subgrid dissipation (see Section 4.6.5). The quantity $I_5 - \frac{1}{2}I_1I_2$ has the smallest flow algebra that includes the flow algebra of the true dissipation.

Using the characterization of two-component flows given by Eq. (4.27), we can easily verify whether the subgrid-scale models of Section 5.2 satisfy model requirement D3 of Section 3.6.5. About half of the considered subgrid-scale models vanish in two-component flows and satisfy this requirement. Satisfaction of requirement D4 of Section 3.6.5 can be checked using Eqs. (4.21) and (4.23), which characterize the pure axisymmetric strain. Only one subgrid-scale model of Section 5.2, namely the σ model, Eq. (5.4), turns off for this flow type.

In the context of irreversibility of subgrid-scale models, we remarked that most eddy viscosities listed in Section 5.2 are positive for all possible flow fields. Indeed, only ν_e^{S3} can become negative, and only for certain values of

the model parameter p . Therefore, most considered eddy viscosity models are consistent with the second law of thermodynamics (requirement D5 of Eq. (3.38)), regardless of the flow.

An eddy viscosity model with a positive eddy viscosity cannot capture backscatter. The gradient model, Eq. (5.11), can account for backscatter but does so in a way that violates the second law of thermodynamics and that causes numerical simulations to blow up (Vreman et al. 1996; Winckelmans et al. 2001; Berselli and Iliescu 2003). Whether the explicit algebraic subgrid-scale stress model, Eq. (5.12), is consistent with the second law of thermodynamics depends on the values of the model constants.

As explained in Section 4.6.4, an eddy viscosity model can satisfy Verstappen’s minimum-dissipation requirement (requirement D6 of Eq. (3.40)) if the form of such a subgrid-scale model satisfies Eq. (4.34) for one or more values of the Poincaré constant. This condition is satisfied by about half of the considered eddy viscosity models.

Do note that eddy viscosity models that have the proper form may fail to satisfy Eq. (4.34) once practical values are used for the model constants. Also note that the QR model only satisfies Eq. (4.34) if we assume a triply periodic integration volume V_{δ} , for which a certain relation exists between I_3 and I_4 (Chae 2005). This assumption, which was employed in deriving the QR model (Verstappen et al. 2010; Verstappen 2011; Verstappen et al. 2014), was not made in the present analysis.

The behavior of the explicit algebraic subgrid-scale stress model, Eq. (5.12), with respect to Verstappen’s minimum-dissipation requirement (requirement D6 of Eq. (3.40)) depends on the complicated function f . The gradient model, Eq. (5.11), does not have a term that is proportional to the rate-of-strain tensor. We, therefore, did not determine whether these models satisfy requirement D6 or not.

5.3.6 Discussion of realizability

As remarked in Section 3.7, we can only assess the realizability of subgrid-scale models that include a model for the generalized subfilter-scale kinetic energy k_t^{mod} . Such a model is not supplied by the eddy viscosity models of Section 5.2. The gradient model and the explicit algebraic subgrid-scale stress model both provide an explicit model for the subfilter-scale kinetic energy and can be shown to be realizable.

5.3.7 Near-wall scaling behavior

The near-wall scaling behavior of the coefficients of the subgrid-scale models considered in Section 5.2 can readily be deduced using the results of Table 4.1. Comparison with the desired behavior, which is also summarized in Table 4.1, shows that only the subgrid-scale models that were designed with the near-wall scaling in mind, namely the WALE, σ and S3PQR models, Eqs. (5.2), (5.4) and (5.6), have the proper near-wall behavior. These subgrid-scale models,

therefore, make sure that dissipative effects are not too prominent near a wall. Damping functions or the dynamic procedure (Germano et al. 1991; Lilly 1992) can be used to correct the near-wall behavior of the other subgrid-scale models (Sagaut 2006).

5.3.8 Concluding remarks

Table 5.1 and the above discussion show that the existing subgrid-scale models that we have considered do not exhibit all the desired properties of Chapter 3. This conclusion can partly be understood from two observations. First, we saw in Section 4.6 that some model constraints of Chapter 3 are not compatible with each other.

Secondly, subgrid-scale models based on the local velocity gradient seem to have some inherent limitations, as we did not find a situation in which invariance under the scaling transformation of Eq. (3.6) (requirement S5 of Eq. (3.10)) and breaking of the spatial scaling transformation of Eq. (3.13) (requirement B2 of Eq. (3.16)) are satisfied simultaneously. Despite these observations, there is room for improvement in the properties of subgrid-scale models that are based on the local velocity gradient.

5.3.9 Effects of the dynamic procedure

In the above analysis of the subgrid-scale models of Section 5.2, we assumed the use of a grid-dependent subgrid characteristic length scale δ as well as a nondynamic determination of model constants. If model constants are determined dynamically (Germano et al. 1991; Lilly 1992), the results contained in Table 5.1 may change.

In particular, if the required filtering operation is not invariant under the time and pressure translations, Eqs. (3.2) and (3.3), the generalized Galilean transformation, Eq. (3.4), orthogonal transformations of the coordinate system, Eq. (3.5), or the solid body rotation of a two-component flow given by Eq. (3.7), the corresponding symmetry properties (requirements S1–4 and S6 of Eqs. (3.8), (3.9) and (3.11)) will be destroyed (Oberlack 1997; Razafindralandy et al. 2007). Invariance with respect to the scaling transformation of Eq. (3.6) (requirement S5 of Eq. (3.10)) can be restored by the dynamic procedure (Oberlack 1997; Razafindralandy et al. 2007), but breaking of the spatial scaling symmetry of Eq. (3.13) (requirement B2 of Eq. (3.16)) will then not be satisfied.

The dynamic procedure can restore time reversal invariance of the modeled subgrid-scale stresses when used without clipping (Carati et al. 2001). As discussed in Section 3.4.3, this feature of the dynamic procedure is not seen as desirable. As discussed in that same section, the filtering operation will in practice not preserve three-dimensional material frame indifference. The dynamic procedure, thus, leads to the desired breaking of this property (requirement B3 of Eq. (3.17)), also when combined with the Smagorinsky model, Eq. (5.1).

The dynamic procedure may, furthermore, restore satisfaction of dissipation requirement D1 of Eq. (3.36) for subgrid-scale models that have an eddy viscosity

that does not vanish in laminar flows. If the dynamic procedure introduces time reversibility, however, consistency with the second law of thermodynamics (requirement D5 of Eq. (3.38)) may be destroyed. Finally, the dynamic procedure is expected to give each subgrid-scale model the proper near-wall scaling behavior (requirement N of Eq. (3.67)).

Application of the dynamic procedure (Germano et al. 1991; Lilly 1992) may, thus, improve some properties of subgrid-scale models. On the other hand, other properties may be destroyed by this procedure.

5.4 Conclusions

In this chapter, we analyzed the behavior of several existing subgrid-scale models that are based on the local velocity gradient with respect to the model requirements of Chapter 3. We saw that the considered subgrid-scale models do not exhibit all the desired properties.

This conclusion can partly be understood from the observation that some model constraints are not compatible with each other. Additionally, subgrid-scale models based on the local velocity gradient do not seem to be able to satisfy all scaling requirements. However, despite these observations, there is room for improvement in the properties and, hence, the behavior of subgrid-scale models that are based on the local velocity gradient.

The dynamic procedure (Germano et al. 1991; Lilly 1992) may aid in improving the properties of such subgrid-scale models. Special care would, however, have to be taken in preserving certain symmetry properties, in breaking spatial scaling invariance and in ensuring consistency with the second law of thermodynamics. Such work on (the filtering operation of) the dynamic procedure is out of the scope of this thesis. In Chapter 6, we will, therefore, focus on creating new subgrid-scale models with (more) built-in desirable properties.

Chapter 6

Constructing new subgrid-scale models

6.1 Introduction

In this chapter, we illustrate how the model constraints of Chapter 3 can be used to construct new physics-based subgrid-scale models with built-in desirable properties. We focus on the construction of subgrid-scale models that are based on the local velocity gradient, which we introduced in Chapter 4 and for which we summarized the model constraints in Table 4.1.

Specifically, in Section 6.2, we outline a systematic procedure that can be used to create new physics-based subgrid-scale models that are based on the local velocity gradient. In Section 6.3, we use this procedure to provide examples of new subgrid-scale models. We discuss the properties of these models in Section 6.4. Brief conclusions are provided in Section 6.5.

6.2 Systematic procedure

As explained in Section 4.5, we can only obtain practical new subgrid-scale models from the general class of Eq. (4.29) if three steps are taken. First, we have to make a selection of model terms. Secondly, we have to find a procedure to define the corresponding model coefficients. Finally, we have to determine the model constant and define the subgrid characteristic length scale of each term. In Section 4.6, we saw that the framework of model requirements of Chapter 3 provides several constraints on the model coefficients and we summarized these constraints in Table 4.1.

However, neither the framework of Chapter 3, nor the model constraints of Table 4.1 suggests a practical procedure to construct new subgrid-scale models. We will, therefore, describe a systematic procedure that can be used to create new physics-based subgrid-scale models from the general class of models of Eq. (4.29). This procedure consists in applying the model constraints of Chapter 3 in a particular order.

Note that the different model constraints do not necessarily play a role in each step of the model construction process. For example, the requirements on the units of the subgrid-scale model (requirement U of Eq. (3.1)) do not constrain the selection of model terms, nor the determination of the model constants. On the other hand, symmetry requirements S1–5, Eqs. (3.8) to (3.10), and

symmetry breaking requirement B2, Eq. (3.16), only restrict the determination of the model constants and the subgrid characteristic length scale. Conservation requirements C1–5 of Section 3.5.2 do not provide any information, as the class of subgrid-scale models of Eq. (4.29) automatically satisfies the considered conservation laws.

6.2.1 Selecting the model terms

To make a selection of model terms of the general class of subgrid-scale models of Eq. (4.29), we first decide if realizability (requirement R of Eqs. (3.59) to (3.63)) or explicit modeling of the generalized subfilter-scale kinetic energy k_t (see Eq. (3.57)) are important for our purposes. If that is the case, we have to retain at least one of the tensors $T^{(0)}$, $T^{(2)}$ or $T^{(3)}$. In other words, α_0 , α_2 and α_3 should not all be zero.

Realizability and modeling of the subfilter-scale kinetic energy are not always of interest, however, as may be the case for simulations of incompressible turbulent flows. Then, we can focus solely on modeling the deviatoric part of the subgrid-scale stresses by taking

$$\alpha_0 = -\frac{1}{3}(\alpha_2 I_1 + \alpha_3 I_2). \quad (6.1)$$

As a second step, we establish which model properties are relevant for the flow(s) under study. One can, for example, choose model terms based on their dissipation behavior. The tensor $T^{(1)}$ (mostly) represents dissipative effects, whereas $T^{(0)}$, $T^{(4)}$ and $T^{(5)}$ do not directly contribute to the subgrid dissipation. Tensors $T^{(2)}$ and $T^{(3)}$ describe both dissipative and nondissipative effects. Sensitivity to rotation and the resulting breaking of three-dimensional material frame indifference (requirement B3 of Eq. (3.17)) can be enforced by including the tensors $T^{(3)}$, $T^{(4)}$ and/or $T^{(5)}$. In Part II of this thesis, we reason which terms of Eq. (4.29) are important for large-eddy simulations of rotating turbulent flows.

6.2.2 Defining the model coefficients

After selecting the model terms, we have to specify the functional dependence of the corresponding model coefficients on the invariants of Eq. (4.6). To that end, we take the following steps for each model term.

First, we decide if a model term needs to have the proper near-wall scaling behavior (requirement N of Eq. (3.67)). If that is not the case, we proceed by selecting one *physical quantity* on which to base the model coefficient. Here, a physical quantity is understood to be either one invariant or a function of the invariants of Eq. (4.6).

Symmetry requirement S6 of Eq. (3.11), symmetry breaking requirements B1 and B3 of Eqs. (3.15) and (3.17), dissipation requirements D1–6 of Section 3.6 and their specialized versions in Table 4.1 can be used to choose the physical quantities that will underlie the coefficients α_1 , α_2 and α_3 of the dissipative

model terms. The physical quantities that will define the model coefficients of the nondissipative terms, α_4 , α_5 and possibly α_0 , can be chosen using the symmetry and symmetry breaking requirements. Realizability (requirement R of Eqs. (3.59) to (3.63), particularized in Eqs. (4.37) to (4.39)) can also provide suggestions for physical quantities. We then define the function $f_{(i)}$ that is part of the model coefficient $\alpha_{(i)}$ (see Eq. (4.5)) as the selected physical quantity to a certain power. The exponent has to be chosen in such a way that we obtain the proper units of time (requirement U of Eq. (3.1), also refer to Table 4.1).

If a certain model term needs to have the proper near-wall scaling behavior, the above procedure does not work and may be adapted as follows. We first select a physical quantity according to the guidelines provided above, with the additional restriction that the near-wall scaling exponent of this quantity has to be higher than zero. We will refer to this quantity as the *primary physical quantity*. We subsequently select one or more *secondary physical quantities*. These quantities should not have a higher near-wall scaling exponent than the primary physical quantity. Moreover, these secondary physical quantities should not vanish in flows in which the primary physical quantity is nonzero.

We then define the function $f_{(i)}$ as a product of the selected primary and secondary physical quantities, where each quantity is given an exponent. The exponents should be chosen to ensure both dimensional consistency (requirement U of Eq. (3.1)) and the proper near-wall scaling (requirement N of Eq. (3.67)).

After specifying the function $f_{(i)}$ for each selected model term, we can assemble the subgrid-scale model according to the definitions of the general class of models, Eq. (4.29), and the model coefficients, Eq. (4.5). Here, the coefficients $\alpha_{(i)}$ of model terms that were not selected may be set to zero.

6.2.3 Determining the model constants and the subgrid characteristic length scales

Finally, we have to determine the model constant $C_{(i)}$ and define the subgrid characteristic length scale $\delta_{(i)}$ of each term of the resulting subgrid-scale model. First focusing on the former, we note that dissipation requirements D4–5 of Section 3.6.5 (also refer to Table 4.1) may provide relations among or bounds on the model constants. Similarly, if one wants to enforce realizability (requirement R of Eqs. (3.59) to (3.63), also see Eqs. (4.37) to (4.39)), the model constants may have to fall within certain ranges of values.

More restrictions apply if model constants are not given fixed numerical values, but are determined dynamically (Germano et al. 1991; Lilly 1992). A dynamic procedure should conform to symmetry requirements S1–6 of Eqs. (3.8) to (3.11) and symmetry breaking requirements B1–3 of Eqs. (3.15) to (3.17). In addition, such a procedure may be used to satisfy dissipation requirements D1–6 of Section 3.6 and the near-wall scaling requirements N of Eq. (3.67).

The framework of model constraints of Chapter 3 does, however, not provide us with specific model constants, nor with a procedure to determine their values. Additional information, whether theoretical or experimental in nature, thus, is required to implement a subgrid-scale model.

The subgrid characteristic length scales $\delta_{(i)}$ can, for example, be defined in terms of the local grid size (see, e.g., Deardorff 1970). Flow-dependent definitions are also possible, however (see, e.g., Trias et al. 2017). Symmetry requirements S1–5 of Eqs. (3.8) to (3.10) and symmetry breaking requirement B2 of Eq. (3.16) provide restrictions on and may be used to motivate the choice of the length scales.

In conclusion, we obtained a systematic procedure for the construction of physics-based subgrid-scale models that have built-in desirable properties. This procedure may also provide bounds on the constants of such models. Additional information is necessary, however, to determine the exact values of these constants and allow for the application of these models.

6.3 Examples of new subgrid-scale models

We now illustrate how new subgrid-scale models may be obtained from the general class of subgrid-scale models of Eq. (4.29) using the procedure outlined in Section 6.2. To obtain general results, we will not make a selection of model terms, nor set the model constants. Rather, we will focus on the definition of the model coefficients. For simplicity of notation, we use the same subgrid characteristic length scale, denoted by δ , for each term.

The selection of physical quantities that are based on the invariants of Eq. (4.6) forms an essential step in defining the model coefficients of the general class of subgrid-scale models of Eq. (4.29), as these quantities largely determine the properties of a model. We first show how physical quantities from existing subgrid-scale models can be used to generalize these models. We then illustrate how new physical quantities can be selected and lead to new physics-based subgrid-scale models.

6.3.1 Generalizations of existing subgrid-scale models

The generalized Smagorinsky or Lund–Novikov model

As shown in Eq. (5.1), the Smagorinsky model (Smagorinsky 1963) is based on invariant I_1 of Eq. (4.6). The proper near-wall scaling behavior (requirement N of Eq. (3.67)) cannot be enforced using this (single) physical quantity. Taking dimensional consistency (requirement U of Eq. (3.1)) into account, we may, however, define a nonlinear subgrid-scale model based on I_1 as

$$\begin{aligned} \tau_{\text{GS}}^{\text{mod}} = & C_0 \delta^2 I_1 I - 2(C_1 \delta)^2 \sqrt{2I_1} S + C_2 \delta^2 S^2 + C_3 \delta^2 W^2 \\ & + C_4 \delta^2 (SW - WS) + C_5 \delta^2 \frac{1}{\sqrt{I_1}} (S^2 W - WS^2). \end{aligned} \quad (6.2)$$

Here, the $C_{(i)}$ denote dimensionless model constants.

We will refer to Eq. (6.2) as the *generalized Smagorinsky* or *generalized Lund–Novikov model*. Different existing subgrid-scale models may be obtained from this model for specific values of the model constants. For example, the

Smagorinsky model of Eq. (5.1) follows when all model constants $C_{(i)}$ with $i \neq 1$ are set to zero. The gradient model (Leonard 1975; Clark et al. 1979) of Eq. (5.11) can also be obtained from Eq. (6.2) for specific model constants. When considering only the deviatoric part of Eq. (6.2), we obtain the general nonlinear model of Lund and Novikov (1992).

The generalized QR model

The QR model (Verstappen et al. 2010; Verstappen 2011; Verstappen et al. 2014), provided in Eq. (5.5), depends on two invariants of the rate-of-strain tensor, namely I_1 and I_3 of Eq. (4.6). Considering both dimensional consistency (requirement U of Eq. (3.1)) and the desired near-wall scaling behavior (requirement N of Eq. (3.67)), we may extend this model to the *generalized QR model*,

$$\begin{aligned} \tau_{\text{GQR}}^{\text{mod}} = & C_0 \delta^2 \frac{I_3^4}{I_1^5} I - 2(C_1 \delta)^2 \frac{\max\{0, -I_3\}^3}{I_1^4} S + C_2 \delta^2 \frac{I_3^4}{I_1^6} S^2 + C_3 \delta^2 \frac{I_3^4}{I_1^6} W^2 \\ & + C_4 \delta^2 \frac{I_3^4}{I_1^6} (SW - WS) + C_5 \delta^2 \frac{\max\{0, -I_3\}^3}{I_1^5} (S^2 W - WS^2). \end{aligned} \quad (6.3)$$

The generalized S3PQR models

Similarly, we may generalize the S3PQR models (Trias et al. 2015) of Eq. (5.6) by considering model coefficients that depend on the three principal invariants P_{GG^T} , Q_{GG^T} and R_{GG^T} of the tensor GG^T , which are given in Eq. (5.8). The resulting *generalized S3PQR models* are given by

$$\begin{aligned} \tau_{\text{GS3}}^{\text{mod}} = & C_0 \delta^2 P_{GG^T}^p Q_{GG^T}^{-(p+1)} R_{GG^T}^{(p+3)/3} I \\ & - 2(C_1 \delta)^2 P_{GG^T}^p Q_{GG^T}^{-(p+1)} R_{GG^T}^{(p+5/2)/3} S \\ & + C_2 \delta^2 P_{GG^T}^p Q_{GG^T}^{-(p+2)} R_{GG^T}^{(p+4)/3} S^2 \\ & + C_3 \delta^2 P_{GG^T}^p Q_{GG^T}^{-(p+2)} R_{GG^T}^{(p+4)/3} W^2 \\ & + C_4 \delta^2 P_{GG^T}^p Q_{GG^T}^{-(p+2)} R_{GG^T}^{(p+4)/3} (SW - WS) \\ & + C_5 \delta^2 P_{GG^T}^p Q_{GG^T}^{-(p+2)} R_{GG^T}^{(p+7/2)/3} (S^2 W - WS^2). \end{aligned} \quad (6.4)$$

The parameter p may be chosen separately for each model term.

As such, we may, for example, obtain the *generalized S3PQ model*,

$$\begin{aligned} \tau_{\text{GS3PQ}}^{\text{mod}} = & C_0 \delta^2 \frac{Q_{GG^T}^2}{P_{GG^T}^3} I - 2(C_1 \delta)^2 \frac{Q_{GG^T}^{3/2}}{P_{GG^T}^{5/2}} S + C_2 \delta^2 \frac{Q_{GG^T}^2}{P_{GG^T}^4} S^2 \\ & + C_3 \delta^2 \frac{Q_{GG^T}^2}{P_{GG^T}^4} W^2 + C_4 \delta^2 \frac{Q_{GG^T}^2}{P_{GG^T}^4} (SW - WS) \\ & + C_5 \delta^2 \frac{Q_{GG^T}^{3/2}}{P_{GG^T}^{7/2}} (S^2 W - WS^2). \end{aligned} \quad (6.5)$$

This model can also be seen as a generalization of the isotropized version of the model of Vreman (2004), which was given in Eq. (5.3).

For different choices of the model parameter p , we can obtain the *generalized S3PR model*,

$$\begin{aligned}\tau_{\text{GS3PR}}^{\text{mod}} &= C_0 \delta^2 \frac{R_{GGT}^{2/3}}{P_{GGT}} I - 2(C_1 \delta)^2 \frac{R_{GGT}^{1/2}}{P_{GGT}} S + C_2 \delta^2 \frac{R_{GGT}^{2/3}}{P_{GGT}^2} S^2 \\ &+ C_3 \delta^2 \frac{R_{GGT}^{2/3}}{P_{GGT}^2} W^2 + C_4 \delta^2 \frac{R_{GGT}^{2/3}}{P_{GGT}^2} (SW - WS) \\ &+ C_5 \delta^2 \frac{R_{GGT}^{1/2}}{P_{GGT}^2} (S^2 W - W S^2),\end{aligned}\quad (6.6)$$

and the *generalized S3QR model*,

$$\begin{aligned}\tau_{\text{GS3QR}}^{\text{mod}} &= C_0 \delta^2 \frac{R_{GGT}}{Q_{GGT}} I - 2(C_1 \delta)^2 \frac{R_{GGT}^{5/6}}{Q_{GGT}} S + C_2 \delta^2 \frac{R_{GGT}^{4/3}}{Q_{GGT}^2} S^2 \\ &+ C_3 \delta^2 \frac{R_{GGT}^{4/3}}{Q_{GGT}^2} W^2 + C_4 \delta^2 \frac{R_{GGT}^{4/3}}{Q_{GGT}^2} (SW - WS) \\ &+ C_5 \delta^2 \frac{R_{GGT}^{7/6}}{Q_{GGT}^2} (S^2 W - W S^2).\end{aligned}\quad (6.7)$$

The generalized AMD model

Finally, the isotropic formulation of the anisotropic minimum-dissipation (AMD) model (Rozema et al. 2015), given by Eq. (5.7), may be expanded to the *generalized AMD model*,

$$\begin{aligned}\tau_{\text{GA}}^{\text{mod}} &= C_0 \delta^2 \frac{(I_3 - I_4)^4}{(I_1 - I_2)^5} I - 2(C_1 \delta)^2 \frac{\max\{0, (-I_3 + I_4)^3\}}{(I_1 - I_2)^4} S \\ &+ C_2 \delta^2 \frac{(I_3 - I_4)^4}{(I_1 - I_2)^6} S^2 + C_3 \delta^2 \frac{(I_3 - I_4)^4}{(I_1 - I_2)^6} W^2 \\ &+ C_4 \delta^2 \frac{(I_3 - I_4)^4}{(I_1 - I_2)^6} (SW - WS) \\ &+ C_5 \delta^2 \frac{\max\{0, (-I_3 + I_4)^3\}}{(I_1 - I_2)^5} (S^2 W - W S^2).\end{aligned}\quad (6.8)$$

We discuss the properties of the above models in Section 6.4.

6.3.2 New subgrid-scale models

Tables 4.1 and 5.2 show that there are several more physical quantities than those employed in the discussed existing models that could be useful for the construction of subgrid-scale models. For example, when aiming to satisfy

symmetry requirement S6 of Eq. (3.11), one could consider all physical quantities based on invariants that vanish in two-component flows, Eq. (4.27). In addition, physical quantities that depend on the rate-of-rotation tensor can aid in satisfying symmetry breaking requirement B3 of Eq. (3.17). Dissipation requirements D1–3 of Section 3.6 show that quantities that vanish in laminar and/or two-component flows could be of interest. Finally, Table 4.1 lists several (combined) quantities that have a nontrivial near-wall scaling behavior.

Of the physical quantities that do not occur in the discussed existing models, we use the second and third principal invariants of the velocity gradient, $Q_G = -\frac{1}{2}(I_1 + I_2)$ and $R_G = \frac{1}{3}I_3 + I_4$ of Eq. (4.7), as well as the invariant $I_5 - \frac{1}{2}I_1I_2$ to construct new physics-based subgrid-scale models. In all three cases, we select different secondary physical quantities to be able to satisfy the near-wall scaling requirements (requirement N of Eq. (3.67)).

The Q_G model

We first take the second principal invariant of the velocity gradient Q_G as primary physical quantity. A quantity that has a lower near-wall scaling exponent than Q_G and only vanishes in flows with a zero velocity gradient is $P_{GG^T} = I_1 - I_2$, the first invariant of the tensor GG^T , given in Eq. (5.8).

Selecting P_{GG^T} as the secondary physical quantity, and enforcing both dimensional consistency (requirement U of Eq. (3.1)) and the near-wall scaling requirements (requirement N of Eq. (3.67)), we can obtain the nonlinear subgrid-scale model given by

$$\begin{aligned} \tau_{Q_G}^{\text{mod}} = & C_0\delta^2 \frac{Q_G^2}{P_{GG^T}} I - 2(C_1\delta)^2 \frac{\max\{0, -Q_G\}^{3/2}}{P_{GG^T}} S + C_2\delta^2 \frac{Q_G^2}{P_{GG^T}^2} S^2 \\ & + C_3\delta^2 \frac{Q_G^2}{P_{GG^T}^2} W^2 + C_4\delta^2 \frac{Q_G^2}{P_{GG^T}^2} (SW - WS) \\ & + C_5\delta^2 \frac{\max\{0, -Q_G\}^{3/2}}{P_{GG^T}^2} (S^2W - WS^2). \end{aligned} \quad (6.9)$$

We will refer to this subgrid-scale model as the Q_G model.

Both the model coefficient of the term that is linear in the rate-of-strain tensor and the last coefficient of this model have been defined to be nonzero when the flow is (locally) dominated by shear, but vanish otherwise. Alternative means to prevent negative values of these model coefficients are, however, possible. One could, for example, use Q_G rather than $-Q_G$ or employ the absolute value of Q_G instead of a clipping procedure.

The R_G model

In a similar fashion, we may use the third principal invariant of the velocity gradient R_G and the invariant P_{GG^T} to construct the R_G model,

$$\tau_{R_G}^{\text{mod}} = C_0\delta^2 \frac{R_G^{4/3}}{P_{GG^T}} I - 2(C_1\delta)^2 \frac{\max\{0, -R_G\}}{P_{GG^T}} S + C_2\delta^2 \frac{R_G^{4/3}}{P_{GG^T}^2} S^2 + \quad (6.10a)$$

$$\begin{aligned}
& + C_3 \delta^2 \frac{R_G^{4/3}}{P_{GG^T}^2} W^2 + C_4 \delta^2 \frac{R_G^{4/3}}{P_{GG^T}^2} (SW - WS) \\
& + C_5 \delta^2 \frac{\max\{0, -R_G\}}{P_{GG^T}^2} (S^2 W - WS^2).
\end{aligned} \tag{6.10b}$$

The vortex-stretching-based model

In view of symmetry requirement S6 of Eq. (3.11), symmetry breaking requirement B3 of Eq. (3.17), dissipation requirements D1–4 of Section 3.6 and the near-wall scaling requirements N of Eq. (3.67), a very useful quantity to base subgrid-scale models on is the invariant $I_5 - \frac{1}{2}I_1I_2$. This nonnegative quantity, which is proportional to the vortex stretching magnitude (see Eq. (4.16)), vanishes in all two-component flows (Eq. (4.27)), as well as in states of pure shear (Eq. (4.21)) and pure rotation (Eq. (4.20)). As a consequence, this quantity is zero in all laminar flows (see Table 5.2). Moreover, this quantity vanishes near solid walls.

The quantity $I_5 - \frac{1}{2}I_1I_2$ can, therefore, be used to correct the near-wall scaling and dissipation behavior of the generalized Smagorinsky model, Eq. (6.2). To that end, we first normalize $I_5 - \frac{1}{2}I_1I_2$ by $-I_1I_2$. The resulting quantity is dimensionless and takes on values between 0 and 1/3 (see Eq. (4.17)). Secondly, we take I_1 as the secondary physical quantity. Finally, imposing dimensional consistency (requirement U of Eq. (3.1)) as well as the desired near-wall scaling behavior (requirement N of Eq. (3.67)), we obtain the *vortex-stretching-based model*,

$$\begin{aligned}
\tau_{\text{VS}}^{\text{mod}} &= C_0 \delta^2 I_1 \left(\frac{I_5 - \frac{1}{2}I_1I_2}{-I_1I_2} \right)^2 I - 2(C_1 \delta)^2 \sqrt{2I_1} \left(\frac{I_5 - \frac{1}{2}I_1I_2}{-I_1I_2} \right)^{3/2} S \\
& + C_2 \delta^2 \left(\frac{I_5 - \frac{1}{2}I_1I_2}{-I_1I_2} \right)^2 S^2 + C_3 \delta^2 \left(\frac{I_5 - \frac{1}{2}I_1I_2}{-I_1I_2} \right)^2 W^2 \\
& + C_4 \delta^2 \left(\frac{I_5 - \frac{1}{2}I_1I_2}{-I_1I_2} \right)^2 (SW - WS) \\
& + C_5 \delta^2 \frac{1}{\sqrt{I_1}} \left(\frac{I_5 - \frac{1}{2}I_1I_2}{-I_1I_2} \right)^{3/2} (S^2 W - WS^2).
\end{aligned} \tag{6.11}$$

This model encompasses the previously proposed vortex-stretching-based eddy viscosity model (Silvis et al. 2017b; Silvis and Verstappen 2018) as well as the nonlinear subgrid-scale model that we will study in Part II of this thesis (also see Silvis et al. 2019).

6.3.3 Other subgrid-scale models

A different choice of primary or secondary physical quantities may give rise to other new subgrid-scale models than those listed in Eqs. (6.2) to (6.11). In addition, new subgrid-scale models may be constructed by selecting one or more terms from one or more of these models.

6.4 Properties of new subgrid-scale models

We can analyze the properties of the new subgrid-scale models of Section 6.3 using Table 4.1. We discuss these properties, which are summarized in Table 6.1, in what follows. As in Section 5.3, we assume that the subgrid characteristic length scale δ of each term is defined in terms of the local grid size and that model constants are determined nondynamically. The possible effects of using the dynamic procedure (Germano et al. 1991; Lilly 1992) on the properties of subgrid-scale models were discussed in Section 5.3.9.

The new subgrid-scale models of Section 6.3 by construction are dimensionally consistent (requirement U of Eq. (3.1)) and conserve mass, momentum, angular momentum, vorticity and vorticity-related quantities (requirements C1–5 of Section 3.5.2). Additionally, with a grid-dependent subgrid characteristic length scale and a nondynamic determination of model constants, these models satisfy time translation, pressure translation, generalized Galilean, rotation and reflection invariance (requirements S1–4 of Eqs. (3.8) and (3.9)), as well as the desired breaking of spatial scaling invariance (requirement B2 of Eq. (3.16)).

On the other hand, the use of a grid-dependent length scale δ precludes satisfaction of symmetry requirement S5 of Eq. (3.10). The subgrid-scale models of Section 6.3 that turn off in two-component flows (see Eq. (4.27)) all satisfy two-dimensional material frame indifference (requirement S6 of Eq. (3.11)). The same holds for the generalized Smagorinsky model, Eq. (6.2), if the terms proportional to W^2 and $SW - WS$ are dropped.

To ensure time irreversibility (requirement B1 of Eq. (3.15)), the subgrid-scale models of Section 6.3 need the terms that are proportional to $T^{(1)}$ or $T^{(5)}$. In other words, at least one of the model constants C_1 and C_5 has to be nonzero. The subgrid-scale models of Section 6.3 all satisfy the desired breaking of three-dimensional material frame indifference (requirement B3 of Eq. (3.17)). The generalized Smagorinsky and QR models, Eqs. (6.2) and (6.3), lose this property, however, if the model constants C_3 , C_4 and C_5 are set to zero.

Comparison of Tables 5.1 and 6.1 shows that the generalized subgrid-scale models of Section 6.3.1 mostly exhibit the same dissipation behavior as the corresponding existing models. Do note that the generalized Smagorinsky model, Eq. (6.2), may have a zero subgrid dissipation for the pure axisymmetric strain (requirement D4 of Section 3.6.5) for certain values of the model constants C_1 and C_2 . Only the newly proposed vortex-stretching-based model, Eq. (6.11), has a zero subgrid dissipation for both two-component flows (Eq. (4.27)) and the pure axisymmetric strain (Eqs. (4.21) and (4.23)).

The subgrid-scale models of Section 6.3 are only consistent with the second law of thermodynamics (requirement D5 of Eq. (3.38)) if the model constants satisfy the inequality provided in Table 4.1. The behavior of the discussed subgrid-scale models with respect to Verstappen’s minimum-dissipation condition (requirement D6 of Eq. (3.40)) was determined based on terms proportional to the rate-of-strain tensor alone.

All discussed subgrid-scale models can be given model constants for which realizability (requirement R of Eqs. (3.59) to (3.63)) is satisfied. The desired

Table 6.1: Summary of the properties of the proposed subgrid-scale models. The properties considered are U: dimensional consistency (Eq. (3.1)); S1–3: time translation, pressure translation and generalized Galilean invariance (Eq. (3.8)); S4: rotation and reflection invariance (Eq. (3.9)); S5: scaling invariance (Eq. (3.10)); S6: two-dimensional material frame indifference (Eq. (3.11)); B1: breaking of time reversal invariance (Eq. (3.15)); B2: breaking of spatial scaling invariance (Eq. (3.16)); B3: breaking of three-dimensional material frame indifference (Eq. (3.17)); C1–5: conservation of mass, momentum, angular momentum, vorticity and vorticity-related quantities (Section 3.5.2); D1: zero subgrid dissipation for laminar flows (Eq. (3.36)); D2: nonzero subgrid dissipation for nonlaminar flows (Eq. (3.37)); D3: zero subgrid dissipation for two-component flows (Section 3.6.5); D4: zero subgrid dissipation for the pure axisymmetric strain (Section 3.6.5); D5: consistency with the second law of thermodynamics (Eq. (3.38)); D6: sufficient eddy viscosity for scale separation (Eq. (4.34)); R: realizability (Eqs. (3.59) to (3.63)); and N: the proper near-wall scaling behavior (Eq. (3.67)). The horizontal rule separates generalizations of existing subgrid-scale models from newly proposed models. Y: The property is satisfied. N: The property is not satisfied. C: The property may be satisfied for certain values of the model constants.

Model	Eq.	U	S1–3	S4	S5	S6	B1 ^a	B2	B3	C1–5	D1	D2	D3	D4	D5	D6	R	N
Gen. Smagorinsky	(6.2)	Y	Y	Y	N	N ^b	Y	Y	Y ^a	Y	N	Y	N	C	C	Y	C	N
Gen. QR	(6.3)	Y	Y	Y	N	Y	Y	Y	Y ^a	Y	Y	N	Y	N	C	N	C	Y
Gen. S3PQR	(6.4)	Y	Y	Y	N	Y ^c	Y ^c	Y	Y	Y	Y ^c	Y ^c	Y ^c	N	C	Y ^c	C	Y
- Gen. S3PQ	(6.5)	Y	Y	Y	N	N	Y	Y	Y	Y	N	Y	N	N	C	Y	C	Y
- Gen. S3PR	(6.6)	Y	Y	Y	N	Y	Y ^c	Y	Y	Y	Y	N	Y	N	C	N	C	Y
- Gen. S3QR	(6.7)	Y	Y	Y	N	Y	Y ^c	Y	Y	Y	Y	N	Y	N	C	N	C	Y
Gen. AMD	(6.8)	Y	Y	Y	N	Y	Y	Y	Y	Y	Y	N	Y	N	C	Y	C	Y
Q_G	(6.9)	Y	Y	Y	N	N	Y	Y	Y	Y	N	Y	N	N	C	Y	C	Y
R_G	(6.10)	Y	Y	Y	N	Y	Y	Y	Y	Y	Y	N	Y	N	C	N	C	Y
Vortex stretching	(6.11)	Y	Y	Y	N	Y	Y	Y	Y	Y	Y	N	Y	Y	C	N	C	Y

^a Property may be destroyed when dropping certain model terms.

^b Property may be restored by dropping certain model terms.

^c Depending on the value of the model parameter p and/or the implementation.

near-wall scaling behavior (requirement N of Eq. (3.67)) is, by construction, satisfied by all subgrid-scale models but the generalized Smagorinsky model, Eq. (6.2).

6.5 Conclusions

Focusing on subgrid-scale models that are based on the local velocity gradient, we proposed a systematic procedure that can be used to construct physics-based subgrid-scale models with built-in desirable properties. This procedure consists in applying the model constraints of Chapter 3 to the selection of model terms, the definition of model coefficients, and the determination of model constants and subgrid characteristic length scales of the general class of subgrid-scale models of Chapter 4. A key step in the proposed procedure is the selection of physical quantities that are based on the combined invariants of the rate-of-strain and rate-of-rotation tensors.

We illustrated how the systematic procedure can be used to generalize existing eddy viscosity models to nonlinear subgrid-scale models with built-in desirable properties. We also showed how new physics-based subgrid-scale models can be constructed. In this fashion, we obtained three new subgrid-scale models, which are, respectively, based on the second and third principal invariants of the velocity gradient, and on the vortex stretching magnitude. The vortex-stretching-based model satisfies most of the discussed model constraints and will form the basis for Part II of this thesis.

Chapter 7

Conclusions and outlook

Conclusions

We studied the construction of subgrid-scale models for large-eddy simulations of incompressible turbulent flows. In particular, we aimed to consolidate a systematic approach of constructing subgrid-scale models. This approach is based on the idea that it is desirable that subgrid-scale models are consistent with important physical and mathematical properties of the Navier–Stokes equations and the turbulent stresses.

We first described in detail several of these properties, among which the symmetries and conservation laws of the Navier–Stokes equations, and the dissipation properties, realizability and near-wall scaling behavior of the turbulent stresses. We also outlined the requirements that subgrid-scale models have to satisfy in order to preserve these physical and mathematical properties.

In addition, we proposed a set of symmetry breaking requirements for subgrid-scale models. We also extended existing requirements for the dissipation of kinetic energy by subgrid-scale models to the dissipation of enstrophy and helicity. We thereby obtained new minimum-dissipation requirements for the dissipation of enstrophy and helicity by subgrid-scale models. The discussed model requirements form a framework that can be used to systematically analyze the properties of existing subgrid-scale models and to construct new physics-based subgrid-scale models for large-eddy simulation.

We focused on the analysis and construction of subgrid-scale models that are based on the local velocity gradient. We introduced a general class of such models, to which we applied the obtained framework of model requirements. As such, we obtained several constraints on the model coefficients of this general class of models. We also observed that this class of models by construction satisfies the discussed conservation requirements.

Moreover, certain symmetries of the incompressible Navier–Stokes equations are preserved if some restrictions on the determination of the model constants and the subgrid characteristic length scale are fulfilled. Certain scaling requirements could, however, not be satisfied. The general class of subgrid-scale models, thus, seems to have some inherent limitations. We also found that some dissipation requirements are not compatible with each other.

Using the constraints on the general class of subgrid-scale models, we analyzed the properties of a number of existing subgrid-scale models that are based on the local velocity gradient. We found that these subgrid-scale models do not exhibit all the desired properties. This conclusion can partly be

understood from the limitations of the considered class of subgrid-scale models and from incompatibilities among the model constraints. There is room for improvement in the properties and, hence, the behavior of subgrid-scale models that are based on the local velocity gradient, however.

We, therefore, proposed a systematic procedure based on the developed framework of model constraints to construct physics-based subgrid-scale models with built-in desirable properties. With this procedure, we generalized several existing eddy viscosity models to nonlinear subgrid-scale models. We also illustrated how new subgrid-scale models can be constructed. Specifically, we obtained three new subgrid-scale models, which are respectively based on the second and third principal invariants of the velocity gradient, and on the vortex stretching magnitude. The proposed vortex-stretching-based model will play an important role in the rest of this work. Being based on the vortex stretching magnitude, this subgrid-scale model turns off in all laminar flows and satisfies most of the discussed model constraints.

Outlook

In future work, it would be interesting to study in more detail the developed framework of model constraints and the proposed subgrid-scale models. In particular, one could assess both the (relative) importance of the various model constraints and the quality of the proposed models by performing large-eddy simulations of different flows with subgrid-scale models having different properties. In this context, we note that Fureby and Tabor (1997) performed an interesting study of the role of realizability in large-eddy simulations.

A study of the effects of the choice of discretization on the desired symmetry, conservation and dissipation properties would also be interesting. Furthermore, one could develop (more) practical tests of Verstappen's minimum-dissipation requirement (Verstappen 2011, 2018) or of the proposed requirements on the dissipation of enstrophy and helicity due to subgrid-scale models. Such practical tests could utilize exact solutions of the Navier–Stokes equations (see, e.g., the work by Ward 2016).

The difficulty of preserving scale invariance using velocity-gradient-based subgrid-scale models calls for a detailed analysis of the symmetry preservation properties of the dynamic procedure (Germano et al. 1991; Lilly 1992). One could, furthermore, consider the use of the integral-length scale approximation (Piomelli et al. 2015; Rouhi et al. 2016) or of flow-dependent definitions of the subgrid characteristic length scale (see, e.g., Trias et al. 2017).

Another idea would be to use the framework of model constraints to analyze and construct subgrid-scale models that are not based on the local velocity gradient. Finally, note that we have focused on the development of model constraints and subgrid-scale models for large-eddy simulations of three-dimensional flows. Given the fundamentally different nature of (quasi)-two-dimensional flows (see, e.g., Alexakis and Biferale 2018), it would be worthwhile to determine how these constraints and models have to be adapted for such flows.



Part II

Application: Large-eddy simulations of rotating turbulent flows

Abstract Rotating turbulent flows form a challenging test case for large-eddy simulation. We, therefore, propose and validate a new subgrid-scale model for such flows. The proposed subgrid-scale model consists of a dissipative eddy viscosity term as well as a nondissipative term that is nonlinear in the rate-of-strain and rate-of-rotation tensors. The two corresponding model coefficients are a function of the vortex stretching magnitude. Therefore, the model is consistent with most of the physical and mathematical properties of the Navier–Stokes equations and turbulent stresses, is suitable for simulations of laminar, transitional and turbulent flows, and is easy to implement. We determine the two model constants using a nondynamic procedure that takes into account the interaction between the model terms.

Using detailed direct numerical and large-eddy simulations of rotating decaying turbulence and spanwise-rotating plane-channel flow, we reveal that the two model terms, respectively, account for dissipation and backscatter of energy, and that the nonlinear term improves predictions of the Reynolds stress anisotropy near solid walls. We also show that the new subgrid-scale model provides good predictions of rotating decaying turbulence and leads to outstanding predictions of spanwise-rotating plane-channel flow over a large range of rotation rates for both coarse and finer grid resolutions. Moreover, the new nonlinear model performs as well as the dynamic Smagorinsky and scaled anisotropic minimum-dissipation models in large-eddy simulations of rotating decaying turbulence and outperforms these models in large-eddy simulations of spanwise-rotating plane-channel flow, without requiring (dynamic) adaptation or near-wall damping of the model constants.

Partly published as

Silvis, M. H., Bae, H. J., Trias, F. X., Abkar, M., and Verstappen, R. (2019).

“A nonlinear subgrid-scale model for large-eddy simulations of rotating turbulent flows”. arXiv: [1904.12748](https://arxiv.org/abs/1904.12748) [[physics.flu-dyn](https://arxiv.org/abs/1904.12748)].

Chapter 8

Introduction

Rotating turbulent flows

Turbulent flows that are subject to solid body rotation are ubiquitous in geophysics, astrophysics and engineering. Consider, for example, flows in the oceans, in the atmosphere or in turbomachinery. Understanding and being able to predict the behavior of such rotating turbulent flows, thus, is of great importance for many applications.

Understanding rotating turbulent flows

Over the past decades, the fundamental understanding of rotating turbulent flows has grown significantly. Both experimental (Hopfinger et al. 1982; Jacquin et al. 1990; Morize et al. 2005; Staplehurst et al. 2008) and numerical (Bardina et al. 1985; Yeung and Zhou 1998; Smith and Waleffe 1999; Mininni et al. 2009; Thiele and Müller 2009; Bourouiba et al. 2012; Sen et al. 2012) studies of flows far from solid boundaries have revealed very marked effects of rotation on turbulence.

Under the influence of rotation, large-scale columnar vortices develop that are aligned with the rotation axis. In addition, the dissipation rate of turbulent kinetic energy reduces and the energy spectrum changes. These effects are caused by the Coriolis force, which modifies the energy transfer in turbulent flows (Bardina et al. 1985; Jacquin et al. 1990; Cambon et al. 1997; Yeung and Zhou 1998; Smith and Waleffe 1999; Chen et al. 2005; Morize et al. 2005; Bourouiba and Bartello 2007; Staplehurst et al. 2008; Mininni et al. 2009; Thiele and Müller 2009; Bourouiba et al. 2012; Sen et al. 2012; Buzzicotti et al. 2018). (Also refer to the reviews by Godeferd and Moisy 2015; Alexakis and Biferale 2018; Sagaut and Cambon 2018, and the references therein.)

Additional interesting effects have been observed in wall-bounded rotating flows. We focus on rotating channel flow subject to spanwise rotation, which was found to be the dominant mode of rotation for such flows (Wu and Kasagi 2004). Experiments (Johnston et al. 1972; Nakabayashi and Kitoh 2005) and numerical simulations (Tafti and Vanka 1991; Kristoffersen and Andersson 1993; Lamballais et al. 1996; Grundestam et al. 2008; Yang and Wu 2012; Dai et al. 2016; Xia et al. 2016; Brethouwer 2017) of spanwise-rotating channel flow have shown that the Coriolis force can both enhance and suppress turbulence.

On one side of a spanwise-rotating channel, rotation reduces the turbulence intensity and may cause flow laminarization. On the other side of the channel,

turbulence will either be enhanced or suppressed, depending on the rotation rate, and large-scale streamwise Taylor–Görtler vortices may occur. The mean streamwise velocity of spanwise-rotating channel flow contains a characteristic linear region. The slope of this region is proportional to the rotation rate, as can be explained using symmetry analysis (Oberlack 2001).

As the rotation rate increases, the Coriolis force will suppress turbulence in a growing part of the channel, until the flow fully laminarizes (Grundestam et al. 2008; Xia et al. 2016; Brethouwer 2017). Laminar behavior may, however, be disturbed with intermittent turbulent bursts (Brethouwer et al. 2014; Brethouwer 2016).

Predicting rotating turbulent flows

Despite the increased fundamental understanding of rotating turbulent flows, the prediction of such flows remains a challenge. This is mainly because many rotating flows contain a very large range of physically relevant scales of motion, which cannot currently be resolved using direct numerical simulations. With the aim to improve the numerical prediction of incompressible rotating turbulent flows, we will, therefore, turn to large-eddy simulation.

Large-eddy simulation and subgrid-scale models

In large-eddy simulation, the large scales of motion in a flow are explicitly computed, whereas the effects of the small-scale motions have to be modeled using subgrid-scale models (see, e.g., the monographs by Sagaut 2006; Pope 2011).

Eddy viscosity models

Eddy viscosity models are commonly used subgrid-scale models. These subgrid-scale models prescribe the net dissipation of kinetic energy caused by small-scale turbulent motions. The Smagorinsky model (Smagorinsky 1963) and its dynamic variant (Germano et al. 1991; Lilly 1992) are, without a doubt, the most well-known eddy viscosity models. Examples of other, more recently developed eddy viscosity models are the WALE model (Nicoud and Ducros 1999), Vreman’s model (Vreman 2004), the σ model (Nicoud et al. 2011), the QR model (Verstappen et al. 2010; Verstappen 2011; Verstappen et al. 2014), the S3PQR models (Trias et al. 2015), the anisotropic minimum-dissipation model (Rozema et al. 2015), the scaled anisotropic minimum-dissipation model (Verstappen 2018) and the vortex-stretching-based eddy viscosity model (Silvis et al. 2017b; Silvis and Verstappen 2018).

Limitations of eddy viscosity models

Although eddy viscosity models are effective in many cases, they have an important drawback. They model turbulence as an essentially dissipative

process. Given the importance of energy transfer in rotating turbulent flows, it seems unlikely that eddy viscosity models are always suitable for large-eddy simulations of such flows. More generally, it has since long been known that the rate-of-strain tensor, which forms the basis of eddy viscosity models, does not correlate well with the turbulent stresses (Clark et al. 1979; Bardina et al. 1983; Liu et al. 1994; Tao et al. 2002; Horiuti 2003).

Scale similarity and gradient models

Bardina et al. (1983), therefore, proposed their well-known scale similarity model, in which the largest unresolved motions are modeled in terms of the smallest resolved motions. A related subgrid-scale model, often referred to as the gradient model, was proposed by Leonard (1975) and Clark et al. (1979). Both subgrid-scale models show a high level of correlation with the turbulent stresses, but do not provide enough dissipation (Clark et al. 1979; Bardina et al. 1983; Liu et al. 1994; Tao et al. 2002; Horiuti 2003).

Therefore, mixed models were introduced, in which the scale similarity or gradient models were combined with an eddy viscosity model (Bardina et al. 1983; Clark et al. 1979; Liu et al. 1994). (Refer to Carati et al. 2001; Tao et al. 2002, for more recent support of mixed subgrid-scale models.) Mixed models with a dynamic eddy viscosity term were also considered and were shown to perform well in simulations of different nonrotating flows (Zang et al. 1993; Vreman et al. 1994a, 1996, 1997; Winckelmans et al. 2001).

Nonlinear subgrid-scale models

Lund and Novikov (1992) generalized the gradient model of Leonard (1975) and Clark et al. (1979). They derived a general subgrid-scale model consisting of five terms, of which one term was linear and the other terms were nonlinear in the rate-of-strain and rate-of-rotation tensors. Determination of the model constants and coefficients, however, turned out to be a challenging problem.

Kosović (1997) proposed a nonlinear subgrid-scale model consisting of three terms and determined the model constants using properties of homogeneous isotropic turbulence. Wang and Bergstrom (2005) proposed a dynamic nonlinear subgrid-scale model based on the same three model terms. Wendling and Oberlack (2007) investigated dynamic models consisting of different combinations of the five model terms of Lund and Novikov (1992). Kosović (1997), Wang and Bergstrom (2005), and Wendling and Oberlack (2007) successfully applied their subgrid-scale models to nonrotating turbulent flows.

Subgrid-scale models for rotating turbulent flows

Subgrid-scale models that are nonlinear in the rate-of-strain and rate-of-rotation tensors have also been used in large-eddy simulations of rotating turbulent flows. Using the terms of Lund and Novikov (1992) as basis tensors, Liu et al. (2004), Yang et al. (2012a), Yang et al. (2012b) and Huang et al. (2017) proposed different nonlinear models for rotating turbulent flows.

These authors, however, only validated their subgrid-scale models in a limited number of tests. Moreover, the dynamic procedures proposed by Yang et al. (2012a) and Yang et al. (2012b) are not applicable to arbitrary, complex geometries. These procedures additionally rely on the assumption that the eddy viscosity and nonlinear terms of their subgrid-scale models do not interact with each other. We will show that this assumption is invalid.

Marstorp et al. (2009) proposed a dynamic and a nondynamic nonlinear subgrid-scale model based on the transport equation for the Reynolds stress anisotropy. They tested these subgrid-scale models in large-eddy simulations of rotating and nonrotating channel flow, and found that their (dynamic) model outperformed the (dynamic) Smagorinsky model. However, the nonlinear subgrid-scale models of Marstorp et al. (2009) require setting four empirical constants, for which no universal values have been found thus far (see, e.g., Marstorp et al. 2009; Montecchia et al. 2017).

A new subgrid-scale model

Building upon our previous work (Silvis et al. 2016; Silvis and Verstappen 2019), we will, therefore, propose and validate a new subgrid-scale model for large-eddy simulations of incompressible rotating turbulent flows. We specifically aim to ensure that this subgrid-scale model (i) accounts for both dissipation and backscatter of energy; (ii) takes into account the interplay between these processes; (iii) respects the properties of the Navier–Stokes equations and turbulent stresses; (iv) can be used in complex geometries; (v) can function without near-wall damping functions and dynamic procedures; (vi) provides good predictions of different types of rotating turbulent flows over different regimes of rotation; and (vii) works well at both coarse and finer spatial resolutions.

Outline

In Chapter 9, we use the framework of model constraints of Chapter 3 and the general class of subgrid-scale models of Chapter 4 to propose a new subgrid-scale model for rotating turbulent flows. In Chapter 10, we study and validate this subgrid-scale model using detailed direct numerical and large-eddy simulations of the two canonical rotating turbulent flows discussed above, namely, rotating decaying turbulence and spanwise-rotating plane-channel flow. We also provide a comparison with the commonly used dynamic Smagorinsky model, the scaled anisotropic minimum-dissipation model and the vortex-stretching-based eddy viscosity model. We present the conclusions of this part of this thesis in Chapter 11.

Chapter 9

A new nonlinear subgrid-scale model

9.1 Introduction

We aim to improve the numerical prediction of incompressible rotating turbulent flows. In this chapter, we will, therefore, propose a new subgrid-scale model for large-eddy simulations of such flows.

In the current study, we focus on the numerical prediction of turbulent flows subject to solid body rotation. As explained in Section 1.2.7, such flows can be described by the incompressible Navier–Stokes equations in a constantly rotating frame, Eq. (1.42). The corresponding equations of large-eddy simulation are given by Eq. (1.78).

The general class of subgrid-scale models based on the local velocity gradient of Eq. (4.29) can parametrize both dissipative and nondissipative processes in turbulent flows. This class of models, therefore, forms a good starting point for the construction of a new subgrid-scale model for rotating turbulent flows. However, as explained in Section 4.5, several challenges have to be overcome to obtain a practical subgrid-scale model from this class. Specifically, we have to make a selection of model terms, define the corresponding model coefficients, and determine the model constant and define the subgrid characteristic length scale of each model term.

In the following sections, we will go through these steps to create a new subgrid-scale model for rotating turbulent flows. In particular, we select the model terms for this subgrid-scale in Section 9.2. In Section 9.3, we define the corresponding model coefficients. We discuss the resulting model in Section 9.4. In Section 9.5, we focus on the determination of the model constants, the definition of the subgrid characteristic length scale and the numerical implementation of the model. Conclusions are provided in Section 9.6.

In what follows, we will both describe and model turbulent flows within the constantly rotating frame that is corresponding to the solid body rotation these flows are subject to. All physical quantities, including the rate-of-rotation tensor W , are defined with respect to this rotating frame.

9.2 Selecting the model terms

We first select the basis tensors for the new subgrid-scale model from Eq. (4.3).

9.2.1 A dissipative component

In turbulent flows, most of the kinetic energy is dissipated through small-scale motions. In a practical large-eddy simulation, these small-scale motions are not (well) resolved, however. A subgrid-scale model should, therefore, contain a dissipative component. Since dissipation of kinetic energy is naturally modeled using eddy viscosity models, we will select the rate-of-strain tensor $T^{(1)} = S$ as our first basis tensor.

9.2.2 A nondissipative component

As mentioned in Section 4.3.3, the subgrid-scale stresses are usually not aligned with the rate-of-strain tensor. Therefore, it is necessary to select a second basis tensor from Eq. (4.3) that is not fully aligned with the rate-of-strain tensor.

The tensor $T^{(4)} = SW - WS$ has several attractive properties. First of all, this tensor is perpendicular to the rate-of-strain tensor and, thus, does not directly contribute to the subgrid dissipation of kinetic energy $D^{k,\text{mod}}$ defined in Eq. (3.35). Therefore, $T^{(4)}$ is a nondissipative tensor that can describe fundamentally different physical phenomena than the rate-of-strain tensor. In fact, the nondissipative and quadratic nature of $T^{(4)}$ suggests that this term can model energy transfer between different scales of motion in turbulent flows.

Secondly, $T^{(4)} = SW - WS$ involves the rate-of-rotation tensor. We can, therefore, expect that this tensor is very suitable for the simulation of rotating flows. Thirdly, $T^{(4)}$ is part of the gradient model of Leonard (1975) and Clark et al. (1979). More specifically, $T^{(4)}$ forms a nondissipative, stable part of the gradient model. The gradient model forms the lowest-order Taylor approximation of the turbulent stress tensor τ_{ij} of Eq. (1.75) in terms of the filter length $\bar{\delta}$. Therefore, $T^{(4)}$ is consistent with a nondissipative part of the true turbulent stress tensor.

Finally, the nonlinear tensor $T^{(4)}$ is not only interesting from a theoretical, but also from a practical point of view. Marstorp et al. (2009) showed that addition of a term involving this nonlinear tensor to an eddy viscosity model can significantly improve predictions of the Reynolds stress anisotropy in rotating and nonrotating turbulent channel flow. Follow-up research by Rasam et al. (2011) and Montecchia et al. (2017) furthermore indicates that such a model also performs well at coarse resolutions, in contrast to the dynamic Smagorinsky model (Germano et al. 1991; Lilly 1992). We have also previously obtained promising results from large-eddy simulations of rotating flows with nonlinear subgrid-scale models involving $T^{(4)}$ (Silvis et al. 2016; Silvis and Verstappen 2019).

9.2.3 Selection

Given the above properties, we select $T^{(4)} = SW - WS$ as the second and final basis tensor for our new subgrid-scale model for rotating turbulent flows. In this fashion, we also avoid the complexity of determining the effects and coupling of

more than two model terms. We, thus, reduce the general class of subgrid-scale models of Eq. (4.29) to the two-term class of models consisting of a dissipative linear eddy viscosity term and a nondissipative nonlinear model term given by

$$\tau^{\text{mod,dev}} = \alpha_1 T^{(1)} + \alpha_4 T^{(4)} = \alpha_1 S + \alpha_4 (SW - WS). \quad (9.1)$$

9.3 Defining the model coefficients

We now focus on defining the two model coefficients α_1 and α_4 . Specifically, we will define the functions f_1 and f_4 that are part of these model coefficients (see Eq. (4.5)). Since the functions $f_{(i)}$ can depend in many dimensionally consistent ways on the combined invariants of the rate-of-strain and rate-of-rotation tensors of Eq. (4.6), we need a procedure to define these functions.

9.3.1 Procedure

We propose to define the functions f_1 and f_4 that are part of the model coefficients α_1 and α_4 by applying the previously devised framework of constraints for the assessment and creation of subgrid-scale models (Silvis et al. 2017a,b; Silvis and Verstappen 2018, n.d. b), which was described in Part I of this thesis. As explained there, this framework is based on the idea that subgrid-scale models should be consistent with the fundamental physical and mathematical properties of the Navier–Stokes equations and the turbulent stresses.

In particular, consistency of subgrid-scale models with the symmetries (Speziale 1985a; Oberlack 1997, 2002; Razafindralandy et al. 2007) and conservation laws (Cheviakov and Oberlack 2014) of the Navier–Stokes equations, and the dissipation properties (Vreman 2004; Razafindralandy et al. 2007; Nicoud et al. 2011; Verstappen 2011), realizability (Vreman et al. 1994b) and near-wall scaling behavior (Chapman and Kuhn 1986) of the turbulent stresses is desired.

As explained in Section 4.6, the general class of subgrid-scale models of Eq. (4.29) by construction satisfies some symmetries and respects the known conservation laws of the Navier–Stokes equations. The two-term class of subgrid-scale models of Eq. (9.1) inherits this desirable behavior.

Do note that our setup, in which we define all physical quantities relative to a rotating frame of choice, makes the subgrid-scale model of Eq. (9.1) invariant under arbitrary time-dependent rotations of the coordinate system. As we explained in Section 3.4.3, this property is not desirable for a turbulence model (Silvis and Verstappen n.d. b). However, as long as we are considering rotating turbulent flows from the rotating frame of reference that corresponds to the imposed solid body rotation, the definition of Eq. (9.1) in terms of relative physical quantities does not form a restriction.

In addition, invariance with respect to the scaling symmetry of the incompressible Navier–Stokes equations can only be satisfied if we choose a subgrid characteristic length scale that is directly related to flow quantities or if a dynamic procedure (Germano et al. 1991; Lilly 1992) is used to determine the model constants (Oberlack 1997; Razafindralandy et al. 2007). As we

explain in Section 9.5, we take a grid-dependent rather than a flow-dependent characteristic length scale and we determine model constants in a nondynamic way. While this choice facilitates the model implementation, scaling invariance will be violated. Finally, for traceless subgrid-scale models such as the class of subgrid-scale models of Eq. (9.1), we cannot determine if realizability is satisfied (Vreman et al. 1994a; Silvis et al. 2017b).

We can use the remaining properties of the incompressible Navier–Stokes equations and the turbulent stresses to define the model coefficients of Eq. (9.1). Specifically, the Navier–Stokes equations provide us with two symmetry constraints. A new subgrid-scale model ideally breaks time reversal invariance (Carati et al. 2001) and satisfies two-dimensional material frame indifference (Oberlack 1997, 2002; Razafindralandy et al. 2007). Note that this latter property only holds in the limit of a two-component incompressible flow and should not be confused with the notion of three-dimensional material frame indifference, which we discussed in Section 3.4.2.

With respect to the properties of the turbulent stress tensor, we have constraints coming from the near-wall scaling behavior of the turbulent stresses (Chapman and Kuhn 1986), the dissipation requirements of Vreman (2004) and Nicoud et al. (2011), consistency with the second law of thermodynamics (Razafindralandy et al. 2007), and the minimum-dissipation requirement of Verstappen (2011). We will now apply these constraints to define the functions f_1 and f_4 that are part of the model coefficients of the class of subgrid-scale models of Eq. (9.1).

9.3.2 Notation

To emphasize that the first term on the right-hand side of Eq. (9.1) is an eddy viscosity term and represents dissipation, we write

$$\alpha_1 = -2\nu_e \tag{9.2}$$

in what follows. We will write the coefficient of the nondissipative nonlinear term as

$$\alpha_4 = \mu_e. \tag{9.3}$$

We will, thus, express the two-term class of subgrid-scale models of Eq. (9.1) as

$$\tau^{\text{mod,dev}} = -2\nu_e S + \mu_e (SW - WS). \tag{9.4}$$

9.3.3 Defining the eddy viscosity

We first focus on defining the eddy viscosity ν_e . The dissipation properties and near-wall scaling behavior of the turbulent stress tensor provide useful constraints for this quantity. Vreman (2004) and Nicoud et al. (2011) argue that subgrid-scale models should not produce subgrid-scale kinetic energy in certain simple flows; otherwise these models could cause unphysical transitions from laminar to turbulent flow states. Nicoud et al. (2011) specifically require that

subgrid-scale models do not cause dissipation of kinetic energy in two-component flows or for the pure axisymmetric strain. Vreman (2004) demands that the subgrid dissipation vanishes (only) in flows for which the true dissipation of kinetic energy is zero. Such flows can be called laminar and, as we showed in Section 4.6.5, correspond to a subset of the two-component flows.

In view of the above requirements, a very useful quantity to base the eddy viscosity on is $I_5 - \frac{1}{2}I_1I_2 = \text{tr}(S^2W^2) - \frac{1}{2}\text{tr}(S^2)\text{tr}(W^2)$ (Silvis and Verstappen 2015; Silvis et al. 2017b; Silvis and Verstappen 2018, n.d. b). This nonnegative quantity vanishes in all two-component (and, therefore, in all laminar) flows, as well as in states of pure shear and pure rotation. Additionally, this quantity vanishes near solid walls. Indeed, while the invariants I_1, I_2, I_5 all attain constant finite values near a wall, $I_5 - \frac{1}{2}I_1I_2$ scales as $\mathcal{O}(x_i^2)$ in terms of a wall-normal coordinate x_i (Silvis and Verstappen 2015, n.d. b).

The quantity $I_5 - \frac{1}{2}I_1I_2$ can, therefore, be used to correct the near-wall scaling and dissipation behavior of the Smagorinsky model (Smagorinsky 1963). To that end, we first normalize $I_5 - \frac{1}{2}I_1I_2$ by $-I_1I_2$. The resulting quantity is dimensionless and, as can be inferred from the following equations, takes on values between 0 and 1/2. A sharper upper bound of 1/3 is provided by Eq. (4.17). Secondly, we impose the desired near-wall scaling of $\nu_e = \mathcal{O}(x_i^3)$ for a wall-normal coordinate x_i (see Table 4.1 or the work by Silvis and Verstappen 2015, n.d. b).

We thereby obtain the definition of the eddy viscosity given by (Silvis et al. 2017b; Silvis and Verstappen 2018)

$$\nu_e = (C_\nu\delta)^2\sqrt{2I_1}\left(\frac{I_5 - \frac{1}{2}I_1I_2}{-I_1I_2}\right)^{3/2}. \quad (9.5)$$

Here, C_ν^2 denotes a positive dimensionless model constant and δ represents the subgrid characteristic length scale. We discuss the values of C_ν and δ in Section 9.5.

As we showed in Eq. (4.16), the quantity $I_5 - \frac{1}{2}I_1I_2$ in Eq. (9.5) is proportional to the squared vortex stretching magnitude. We can, therefore, rewrite the eddy viscosity of Eq. (9.5) as

$$\nu_e = (C_\nu\delta)^2\frac{1}{2}|S|f_{\text{VS}}^3, \quad (9.6)$$

where the normalized vortex stretching magnitude is defined by

$$f_{\text{VS}} = \frac{|S\vec{\omega}|}{|S||\vec{\omega}|} \quad (9.7)$$

and the matrix and vector norms in Eqs. (9.6) and (9.7) are defined in Eq. (4.10). By the Cauchy–Schwarz inequality, the vortex stretching magnitude of Eq. (9.7) is bounded from below and above: $0 \leq f_{\text{VS}} \leq 1$. Using Eq. (4.17), we can even show that the upper bound $f_{\text{VS}}^2 \leq \frac{2}{3}$ holds.

We previously termed an eddy viscosity model with the eddy viscosity of Eqs. (9.5) and (9.6) the *vortex-stretching-based eddy viscosity model* (Silvis et al. 2017b).

9.3.4 Defining the coefficient of the nonlinear term

Since the nonlinear tensor $SW - WS$ of Eq. (9.4) is nondissipative, the above-mentioned dissipation requirements cannot be applied to define μ_e . However, it makes sense to demand that the entire subgrid-scale model turns off in laminar flows. We additionally have a desired near-wall scaling behavior of $\mu_e = \mathcal{O}(x_i^4)$ for a wall-normal coordinate x_i (see Table 4.1 or the work by Silvis and Verstappen 2015, n.d. b).

We will, therefore, also define the model coefficient μ_e in terms of the normalized vortex stretching magnitude f_{VS} of Eq. (9.7):

$$\mu_e = C_\mu \delta^2 \left(\frac{I_5 - \frac{1}{2} I_1 I_2}{-I_1 I_2} \right)^2 = C_\mu \delta^2 \frac{1}{4} f_{\text{VS}}^4. \quad (9.8)$$

Here, C_μ denotes a dimensionless constant that can take on both positive and negative values. We discuss the values of C_μ and δ in Section 9.5.

9.4 The new nonlinear subgrid-scale model

Combining the expression of the two-term class of subgrid-scale models of Eq. (9.4) with the eddy viscosity ν_e of Eq. (9.6), the nonlinear model coefficient μ_e of Eq. (9.8) and the normalized vortex stretching magnitude f_{VS} of Eq. (9.7), we obtain the full expression of our new subgrid-scale model:

$$\begin{aligned} \tau^{\text{mod,dev}} = & -2(C_\nu \delta)^2 \frac{1}{2} |S| \left(\frac{|S\vec{\omega}|}{|S||\vec{\omega}|} \right)^3 S \\ & + C_\mu \delta^2 \frac{1}{4} \left(\frac{|S\vec{\omega}|}{|S||\vec{\omega}|} \right)^4 (SW - WS). \end{aligned} \quad (9.9)$$

Given the dependence on the vortex stretching magnitude, we will refer to this model as the *vortex-stretching-based nonlinear model*.

The vortex-stretching-based nonlinear model by construction has several desirable properties. First of all, this subgrid-scale model is consistent with most of the physical and mathematical properties of the Navier–Stokes equations and the turbulent stresses. Indeed, the vortex-stretching-based nonlinear model preserves most of the symmetries of the Navier–Stokes equations, including two-dimensional material frame indifference, and conserves mass, momentum, angular momentum, vorticity and vorticity-related quantities.

Additionally, the eddy viscosity of this subgrid-scale model is nonnegative. Thereby, time reversal invariance is broken, as desired, and consistency with the second law of thermodynamics is enforced. Also, the form of the eddy viscosity satisfies the minimum-dissipation requirement of Verstappen (2011) for all flows but the axisymmetric strain.

The full vortex-stretching-based nonlinear model turns off in laminar flows, as well as in simple flows like purely rotational and pure shear flows. Moreover, this subgrid-scale model has the correct scaling behavior near solid walls. The vortex-stretching-based nonlinear model, thus, respects fundamental properties of

turbulent flows and can be used in arbitrary, complex flow configurations without requiring near-wall damping functions or dynamic procedures. Additionally, by vanishing in laminar flows, this subgrid-scale model is suitable for simulations of laminar, transitional and turbulent flows.

Secondly, the two terms of the vortex-stretching-based nonlinear model represent different physical phenomena. The first term, which we will refer to as the eddy viscosity term, describes dissipation of kinetic energy. The second term, which we will call the nonlinear term, is perpendicular to the rate-of-strain tensor and is consistent with a nondissipative part of the turbulent stress tensor. The nonlinear term can, therefore, represent nondissipative processes in turbulent flows and can help us go beyond the limitations of eddy viscosity models.

9.5 Implementing the new subgrid-scale model

The vortex-stretching-based nonlinear model of Eq. (9.9) can only be used in practice once the two model constants and the subgrid characteristic length scale are defined. The framework of model constraints of Chapter 3 does, however, not provide us with specific values of the model constants, nor with a procedure to determine their values. Therefore, additional information, whether theoretical or experimental in nature, is needed to determine the model constants of Eq. (9.9).

In this work, we will determine the model constants of the vortex-stretching-based nonlinear model using numerical simulation data. To facilitate this process, we first estimate the expected order of magnitude of these constants.

9.5.1 Estimating the model constants

To estimate the order of magnitude of the model constants of the vortex-stretching-based nonlinear model, we look at nonrotating flows. Additionally, we assume that the two model constants can be set independently.

Ignoring the nonlinear term, we can estimate the constant C_ν of the eddy viscosity term of Eq. (9.9) that is appropriate for nonrotating flows using a simple dissipation argument. We require that the eddy viscosity term has the same average subgrid dissipation of kinetic energy for nonrotating homogeneous isotropic turbulence as the Smagorinsky model (Nicoud and Ducros 1999; Nicoud et al. 2011; Trias et al. 2015). This average subgrid dissipation can, for example, be computed using the velocity field of a homogeneous isotropic turbulent flow, either coming from an experiment or a numerical simulation (Nicoud and Ducros 1999).

In this work, we estimate the average subgrid dissipation of the eddy viscosity term and the Smagorinsky model in nonrotating homogeneous isotropic turbulence using a large number of synthetic velocity gradients. These velocity gradients are given by traceless random matrices (Nicoud et al. 2011; Trias et al. 2015) sampled from a uniform distribution (Silvis et al. 2017b). We then equate the two averages to obtain an estimate of the model constant C_ν . A set

of scripts that can perform this estimation of the constants of eddy viscosity models has been made freely available.¹

We obtain

$$C_\nu^2 = 0.3373 \approx 0.34 \quad (9.10)$$

for a Smagorinsky constant of 0.17. We previously showed that good predictions of nonrotating decaying homogeneous isotropic turbulence and plane-channel flow can be obtained using the eddy viscosity term of Eq. (9.9) with a model constant close to the value of Eq. (9.10) (Silvis et al. 2017a,b).

Since the nonlinear term of the vortex-stretching-based nonlinear model of Eq. (9.9) is nondissipative, the model constant C_μ cannot be estimated using the above dissipation argument. Moreover, since subgrid-scale models at least have to capture the net dissipation of kinetic energy that characterizes turbulence, the nonlinear term is not suitable as a standalone subgrid-scale model.

If we assume that the dissipation of kinetic energy is accounted for, we can, however, determine the expected order of magnitude of C_μ for nonrotating flows. To that end, we compare the average value of the coefficient of the nonlinear term $SW - WS$ of Eq. (9.9) with the proportionality constant of the same nonlinear term in the gradient model of Leonard (1975) and Clark et al. (1979) (see Eq. (5.11)). The gradient model forms the lowest-order Taylor approximation of the turbulent stress tensor of Eq. (1.75) in terms of the filter length $\bar{\delta}$ and generally has a proportionality constant of 1/12 (Berselli et al. 2006).

The average value of the coefficient of the nonlinear term of Eq. (9.9) can be determined from a large number of synthetic velocity gradients with the previously mentioned set of scripts.² Comparing the resulting average with the proportionality constant of 1/12 of the gradient model, we expect that a suitable value for the constant of the nonlinear term will be of the order of

$$C_\mu \sim 2.0 - 2.5. \quad (9.11)$$

9.5.2 Determining the model constants

Although the two terms of the vortex-stretching-based nonlinear model represent different physics, they are not dynamically independent of each other. Indeed, as we will see in Section 10.3.3, the eddy viscosity term modulates the effects of the nonlinear term. Also, the nonlinear term will have an (indirect) effect on the dissipation of kinetic energy. Therefore, the two model constants of the vortex-stretching-based nonlinear model cannot be set independently.

As a consequence, the model constant estimates of Eqs. (9.10) and (9.11) cannot be employed together, neither for nonrotating, nor for rotating turbulent flows. We have to modify these estimates to obtain suitable model constants for the vortex-stretching-based nonlinear model.

¹ See <https://github.com/mauritssilvis/lesTools> for a set of scripts that can be used to estimate the model constants of subgrid-scale models for large-eddy simulation.

² See Footnote 1.

In Section 10.3.3, we will propose a nondynamic method to determine the model constants that takes into account the interplay between the two model terms. This method leads to

$$C_\nu^2 = 0.1687 \approx 0.17, \quad C_\mu = 5. \quad (9.12)$$

We discuss the physical basis and interpretation of these values in Sections 10.3.3 and 10.3.4.

9.5.3 Defining the subgrid characteristic length scale

We also have to define the subgrid characteristic length scale δ of the vortex-stretching-based nonlinear model of Eq. (9.9). For simplicity, we will assume that the different physical processes that are described by the two terms of this model can be characterized using the same length scale. For ease of implementation we will define this length scale in terms of the grid spacings. Specifically, we take Deardorff's classical definition for the subgrid characteristic length scale (Deardorff 1970),

$$\delta = (\Delta x_1 \Delta x_2 \Delta x_3)^{1/3}. \quad (9.13)$$

Here, the Δx_i represent the dimensions of the local grid cell.

9.5.4 Numerical implementation

As can be inferred from Eqs. (9.9) and (9.13), the vortex-stretching-based nonlinear model only relies on two quantities, namely, the velocity gradient and the grid cell sizes. Both quantities are normally available in numerical simulations of turbulent flows. The vortex-stretching-based nonlinear model, therefore, is easy to implement. In addition, most of the constituents of the nonlinear term follow from computing the eddy viscosity term. Computing the two terms of Eq. (9.9), therefore, is only slightly more costly than computation of the eddy viscosity term alone.

To obtain the best results with the vortex-stretching-based nonlinear model of Eq. (9.9) with the model constants of Eq. (9.12), we recommend the use of a numerical implementation that preserves the different nature of the two model terms. That is, a dissipative implementation is desired for the eddy viscosity term, while the nonlinear term should conserve kinetic energy.

More generally, we recommend the use of a discretization in which the convective and Coriolis force terms of the equations of large-eddy simulation in a rotating frame, Eq. (1.78), as well as the nonlinear term of the subgrid-scale model conserve kinetic energy. At the same time, the diffusive term of Eq. (1.78) and the eddy viscosity term of the vortex-stretching-based model should be implemented in such a way that they can only cause (a nonnegative) dissipation of kinetic energy.

9.6 Conclusions

In the current chapter, we proposed a new subgrid-scale model for large-eddy simulations of incompressible rotating turbulent flows. The proposed model consists of an eddy viscosity term, as well as a term that is nonlinear in the rate-of-strain and rate-of-rotation tensors. We defined the corresponding model coefficients using the vortex stretching magnitude. The proposed model, which we called the vortex-stretching-based nonlinear model, has several desirable properties.

First of all, being based on the framework of model constraints discussed in Part I of this thesis, this subgrid-scale model is consistent with most of the physical and mathematical properties of the Navier–Stokes equations and the turbulent stresses. Therefore, the vortex-stretching-based nonlinear model respects fundamental properties of turbulent flows and can be used in arbitrary, complex flow configurations without requiring near-wall damping functions or dynamic procedures. Moreover, by turning off in laminar flows, this subgrid-scale model is suitable for simulations of laminar, transitional and turbulent flows.

Secondly, the two terms of the model represent different physical phenomena. The eddy viscosity term describes dissipation of kinetic energy, while the nonlinear term can represent nondissipative processes in turbulent flows. The vortex-stretching-based nonlinear model may, therefore, take us beyond the limitations of eddy viscosity models and can be used to model rotating turbulent flows. Finally, the model is easy to implement.

In Chapter 10, we study and validate the vortex-stretching-based nonlinear model using direct numerical and large-eddy simulations of rotating turbulent flows. We will also determine the constants of this model.

Chapter 10

Numerical results

10.1 Introduction

In Chapter 9, we proposed a new subgrid-scale model for large-eddy simulations of rotating turbulent flows, namely the vortex-stretching-based nonlinear model given by Eq. (9.9). We will now study this subgrid-scale model using detailed direct numerical and large-eddy simulations of rotating decaying turbulence and spanwise-rotating plane-channel flow. We also compare predictions from this subgrid-scale model and the commonly used dynamic Smagorinsky model (Germano et al. 1991; Lilly 1992), the scaled anisotropic minimum-dissipation model (Verstappen 2018) and the vortex-stretching-based eddy viscosity model (Silvis et al. 2017b; Silvis and Verstappen 2018).

In Section 10.2, we discuss the numerical methods we used for our direct numerical and large-eddy simulations. Sections 10.3 and 10.4 are dedicated to our simulations of rotating decaying turbulence and spanwise-rotating plane-channel flow, respectively.

10.2 Numerical method

We obtained all numerical results presented in what follows using incompressible Navier–Stokes solvers that employ staggered finite-volume or finite-difference methods of second-order spatial accuracy, based on the discretization of Verstappen and Veldman (2003). This discretization ensures conservation of kinetic energy by the convective and Coriolis force terms, as well as a strictly positive dissipation by the diffusive term of the incompressible Navier–Stokes equations and the equations of large-eddy simulation in a rotating frame of reference, Eqs. (1.42) and (1.78).

To ensure a dissipative implementation of the eddy viscosity term of the vortex-stretching-based nonlinear model and conservation of kinetic energy by the nonlinear term, we discretize these terms according to the work by Remmerswaal (2016). That is, we compute the eddy viscosity ν_e , the coefficient of the nonlinear term μ_e and the nonlinear tensor $SW - WS$ of the vortex-stretching-based nonlinear model of Eq. (9.9) after interpolating the velocity gradient to the grid cell centers.

The diagonal elements of the subgrid-scale model readily follow, while the off-diagonal elements are computed by interpolating the cell-centered values of ν_e , μ_e and $SW - WS$ to the grid cell edges, by computing the off-diagonal

elements of the rate-of-strain tensor S in the grid cell edges and by computing all necessary products and sums. Unlike many other possible procedures, this method ensures orthogonality of the rate-of-strain tensor and nonlinear term on a staggered grid and, hence, ensures conservation of kinetic energy by the nonlinear term (Remmerswaal 2016).

An explicit two-step one-leg time integration scheme of second order accuracy, which is similar to an Adams-Bashforth scheme, is used for the integration of the convective, viscous, Coriolis force and subgrid-scale model terms (Verstappen and Veldman 2003). A projection method, which involves solution of a Poisson equation for the pressure, is used to ensure incompressibility of the velocity field (Kim and Moin 1985).

10.3 Rotating decaying turbulence

In the current section, we study the vortex-stretching-based nonlinear model of Eq. (9.9) using direct numerical and large-eddy simulations of rotating decaying turbulence. Rotating decaying turbulence is a prototypical rotating turbulent flow that allows us to study the effects of rotation on turbulence, without the influence of external forces, walls, etc.

With this initial test case, we have three aims. First of all, we want to understand the workings and interplay of the two terms of the vortex-stretching-based nonlinear model. Secondly, we want to determine the values of the model constants of this model. Finally, we want to make a first comparison of this new subgrid-scale model with existing subgrid-scale models.

10.3.1 Test case

Experimental background

The test case of rotating decaying turbulence used in this work is inspired by the experiments of Comte-Bellot and Corrsin (1971) on nonrotating decaying turbulence. In their experiments, Comte-Bellot and Corrsin investigated the properties of decaying (roughly) isotropic turbulence, which was generated by a regular grid in a uniform flow of air. Among other quantities, they measured energy spectra at three different stations downstream of the grid.

Numerical setup

We simulate the flow of the experiment by Comte-Bellot and Corrsin (1971) inside a triply periodic cubic box with edge length $L_{\text{ref}} = 11M = 55.88$ cm (Rozema et al. 2015; Silvis et al. 2017b). Here, $M = 5.08$ cm represents the mesh size of the turbulence-generating grid. We imagine that the simulation box is moving away from the turbulence-generating grid with the initial mean velocity of the flow of air in the experiment, $U_0 = 1000$ cm s⁻¹. The time in the numerical simulations, thus, corresponds to the distance from the grid in the experiment. In the simulations performed for the current study, we exposed

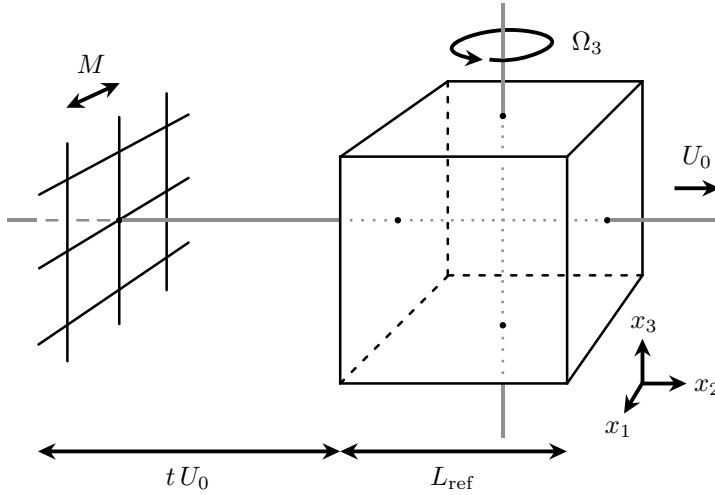


Figure 10.1: Schematic illustration of the flow geometry of our numerical simulations of rotating decaying turbulence.

the flow in the box to rotation about the vertical (x_3) axis through addition of the Coriolis force. A schematic illustration of this simulation setup is shown in Fig. 10.1.

Initial conditions

The initial conditions of the numerical simulations were chosen to have the same energy spectrum as the flow at the first measurement station of the experiment by Comte-Bellot and Corrsin (1971). Generation of these initial conditions was achieved with the procedure outlined by Rozema et al. (2015), using the scripts that these authors made publicly available.¹

In the first step of this procedure, an incompressible velocity field with random phases is created (Kwak et al. 1975), which has an energy spectrum that fits the spectrum measured at the first station. Secondly, to adjust the phases, this velocity field is fed into a preliminary numerical simulation. Preliminary large-eddy simulations were run with the QR model (Verstappen et al. 2010; Verstappen 2011; Verstappen et al. 2014). Finally, a rescaling operation (Kang et al. 2003) is applied to the velocity field, to again match the energy spectrum of the flow in the first measurement station.

For the purposes of the current research, the Coriolis force term was turned on in the preliminary simulations, and the above procedure was repeated for each rotation rate and spatial resolution investigated below. The resulting velocity fields served as initial conditions for our numerical simulations.

¹ See <https://github.com/hjbae/CBC> for a set of scripts that can be used to generate initial conditions for numerical simulations of homogeneous isotropic turbulence.

Physical parameters

From the text accompanying Eqs. (1.34) and (1.44) in Sections 1.2.6 and 1.2.7, it is clear that our test case of rotating decaying turbulence can be characterized using two dimensionless parameters. These parameters are the Reynolds and rotation numbers, respectively given by

$$Re = \frac{u_{\text{ref}} L_{\text{ref}}}{\nu}, \quad Ro = \frac{2\Omega_3 L_{\text{ref}}}{u_{\text{ref}}}. \quad (10.1)$$

Here, u_{ref} and L_{ref} represent a reference velocity and length scale, respectively. The kinematic viscosity is again denoted by ν . The quantity Ω_3 represents the rotation rate about the vertical (x_3) axis.

We take as reference velocity $u_{\text{ref}} = 27.19 \text{ cm s}^{-1}$, which corresponds to the initial root-mean-square turbulence intensity of the flow. That is, at the first station, Comte-Bellot and Corrsin (1971) measured a turbulent kinetic energy per unit mass given by $E_{\text{kin}} = 3u_{\text{ref}}^2/2$. With the previously mentioned reference length scale, $L_{\text{ref}} = 55.88 \text{ cm}$, and the value of the viscosity of air in the experiment, $\nu = 0.15 \text{ cm}^2 \text{ s}^{-1}$, the initial Reynolds number is given by $Re = 10\,129$. In our simulations, we vary the rotation number from $Ro = 0$ (no rotation) to $Ro = 200$ (rapid rotation). Note that the rotation number is inversely proportional to the Rossby number, which is also used to characterize rotating flows.

We can alternatively define the Reynolds and rotation numbers of Eq. (10.1) using the (longitudinal) integral length scale L and the (transverse) Taylor microscale λ . We will denote these dimensionless parameters as Re_L , Re_λ , Ro_L and Ro_λ . The rotation numbers based on the integral length scale and the Taylor microscale give information about the strength of the Coriolis force (Jacquin et al. 1990; Cambon et al. 1997; Bourouiba and Bartello 2007).

If $Ro_L < 1$, the rotation is weak and the dynamics of the flow are not affected by the Coriolis force. When, on the other hand, $Ro_L \gtrsim 1$, rotation impacts the large scales of motion. As long as the Taylor-microscale rotation number satisfies $Ro_\lambda < 1$, the small-scale motions are not affected by the Coriolis force. Finally, if $Ro_\lambda \gtrsim 1$, the rotation is rapid. That is, all scales of motion are influenced by rotation and the Coriolis force dominates the convective nonlinear term.

Physical quantities

In Sections 10.3.2 to 10.3.4, we discuss results obtained from direct numerical and large-eddy simulations of rotating decaying turbulence. We specifically show three-dimensional energy spectra $E(|k|)$ at time $t \approx 171M/U_0$, which corresponds to the third measurement station of the experiment of Comte-Bellot and Corrsin (1971). The energy spectra are provided per unit mass and in units of $u_{\text{ref}}^2 L_{\text{ref}}/(2\pi)$. Moreover, they are a function of the magnitude of the wavenumber k , which is given in units of $2\pi/L_{\text{ref}}$. Note that a small wavenumber corresponds to a large-scale motion, while large wavenumbers correspond to small scales of motion.

We also report the turbulent kinetic energy per unit mass E_{kin} , defined as

$$E_{\text{kin}} = \int_{k=0}^{\infty} E(|k|) dk. \quad (10.2)$$

Since integration is limited to a finite wavenumber range in numerical simulations, the quantity E_{kin} computed from a coarse-grid simulation at best represents the resolved turbulent kinetic energy. To allow for a fair comparison between direct numerical and large-eddy simulations, we, therefore, also consider the turbulent kinetic energy up to the grid cutoff of our large-eddy simulations,

$$E_{\text{kin,C}} = \int_{k=0}^{k_C} E(|k|) dk. \quad (10.3)$$

Here, k_C represents the wavenumber of the grid cutoff of our large-eddy simulations. That is, k_C corresponds to the wavelength of the point-to-point oscillation of the grid. This wavelength is given by 2Δ , in terms of a uniform grid size $\Delta = \Delta x_1 = \Delta x_2 = \Delta x_3$.

With a sharp spectral cutoff filter, $E_{\text{kin,C}}$ represents the turbulent kinetic energy of all motions that have a size at least equal to 2Δ and equals the filtered turbulent kinetic energy. In what follows, the turbulent kinetic energy per unit mass E_{kin} is given in units of $3u_{\text{ref}}^2/2$. The turbulent kinetic energy up to the grid cutoff $E_{\text{kin,C}}$ will be normalized with respect to its initial value. Both variants of the turbulent kinetic energy are shown as a function of nondimensional time tU_0/M .

Grid resolution

In our numerical simulations of rotating decaying turbulence, we employed uniform, isotropic grids with periodic boundary conditions. Using a grid convergence study (see Appendix B.1), we determined that a spatial resolution of 64^3 grid points is most suitable for large-eddy simulations of this flow. For this grid resolution, around 80% of the initial turbulent kinetic energy of the flow is resolved, which is the percentage that is generally strived for in large-eddy simulations (Pope 2011). Furthermore, the integral length scale, which forms the characteristic size of the large eddies, can be resolved on this grid.

We also found that as much as 99% of the initial turbulent kinetic energy is resolved using a 512^3 grid. With this resolution, the grid size is only 3.5 times larger than the Kolmogorov length, close to the recommended value of 2 (Pope 2011). Moreover, energy spectra obtained from simulations on 256^3 and 512^3 grids practically collapse up to the 128^3 grid cutoff at $k_C L_{\text{ref}}/(2\pi) = 64$. Numerical results obtained using a 512^3 grid, therefore, are accurate enough to reveal the physical behavior of rotating decaying turbulence and to serve as reference data for our large-eddy simulations.²

² Refer to Appendix B.1 for more details on the grid convergence study of our numerical simulations of rotating decaying turbulence.

Table 10.1: Initial rotation and Reynolds numbers of our direct numerical simulations of rotating decaying turbulence on a 512^3 grid.

Ro	Ro_L	Ro_λ	Re	Re_L	Re_λ
0	0.0	0.00	10 129	367	78
50	2.6	0.55	10 129	367	78
100	5.2	1.10	10 129	367	78
200	10.4	2.21	10 129	367	78

10.3.2 Physical behavior

To prepare for our large-eddy simulations, we first discuss the typical physical behavior of rotating decaying turbulence using results from direct numerical simulations. We specifically discuss the effects of rotation on the energy spectra and turbulent kinetic energy of rotating decaying turbulence with initial Reynolds number $Re = 10\,129$ and rotation numbers $Ro = 0$ to 200. The results communicated in this section were obtained using a 512^3 grid resolution and were partly reported previously (Silvis et al. 2016).

Physical parameters

Table 10.1 shows the initial physical parameters of our direct numerical simulations of rotating decaying turbulence. The rotation numbers based on the integral length scale and Taylor microscale, Ro_L and Ro_λ , show that these simulations probe different regimes of rotation. First, for $Ro = 0$, we have a flow without imposed rotation. Secondly, for $Ro = 50$, rotation affects the large scales of motion (as $Ro_L > 1$), but not the small-scale motions (as $Ro_\lambda < 1$).

As the rotation number increases to $Ro = 100$, the small-scale motions may start to be influenced also (as $Ro_\lambda \sim 1$). Finally, for $Ro = 200$, we reach a state of rapid rotation in which all scales of motion are affected by the Coriolis force (as $Ro_\lambda > 1$). The initial Reynolds numbers take on the same value for each rotation rate since we start all simulations from velocity fields with the same energy spectrum.

Energy spectrum and turbulent kinetic energy

Figure 10.2 shows the energy spectra and turbulent kinetic energy computed from our direct numerical simulations of rotating decaying turbulence. From the energy spectra in Fig. 10.2(a), we see that both $Ro = 50$ and $Ro = 100$ correspond to an intermediate regime of rotation in which the large-scale motions are affected by the Coriolis force, but the small-scale motions are not. For $Ro = 200$, we observe a state of rapid rotation in which all scales of motion are affected by rotation. An increase in the rotation number goes along with a characteristic steepening of the energy spectrum.

From Fig. 10.2(b) we clearly see that the dissipation rate of turbulent kinetic energy reduces in turbulence that is subjected to rotation. The reduced

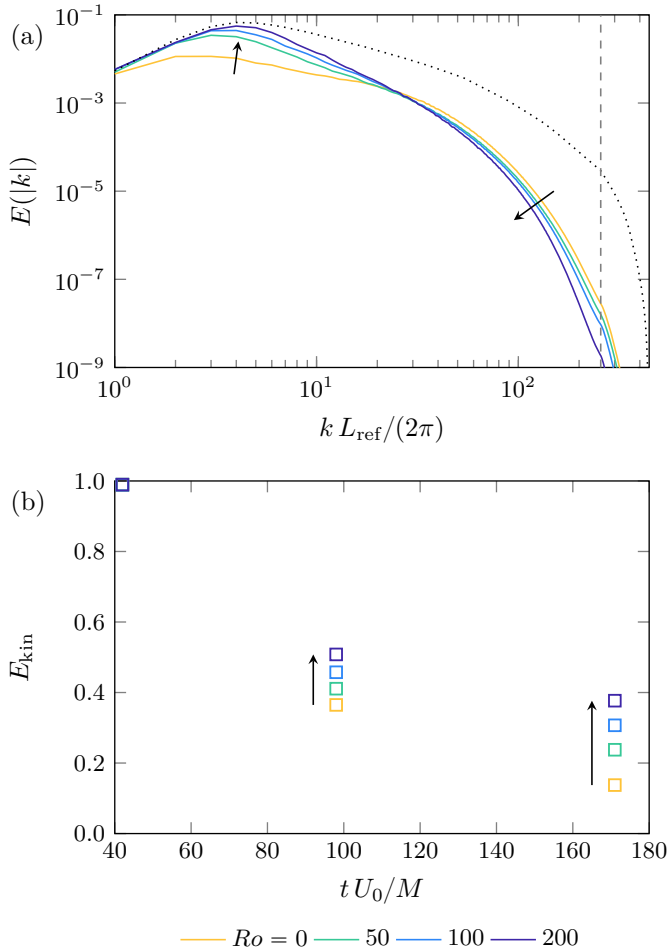


Figure 10.2: Rotation number dependence of (a) the energy spectrum at time $t \approx 171M/U_0$ and (b) the turbulent kinetic energy of rotating decaying turbulence with initial Reynolds number $Re = 10\,129$. Results were obtained from direct numerical simulations on a 512^3 grid. The dotted line and the vertical dashed line, respectively, represent the initial energy spectrum and the 512^3 grid cutoff. Arrows indicate the direction of increasing rotation number.

dissipation rate of turbulent kinetic energy is a nontrivial effect of the Coriolis force. This force does not appear in the evolution equation of the (turbulent) kinetic energy and, therefore, does not produce nor dissipate (turbulent) kinetic energy. The Coriolis force, however, indirectly reduces the viscous dissipation of turbulent kinetic energy by causing transfer of energy from small to large-scale motions. Rotating turbulent flows can, therefore, be expected to form a challenging test case for dissipative subgrid-scale models, such as eddy viscosity models.

10.3.3 Effects of the nonlinear subgrid-scale model

In the current section, we study the effects and interplay of the two terms of the vortex-stretching-based nonlinear model of Eq. (9.9) using large-eddy simulations of nonrotating and rotating decaying turbulence. We also propose a nondynamic procedure to determine the model constants of this subgrid-scale model.

Decaying homogeneous isotropic turbulence

Figure 10.3 shows predictions of the energy spectrum and turbulent kinetic energy of decaying homogeneous isotropic turbulence with initial Reynolds number $Re = 10\,129$ and rotation number $Ro = 0$. These results were obtained from large-eddy simulations on a 64^3 grid with the vortex-stretching-based nonlinear model.

To determine the effects of the eddy viscosity term, we varied the model constant C_ν from $C_\nu^2 = 0$ to $C_\nu^2 \approx 0.68$ (twice the value suggested in Eq. (9.10)). Figure 10.3(a) shows that energy piles up close to the grid cutoff, which is located at $k_C L_{\text{ref}} / (2\pi) = 32$, in the absence of eddy viscosity ($C_\nu^2 = 0$). For $C_\nu^2 \approx 0.68$, which gives rise to a large value of the eddy viscosity, no pile-up of energy occurs. The eddy viscosity term, thus, causes dissipation of turbulent kinetic energy, as expected. We also see that the pile-up of energy that is visible for $C_\nu^2 = 0$ goes along with a depletion of energy of the large and intermediate scales of motion. This depletion is not visible for $C_\nu^2 \approx 0.68$. The eddy viscosity term, thus, has a significant impact on the whole energy spectrum through dissipation.

A similar effect can be observed when comparing the energy spectra of underresolved and well-resolved numerical simulations of decaying turbulence (see Fig. B.1 in Appendix B.1). In simulations with a low spatial resolution, energy piles up close to the grid cutoff, whereas this pile-up does not occur in high-resolution simulations. Increasing the spatial resolution and increasing the eddy viscosity, thus, have a similar effect on the energy spectrum. This similarity, of course, explains why eddy viscosity models are often used in large-eddy simulations.

To reveal the effects of the nonlinear term, we varied C_μ from -15 to 15 (a wide range around the value suggested in Eq. (9.11)). As Fig. 10.3(a) shows, the nonlinear model term significantly modulates the energy levels of the large

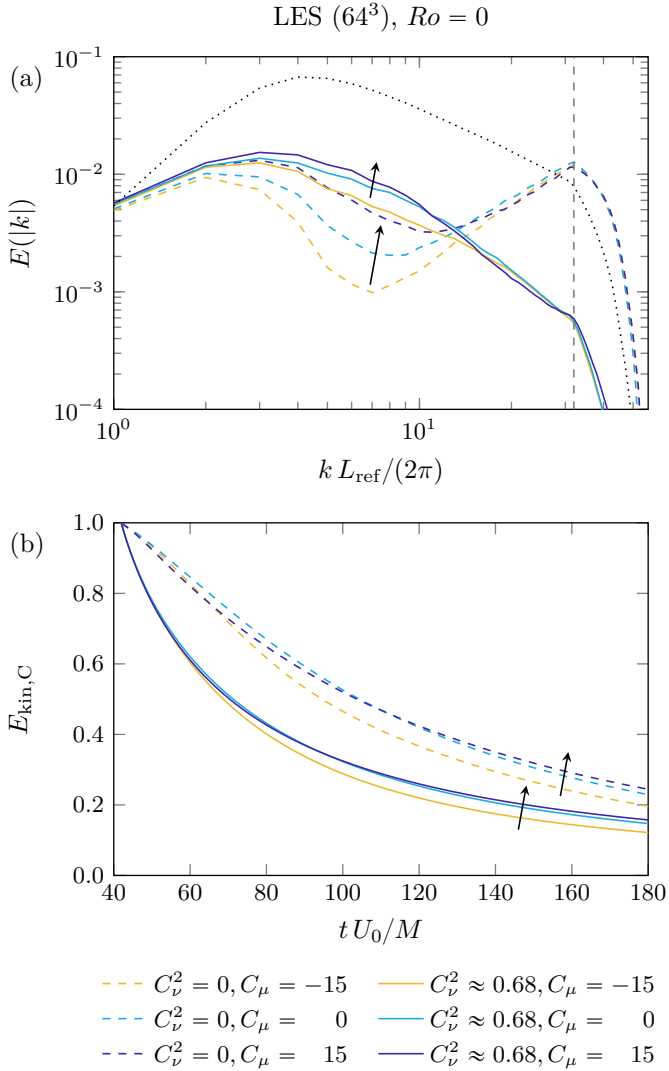


Figure 10.3: Model constant dependence of predictions of (a) the energy spectrum at time $t \approx 171M/U_0$ and (b) the normalized turbulent kinetic energy up to the 64^3 grid cutoff of decaying homogeneous isotropic turbulence with initial Reynolds number $Re = 10\,129$ and rotation number $Ro = 0$. Results were obtained from large-eddy simulations (LESs) on a 64^3 grid with the vortex-stretching-based nonlinear model with various values of the model constants C_ν and C_μ . The dotted line and the vertical dashed line, respectively, represent the initial energy spectrum and the 64^3 grid cutoff. Arrows indicate the direction of increasing C_μ .

and, especially, of the intermediate scales of motion. We observe either of two effects depending on the sign of the model constant C_μ .

For negative C_μ , the nonlinear term causes (additional) forward scatter of kinetic energy from the large and intermediate scales to the grid scale. For positive C_μ , the nonlinear term causes backscatter of energy, from the smaller toward the larger resolved scales of motion, and/or inhibits the forward energy cascade. The eddy viscosity and nonlinear terms of the vortex-stretching-based nonlinear model, thus, describe distinct physical effects, namely, dissipation and transfer of energy, respectively.

As Fig. 10.3(a) shows, however, the effects of the nonlinear term reduce as the constant C_ν of the eddy viscosity term grows. The two model terms, thus, interact. This same conclusion can be drawn from Fig. 10.3(b), which shows that the nonlinear term modulates the dissipation rate of turbulent kinetic energy. Do note that the nonlinear term does not in itself cause dissipation of energy. Rather, the nonlinear model term causes energy transfer to or from the smallest resolved scales of motion, whereby this term indirectly influences the dissipation that is most active at those scales.

Thus, despite their different nature, the eddy viscosity and nonlinear terms of the vortex-stretching-based nonlinear model are not dynamically independent and the commonly used assumption (see, e.g., Yang et al. 2012a; Yang et al. 2012b) that dissipative eddy viscosity and nondissipative nonlinear terms can be treated independently is invalid. As a consequence, the model constants of the vortex-stretching-based nonlinear model cannot be set independently of each other. Rather, we need to determine C_ν and C_μ such that the interplay between the two model terms is taken into account. To that end, we discuss the behavior of the vortex-stretching-based nonlinear model in rotating decaying turbulence.

Rotating decaying turbulence

Figure 10.4 shows predictions of the energy spectrum and turbulent kinetic energy of decaying turbulence with initial Reynolds number $Re = 10\,129$ at rotation numbers $Ro = 0$ and 200. These results were obtained from large-eddy simulations on a 64^3 grid using the vortex-stretching-based nonlinear model with $C_\nu^2 \approx 0.17$ and values of the nonlinear model constant between $C_\mu = -15$ and 15. A smaller value of C_ν is considered for Fig. 10.4 than for Fig. 10.3 to be able to study the combined effects of the eddy viscosity term and rotation on predictions of rotating decaying turbulence.

Figure 10.4 shows that the increase in forward (backward) scatter for negative (positive) model constant C_μ also occurs at nonzero rotation numbers. For $Ro = 200$, these effects are much smaller than for $Ro = 0$, however. Thus, the effects of the nonlinear term reduce both when the eddy viscosity increases and when the rotation number grows. When high rotation rates ($Ro \geq 200$) are combined with large eddy viscosities ($C_\nu^2 > 0.34$), the nonlinear model term turns off entirely.

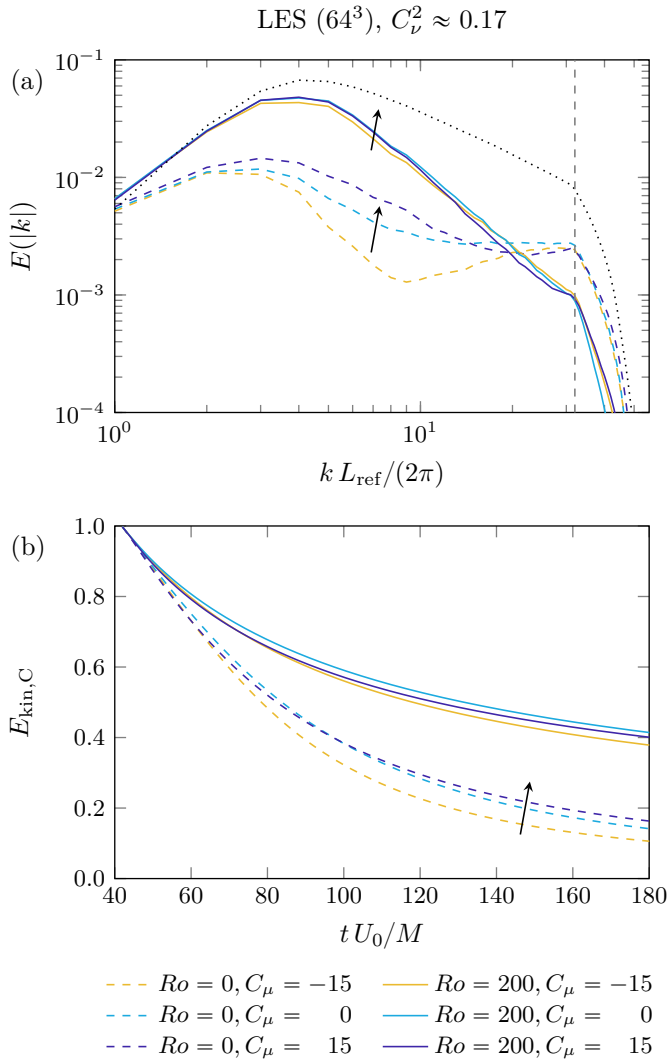


Figure 10.4: Model constant and rotation number dependence of predictions of (a) the energy spectrum at time $t \approx 171M/U_0$ and (b) the normalized turbulent kinetic energy up to the 64^3 grid cutoff of (rotating) decaying turbulence with initial Reynolds number $Re = 10\,129$. Results were obtained from large-eddy simulations (LESs) on a 64^3 grid with the vortex-stretching-based nonlinear model with $C_\nu^2 \approx 0.17$ and various values of C_μ . The dotted line and the vertical dashed line, respectively, represent the initial energy spectrum and the 64^3 grid cutoff. Arrows indicate the direction of increasing C_μ .

Determining the model constants

Using this observation, we can propose a nondynamic method to determine the model constants of the vortex-stretching-based nonlinear model, which takes into account the interplay between the two model terms. Namely, we first determine the value of the model constant C_ν for which the eddy viscosity term provides the correct (reduced) dissipation of turbulent kinetic energy in large-eddy simulations of rapidly rotating decaying turbulence. From our direct numerical and large-eddy simulations of rotating decaying turbulence with $Ro = 200$, we found that this dissipation is provided for half the value of the model constant mentioned in Eq. (9.10), i.e., $C_\nu^2 = 0.1687 \approx 0.17$.

The resulting eddy viscosity term will, however, not dissipate enough turbulent kinetic energy in large-eddy simulations of decaying turbulence exposed to a lower rotation rate. As a result, forward scatter of energy will deplete the intermediate and/or large scales of motion. To counter this forward scatter of energy, we secondly determine the model constant C_μ for which the nonlinear term provides sufficient backscatter in large-eddy simulations of rotating decaying turbulence at intermediate rotation rates. From our direct numerical and large-eddy simulations with $Ro = 50$ and 100 we found $C_\mu \approx 5$, which is about twice the value suggested in Eq. (9.11). The determined values of C_ν and C_μ constitute the model constants of the vortex-stretching-based nonlinear model provided in Eq. (9.12) of Section 9.5.

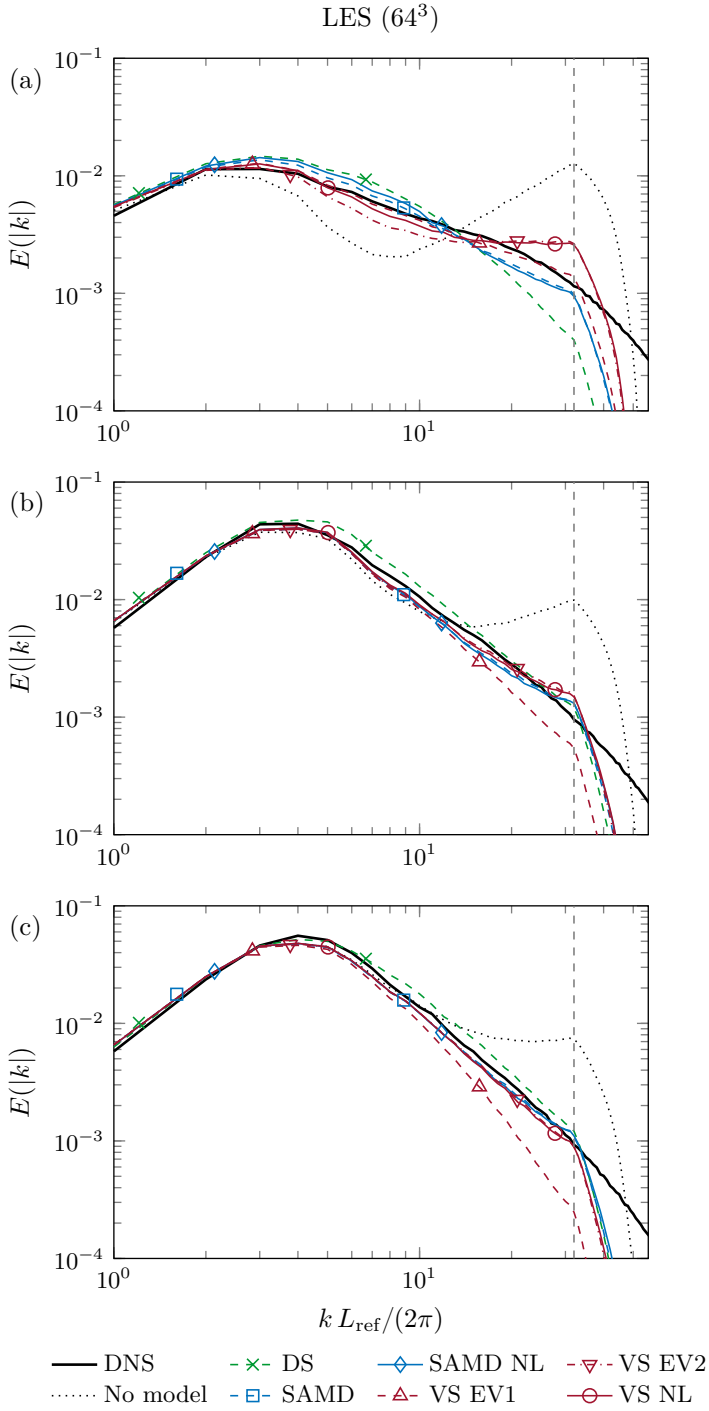
10.3.4 Large-eddy simulations of rotating decaying turbulence

We now present a detailed comparison of predictions of rotating decaying turbulence obtained with the vortex-stretching-based nonlinear model and with several eddy viscosity models.

Subgrid-scale models

We specifically discuss large-eddy simulations performed with the dynamic Smagorinsky model (Germano et al. 1991; Lilly 1992); the scaled anisotropic minimum-dissipation model (Verstappen 2018) with and without an added

Figure 10.5: Predictions of the energy spectrum of rotating decaying turbulence with rotation number (a) $Ro = 0$, (b) $Ro = 100$ and (c) $Ro = 200$, and initial Reynolds number $Re = 10129$ at time $t \approx 171M/U_0$. Results were obtained from direct numerical simulations (DNSs) on a 512^3 grid as well as from large-eddy simulations (LESs) on a 64^3 grid without a model, and with the dynamic Smagorinsky model (DS); the scaled anisotropic minimum-dissipation model without (SAMD) and with a nonlinear model term with $C_\mu = 5$ (SAMD NL); the vortex-stretching-based eddy viscosity model with $C_\nu^2 \approx 0.34$ (VS EV1) and $C_\nu^2 \approx 0.17$ (VS EV2); and the vortex-stretching-based nonlinear model with $C_\nu^2 \approx 0.17$ and $C_\mu = 5$ (VS NL). The vertical dashed lines represent the 64^3 grid cutoff.



nonlinear term; two variants of the vortex-stretching-based eddy viscosity model (Silvis et al. 2017b; Silvis and Verstappen 2018); and the new vortex-stretching-based nonlinear model of Eq. (9.9).

The scaled anisotropic minimum-dissipation model of Verstappen (2018) forms an adaptation of the anisotropic minimum-dissipation model of Rozema et al. (2015). On anisotropic grids these two models provide different results, but they are the same for the isotropic grids used in our large-eddy simulations of rotating decaying turbulence.

Energy spectrum and turbulent kinetic energy

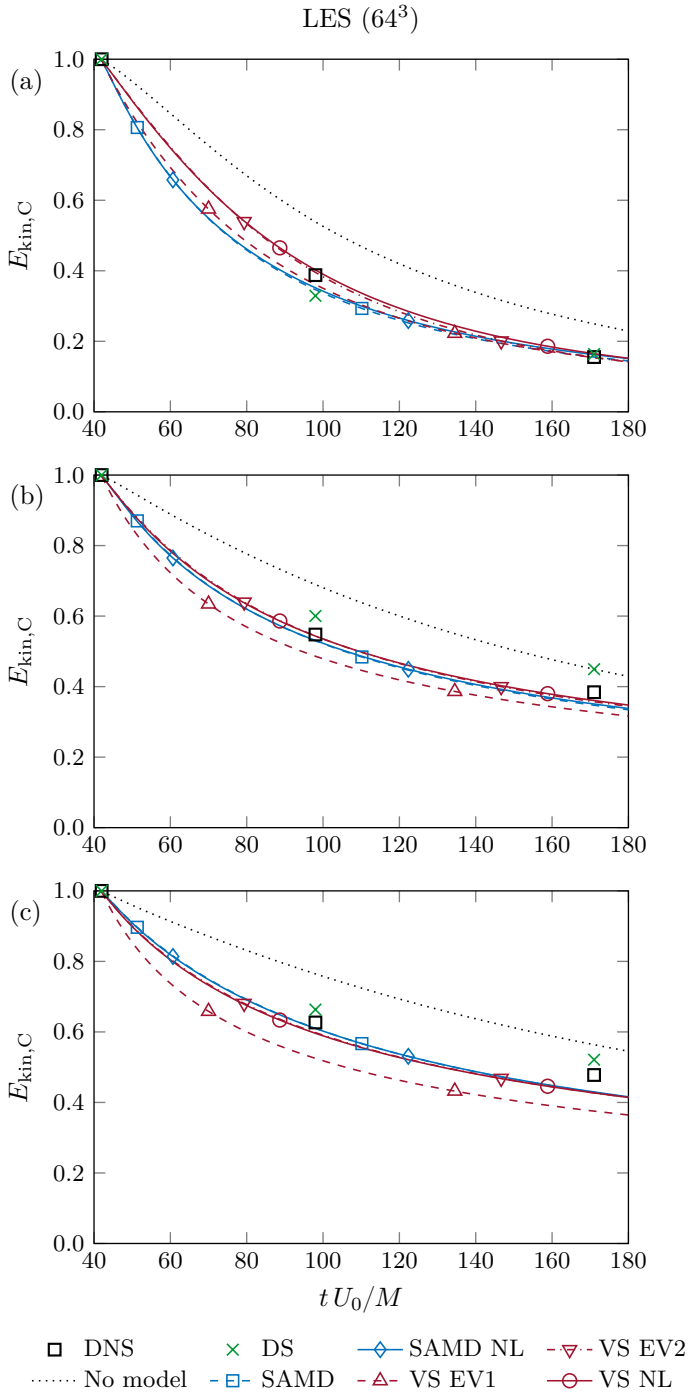
Figures 10.5 and 10.6 show predictions of the energy spectrum and turbulent kinetic energy of decaying turbulence with initial Reynolds number $Re = 10\,129$ and rotation numbers $Ro = 0, 100, 200$. These results were obtained from large-eddy simulations on a 64^3 grid. We discuss the results contained in Figs. 10.5 and 10.6 per subgrid-scale model.

The energy spectra in Fig. 10.5 show that the dynamic Smagorinsky model overpredicts the energy content of the large to intermediate scales of motion for all considered rotation numbers. In the nonrotating case, the small-scale energy content is underestimated. Better predictions of the energy content of the small scales of motion are obtained for decaying turbulence subject to rotation. Due to the overestimation of the large-scale kinetic energy, the dynamic Smagorinsky model, however, overpredicts the total turbulent kinetic energy of rotating decaying turbulence (see Fig. 10.6(b, c)).

The scaled anisotropic minimum-dissipation model also slightly overpredicts the large-scale and underpredicts the small-scale kinetic energy of nonrotating decaying turbulence (see Fig. 10.5(a)). In rotating decaying turbulence, the scaled anisotropic minimum-dissipation model slightly underestimates the energy content of the intermediate scales. Apart from some pile-up of energy for $Ro = 100$, the general shape of the spectrum is predicted well by this model, however.

If we consider the fact that the scaled anisotropic minimum-dissipation model is based on a kinetic energy balance (Rozema et al. 2015; Verstappen 2018), which does not include the Coriolis force, this model actually leads to surprisingly good predictions of rotating decaying turbulence. Adding the

Figure 10.6: Predictions of the normalized turbulent kinetic energy up to the 64^3 grid cutoff of rotating decaying turbulence with rotation number (a) $Ro = 0$, (b) $Ro = 100$ and (c) $Ro = 200$, and initial Reynolds number $Re = 10\,129$. Results were obtained from direct numerical simulations (DNSs) on a 512^3 grid as well as from large-eddy simulations (LESs) on a 64^3 grid without a model, and with the dynamic Smagorinsky model (DS); the scaled anisotropic minimum-dissipation model without (SAMD) and with a nonlinear model term with $C_\mu = 5$ (SAMD NL); the vortex-stretching-based eddy viscosity model with $C_\nu^2 \approx 0.34$ (VS EV1) and $C_\nu^2 \approx 0.17$ (VS EV2); and the vortex-stretching-based nonlinear model with $C_\nu^2 \approx 0.17$ and $C_\mu = 5$ (VS NL).



nonlinear term of the vortex-stretching-based nonlinear model (with model constant $C_\mu = 5$) to the scaled anisotropic minimum-dissipation model does not have a significant impact on these predictions. This result could be expected, since the above-mentioned kinetic energy balance does not take into account a nonlinear model term that is causing energy transfer.

Figures 10.5 and 10.6 also contain results obtained with the vortex-stretching-based eddy viscosity models with $C_\nu^2 \approx 0.34$ and $C_\nu^2 \approx 0.17$. For $C_\nu^2 \approx 0.34$, the value of the model constant suggested in Eq. (9.10), we obtain a very good prediction of the energy spectrum of nonrotating decaying turbulence (see Fig. 10.5(a)). This result was expected, given the dissipation estimate used to determine this model constant. For rotating turbulence, this model is much too dissipative, however, as evidenced by Figs. 10.5(b, c) and 10.6(b, c).

On the other hand, the vortex-stretching-based eddy viscosity model with $C_\nu^2 \approx 0.17$ gives good predictions of rotating decaying turbulence. Indeed, this subgrid-scale model only slightly underestimates the energy of the large and intermediate scales of motion for $Ro = 100$ and 200, and only leads to some pile-up of energy at the grid scale for $Ro = 100$ (see Fig. 10.5(b, c)). Expectedly, energy piles up at the grid scale for the nonrotating case, which goes along with the excess forward scatter of intermediate-scale energy that we discussed in Section 10.3.3. Predicting both rotating and nonrotating decaying turbulence, thus, is challenging for eddy viscosity models.

The vortex-stretching-based nonlinear model, for which $C_\nu^2 \approx 0.17$ and $C_\mu = 5$, does not remove the pile-up of energy caused by the vortex-stretching-based eddy viscosity model with $C_\nu^2 \approx 0.17$ in large-eddy simulations of nonrotating decaying turbulence. More important than avoiding this pile-up of energy, however, is that this model improves the prediction of the intermediate-scale energy content of nonrotating decaying turbulence (refer to Fig. 10.5(a)). At the same time, this model provides good approximations of the energy spectra of rotating decaying turbulence, as shown in Fig. 10.5(b, c). Indeed, the intermediate-scale energy content of rotating decaying turbulence is only slightly underestimated and little pile-up of energy occurs for $Ro = 100$.

By accounting for both dissipation and backscatter of energy, the vortex-stretching-based nonlinear model, thus, provides good predictions of rotating decaying turbulence over different regimes of rotation. Moreover, despite being a nondynamic model, the vortex-stretching-based nonlinear model performs at least as well as the dynamic Smagorinsky and scaled anisotropic minimum-dissipation models.

10.4 Spanwise-rotating plane-channel flow

We now study in detail the performance of the vortex-stretching-based nonlinear model using direct numerical and large-eddy simulations of a prototypical wall-bounded rotating turbulent flow, namely, spanwise-rotating plane-channel flow. We also compare predictions obtained using this subgrid-scale model with results from other subgrid-scale models.

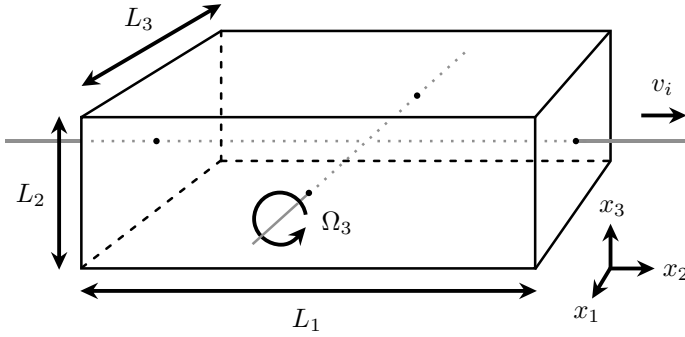


Figure 10.7: Schematic illustration of the flow geometry of our numerical simulations of spanwise-rotating plane-channel flow.

10.4.1 Test case

A spanwise-rotating plane-channel flow is a plane Poiseuille flow that is subjected to rotation about the spanwise (x_3) axis. A schematic illustration of such a flow is shown in Fig. 10.7.

Physical parameters

Spanwise-rotating plane-channel flow can be characterized by two dimensionless parameters. We employ the friction Reynolds and rotation numbers,

$$Re_\tau = \frac{u_\tau d}{\nu}, \quad Ro_\tau = \frac{2\Omega_3 d}{u_\tau}. \quad (10.4)$$

Here, u_τ represents the friction velocity and d is the channel half-width. The kinematic viscosity is denoted by ν and the rotation rate about the x_3 -axis is given by Ω_3 .

The Coriolis force induces an asymmetry in the flow in a spanwise-rotating plane channel. Therefore, the friction velocity u_τ is defined as

$$u_\tau = \sqrt{\frac{1}{2}(u_\tau^u)^2 + \frac{1}{2}(u_\tau^s)^2}, \quad (10.5)$$

where u_τ^u and u_τ^s are the friction velocities on the so-called unstable and stable sides of the channel, respectively. For the positive rates of rotation we consider here ($\Omega_3 \geq 0$, $Ro_\tau \geq 0$), these friction velocities are given by

$$u_\tau^u = \sqrt{\nu \left. \frac{d\langle v_1 \rangle}{dx_2} \right|_{x_2=0}}, \quad u_\tau^s = \sqrt{-\nu \left. \frac{d\langle v_1 \rangle}{dx_2} \right|_{x_2=2d}}. \quad (10.6)$$

Here, v_1 represents the streamwise velocity, the wall-normal coordinate is denoted as x_2 , and $\langle \cdot \rangle$ is an average over time as well as over the homogeneous streamwise (x_1) and spanwise (x_3) directions.

The friction Reynolds numbers corresponding to the unstable and stable sides of the channel will be denoted by Re_τ^u and Re_τ^s , respectively. Where convenient we will provide distances in terms of the viscous length scales given by the ratio of the viscosity ν and any of the three friction velocities u_τ^u , u_τ^s or u_τ^c , respectively indicated by the superscripts ‘u’, ‘s’ and ‘c’ (for the channel center), as well as a +.

In our numerical simulations of spanwise-rotating plane-channel flow, we impose a constant pressure gradient in the streamwise (x_1) direction to ensure that $Re_\tau \approx 395$. The rotation number ranges from $Ro_\tau = 0$ (no rotation) to $Ro_\tau = 1000$ (very rapid rotation). The flow domain is either given the dimensions $L_1 \times L_2 \times L_3 = 2\pi d \times 2d \times \pi d$ or $L_1 \times L_2 \times L_3 = 3\pi d \times 2d \times \pi d$.

Physical quantities

In Sections 10.4.2 to 10.4.5, we study first- and second-order statistics of the velocity field of spanwise-rotating plane-channel flow. We focus in particular on the mean streamwise velocity $\langle v_1 \rangle$ and the Reynolds stresses R_{ij} , which we define as

$$R_{ij} = \langle v_i v_j \rangle - \langle v_i \rangle \langle v_j \rangle. \quad (10.7)$$

As in Eq. (10.6), $\langle \cdot \rangle$ denotes an average over time, and over the homogeneous streamwise (x_1) and spanwise (x_3) directions.

Many commonly used subgrid-scale models, including those employed in the current work, are traceless. Traceless subgrid-scale models do not incorporate a model for the subfilter-scale kinetic energy and can, therefore, only predict the deviatoric part of the Reynolds stresses (Winckelmans et al. 2002). This quantity, which is also called the Reynolds stress anisotropy, is defined as

$$R_{ij}^{\text{dev}} = R_{ij} - \frac{1}{3} R_{kk} \delta_{ij}. \quad (10.8)$$

Note that only the diagonal elements of the Reynolds stress anisotropy and Reynolds stress tensors differ.

In principle, we can only make a fair comparison between the Reynolds stress (anisotropy) from our direct numerical and large-eddy simulations if the stress (anisotropy) from our large-eddy simulations is compensated by the average subgrid-scale model contribution (Winckelmans et al. 2002). In large-eddy simulations of (spanwise-rotating) channel flow, the diagonal elements of eddy viscosity models generally have a magnitude of at most a few percent relative to the Reynolds stress anisotropy. On the other hand, the diagonal elements of the nonlinear model term of Eq. (9.9) can take on values of the order of the Reynolds stress anisotropy.

Compensating the diagonal elements of the Reynolds stress anisotropy by the subgrid-scale model contribution, therefore, is not necessary for eddy viscosity models, but is essential when including the nonlinear term. Since the model contribution can be of the order of the Reynolds shear stress for all subgrid-scale models, compensation of this stress component is necessary for both eddy

viscosity and nonlinear models. In addition to the mean streamwise velocity, we, therefore, report the compensated Reynolds shear stress and compensated Reynolds stress anisotropy where applicable.

Given the averaging procedure of the $\langle \cdot \rangle$ operator, the mean streamwise velocity and (compensated) Reynolds stress (anisotropy) only depend on the wall-normal coordinate x_2 . Below, these quantities are shown in units of the friction velocity u_τ , as indicated by a superscript +.

Alternative physical parameters

From the mean streamwise velocity $\langle v_1 \rangle$, we can compute the bulk velocity

$$U_b = \frac{1}{2d} \int_{x_2=0}^{2d} \langle v_1 \rangle dx_2. \quad (10.9)$$

The bulk velocity allows us to define different dimensionless parameters that characterize spanwise-rotating channel flow, namely, the bulk Reynolds and rotation numbers. These numbers can be defined as

$$Re_b = \frac{U_b d}{\nu}, \quad Ro_b = \frac{2\Omega_3 d}{U_b}. \quad (10.10)$$

Here, the bulk Reynolds number Re_b does not include a factor 2, to ensure similarity between the parameters of Eqs. (10.4) and (10.10).

The bulk Reynolds and rotation numbers are commonly used to characterize simulations of spanwise-rotating plane-channel flow in which a constant mass flow is enforced. To expedite comparison with such simulations, we report both the friction-velocity-based dimensionless numbers of Eq. (10.4) and the bulk-velocity-based numbers of Eq. (10.10) in what follows.

Grid resolution

In our numerical simulations of spanwise-rotating plane-channel flow, we employ periodic boundary conditions in the streamwise (x_1) and spanwise (x_3) directions. We use a uniform grid spacing in these periodic directions. To allow for wall-resolved large-eddy simulations, the grid is stretched in the wall-normal (x_2) direction. The wall-normal coordinates of the grid points in the lower half of the channel ($0 \leq x_2 \leq d$) are defined by

$$x_{2,(j)} = d \frac{\sinh(\gamma j/N_2)}{\sinh(\gamma/2)} \quad \text{for } j = 0, 1, \dots, N_2/2, \quad (10.11)$$

where N_2 represents the number of grid points in the wall-normal direction and the stretching parameter γ is given the value 7. The grid points in the upper half of the channel ($d \leq x_2 \leq 2d$) follow from mirroring the coordinates of Eq. (10.11) in the channel center.

Using a grid convergence study (see Appendix B.2), we found that numerical simulations of spanwise-rotating plane-channel flow with $Re_\tau \approx 395$ and domain

sizes $2\pi d \times 2d \times \pi d$ and $3\pi d \times 2d \times \pi d$ could benefit from subgrid-scale modeling for spatial resolutions of 32^3 to 64^3 grid points. We also found that first- and second-order velocity field statistics obtained with spatial resolutions between 128^3 and $256 \times 128 \times 256$ grid cells lie very close to each other, verifying the accuracy of these results. We, therefore, use a $256 \times 128 \times 256$ grid for our direct numerical simulations of spanwise-rotating plane-channel flow, and resolutions of 32^3 and 64^3 grid points for our large-eddy simulations, for both domain sizes.³

Time integration

As mentioned in Section 10.1, we use an explicit scheme for the time integration of the convective, viscous and Coriolis force terms of the Navier–Stokes equations. These terms, therefore, restrict the time step size in our simulations. To ensure stable integration of the convective and viscous terms, we use time steps of at most $\Delta t = 1 \times 10^{-3} d/u_\tau$, $2.5 \times 10^{-4} d/u_\tau$ and $2 \times 10^{-5} d/u_\tau$ for our numerical simulations of nonrotating channel flow on 32^3 , 64^3 and $256 \times 128 \times 256$ grids, respectively.

The Coriolis force term has a numerical stability condition that does not depend on the grid size, but on the rotation rate. We found that time steps of size $\Delta t \lesssim 1/(10Ro_\tau) d/u_\tau$ lead to stable integration of this term. For coarse-grid simulations with a high rotation number, the Coriolis force, thus, restricts the time step more than the convective and viscous forces. Consequently, we used smaller time steps than indicated above for such simulations.

To ensure convergence of the mean streamwise velocity and elements of the Reynolds stress (anisotropy), we divide each channel flow simulation into two phases. We first let the turbulence in the channel develop into a statistically steady state. Then we record the average velocity and Reynolds stresses. As we will see in Section 10.4.2, the numerical results presented here have been obtained from sufficiently long runs of statistically steady flows.

Turbulent bursts and other flow instabilities

In our numerical simulations of spanwise-rotating plane-channel flow, we observed two types of turbulent instabilities, namely, turbulent bursts and a quasi-periodic collapse of the mean streamwise velocity (see Appendix C).

Turbulent bursts are resonant instabilities that only occur for certain domain sizes, and Reynolds and rotation numbers (Brethouwer et al. 2014; Brethouwer 2016). In our direct numerical simulations of spanwise-rotating plane-channel flow with domain size $2\pi d \times 2d \times \pi d$, we observed turbulent bursts for the rotation numbers $Ro_\tau = 25$ to 100, while these turbulent instabilities do not seem to occur on a $3\pi d \times 2d \times \pi d$ domain. Turbulent bursts last for approximately 3 d/u_τ time units and can be alternated with calmer flow periods of 100 d/u_τ

³ Refer to Appendix B.2 for more details on the grid convergence study of our numerical simulations of spanwise-rotating plane-channel flow.

time units. Their magnitude is so large, however, that they lead to large peaks in long-time averages of the Reynolds stresses.

We also observed a quasi-periodic collapse of the mean streamwise velocity for several rotation numbers $Ro_\tau \geq 150$ with the domain size $3\pi d \times 2d \times \pi d$, but not for the $2\pi d \times 2d \times \pi d$ domain. In this cyclic collapse, the mean streamwise velocity drastically reduces and recovers over a period of approximately $300 d/u_\tau$ time units. Each collapse seems to be preceded and caused by a steady growth of turbulence close to the unstable wall of the channel. Given the long time scale of this cycle, this process is likely due to the quasi-periodic fluctuation of Taylor–Görtler vortices (Dai et al. 2016).

Both turbulent bursts and the quasi-periodic collapse of the mean streamwise velocity have a large impact on flow statistics that is difficult to foresee. Since we want to make a fair comparison between predictions of rotating turbulent flows provided by different subgrid-scale models, we had better prevent these turbulent instabilities.

We, therefore, choose the domain size $3\pi d \times 2d \times \pi d$ for numerical simulations of spanwise-rotating plane-channel flow with rotation numbers $0 \leq Ro_\tau \leq 100$ and the domain size $2\pi d \times 2d \times \pi d$ for the rotation numbers $125 \leq Ro_\tau \leq 1000$. In coarse-grid simulations on a $2\pi d \times 2d \times \pi d$ domain, turbulent bursts may occur for rotation numbers over $Ro_\tau = 100$. In that case, we also use the $3\pi d \times 2d \times \pi d$ domain.⁴

10.4.2 Physical behavior

To prepare for our large-eddy simulations, we first discuss the typical physical behavior of spanwise-rotating plane-channel flow using results from direct numerical simulations.

Physical parameters

We specifically discuss the effects of rotation on the first- and second-order statistics of the velocity field of spanwise-rotating plane-channel flow with friction Reynolds number $Re_\tau \approx 395$. The rotation number covers the large range of values from $Ro_\tau = 0$ to $Ro_\tau = 1000$.

Table 10.2 shows the physical parameters as well as the grid spacings in units of the viscous length scales of our direct numerical simulations of spanwise-rotating plane-channel flow. A few important observations can be made from this table. First, the bulk rotation number Ro_b does not vary linearly with the friction rotation number Ro_τ . Indeed, Ro_b makes a jump from 0 to 0.9 when Ro_τ increases from 0 to 25, while Ro_b increments in smaller steps for a further increase in Ro_b . The initial jump in the bulk rotation number seems to indicate that $Ro_\tau = 25$ represents a significant rotation rate.

Secondly, the friction Reynolds number corresponding to the unstable wall, Re_τ^u , is larger than Re_τ for most nonzero rotation numbers. The opposite holds

⁴ Refer to Appendix C for more details on our observations of turbulent instabilities in numerical simulations of spanwise-rotating plane-channel flow.

Table 10.2: Rotation and Reynolds numbers, and grid spacings in units of the viscous length scales of our direct numerical simulations of spanwise-rotating plane-channel flow with friction Reynolds number $Re_\tau \approx 395$ on a $256 \times 128 \times 256$ grid. The horizontal rule separates the results with domain size $3\pi d \times 2d \times \pi d$ from those with domain size $2\pi d \times 2d \times \pi d$.

Ro_τ	Ro_b	Re_b	Re_τ	Re_τ^u	Re_τ^s	$\Delta x_1^{u,+}$	$\Delta x_1^{s,+}$	$\Delta x_2^{u,+}$	$\Delta x_2^{c,+}$	$\Delta x_2^{s,+}$	$\Delta x_3^{u,+}$	$\Delta x_3^{s,+}$
0	0	6823	395	395	395	15	15	0.7	21	0.7	5	5
25	0.9	11 509	395	489	269	18	10	0.8	21	0.4	6	3
50	1.2	16 862	395	471	299	17	11	0.8	21	0.5	6	4
75	1.3	22 095	394	454	322	17	12	0.8	21	0.5	6	4
100	1.5	26 857	393	441	338	16	12	0.7	21	0.6	5	4
125	1.6	31 412	395	432	353	11	9	0.7	21	0.6	5	4
150	1.7	35 281	394	424	362	10	9	0.7	21	0.6	5	4
175	1.8	38 724	394	417	370	10	9	0.7	21	0.6	5	5
200	1.9	41 786	395	412	377	10	9	0.7	21	0.6	5	5
225	2.0	44 450	395	408	382	10	9	0.7	21	0.6	5	5
250	2.1	46 681	395	404	386	10	9	0.7	21	0.6	5	5
500	3.8	52 312	396	396	396	10	10	0.7	21	0.7	5	5
1000	7.6	52 313	396	396	396	10	10	0.7	21	0.7	5	5

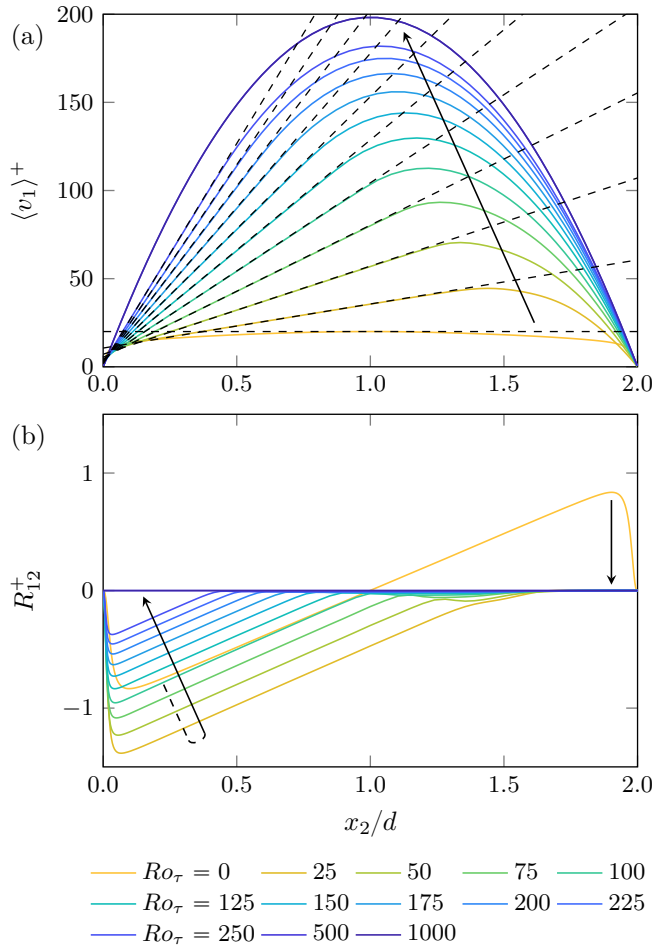


Figure 10.8: Rotation number dependence of the dimensionless (a) mean streamwise velocity and (b) Reynolds shear stress of spanwise-rotating plane-channel flow with friction Reynolds number $Re_\tau \approx 395$. Results were obtained from direct numerical simulations on a $256 \times 128 \times 256$ grid. The dashed lines have slope Ro_τ . Arrows indicate the direction of increasing rotation number.

for the friction Reynolds number corresponding to the stable wall, Re_τ^s . The three friction Reynolds numbers are equal for the rotation numbers $Ro_\tau = 500$ and 1000. We will shortly see that these effects are due to (partial) laminarization of the flow, caused by the Coriolis force.

Thirdly, all values of the friction Reynolds number Re_τ lie within 0.5% of 395. This observation indicates our results have converged in time. The data-taking phase was between 28 and 40 time units of d/u_τ long for each simulation, corresponding to 70 (for $Ro_\tau = 0$) to 600 (for $Ro_\tau = 1000$) channel flow-through times with respect to the bulk velocity U_b . Finally, the values of the grid spacings in units of the viscous length scales show that we have run fine wall-resolved direct numerical simulations (Georgiadis et al. 2010).

Mean velocity and Reynolds shear stress

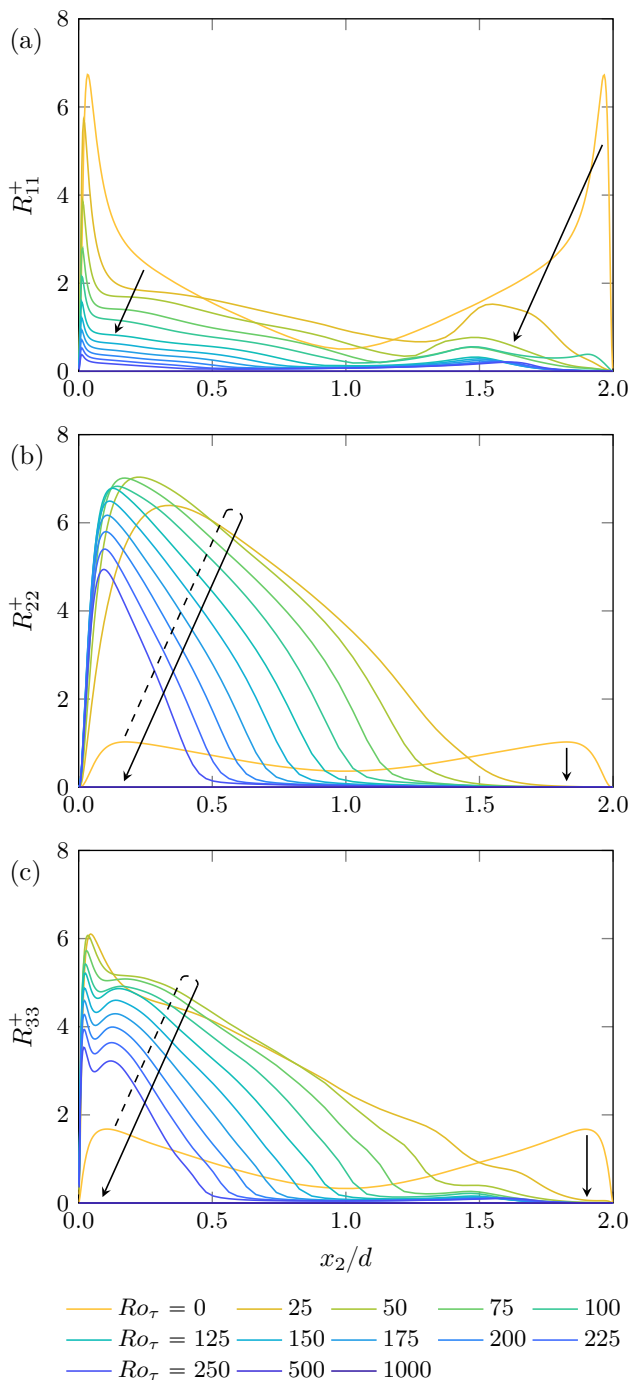
Figure 10.8 shows the mean streamwise velocity and Reynolds shear stress computed from our direct numerical simulations of spanwise-rotating plane-channel flow. The mean streamwise velocity shown in Fig. 10.8(a) clearly exhibits a linear region with slope Ro_τ . This linear region is linked to a parabolic part of the velocity profile, which grows as the rotation number increases and indicates (partial) laminarization of the flow (Xia et al. 2016).

For the two largest rotation numbers considered here, namely $Ro_\tau = 500$ and 1000, the entire velocity profile is parabolic. This parabolic profile has a slope of magnitude 395 on both walls of the channel. We can, thus, confirm the hypothesis that full laminarization occurs when the mean streamwise velocity has a slope of $2\Omega_3$ at the wall (Grundestam et al. 2008) or, equivalently, when the friction rotation and Reynolds numbers are equal (Xia et al. 2016).

The Reynolds shear stress, provided in Fig. 10.8(b), also shows that the flow in a plane channel laminarizes over a growing region when the spanwise rotation rate increases. We do, however, observe two additional interesting effects. First, the Reynolds shear stress in the lower part of the channel (close to $x_2 = 0$) initially increases in intensity as the rotation number grows and is larger than the shear stress in the nonrotating channel up to $Ro_\tau = 100$. The stress decreases for larger rotation numbers. Secondly, the shear stress in the upper part of the channel (close to $x_2 = 2d$) has already decayed to zero for $Ro_\tau = 25$. This rotation number, therefore, indeed represents a significant rotation rate.

These results are consistent with previous observations at other friction Reynolds numbers (Grundestam et al. 2008; Xia et al. 2016; Brethouwer 2017) and we adopt the existing terminology (Johnston et al. 1972; Grundestam et al.

Figure 10.9: Rotation number dependence of the dimensionless (a) streamwise, (b) wall-normal and (c) spanwise Reynolds stress of spanwise-rotating plane-channel flow with friction Reynolds number $Re_\tau \approx 395$. Results were obtained from direct numerical simulations on a $256 \times 128 \times 256$ grid. Arrows indicate the direction of increasing rotation number.



2008; Yang and Wu 2012; Brethouwer 2017) of unstable and stable sides of the channel for the regions close to $x_2 = 0$ and $x_2 = 2d$, respectively.

Reynolds stresses

Figure 10.9 shows the behavior of the diagonal Reynolds stresses of spanwise-rotating plane-channel flow. In the stable part of the channel, the streamwise Reynolds stress reduces as the rotation number increases, but not as quickly as the Reynolds shear stress (compare figures 10.8(b) and 10.9(a)). In the unstable part of the channel, the streamwise Reynolds stress reduces monotonically as the rotation number increases and seems to exhibit a linear behavior, as previously reported for $Re_\tau \approx 180$ by Xia et al. (2016).

The wall-normal and spanwise Reynolds stresses, respectively provided in Fig. 10.9(b, c), quickly vanish in a growing (stable) region as the rotation number increases, but they exhibit a nonmonotonic behavior in the unstable part of the channel. Therefore, the turbulent kinetic energy, which is given by half the sum of the diagonal Reynolds stresses, does not vary monotonically with the rotation number, as previously observed for $Re_\tau \approx 180$ by Xia et al. (2016). In the unstable part of a spanwise-rotating channel, both the wall-normal and spanwise Reynolds stresses are larger than the streamwise stress, a feature that nonrotating channel flow does not have.

Reynolds stress anisotropy

The diagonal Reynolds stresses presented in Fig. 10.9 reveal important aspects of the behavior of spanwise-rotating plane-channel flow. However, these Reynolds stresses are not suitable as reference data for our large-eddy simulations. Rather, since we employ traceless subgrid-scale models, we need to compare the (compensated) Reynolds stress anisotropy from our direct numerical and large-eddy simulations.

Figure 10.10 shows the diagonal elements of the Reynolds stress anisotropy computed from our direct numerical simulations. The most notable differences between the full and deviatoric Reynolds stresses of Figs. 10.9 and 10.10 are as follows. First, the streamwise Reynolds stress anisotropy, which is shown in Fig. 10.10(a), is (mostly) negative in the unstable part of rotating channel flow. Secondly, this quantity has the largest magnitude of all three normal stresses, although the wall-normal stress anisotropy shown in Fig. 10.10(b) is only slightly smaller. Finally, the spanwise Reynolds stress anisotropy, shown in Fig. 10.10(c), only attains a magnitude comparable to the other stresses close

Figure 10.10: Rotation number dependence of the dimensionless (a) streamwise, (b) wall-normal and (c) spanwise Reynolds stress anisotropy of spanwise-rotating plane-channel flow with friction Reynolds number $Re_\tau \approx 395$. Results were obtained from direct numerical simulations on a $256 \times 128 \times 256$ grid. Arrows indicate the direction of increasing rotation number.

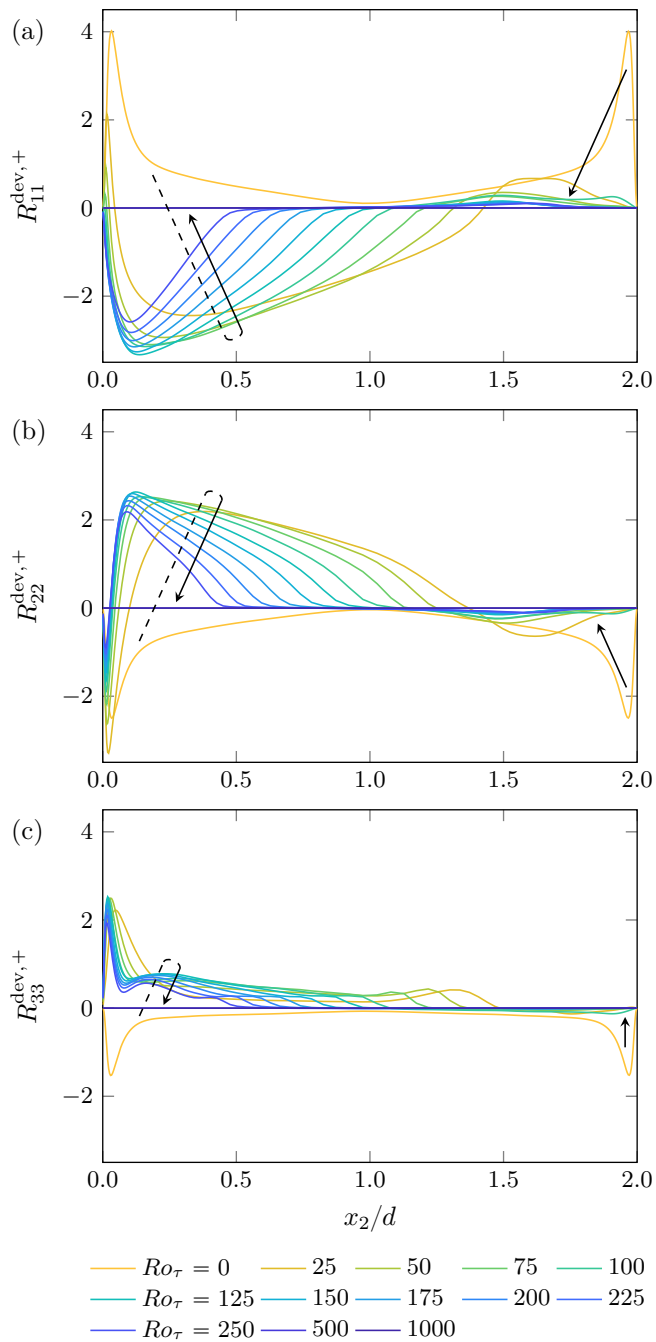


Table 10.3: Rotation and Reynolds numbers, and grid spacings in units of the viscous length scales of our numerical simulations of spanwise-rotating plane-channel flow with friction Reynolds number $Re_\tau \approx 395$ and friction rotation number $Ro_\tau = 100$. Details are shown of direct numerical simulations (DNSs) on a $256 \times 128 \times 256$ grid as well as of large-eddy simulations on a 32^3 grid without a model, and with the dynamic Smagorinsky model (DS); the scaled anisotropic minimum-dissipation model without (SAMD) and with a nonlinear model term with $C_\mu = 5$ (SAMD NL); the vortex-stretching-based eddy viscosity model with $C_\nu^2 \approx 0.34$ (VS EV1) and $C_\nu^2 \approx 0.17$ (VS EV2); and the vortex-stretching-based nonlinear model with $C_\nu^2 \approx 0.17$ and $C_\mu = 5$ (VS NL).

Label	Ro_b	Re_b	Re_τ	Re_τ^u	Re_τ^s	$\Delta x_1^{u,+}$	$\Delta x_1^{s,+}$	$\Delta x_2^{u,+}$	$\Delta x_2^{c,+}$	$\Delta x_2^{s,+}$	$\Delta x_3^{u,+}$	$\Delta x_3^{s,+}$
DNS	1.46	26 857	393	441	338	16	12	0.7	21	0.6	5	4
No model	1.62	24 400	395	454	325	134	96	3.0	78	2.2	45	32
DS	1.56	25 362	395	448	333	132	98	3.0	78	2.2	44	33
SAMD	1.63	24 270	395	437	348	129	103	2.9	78	2.3	43	34
SAMD NL	1.77	22 368	395	441	343	130	101	2.9	78	2.3	43	34
VS EV1	1.53	25 810	395	446	336	131	99	3.0	78	2.2	44	33
VS EV2	1.53	25 896	395	446	336	131	99	3.0	78	2.2	44	33
VS NL	1.58	25 035	395	449	332	132	98	3.0	78	2.2	44	33

to the unstable wall, but otherwise is rather small. Since only the diagonal elements of the Reynolds stress anisotropy and Reynolds stress tensors differ, the Reynolds shear stress R_{12} of Fig. 10.8 remains as is.

In conclusion, spanwise-rotating plane-channel flow exhibits a rich physical behavior with an interesting interplay between the Coriolis force and turbulence. Therefore, spanwise-rotating plane-channel flow forms a very interesting test case for large-eddy simulation.

10.4.3 Large-eddy simulations of spanwise-rotating plane-channel flow

In the current section, and in Sections 10.4.4 and 10.4.5, we present large-eddy simulations of spanwise-rotating plane-channel flow.

Subgrid-scale models

As in Section 10.3.4, these large-eddy simulations were performed using the dynamic Smagorinsky model (Germano et al. 1991; Lilly 1992); the scaled anisotropic minimum-dissipation model (Verstappen 2018) with and without a supplemented nonlinear model term; two variants of the vortex-stretching-based eddy viscosity model (Silvis et al. 2017b; Silvis and Verstappen 2018); and the vortex-stretching-based nonlinear model of Eq. (9.9).

Physical parameters

We first discuss large-eddy simulations of spanwise-rotating plane-channel flow with friction Reynolds number $Re_\tau \approx 395$ and rotation number $Ro_\tau = 100$ on a 32^3 grid. For $Ro_\tau = 100$, the interface between the stable laminar and unstable turbulent regions approximately lies in the middle of the channel. Given the stretching of the grid (refer to Eq. (10.11)), this rotation number can be expected to be most challenging for subgrid-scale models.

Table 10.3 shows the physical parameters as well as the grid spacings in units of the viscous length scales of our simulations. The large-eddy simulation without a model results in a bulk Reynolds number that is too small and a friction Reynolds number corresponding to the unstable (stable) wall that is too high (low). The dynamic Smagorinsky model and the different vortex-stretching-based subgrid-scale models provide better predictions of these dimensionless numbers, whereas the scaled anisotropic minimum-dissipation model behaves worse than the no-model result. We will see corresponding behavior in predictions of the mean streamwise velocity.

The grid sizes in terms of the viscous length scales indicate that we have performed coarse large-eddy simulations (Georgiadis et al. 2010; Choi and Moin 2012). Specifically, the first grid point off the unstable wall is located at $\Delta x_2^{u,+} \approx 3.0$ in these simulations, which is larger than the recommended value $\Delta x_2^{u,+} \approx 1.0$.

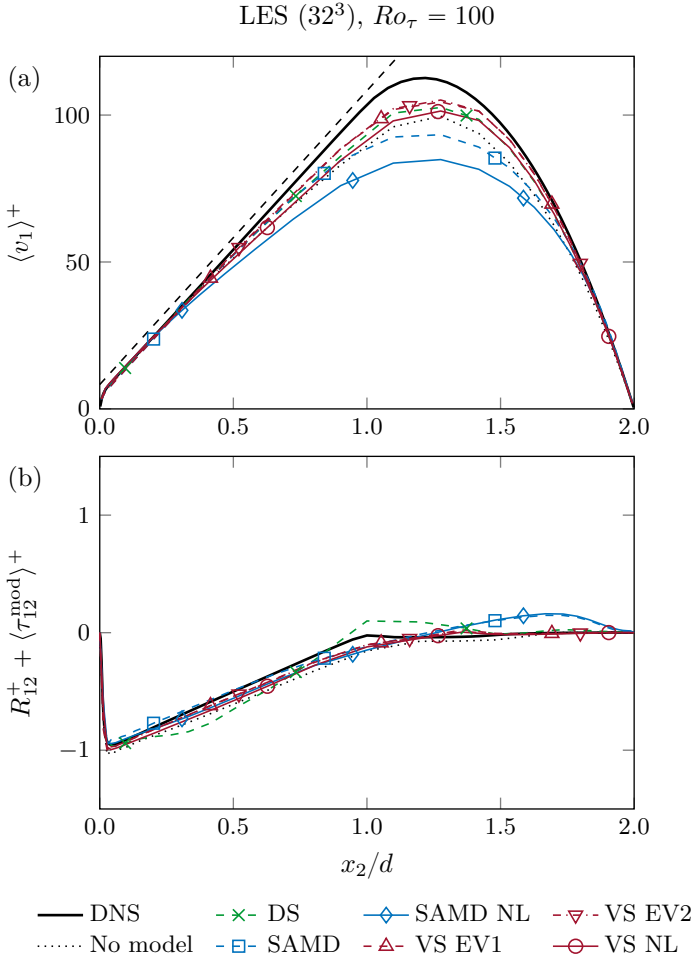
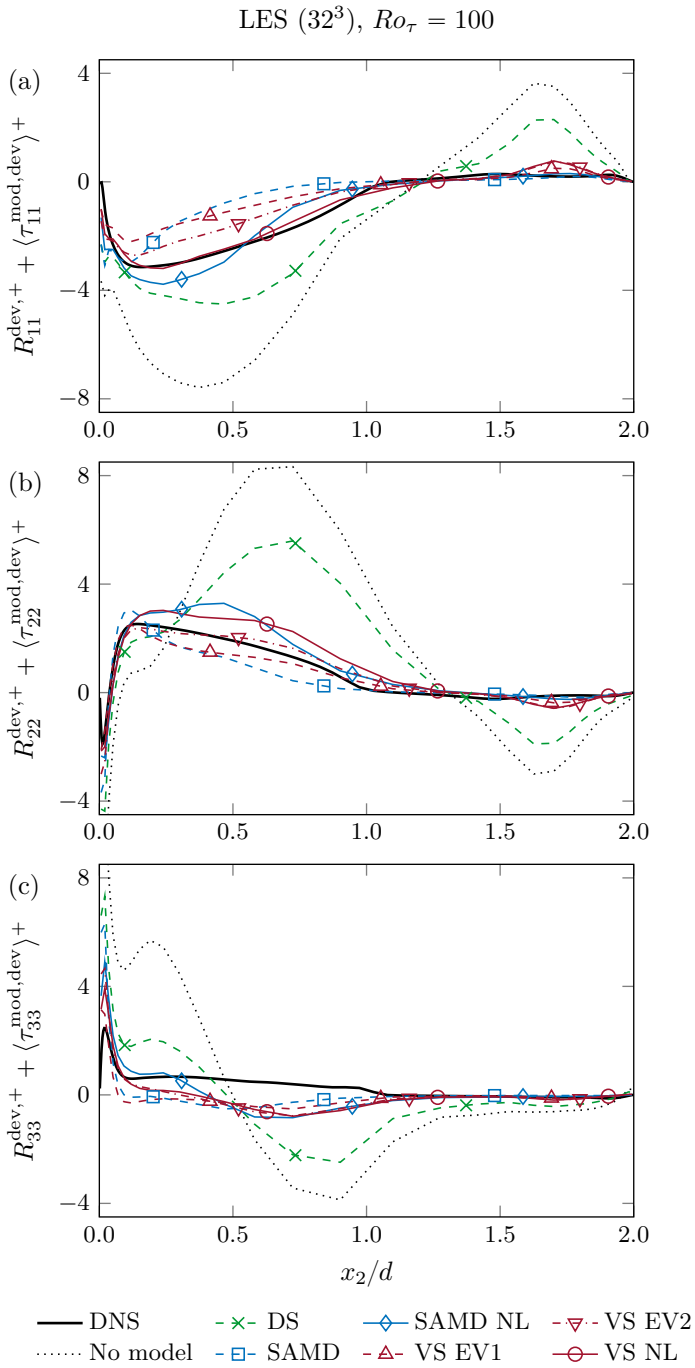


Figure 10.11: Predictions of the dimensionless (a) mean streamwise velocity and (b) compensated Reynolds shear stress of spanwise-rotating plane-channel flow with friction Reynolds number $Re_\tau \approx 395$ and friction rotation number $Ro_\tau = 100$. The dashed line has slope $Ro_\tau = 100$.

Figure 10.12: Predictions of the dimensionless compensated (a) streamwise, (b) wall-normal and (c) spanwise Reynolds stress anisotropy of spanwise-rotating plane-channel flow with friction Reynolds number $Re_\tau \approx 395$ and friction rotation number $Ro_\tau = 100$. Results were obtained from direct numerical simulations (DNSs) on a $256 \times 128 \times 256$ grid as well as from large-eddy simulations (LESs) on a 32^3 grid without a model, and with the dynamic Smagorinsky model (DS); the scaled anisotropic minimum-dissipation model without (SAMD) and with a nonlinear model term with $C_\mu = 5$ (SAMD NL); the vortex-stretching-based eddy viscosity model with $C_\nu^2 \approx 0.34$ (VS EV1) and $C_\nu^2 \approx 0.17$ (VS EV2); and the vortex-stretching-based nonlinear model with $C_\nu^2 \approx 0.17$ and $C_\mu = 5$ (VS NL).



Mean velocity and Reynolds shear stress

Figure 10.11 shows predictions of the mean streamwise velocity and compensated Reynolds shear stress of spanwise-rotating plane-channel flow with friction Reynolds number $Re_\tau \approx 395$ and rotation number $Ro_\tau = 100$ obtained using a 32^3 grid. Figure 10.11(a) shows that the dynamic Smagorinsky model and the vortex-stretching-based eddy viscosity models with $C_\nu^2 \approx 0.34$ and $C_\nu^2 \approx 0.17$ only slightly improve the prediction of the height and slope of the mean velocity with respect to the no-model result. The scaled anisotropic minimum-dissipation model provides a worse result than the simulation without a subgrid-scale model.

The vortex-stretching-based nonlinear model (with $C_\nu^2 \approx 0.34$ and $C_\mu = 5$) leads to a mean streamwise velocity that lies very close to the result of the vortex-stretching-based eddy viscosity models. This observation can be understood from the fact that predictions of the mean streamwise velocity are mostly determined by the eddy viscosity term and are not affected much by the nonlinear model term if $|C_\mu| \leq 10$. In contrast to this observation, addition of the nonlinear model term to the scaled anisotropic minimum-dissipation model deteriorates the prediction of the mean velocity. Given the results of large-eddy simulations on a 64^3 grid that we present in Section 10.4.5, this problem is likely caused by a lack of spatial resolution.

Figure 10.11(b) shows that most subgrid-scale models give rise to a Reynolds shear stress that lies closer to the no-model result than to the reference data from direct numerical simulations. Predicting the mean streamwise velocity and Reynolds shear stress of spanwise-rotating plane-channel flow with $Re_\tau \approx 395$ and $Ro_\tau = 100$, thus, is very challenging for subgrid-scale models at a 32^3 grid resolution.

Reynolds stress anisotropy

Figure 10.12 shows predictions of the diagonal elements of the compensated Reynolds stress anisotropy of spanwise-rotating plane-channel flow for $Ro_\tau = 100$ obtained on a 32^3 grid. The dynamic Smagorinsky model overestimates the diagonal elements of the Reynolds stress anisotropy in both the unstable and stable parts of the channel. The results obtained using this model even qualitatively follow the no-model results.

The scaled anisotropic minimum-dissipation model underpredicts the Reynolds stress anisotropy in most of the unstable part of the channel. Peaks close to the unstable wall do lie close to the reference data from direct numerical simulations, but tend to overshoot (see the wall-normal Reynolds stress anisotropy in Fig. 10.12(b)).

The vortex-stretching-based eddy viscosity model with $C_\nu^2 \approx 0.34$ also underpredicts the Reynolds stress anisotropy in the unstable part of the channel. In addition, this model produces small peaks close to the unstable wall. The vortex-stretching-based eddy viscosity model with $C_\nu^2 \approx 0.17$ provides a good prediction of the wall-normal Reynolds stress anisotropy, but underestimates the magnitude of the streamwise stress anisotropy. Eddy viscosity models, thus,

fail to predict the Reynolds stress anisotropy of spanwise-rotating plane-channel flow at the current coarse resolution.

In contrast, the vortex-stretching-based nonlinear model provides an almost perfect prediction of the streamwise Reynolds stress anisotropy, as well as better estimates of the shape and magnitude of the wall-normal and spanwise Reynolds stress anisotropy than most considered eddy viscosity models. Specifically, the vortex-stretching-based nonlinear model does not produce any near-wall peaks in the Reynolds stress anisotropy.

Although leading to a too high magnitude of the Reynolds stress anisotropy, addition of the nonlinear model term to the scaled anisotropic minimum-dissipation model also improves the shape of the predictions and removes the peaks near the unstable wall.

10.4.4 Rotation number dependence of large-eddy simulations

We now generalize the observations of Section 10.4.3 to a large range of rotation rates.

Predictions at $Ro_\tau = 50$

To that end, we first discuss Figs. 10.13 and 10.14, which show the mean streamwise velocity, compensated Reynolds shear stress and compensated Reynolds stress anisotropy of spanwise-rotating plane-channel flow with friction Reynolds number $Re_\tau \approx 395$ and rotation number $Ro_\tau = 50$ as computed from large-eddy simulations on a 32^3 grid.

Comparing Figs. 10.13 and 10.14 with Figs. 10.11 and 10.12, we see that all considered subgrid-scale models provide qualitatively similar predictions of spanwise-rotating plane-channel flow for $Ro_\tau = 50$ and $Ro_\tau = 100$, up to one notable difference. For $Ro_\tau = 50$, the scaled anisotropic minimum-dissipation model and the vortex-stretching-based eddy viscosity models with $C_\nu^2 \approx 0.34$ and $C_\nu^2 \approx 0.17$ produce large spurious peaks in the Reynolds stress anisotropy close to the unstable wall (see Fig. 10.14). These peaks likely arise due to a lack of dissipation of turbulent kinetic energy close to the unstable wall, which is caused by the coarse grid resolution in that area.

The nonlinear model term entirely removes these near-wall peaks in the Reynolds stress anisotropy, as evidenced by the results of the vortex-stretching-based nonlinear model and the scaled anisotropic minimum-dissipation model with an added nonlinear term. The nonlinear model term of Eq. (9.9), thus, significantly improves predictions of the near-wall Reynolds stress anisotropy.

Mean velocity for $Ro_\tau = 0 - 1000$

To further generalize the observations of Section 10.4.3, Fig. 10.15 shows the bulk Reynolds number and friction Reynolds numbers at both walls of spanwise-rotating plane-channel flow with $Re_\tau \approx 395$ and rotation numbers $Ro_\tau = 0 - 500$

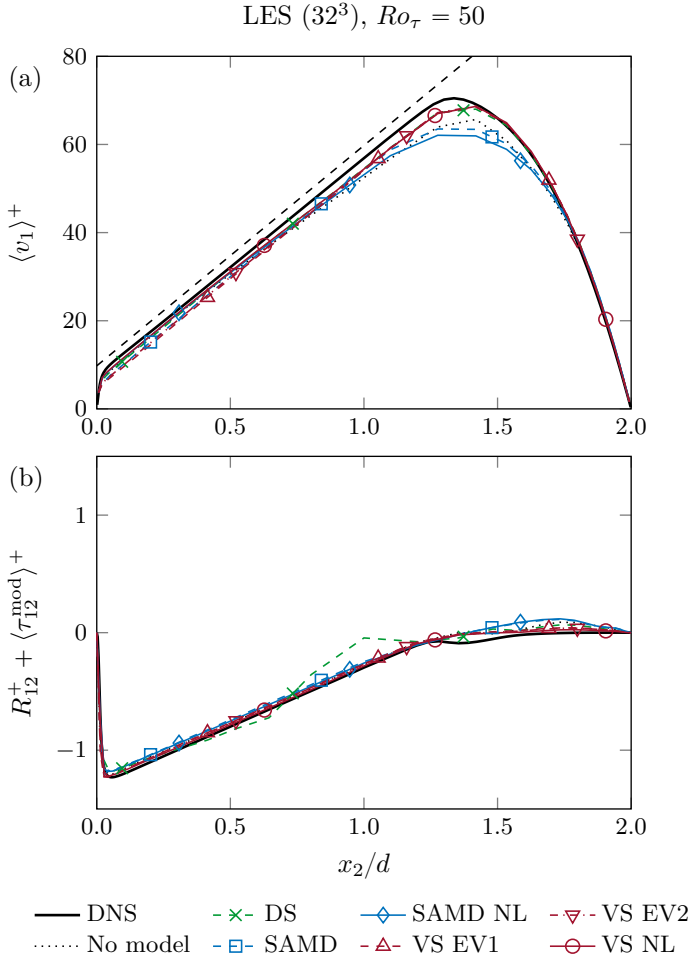
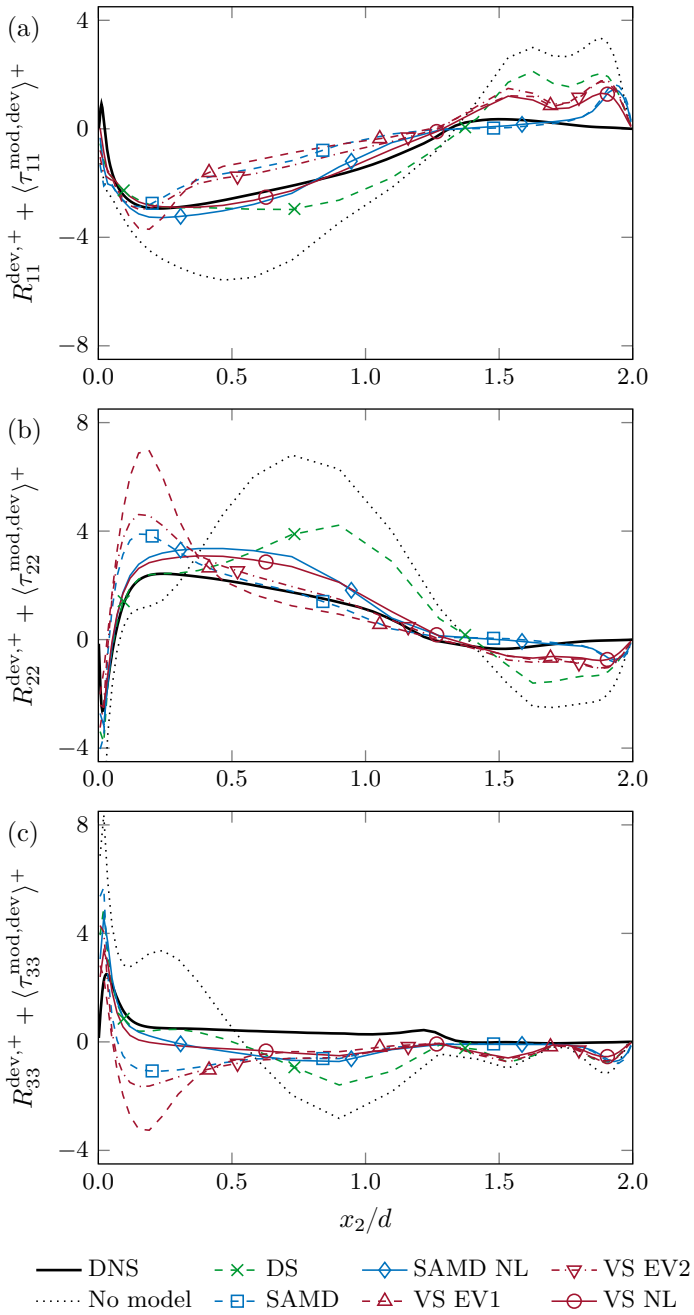


Figure 10.13: Predictions of the dimensionless (a) mean streamwise velocity and (b) compensated Reynolds shear stress of spanwise-rotating plane-channel flow with friction Reynolds number $Re_\tau \approx 395$ and friction rotation number $Ro_\tau = 50$. The dashed line has slope $Ro_\tau = 50$.

Figure 10.14: Predictions of the dimensionless compensated (a) streamwise, (b) wall-normal and (c) spanwise Reynolds stress anisotropy of spanwise-rotating plane-channel flow with friction Reynolds number $Re_\tau \approx 395$ and friction rotation number $Ro_\tau = 50$. Results were obtained from direct numerical simulations (DNSs) on a $256 \times 128 \times 256$ grid as well as from large-eddy simulations (LESs) on a 32^3 grid without a model, and with the dynamic Smagorinsky model (DS); the scaled anisotropic minimum-dissipation model without (SAMD) and with a nonlinear model term with $C_\mu = 5$ (SAMD NL); the vortex-stretching-based eddy viscosity model with $C_\nu^2 \approx 0.34$ (VS EV1) and $C_\nu^2 \approx 0.17$ (VS EV2); and the vortex-stretching-based nonlinear model with $C_\nu^2 \approx 0.17$ and $C_\mu = 5$ (VS NL).

LES (32^3) , $Ro_\tau = 50$



as obtained from large-eddy simulations on 32^3 grids. These bulk and friction Reynolds numbers, respectively, characterize the magnitude and shape of the mean velocity profile.

For rotation numbers up to $Ro_\tau = 75$, the dynamic Smagorinsky and vortex-stretching-based subgrid-scale models predict bulk and friction Reynolds numbers that lie close to the reference results from our direct numerical simulations. For $100 \leq Ro_\tau \leq 250$, these models, however, lead to a bulk Reynolds number that lies only slightly above the no-model result. These models also overpredict (underpredict) the friction Reynolds number at the unstable (stable) wall for this range of rotation numbers, but do improve the no-model result.

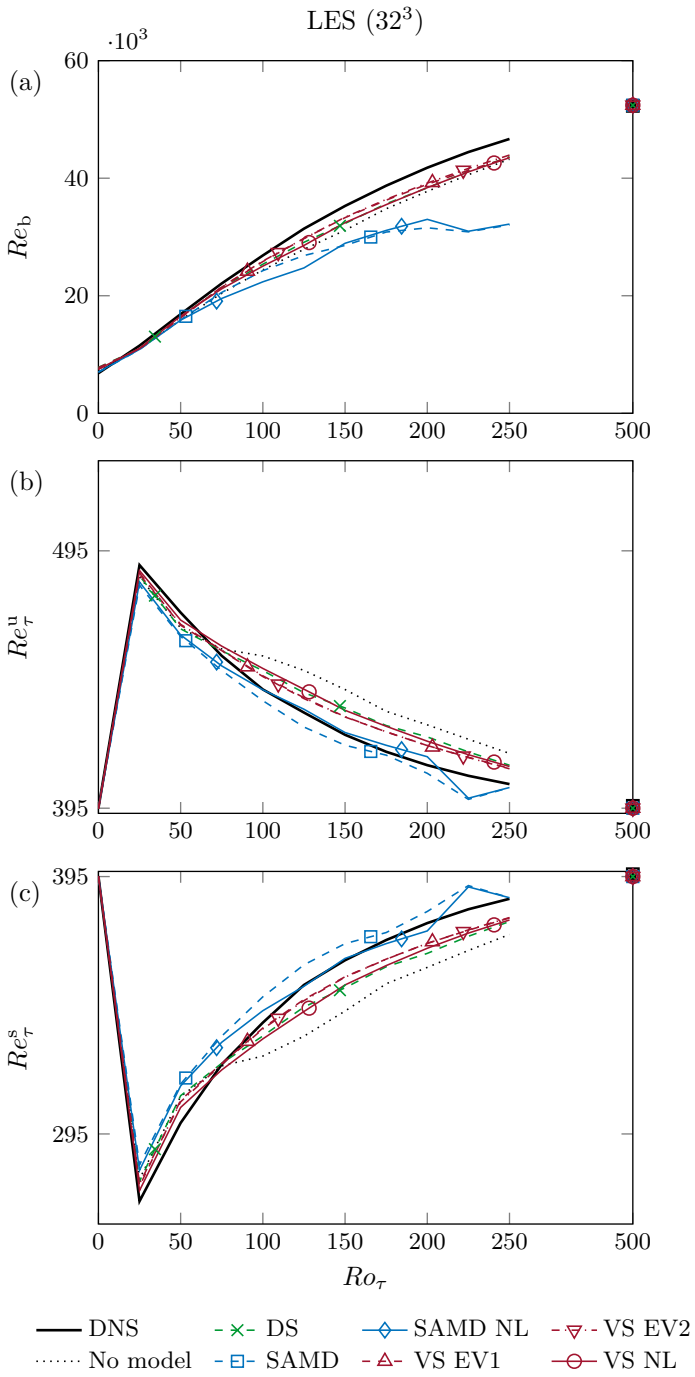
The scaled anisotropic minimum-dissipation model greatly underpredicts the bulk Reynolds number and underestimates (overestimates) the friction Reynolds number at the unstable (stable) wall for most rotation numbers. All simulations (including the no-model large-eddy simulation) predict the correct bulk and friction Reynolds numbers of laminarized spanwise-rotating plane-channel flow at $Ro_\tau = 500$ and $Ro_\tau = 1000$, namely, $Re_b \approx 52\,312$ and $Re_\tau^u \approx Re_\tau^s \approx Re_\tau \approx 395$. The nonlinear model term has little effect on the bulk and friction Reynolds numbers.

All considered subgrid-scale models, thus, provide mean streamwise velocity profiles that are qualitatively similar to the previously discussed cases with rotation numbers $Ro_\tau = 50$ and 100 for a large range of rotation rates. Specifically, the vortex-stretching-based subgrid-scale models provide predictions of the mean velocity that are as good as the results obtained using the dynamic Smagorinsky model. The scaled anisotropic minimum-dissipation model usually (greatly) underestimates the mean velocity and, thus, fails to predict this quantity. For the vortex-stretching-based nonlinear model, the mean velocity is mostly determined by the eddy viscosity and not affected much by the nonlinear model term.

Reynolds stress anisotropy for $Ro_\tau = 0 - 1000$

On the other hand, predictions of the Reynolds stress anisotropy are affected, and improved significantly, by the nonlinear model term over a large range of rotation numbers. We have observed that the vortex-stretching-based nonlinear

Figure 10.15: Rotation number dependence of predictions of the (a) bulk Reynolds number, (b) friction Reynolds number on the unstable side and (c) friction Reynolds number on the stable side of spanwise-rotating plane-channel flow with friction Reynolds number $Re_\tau \approx 395$. Results were obtained from direct numerical simulations (DNSs) on a $256 \times 128 \times 256$ grid as well as from large-eddy simulations (LESs) on a 32^3 grid without a model, and with the dynamic Smagorinsky model (DS); the scaled anisotropic minimum-dissipation model without (SAMD) and with a nonlinear model term with $C_\mu = 5$ (SAMD NL); the vortex-stretching-based eddy viscosity model with $C_\nu^2 \approx 0.34$ (VS EV1) and $C_\nu^2 \approx 0.17$ (VS EV2); and the vortex-stretching-based nonlinear model with $C_\nu^2 \approx 0.17$ and $C_\mu = 5$ (VS NL).



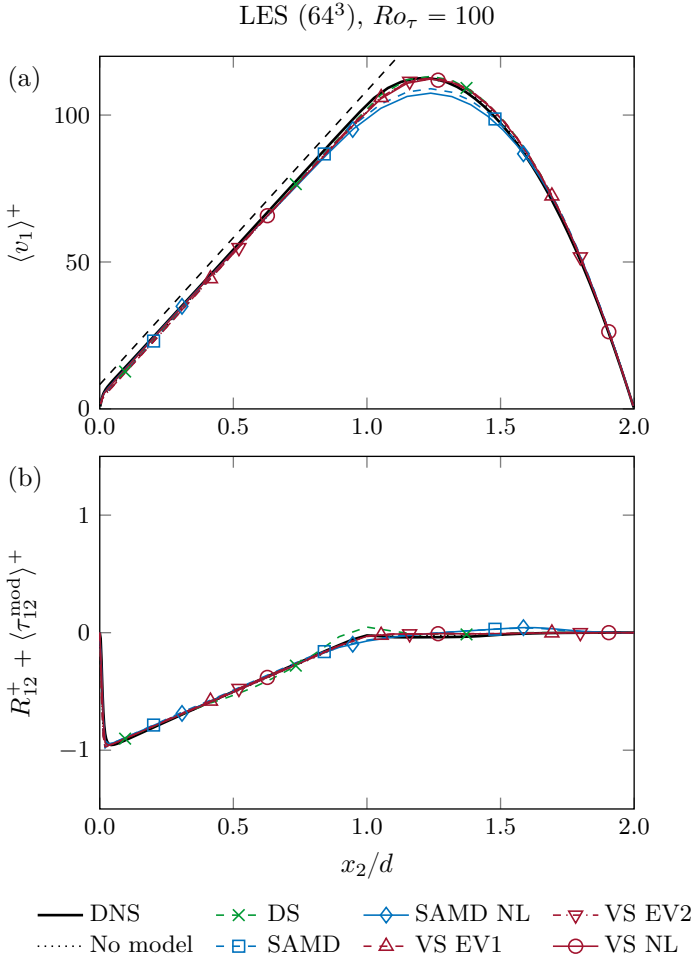
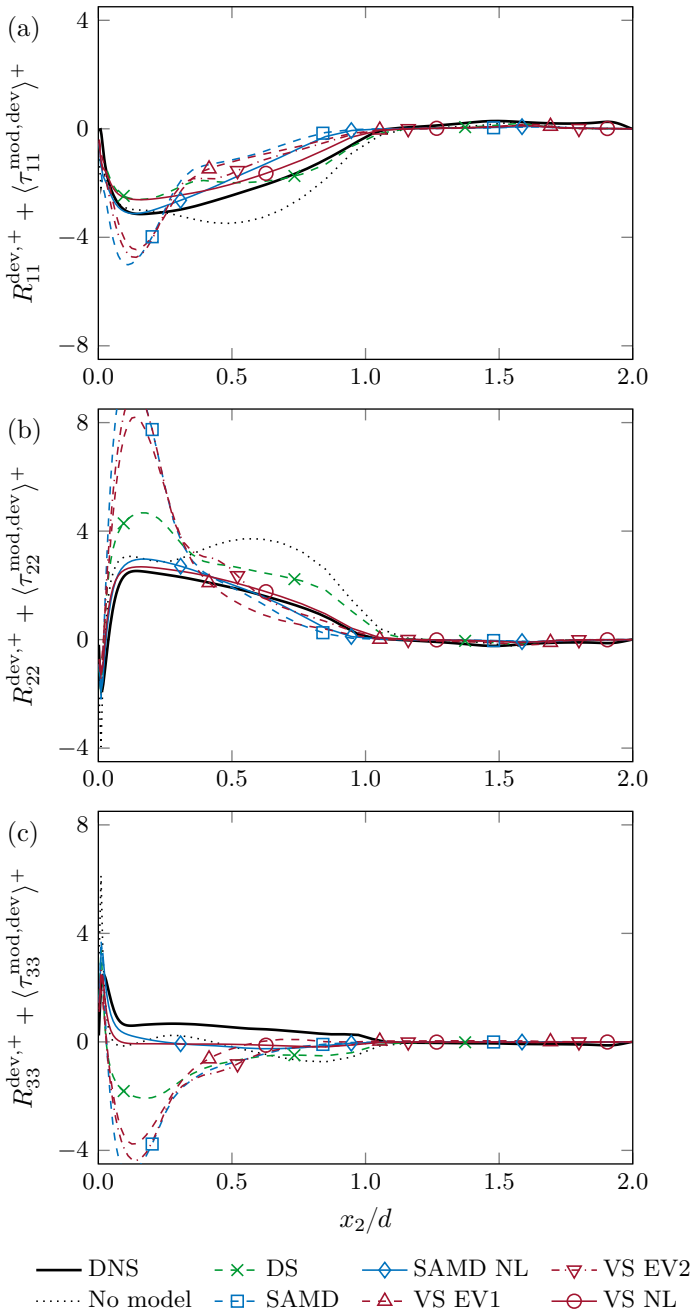


Figure 10.16: Predictions of the dimensionless (a) mean streamwise velocity and (b) compensated Reynolds shear stress of spanwise-rotating plane-channel flow with friction Reynolds number $Re_\tau \approx 395$ and friction rotation number $Ro_\tau = 100$. The dashed line has slope $Ro_\tau = 100$.

Figure 10.17: Predictions of the dimensionless compensated (a) streamwise, (b) wall-normal and (c) spanwise Reynolds stress anisotropy of spanwise-rotating plane-channel flow with friction Reynolds number $Re_\tau \approx 395$ and friction rotation number $Ro_\tau = 100$. Results were obtained from direct numerical simulations (DNSs) on a $256 \times 128 \times 256$ grid as well as from large-eddy simulations (LESs) on a 64^3 grid without a model, and with the dynamic Smagorinsky model (DS); the scaled anisotropic minimum-dissipation model without (SAMD) and with a nonlinear model term with $C_\mu = 5$ (SAMD NL); the vortex-stretching-based eddy viscosity model with $C_\nu^2 \approx 0.34$ (VS EV1) and $C_\nu^2 \approx 0.17$ (VS EV2); and the vortex-stretching-based nonlinear model with $C_\nu^2 \approx 0.17$ and $C_\mu = 5$ (VS NL).

LES (64^3), $Ro_\tau = 100$



model provides much better predictions of the Reynolds stress anisotropy than the considered eddy viscosity models for the rotation numbers from $Ro_\tau = 50$ to $Ro_\tau = 250$ (as shown for $Ro_\tau = 50$ and $Ro_\tau = 100$ in Figs. 10.12 and 10.14). The nonlinear term of the vortex-stretching-based nonlinear model plays a key role in obtaining these results, by improving estimates of the near-wall Reynolds stress anisotropy. Over the above range of rotation rates, the same model constants as in Sections 10.3.4 and 10.4.3 can be used without requiring (dynamic) adaptation or near-wall damping.

For $Ro_\tau = 25$, the vortex-stretching-based nonlinear model term also leads to improved predictions of the Reynolds stress anisotropy when compared to eddy viscosity models. In this case, taking $C_\nu^2 \approx 0.34$ rather than $C_\nu^2 \approx 0.17$ may be beneficial, however. In a flow without spanwise rotation, for which $Ro_\tau = 0$, the nonlinear term of the vortex-stretching-based nonlinear model has almost no effect on the Reynolds stress anisotropy. This quantity, then, is determined by the eddy viscosity term. For the very high rotation rates for which full laminarization occurs, such as $Ro_\tau = 500$ and 1000, the nonlinear model properly turns off.

10.4.5 Resolution dependence of large-eddy simulations

To determine the effects of the grid resolution on our results, we consider large-eddy simulations on a 64^3 grid. Figures 10.16 and 10.17 show the mean streamwise velocity, compensated Reynolds shear stress and compensated diagonal elements of the Reynolds stress anisotropy of spanwise-rotating plane-channel flow with friction Reynolds number $Re_\tau \approx 395$ and rotation number $Ro_\tau = 100$ as computed from large-eddy simulations with this resolution.

Mean velocity and Reynolds shear stress

All considered subgrid-scale models give a very good prediction of the mean streamwise velocity and Reynolds shear stress for this resolution and rotation number (refer to Fig. 10.16). Good estimates of these quantities are also provided over the range of rotation numbers $50 \leq Ro_\tau \leq 200$ by all subgrid-scale models but the scaled anisotropic minimum-dissipation model (not shown).

Reynolds stress anisotropy

The predictions of the Reynolds stress anisotropy obtained using the dynamic Smagorinsky model improved significantly with respect to the results obtained on a 32^3 grid (compare Fig. 10.12). Nonetheless, the dynamic Smagorinsky model produces spurious peaks in the Reynolds stress anisotropy close to the unstable wall.

Similarly, the vortex-stretching-based eddy viscosity models with $C_\nu^2 \approx 0.34$ and $C_\nu^2 \approx 0.17$ generate very large spurious peaks close to the unstable wall. Since we implemented these models using Deardorff's length scale (see Eq. (9.13)), it seems likely that these peaks are caused by a lack of near-wall

dissipation by the subgrid-scale model (Trias et al. 2017). The scaled anisotropic minimum-dissipation model also causes spurious near-wall peaks in the Reynolds stress anisotropy. We obtained similar results over the range of rotation numbers from $Ro_\tau = 75$ to 200 (not shown). The considered eddy viscosity models, thus, fail to give good predictions of the Reynolds stress anisotropy on both 32^3 and 64^3 grid.

As was the case for the large-eddy simulations of spanwise-rotating plane-channel flow with $Ro_\tau = 50$ on a 32^3 grid, the spurious near-wall peaks produced by the scaled anisotropic minimum-dissipation model and the vortex-stretching-based eddy viscosity model with $C_\nu^2 \approx 0.17$ are removed entirely by adding the nonlinear term. Moreover, with this improved description of near-wall effects, these nonlinear models both give very good predictions of the Reynolds stress anisotropy. Again, qualitatively similar results were obtained for $75 \leq Ro_\tau \leq 200$ (not shown).

The vortex-stretching-based nonlinear model, thus, gives outstanding predictions of spanwise-rotating plane-channel flow in large-eddy simulations with both coarse (32^3) and finer (64^3) spatial resolutions. Moreover, this new model outperforms the dynamic Smagorinsky and scaled anisotropic minimum-dissipation models without requiring (near-wall) damping or dynamic adaptation of the model constants.

Chapter 11

Conclusions and outlook

Conclusions

In this part of this thesis, we aimed to improve the numerical prediction of incompressible rotating turbulent flows. To that end, we proposed and validated a new nonlinear subgrid-scale model for large-eddy simulations of such flows.

A new nonlinear subgrid-scale model

The first term of the proposed subgrid-scale model is a dissipative eddy viscosity term that is linear in the rate-of-strain tensor, while the second term, which is nonlinear in the rate-of-strain and rate-of-rotation tensors, is nondissipative. We defined the two corresponding model coefficients in terms of the vortex stretching magnitude and named the resulting model the vortex-stretching-based nonlinear model.

The vortex-stretching-based nonlinear model by construction is consistent with most of the physical and mathematical properties of the Navier–Stokes equations and turbulent stresses. This model, therefore, respects fundamental properties of turbulent flows and can be used in complex flow configurations without requiring near-wall damping functions or dynamic procedures. Moreover, the model is suitable for simulations of laminar, transitional and turbulent flows. Being based on the local velocity gradient and grid size, the vortex-stretching-based nonlinear model also is easy to implement.

To preserve the different nature of the two terms of the model in numerical simulations, we recommended a purely dissipative implementation for the eddy viscosity term, whereas the nonlinear term should conserve kinetic energy. We also recommended the use of a discretization in which the convective and Coriolis force terms of the incompressible Navier–Stokes equations conserve kinetic energy, and in which the diffusive term only causes dissipation.

Numerical results

We studied and validated the vortex-stretching-based nonlinear model using detailed direct numerical and large-eddy simulations of rotating decaying turbulence and spanwise-rotating plane-channel flow. We also compared the predictions from this model with results from the commonly used dynamic Smagorinsky model, the scaled anisotropic minimum-dissipation model and the vortex-stretching-based eddy viscosity model.

Using large-eddy simulations of rotating decaying turbulence, we revealed that the two terms of the vortex-stretching-based nonlinear model describe distinct physical effects. The eddy viscosity and nonlinear terms, respectively, cause dissipation and transfer of energy. We also showed that the two terms interact with each other. The commonly used assumption that dissipative eddy viscosity and nondissipative nonlinear terms can be treated separately, thus, is invalid.

We, therefore, proposed a nondynamic procedure to determine the model constants of the vortex-stretching-based nonlinear model, which takes into account the interplay between the two model terms. For the resulting values of the model constants, the eddy viscosity term models dissipation of energy, while the nonlinear term accounts for backscatter of energy. Moreover, the vortex-stretching-based nonlinear model provided good predictions of nonrotating and rotating decaying turbulence, performing at least as well as the dynamic Smagorinsky and scaled anisotropic minimum-dissipation models.

We subsequently showed that the dynamic Smagorinsky model, the scaled anisotropic minimum-dissipation model and the vortex-stretching-based eddy viscosity model fail to predict the Reynolds stress anisotropy of spanwise-rotating plane-channel flow. These eddy viscosity models specifically tend to produce spurious near-wall peaks in the Reynolds stress anisotropy. On coarse grids, the scaled anisotropic minimum-dissipation model even failed to predict the mean streamwise velocity. Spanwise-rotating plane-channel flow, thus, forms a challenging test case for eddy viscosity models.

In contrast, the vortex-stretching-based nonlinear model gave outstanding predictions of the Reynolds stress anisotropy of spanwise-rotating plane-channel flow over a large range of rotation rates, for both coarse and finer grid resolutions. The nonlinear model term played a key role in generating these results, by improving estimates of the near-wall Reynolds stress anisotropy. At the same time, predictions of the mean velocity are as good as those obtained using the dynamic Smagorinsky model. The same model constants that were determined using large-eddy simulations of rotating decaying turbulence could be used for the large-eddy simulations of spanwise-rotating plane-channel flow.

The vortex-stretching-based nonlinear model, thus, performs as well as the dynamic Smagorinsky and scaled anisotropic minimum-dissipation models in large-eddy simulations of rotating decaying turbulence and outperforms these models in large-eddy simulations of spanwise-rotating plane-channel flow. Moreover, this proposed model does not require (dynamic) adaptation or near-wall damping of the model constants in the considered test cases.

Outlook

In future work, it would be interesting to investigate in detail the performance of the vortex-stretching-based nonlinear model in large-eddy simulations of (different) rotating turbulent flows with a higher Reynolds number. One could also analyze the ability of the vortex-stretching-based nonlinear model to predict

(coherent) flow structures, such as the Taylor–Görtler vortices that may occur in spanwise-rotating plane-channel flow (Dai et al. 2016). Such a study may also provide insights into the mechanism through which the new model provides better predictions of spanwise-rotating plane-channel flow than the considered eddy viscosity models.

Other points of interest for future studies could be adaptation of the vortex-stretching-based nonlinear model to describe rotating turbulent flows from an inertial frame of reference or the development of a dynamic procedure to determine the constants of this model. As should be clear from the current work, such a dynamic procedure should take into account the interplay of the two model terms. Future studies could also investigate the use of a flow-dependent length scale (see, e.g., Trias et al. 2017) or develop separate length scales for the two model terms.

Finally, our results indicate that supplementing the scaled anisotropic minimum-dissipation model with the nonlinear term of the vortex-stretching-based nonlinear model is beneficial. Combining this nonlinear term with other eddy viscosity models could also be interesting, as long as the interplay between the eddy viscosity and nonlinear terms is taken into account. Moreover, to get insights into the relation between the velocity-gradient-based subgrid-scale models considered in this work on the one hand and mixed models on the other hand, one could perform a comparison with the recently proposed minimum-dissipation-Bardina model (Streher et al. 2018, 2020).



Appendices

Appendix A

Independence of the basis tensors

In this appendix, we show that at most six of the tensors of Eq. (4.3) are simultaneously linearly independent. We also show which tensors are linearly independent for which flows.

A.1 The generalized Cayley–Hamilton theorem

The Cayley–Hamilton theorem (Hamilton 1853; Cayley 1858) states that a square matrix satisfies its own characteristic equation. For a 3×3 matrix A , this equation is given by

$$A^3 - P_A A^2 + Q_A A - R_A I = 0. \quad (\text{A.1})$$

Here, P_A , Q_A and R_A , respectively, are the first, second and third principal invariants of A (see Eq. (3.56)). According to Eq. (A.1), any expression involving third or higher powers of a 3×3 matrix can be written as a linear combination of terms containing lower powers of that matrix.

Rivlin (1955) generalized Eq. (A.1) to the relation

$$\begin{aligned} & ABC + ACB + BCA + BAC + CAB + CBA \\ & - A[\text{tr}(BC) - \text{tr}(B)\text{tr}(C)] - B[\text{tr}(CA) - \text{tr}(C)\text{tr}(A)] \\ & - C[\text{tr}(AB) - \text{tr}(A)\text{tr}(B)] - (BC + CB)\text{tr}(A) \\ & - (CA + AC)\text{tr}(B) - (AB + BA)\text{tr}(C) \\ & + I[\text{tr}(A)\text{tr}(B)\text{tr}(C) - \text{tr}(A)\text{tr}(BC) - \text{tr}(B)\text{tr}(CA) \\ & - \text{tr}(C)\text{tr}(AB) + \text{tr}(ABC) + \text{tr}(CBA)] = 0, \end{aligned} \quad (\text{A.2})$$

which holds for any three 3×3 matrices A, B and C . This *generalized Cayley–Hamilton theorem* may be used to reduce the powers in expressions involving products of different matrices.

A.2 The Gram–Schmidt orthogonalization process

As discussed in Section 4.4, the generalized Cayley–Hamilton theorem, Eq. (A.2), can be used to express all symmetric tensors (matrices) involving the rate-of-strain and rate-of-rotation tensors, S and W , in terms of the tensors of Eq. (4.3). Equation (A.2) cannot be used to establish any relations among these tensors.

We can, however, use the Gram–Schmidt orthogonalization process (see, e.g., Leon 2006) to show that not all the tensors of Eq. (4.3) are linearly independent. For the symmetric tensors of Eq. (4.3), this iterative orthogonalization process can be expressed as

$$T'^{(i)} = T^{(i)} - \sum_{j=0}^{i-1} \frac{\text{tr}(T^{(i)}T'^{(j)})}{\text{tr}(T'^{(j)}T'^{(j)})} T'^{(j)}, \quad (\text{A.3})$$

where the index i is to be increased from 1 to 10 in unit steps and we define $T'^{(0)} = T^{(0)}$. The prime in $T'^{(i)}$ indicates that this tensor is orthogonal to any $T'^{(j)}$, that is,

$$\text{tr}(T'^{(i)}T'^{(j)}) = 0, \quad (\text{A.4})$$

for $i \neq j$.

A.3 Basis tensor projections

To orthogonalize the tensors of Eq. (4.3) according to the Gram–Schmidt process of Eq. (A.3), we have to compute the projections

$$P_{(i),(j)} = \text{tr}(T^{(i)}T^{(j)}) \quad (\text{A.5})$$

for $0 \leq i, j \leq 10$. With the aid of the generalized Cayley–Hamilton theorem, Eq. (A.2), we can express these projections in terms of the invariants of Eq. (4.6). In particular, noting that $P_{(j),(i)} = P_{(i),(j)}$, we can express all nonzero projections through

$$\begin{aligned} P_{0,0} &= 3, & P_{8,5} &= \frac{1}{3}I_1I_2I_3 - 2I_3I_5, \\ P_{1,1} &= I_1, & P_{8,7} &= -I_1I_2I_5 - \frac{1}{3}I_2I_3I_4 + 4I_5^2, \\ P_{2,0} &= I_1, & P_{8,8} &= \frac{1}{2}I_1^3I_2 - 2I_1^2I_5 \\ & & & + \frac{4}{3}I_1I_3I_4 + \frac{1}{3}I_2I_3^2, \\ P_{2,1} &= I_3, & P_{9,0} &= 2I_5, \\ P_{2,2} &= \frac{1}{2}I_1^2, & P_{9,1} &= I_1I_4 + \frac{2}{3}I_2I_3, \\ P_{3,0} &= I_2, & P_{9,2} &= I_1I_5 + \frac{2}{3}I_3I_4, \\ P_{3,1} &= I_4, & P_{9,3} &= I_2I_5, \\ P_{3,2} &= I_5, & P_{9,4} &= 2I_6, \\ P_{3,3} &= \frac{1}{2}I_2^2, & P_{9,6} &= \frac{1}{2}I_1I_2I_4 + \frac{1}{2}I_2^2I_3 + 2I_4I_5, \\ P_{4,4} &= I_1I_2 - 6I_5, & P_{9,7} &= -2I_2I_6, \\ P_{5,4} &= -I_1I_4 - I_2I_3, & P_{9,8} &= 2I_1I_6, \\ P_{5,5} &= -\frac{1}{2}I_1^2I_2 + I_1I_5 - 2I_3I_4, & P_{9,9} &= \frac{1}{4}I_1^2I_2^2 - \frac{1}{2}I_1I_2I_5 \\ & & & + I_2I_3I_4 + 2I_5^2, \\ P_{6,0} &= 2I_4, \\ P_{6,1} &= 2I_5, \end{aligned} \quad (\text{A.6a})$$

$$\begin{aligned}
P_{6,2} &= I_1 I_4 + \frac{2}{3} I_2 I_3, & P_{10,1} &= 2I_6, \\
P_{6,3} &= I_2 I_4, & P_{10,4} &= \frac{1}{3} I_2^2 I_3 + 2I_4 I_5, \\
P_{6,5} &= -2I_6, & P_{10,5} &= \frac{1}{2} I_1^2 I_2^2 - 2I_1 I_2 I_5 \\
& & & \quad + \frac{4}{3} I_2 I_3 I_4 + 2I_5^2, \\
P_{6,6} &= -\frac{1}{2} I_1 I_2^2 + 3I_2 I_5 + 2I_4^2, & P_{10,6} &= 2I_2 I_6, \\
P_{7,2} &= -2I_6, & P_{10,7} &= -\frac{1}{6} I_2^3 I_3 - I_2 I_4 I_5, \\
P_{7,4} &= -I_1 I_2^2 + 4I_2 I_5 + 2I_4^2, & P_{10,8} &= -\frac{1}{2} I_1^2 I_2 I_4 + 2I_1 I_4 I_5 \\
P_{7,5} &= \frac{1}{3} I_2^2 I_3 + 2I_4 I_5, & & \quad + \frac{1}{3} I_2 I_3 I_5 - \frac{4}{3} I_3 I_4^2, \\
P_{7,7} &= \frac{1}{2} I_1 I_2^3 - 2I_2^2 I_5 - I_2 I_4^2, & P_{10,10} &= -\frac{1}{4} I_1^2 I_2^3 + I_1 I_2^2 I_5 \\
P_{8,3} &= 2I_6, & & \quad - \frac{2}{3} I_2^2 I_3 I_4 - I_2 I_5^2. \\
P_{8,4} &= I_1^2 I_2 - 4I_1 I_5 + 2I_3 I_4, & &
\end{aligned} \tag{A.6b}$$

A.4 Orthogonalized basis tensors

Working out the sum in Eq. (A.3) for $i = 1, 2, \dots, 10$ and using Eq. (A.6), we can show that the first six orthogonalized basis tensors corresponding to Eq. (4.3) are given by (Silvis and Verstappen 2015)

$$\begin{aligned}
T^{(0)} &= I, \\
T^{(1)} &= S, \\
T^{(2)} &= S^2 - \frac{I_1}{3} I - \frac{I_3}{I_1} S, \\
T^{(3)} &= W^2 - \frac{I_2}{3} I - \frac{I_4}{I_1} S - \frac{I_5 - \frac{I_1 I_2}{3} - \frac{I_3 I_4}{I_1}}{\frac{I_2^2}{6} - \frac{I_3^2}{I_1}} T^{(2)}, \\
T^{(4)} &= SW - WS, \\
T^{(5)} &= S^2 W - W S^2 - \frac{-I_1 I_4 - I_2 I_3}{I_1 I_2 - 6I_5} (SW - WS).
\end{aligned} \tag{A.7}$$

Moreover, we can show that the tensors $T^{(6)}$ and $T^{(7)}$ are zero, unless $T^{(2)}$ and $T^{(5)}$ vanish. In this latter case,

$$\begin{aligned}
T^{(6)} &= SW^2 + W^2 S - \frac{2I_4}{3} I - \frac{2I_5}{I_1} S - \frac{\frac{I_2 I_4}{3} - \frac{2I_4 I_5}{I_1}}{\frac{I_2^2}{6} - \frac{I_3^2}{I_1}} T^{(3)}, \\
T^{(7)} &= W S W^2 - W^2 S W - \frac{-I_1 I_2^2 + 4I_2 I_5 + 2I_4^2}{I_1 I_2 - 6I_5} (SW - WS).
\end{aligned} \tag{A.8}$$

Finally, the last three orthogonalized tensors are always zero, that is,

$$\begin{aligned}
T^{(8)} &= 0, \\
T^{(9)} &= 0, \\
T^{(10)} &= 0.
\end{aligned} \tag{A.9}$$

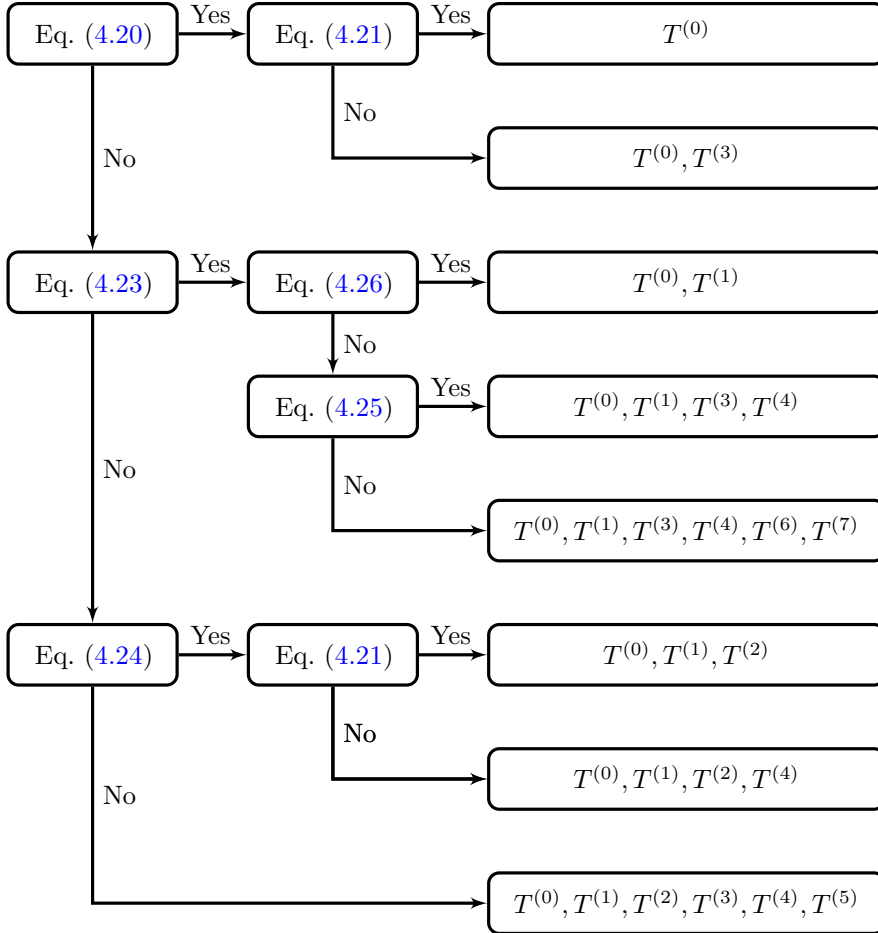


Figure A.1: Decision tree that shows which basis tensors of Eq. (4.3) are linearly independent for which flows. Special flows are given by Eq. (4.20): purely rotational flow; Eq. (4.21): pure shear flow; Eq. (4.23): axisymmetric strain; Eq. (4.24): the vorticity is aligned with one of the directions of principal strain; Eq. (4.25): the vorticity is perpendicular to the direction of the largest principal strain of an axisymmetric strain; Eq. (4.26): the vorticity is aligned with the direction of the largest principal strain of an axisymmetric strain.

A.5 Independence of the basis tensors

Equation (A.9) indicates that the tensors $T^{(8)}$, $T^{(9)}$ and $T^{(10)}$ can always be expressed in terms of the tensors $T^{(0)}$ to $T^{(7)}$. The former three tensors do, therefore, not provide an independent contribution to the sum of Eq. (4.4). Which of the tensors $T^{(0)}$ to $T^{(7)}$ form a linearly independent basis depends on the flow, as indicated by Fig. A.1. As this figure shows, at most six tensors of Eq. (4.3) are simultaneously linearly independent. The tensors $T^{(0)}$ to $T^{(5)}$ form a linearly independent basis for all but a few special flows.

Appendix B

Convergence of numerical results

In this appendix, we discuss how the numerical results of Chapter 10 depend on the spatial resolution that we used in our simulations.

B.1 Rotating decaying turbulence

We first discuss how our numerical predictions of decaying rotating turbulence vary with the spatial resolution. We will thereby confirm the grid convergence of the direct numerical simulations we presented in Section 10.3.2 and provide additional motivation for the choice of resolution of the large-eddy simulations of Sections 10.3.3 and 10.3.4.

B.1.1 Energy spectrum and turbulent kinetic energy

Figure B.1 shows predictions of the energy spectrum and turbulent kinetic energy of decaying homogeneous isotropic turbulence with initial Reynolds number $Re = 10\,129$ and rotation number $Ro = 0$. These results were obtained from (underresolved) direct numerical simulations on grids with 32^3 to 512^3 grid cells.

The energy spectra in Fig. B.1(a) show that a significant amount of energy piles up near the grid cutoff in the simulations with 32^3 and 64^3 grid cells (for which the cutoff is located at $k_C L_{\text{ref}}/(2\pi) = 16$ and 32 , respectively). Pile-up of energy occurs less, but is still visible, when a 128^3 resolution is employed. There is very little pile-up in the simulation with 256^3 grid cells. In addition, the simulations with 32^3 to 128^3 grid cells show a clear depletion of the energy of the large and/or intermediate scales of motion. This depletion does not occur at resolutions of 256^3 and 512^3 grid cells.

In addition, Fig. B.1(b) shows that not all the turbulent kinetic energy that is initially present in the flow of the experiment of Comte-Bellot and Corrsin (1971) can be resolved at low spatial resolutions. Only 62% of the initial turbulent kinetic energy is resolved when a 32^3 grid is used, whereas around 81% of this quantity is resolved in the simulation with 64^3 grid cells. As much as 99% of the initial turbulent kinetic energy is resolved in the simulation with a 512^3 grid. Figure B.1(b) also shows that less turbulent kinetic energy is dissipated in low-resolution numerical simulations of decaying turbulence than in simulations with a high spatial resolution.

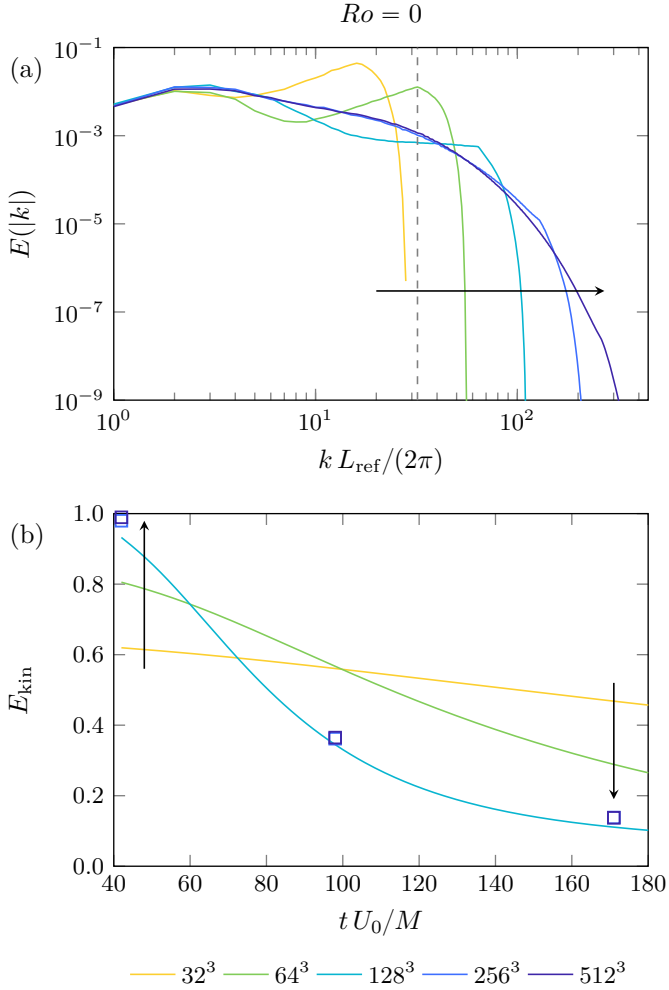


Figure B.1: Spatial resolution dependence of predictions of (a) the energy spectrum at time $t \approx 171M/U_0$ and (b) the resolved turbulent kinetic energy of decaying homogeneous isotropic turbulence with initial Reynolds number $Re = 10129$ and rotation number $Ro = 0$. Results were obtained from (underresolved) direct numerical simulations on grids with 32^3 to 512^3 grid cells. The vertical dashed line represents the 64^3 grid cutoff. Arrows indicate the direction of increasing spatial resolution.

B.1.2 Grid convergence of direct numerical simulations

Adding to the above, we see that the energy spectra obtained from the simulations with 256^3 and 512^3 grid cells practically collapse up to the 128^3 grid cutoff at $k_C L_{\text{ref}}/(2\pi) = 64$. Furthermore, on a 512^3 grid, the transition between the fully resolved part of the energy spectrum (before the grid cutoff at $k_C L_{\text{ref}}/(2\pi) = 256$) and the partially resolved part (after the cutoff) is rather smooth. Finally, the grid size in these simulations is only 3.5 times larger than the Kolmogorov length, close to the recommended value of 2 (Pope 2011).

The numerical simulation with 512^3 grid cells, therefore, provides predictions of decaying homogeneous isotropic turbulence that are accurate enough to reveal the typical behavior of rotating decaying turbulence and to serve as reference data for our large-eddy simulations. The numerical predictions of rotating decaying turbulence that we presented in Section 10.3.2 are also sufficiently accurate using a resolution of 512^3 grid cells.

B.1.3 Spatial resolution of large-eddy simulations

As remarked above, only around 60% of the initial turbulent kinetic energy is resolved in the decaying turbulence simulation with a 32^3 grid. This percentage is quite low in comparison with the 80% that is generally strived for in large-eddy simulations (Pope 2011). In addition, the transverse integral length scale initially has a wavenumber $k L_{\text{ref}}/(2\pi) \approx 23$ and can, therefore, not be resolved on a 32^3 grid (which has a grid cutoff $k_C L_{\text{ref}}/(2\pi) = 16$).

As such, (large) eddies of the size of this length scale cannot be resolved on this grid and a 32^3 grid must be judged as too coarse for large-eddy simulations of decaying turbulence. On the other hand, a 128^3 grid resolution seems too fine for large-eddy simulations. On such a grid, over 90% of the initial turbulent kinetic energy is resolved. Thus, little room is left for reduction of the computational cost with respect to a fully resolved simulation, especially if a subgrid-scale model is included.

With a spatial resolution of 64^3 grid cells around 80% of the initial turbulent kinetic energy of our test case of decaying turbulence is resolved. Also, both the longitudinal and transverse integral length scales, which form the characteristic size of the large eddies, can be resolved on this grid. Of the considered grid resolutions, a number of 64^3 grid cells, therefore, is most suitable for our large-eddy simulations of nonrotating decaying turbulence. As we start our simulations of rotating and nonrotating decaying turbulence with the same initial energy spectrum, a 64^3 grid resolution is also suitable for large-eddy simulations of rotating decaying turbulence.

B.2 Spanwise-rotating plane-channel flow

In this section, we discuss how our numerical predictions of spanwise-rotating plane-channel flow depend on the employed spatial resolution. We will thereby verify the accuracy of the direct numerical simulations of Section 10.4.2, we will

Table B.1: Grid resolutions, physical parameters and grid spacings in units of the viscous length scales of our (underresolved) direct numerical simulations of spanwise-rotating plane-channel flow with friction Reynolds number $Re_\tau \approx 395$ and friction rotation number $Ro_\tau = 100$.

N_1	N_2	N_3	Ro_b	Re_b	Re_τ	Re_τ^u	Re_τ^s	$\Delta x_1^{u,+}$	$\Delta x_1^{s,+}$	$\Delta x_2^{u,+}$	$\Delta x_2^{c,+}$	$\Delta x_2^{s,+}$	$\Delta x_3^{u,+}$	$\Delta x_3^{s,+}$
32	32	32	1.62	24 400	395	454	325	134	96	3.0	78	2.2	45	32
32	64	32	1.52	25 969	395	452	328	133	97	1.5	41	1.1	44	32
64	64	64	1.48	26 759	395	443	341	65	50	1.5	41	1.1	22	17
64	128	64	1.46	27 047	395	441	342	65	50	0.7	21	0.6	22	17
128	128	128	1.46	27 071	395	442	341	33	25	0.7	21	0.6	11	8
128	256	128	1.46	26 974	394	442	340	33	25	0.4	11	0.3	11	8
256	128	256	1.46	26 857	393	441	338	16	12	0.7	21	0.6	5	4
256	256	256	1.47	26 587	391	439	336	16	12	0.4	11	0.3	5	4

reason that coarse-grid numerical simulations of spanwise-rotating plane-channel flow with friction Reynolds number $Re_\tau \approx 395$ can benefit from subgrid-scale modeling and we will determine suitable spatial resolutions for large-eddy simulations of such a flow.

All results reported in this appendix were obtained from (underresolved) direct numerical simulations of spanwise-rotating plane-channel flow of domain size $3\pi d \times 2d \times \pi d$ with friction Reynolds number $Re_\tau \approx 395$ and friction rotation number $Ro_\tau = 100$. Grid resolutions range from 32^3 to 256^3 grid cells.

B.2.1 Physical parameters

Table B.1 shows the physical parameters as well as the grid spacings in units of the viscous length scales of our direct numerical simulations of spanwise-rotating plane-channel flow. A few important observations can be made from this table. First, the bulk rotation number Ro_b , which was defined in Eq. (10.10), tends to decrease as the grid resolution increases. At the same time, the bulk Reynolds number Re_b increases. Secondly, the friction Reynolds number corresponding to the unstable (stable) wall, is too high (low) for grids having $N_1 = N_3 = 32$ grid points in the streamwise and spanwise directions. Thirdly, the value of Re_τ lies within 0.5% of the desired value for all simulations with up to $256 \times 128 \times 256$ grid points.

Finally, given the recommended grid sizes for direct numerical and large-eddy simulations (Georgiadis et al. 2010; Choi and Moin 2012), the simulations with 32, 64, 128 and 256 grid points in the streamwise (x_1) and spanwise (x_3) directions can, respectively, be considered coarse large-eddy simulations, fine large-eddy simulations, coarse direct numerical simulations and fine direct numerical simulations. Not all these simulations are wall resolved, however. In the simulation with $N_2 = 32$ wall-normal grid points, the first grid point off the unstable wall is located at $\Delta x_2^{u,+} \approx 3.0$, which is larger than the recommended value of $\Delta x_2^{u,+} \approx 1.0$. For $N_2 = 64$, we see that $\Delta x_2^{u,+} \approx 1.5$. For the simulations we just referred to as direct numerical simulations, the first grid point is located close to the unstable wall at $\Delta x_2^{u,+} < 1.0$.

B.2.2 Mean streamwise velocity and Reynolds stresses

Figure B.2 shows predictions of the mean streamwise velocity and streamwise Reynolds stress anisotropy of spanwise-rotating plane-channel flow with friction Reynolds number $Re_\tau \approx 395$ and rotation number $Ro_\tau = 100$. As can be seen from Fig. B.2(a), the simulation with a spatial resolution of 32^3 grid cells leads to underprediction of the mean streamwise velocity profile as well as an incorrect prediction of the slope of this profile. An increase of the wall-normal resolution to $N_2 = 64$ grid cells improves the slope of the mean velocity profile. All the results with grid resolutions of 64^3 and higher lie very close to each other.

Figure B.2(b) shows that the simulations with 32^3 and $32 \times 64 \times 32$ grid cells severely overestimate the magnitude of the streamwise stress anisotropy in the unstable part of the channel. These simulations also predict a (large)

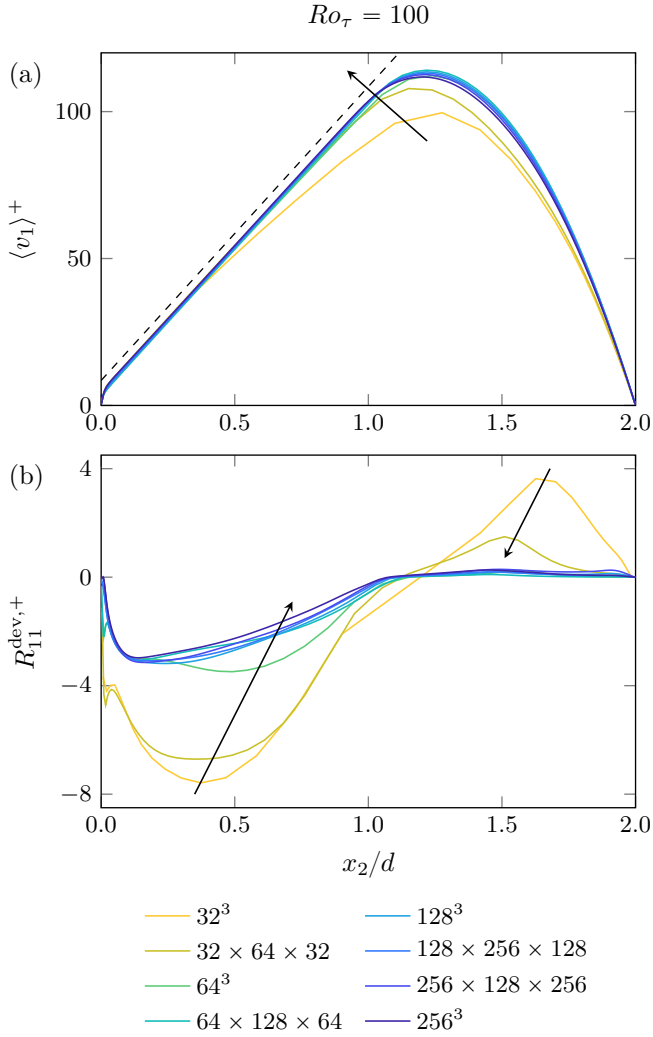


Figure B.2: Spatial resolution dependence of the dimensionless (a) mean streamwise velocity and (b) streamwise Reynolds stress anisotropy of spanwise-rotating plane-channel flow with friction Reynolds number $Re_\tau \approx 395$ and friction rotation number $Ro_\tau = 100$. Results were obtained from (underresolved) direct numerical simulations on grids with 32^3 to 256^3 grid cells. The dashed line has slope $Ro_\tau = 100$. Arrows indicate the direction of increasing spatial resolution.

nonzero streamwise stress anisotropy close to the stable wall. With a 64^3 grid, the magnitude of the streamwise stress anisotropy is slightly overestimated. All results obtained with resolutions between 128^3 and $256 \times 128 \times 256$ grid cells lie very close to each other. Predictions obtained with a 256^3 grid deviate a bit from the expected trend.

B.2.3 Convergence of direct numerical simulations

Since the predictions of spanwise-rotating plane-channel flow provided by simulations with 128^3 to $256 \times 128 \times 256$ grid cells lie very close to each other and as the friction Reynolds number computed from these simulations lies within 0.5% of $Re_\tau = 395$, the results from our fine wall-resolved direct numerical simulations on a $256 \times 128 \times 256$ grid have converged in terms of spatial resolution and time averaging. Therefore, the results obtained on a $256 \times 128 \times 256$ grid were chosen as the reference direct numerical simulation results in the current work.

B.2.4 Spatial resolution of large-eddy simulations

The above observations show that numerical simulations of spanwise-rotating plane-channel flow using 32^3 to 64^3 grid cells could benefit from the addition of a subgrid-scale model, even if the friction Reynolds number is only $Re_\tau \approx 395$. We, therefore, consider these resolutions suitable for our large-eddy simulations of spanwise-rotating plane-channel flow. Both simulations with 32^3 grid cells, for which the distance between the unstable wall and the first grid point is $\Delta x_2^{u,+} \approx 3.0$, and simulations with 64^3 grid cells, for which $\Delta x_2^{u,+} \approx 1.5$, can be expected to be challenging for subgrid-scale models.

Appendix C

Turbulent bursts and other flow instabilities

In this appendix, we provide more details regarding the turbulent instabilities that we observed in our numerical simulations of spanwise-rotating plane-channel flow and that we briefly discussed in Section 10.4.1. Figure C.1 shows the time dependence of the Reynolds shear stress and mean streamwise velocity of spanwise-rotating plane-channel flow at specific friction rotation numbers and for a different choice of the domain size than in Section 10.4.

C.1 Turbulent bursts

In particular, Fig. C.1(a) shows a sequence of short-time averages of the Reynolds shear stress of spanwise-rotating plane-channel flow with friction Reynolds number $Re_\tau \approx 395$, friction rotation number $Ro_\tau = 100$ and domain size $2\pi d \times 2d \times \pi d$. These results were obtained from direct numerical simulations on a $256 \times 128 \times 256$ grid. Each line corresponds to an average over $0.06 d/u_\tau$ time units. Between 0.25 and 1.50 time units elapse between the lines.

In contrast to the data that form the basis for the Reynolds shear stress shown in Fig. 10.8(b), the Reynolds shear stress in Fig. C.1(a) varies vigorously in time. Large peaks of high turbulence intensity develop close to and move away from what we referred to as the stable wall of the channel. These peaks have a magnitude that is even higher than the peaks of turbulence in the Reynolds shear stress of the nonrotating channel. The time it takes for the Reynolds shear stress to return to its initial, partly laminar state is approximately $3 d/u_\tau$ time units. It may take up to a $100 d/u_\tau$ time units before a similar cycle as shown here occurs again.

The behavior of the Reynolds stress shown in Fig. C.1(a) is caused by turbulent bursts (Brethouwer et al. 2014; Brethouwer 2016). These bursts do not seem to occur in our direct numerical simulations of spanwise-rotating channels having dimensions $3\pi d \times 2d \times \pi d$, while for a domain size of $2\pi d \times 2d \times \pi d$ we observed turbulent bursts for the rotation numbers $Ro_\tau = 25$ to 100.

C.2 Quasi-periodic collapse of the mean velocity

Figure C.1(b) shows a sequence of short-time averages of the mean streamwise velocity of a spanwise-rotating plane-channel flow with friction Reynolds number

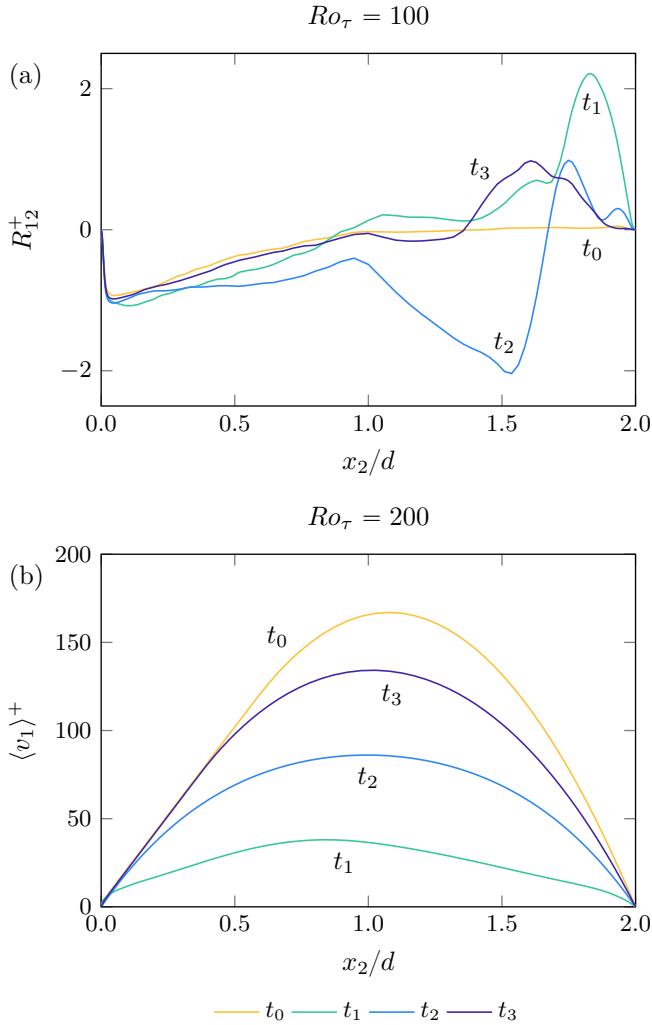


Figure C.1: Time dependence of flow instabilities in (a) the dimensionless Reynolds shear stress of spanwise-rotating plane-channel flow of size $2\pi d \times 2d \times \pi d$ with friction Reynolds number $Re_\tau \approx 395$ and friction rotation number $Ro_\tau = 100$ and (b) the dimensionless mean streamwise velocity of spanwise-rotating plane-channel flow of size $3\pi d \times 2d \times \pi d$ with friction Reynolds number $Re_\tau \approx 395$ and friction rotation number $Ro_\tau = 200$. Results were obtained from direct numerical simulations on $256 \times 128 \times 256$ and 128^3 grids, respectively. Labels indicate the direction of time.

$Re_\tau \approx 395$, friction rotation number $Ro_\tau = 200$ and domain size $3\pi d \times 2d \times \pi d$. These results were obtained from direct numerical simulations on a 128^3 grid. Each line corresponds to an average over $10 d/u_\tau$ time units. Between 70 and 90 time units elapse between the lines.

In contrast to the data underlying the mean velocity shown in Fig. 10.8(a), the results in Fig. C.1(b) significantly change in time. The mean streamwise velocity drastically reduces and slowly rises again over a period of approximately $280 d/u_\tau$ time units. This collapse of the mean velocity profile seems to be preceded and caused by a steady growth of turbulence close to the unstable wall of the channel. After the collapse, the mean velocity profile slowly recovers its original magnitude and shape. At the same time, the turbulence on the unstable side of the channel grows and can be expected to cause another collapse. Given the very slow time scale of this recurring collapse and recovery of the mean streamwise velocity, it seems likely that this process is caused by the quasi-periodic fluctuation of Taylor–Görtler vortices (Dai et al. 2016).

We observed this quasi-periodic collapse of the mean streamwise velocity for several rotation numbers $Ro_\tau \geq 150$ in numerical simulations of spanwise-rotating plane-channel flow of domain size $3\pi d \times 2d \times \pi d$. We did, however, not observe this collapse on $2\pi d \times 2d \times \pi d$ domains. Apparently, Taylor–Görtler vortices do not fit well on this domain size.

C.3 Impact on flow statistics

Although turbulent bursts occur infrequently, their magnitude is so large that they lead to peaks in long-time averages of the Reynolds shear stress. Similarly, the mean velocity and diagonal Reynolds stresses of rotating channel flows can be affected significantly by turbulent bursts. We previously observed a multi-peak structure in the diagonal Reynolds stresses in the stable region of the channel (Silvis and Verstappen 2019). Thereby, turbulent bursts complicate taking time averages in numerical simulations.

Turbulent bursts are particularly troubling for simulations with a constant-pressure-gradient forcing. A turbulent burst locally increases the wall shear stress at the stable wall of the channel. Since the constant-pressure-gradient forcing aims to set a global friction Reynolds number, the wall shear stress at the unstable wall then has to decrease. A turbulent burst on the stable side of the channel, thus, influences the flow over the entire channel. Removing a turbulent burst from the stored time-averaged data is not only difficult, it also has a significant negative effect on the convergence to the desired global friction Reynolds number. Moreover, since turbulent bursts occur at irregular moments in time, comparing results of different simulations becomes impossible.

As is the case with turbulent bursts, the observed quasi-periodic collapse has a significant impact on flow statistics. As we reasoned in Section 10.4.1, we should, therefore, choose the domain length of the spanwise-rotating plane-channel flows in such a way that neither of the two discussed turbulent instabilities occurs in numerical simulations.

List of acronyms

General acronyms

Acronym	Meaning	Page
2C	Two component	90
2DMFI	Two-dimensional material frame indifference	41
3D	Three dimensional	90
3DMFI	Three-dimensional material frame indifference	43
CFD	Computational fluid dynamics	5
DNS	Direct numerical simulation	5
LES	Large-eddy simulation	6
RANS	Reynolds-averaged Navier–Stokes	6
SFS	Subfilter-scale	27
SGS	Subgrid-scale	6

Model acronyms

Acronym	Meaning	Page
AMD	Anisotropic minimum-dissipation model	86
DS	Dynamic Smagorinsky model	138
EASSM	Explicit algebraic subgrid-scale stress model	87
SAMD	Scaled anisotropic minimum-dissipation model	138
SAMD NL	Scaled anisotropic minimum-dissipation model with a nonlinear model term	138
VS EV1	Vortex-stretching based eddy viscosity model with $C_v^2 \approx 0.34$	138
VS EV2	Vortex-stretching based eddy viscosity model with $C_v^2 \approx 0.17$	138
VS NL	Vortex-stretching-based nonlinear model	138

List of symbols

Latin symbols

Symbol	Meaning	Reference
A_{ij}	Matrix	App. A.1
a	Scaling transformation parameter	Eq. (3.6)
B_{ij}	Matrix	App. A.1
b	Scaling transformation parameter	Eq. (3.13)
$C^{(i)}$	Model constant	Eq. (4.5)
C_M	Model constant of model with label M	Sec. 5.2
C_{ij}	Matrix	App. A.1
$c^{(i)}$	Constant	Sec. 4.6.7
C_{δ}	Poincaré constant	Eq. (3.39)
C_{μ}	Model constant of nonlinear model term	Eq. (9.8)
C_{ν}	Model constant of eddy viscosity term	Eq. (9.5)
D^e	True or subfilter dissipation of enstrophy	Eq. (3.42)
$D^{e,\text{mod}}$	Modeled or subgrid dissipation of enstrophy	Eq. (3.43)
D^h	True or subfilter dissipation of helicity	Eq. (3.49)
$D^{h,\text{mod}}$	Modeled or subgrid dissipation of helicity	Eq. (3.50)
D^k	True or subfilter dissipation of kinetic energy	Eq. (3.34)
$D^{k,\text{mod}}$	Modeled or subgrid dissipation of kinetic energy	Eq. (3.35)
$D_M^{k,\text{mod}}$	Subgrid dissipation of kinetic energy of model with label M	Eq. (5.13)
d	Plane-channel half-width	Eq. (10.4)
$E(k)$	Three-dimensional energy spectrum	Sec. 10.3.1
E_{kin}	Turbulent kinetic energy per unit mass	Eq. (10.2)
$E_{\text{kin},C}$	Turbulent kinetic up to the grid cutoff	Eq. (10.3)
e	Short-hand for $e(v)$	Eq. (1.81)
$e(u)$	Enstrophy density	Eq. (1.52)
$e(v)$	Enstrophy density of large-scale velocity field	Eq. (1.81)
F	Scalar potential	Eq. (1.14)
f	Arbitrary function	
f_{VS}	Normalized vortex stretching magnitude	Eq. (9.7)
f_i	Body force	Eq. (1.7)
$f^{(i)}$	Arbitrary function	
$G(\square)$	Filter kernel	Eq. (1.68)
G_{ij}	Short-hand for $G_{ij}(v)$	Eq. (1.80)
$G_{ij}(u)$	Velocity gradient	Eq. (1.18)
$G_{ij}(v)$	Large-scale velocity gradient	Eq. (1.80)
g	Arbitrary function	

Symbol	Meaning	Reference
g	Gravitational acceleration	Sec. 1.2.5
h	Short-hand for $h(v)$	Eq. (1.81)
$h(u)$	Helicity density	Eq. (1.53)
$h(v)$	Helicity density of large-scale velocity field	Eq. (1.81)
I	Identity matrix	Eq. (3.58)
$I_{(i)}$	Combined invariant of the rate-of-strain and rate-of-rotation tensors	Eq. (4.6)
J	Invariant used in the WALE model	Eq. (5.2)
k	Short-hand for $k(v)$	Eq. (1.81)
k	Wavenumber	Sec. 10.3.1
$k(u)$	Kinetic energy per unit mass	Eq. (1.51)
$k(v)$	Kinetic energy per unit mass of large-scale velocity field	Eq. (1.81)
k_i	Eigenvalue of turbulent stress tensor	Eq. (3.56)
k_C	Wavenumber of the grid cutoff	Eq. (10.3)
k_t	Generalized subfilter-scale kinetic energy	Eq. (3.57)
k_t^{mod}	Model for the generalized subfilter-scale kinetic energy	Eq. (3.58)
L	Length	Eq. (1.62)
L	Longitudinal integral length scale	Sec. 10.3.1
L_i	Domain size in the x_i -direction	Sec. 10.4.1
L_{ref}	Reference length scale	Eq. (1.16)
M	Mesh size of turbulence-generating grid	Sec. 10.3.1
N_i	Number of grid points in the x_i -direction	Eq. (10.11)
n_i	Outward-pointing unit normal of control volume	Eq. (1.1)
$P(u)$	Probability density function	Eq. (1.55)
$P(t)$	Time variation of the (background) pressure	Eq. (3.3)
P_A	First principal invariant of a matrix A	Eq. (3.56)
$P_{(i),(j)}$	Basis tensor projections	Eq. (A.5)
p	Pressure	Eq. (1.12)
p	S3PQR model parameter	Eq. (5.6)
\bar{p}	Filtered pressure	Eq. (1.74)
$\langle p \rangle$	Mean pressure	Eq. (1.63)
$Q_{(n)}$	Set of flow types for which $G_{ij}(u)$ has n zero elements	Table 5.2
Q_A	Second principal invariant of a matrix A	Eq. (3.56)
Q_{ij}	Orthogonal matrix	Eq. (3.5)
$Q_{ij}(t)$	Possibly time-dependent rotation matrix	Eq. (1.36)
q	Large-scale pressure	Eq. (1.76)
R_A	Third principal invariant of a matrix A	Eq. (3.56)
R_{ij}	Short-hand for $R_{ij}(v)$	Eq. (1.81)
$R_{ij}(u)$	Reynolds stress tensor	Eq. (1.65)
$R_{ij}(v)$	Reynolds stress tensor of resolved velocity field	Eq. (1.81)
Re	Reynolds number	Eq. (1.34)

Symbol	Meaning	Reference
Re_b	Bulk Reynolds number	Eq. (10.10)
Re_L	Reynolds number based on integral length scale	Sec. 10.3.1
Re_λ	Reynolds number based on Taylor microscale	Sec. 10.3.1
Re_τ	Reynolds number based on friction velocity	Eq. (10.4)
Ro	Rotation number	Eq. (1.44)
Ro_b	Bulk rotation number	Eq. (10.10)
Ro_L	Rotation number based on integral length scale	Sec. 10.3.1
Ro_λ	Rotation number based on Taylor microscale	Sec. 10.3.1
Ro_τ	Rotation number based on friction velocity	Eq. (10.4)
r	Constant	Sec. 3.7.2
S	Surface of control volume	Eq. (1.1)
S_{ij}	Short-hand for $S_{ij}(v)$	Eq. (1.80)
$S_{ij}(u)$	Rate-of-strain tensor	Eq. (1.25)
$S_{ij}(\bar{u})$	Filtered rate-of-strain tensor	Eq. (1.74)
$S_{ij}(\langle u \rangle)$	Mean rate-of-strain tensor	Eq. (1.64)
$S_{ij}(v)$	Large-scale rate-of-strain tensor	Eq. (1.76)
s	Constant	Sec. 3.7.2
T	Time interval	Eq. (1.61)
T	Time shift	Eq. (3.2)
$T_{ij}^{(k)}$	Basis tensor	Eq. (4.3)
t	Time coordinate	Eq. (1.1)
U_0	Initial mean velocity	Sec. 10.3.1
U_b	Bulk velocity	Eq. (10.9)
u	Arbitrary function of space and time	Eq. (1.67)
u	Random variable	Eq. (1.55)
u_i	Velocity field	Eq. (1.1)
\bar{u}_i	Filtered velocity field	Eq. (1.74)
$\langle u_i \rangle$	Mean velocity field	Eq. (1.54)
u'_i	Fluctuating velocity field	Eq. (1.54)
u_{ref}	Reference velocity scale	Eq. (1.16)
u_τ	Friction velocity	Eq. (10.4)
V	(Control) volume	Eq. (1.1)
$V_{\bar{\delta}}$	(Control) volume characterized by $\bar{\delta}$	Eq. (3.39)
v	Random variable	Eq. (1.58)
v_i	Large-scale or resolved velocity field	Eq. (1.76)
\bar{v}_i	Velocity averaged over $V_{\bar{\delta}}$	Eq. (3.39)
$\langle v_i \rangle$	Average resolved velocity field	Eq. (10.6)
W_{ij}	Short-hand for $W_{ij}(v)$	Eq. (1.80)
$W_{ij}(u)$	Rate-of-rotation tensor	Eq. (1.26)
$W_{ij}(v)$	Large-scale rate-of-rotation tensor	Eq. (1.80)
$X_i(t)$	Spatial translation	Eq. (3.4)
x_i	Spatial coordinates	Sec. 1.2.2

Greek symbols

Symbol	Meaning	Reference
$\alpha_{(i)}$	Model coefficient	Eq. (4.5)
γ	Grid stretching parameter	Eq. (10.11)
Δ	Uniform grid size	Sec. 10.3.1
Δt	Time step size	Sec. 10.4.1
Δx_i	Grid size in x_i -direction	Eq. (9.13)
δ	Subgrid characteristic length scale	Sec. 3.6.7
$\bar{\delta}$	Filter length (bar)	Eq. (1.70)
$\tilde{\delta}$	Length scale (tilde)	Sec. 3.6.7
$\delta_{(i)}$	Subgrid characteristic length scale	Eq. (4.5)
δ_{ij}	Kronecker delta	Eq. (1.10)
ϵ_{ijk}	Levi-Civita symbol or alternating tensor	Eq. (1.38)
λ	Transverse Taylor microscale	Sec. 10.3.1
μ	Dynamic viscosity	Eq. (1.24)
μ_e	Coefficient of nonlinear model term	Eq. (9.8)
$\mu_{(i)}$	Scalar related to μ_{ijkl}	Eq. (1.20)
μ_{ijkl}	Viscosity coefficient	Eq. (1.19)
ν	Kinematic viscosity	Eq. (1.30)
ν_e	Eddy viscosity	Eq. (4.1)
ν_e^M	Eddy viscosity of model with label M	Sec. 5.2
ρ	Mass density	Eq. (1.1)
σ_i	Singular value of G_{ij}	Eq. (5.4)
σ_{ij}	Stress tensor	Eq. (1.7)
τ_{ij}	Short-hand for $\tau_{ij}(u)$	Eq. (1.79)
$\tau_{ij}(u)$	Turbulent stress tensor	Eq. (1.75)
τ_{ij}^{mod}	Short-hand for $\tau_{ij}^{\text{mod}}(v)$	Eq. (1.80)
$\tau_{ij}^{\text{mod}}(v)$	Turbulence or subgrid-scale (stress) model	Eq. (1.76)
ψ	Two-dimensional stream function	Eq. (3.7)
Ω_i	Rotation rate about the x_i -axis	Sec. 1.2.7
ω_i	Short-hand for $\omega_i(v)$	Eq. (1.81)
$\omega_i(u)$	Vorticity	Eq. (1.50)
$\omega_i(\bar{u})$	Filtered vorticity	Eq. (3.42)
$\omega_i(v)$	Large-scale vorticity	Eq. (1.81)

Subscripts and superscripts

Symbol	Meaning	Reference
*	Dimensionless quantity (asterisk)	Eq. (1.16)
+	Quantity in units of the friction velocity (plus)	Sec. 10.4.1
2D	Two dimensional	Sec. 1.2.7
3D	Three dimensional	Eq. (3.14)

Symbol	Meaning	Reference
b	Bulk	Eq. (10.9)
C	Cutoff	Eq. (10.3)
c	Center	Sec. 10.4.1
centr	Centrifugal	Eq. (1.41)
Cor	Coriolis	Eq. (1.49)
dev	Deviatoric part of tensor	Eq. (1.11)
e	Eddy (viscosity)	Eq. (4.1)
<i>i</i>	Index	Sec. 1.2
<i>j</i>	Index	Sec. 1.2
<i>k</i>	Index	Sec. 1.2
kin	Kinetic	Eq. (10.2)
<i>l</i>	Index	Sec. 1.2
<i>m</i>	Index	Sec. 1.2
mod	Model	Eq. (1.76)
<i>n</i>	Index	Sec. 1.2
ref	Reference	Eq. (1.16)
s	Stable	Eq. (10.6)
<i>T</i>	Transpose of a matrix	Eq. (5.8)
t	Turbulent	Eq. (3.57)
u	Unstable	Eq. (10.6)
visc	Viscous	Eq. (1.19)

Model subscripts and superscripts

Symbol	Meaning	Reference
A	Anisotropic minimum-dissipation model	Eq. (5.7)
E	Explicit algebraic subgrid-scale stress model	Eq. (5.12)
G	Gradient model	Eq. (5.11)
GA	Generalized anisotropic minimum-dissipation model	Eq. (6.8)
GS	Generalized Smagorinsky or Lund–Novikov model	Eq. (6.2)
GQR	Generalized QR model	Eq. (6.3)
GS3	Generalized S3PQR model	Eq. (6.4)
QG	Q_G model	Eq. (6.9)
QR	QR model	Eq. (5.5)
RG	R_G model	Eq. (6.10)
S	Smagorinsky model	Eq. (5.1)
S3	S3PQR model	Eq. (5.6)
V	Vreman’s model	Eq. (5.3)
VS	Vortex-stretching-based model	Eq. (6.11)
W	WALE model	Eq. (5.2)
σ	σ model	Eq. (5.4)

Model constraints

Symbol	Meaning	Reference
B1–B3	Symmetry breaking requirements	Eq. (3.15)
C1–C5	Conservation requirements	Sec. 3.5.2
D1–D18	Dissipation requirements	Sec. 3.6
N	Near-wall scaling requirements	Eq. (3.67)
R	Realizability requirements	Sec. 3.7.2
S1–S6	Symmetry requirements	Eq. (3.8)
U	Dimensional requirements	Eq. (3.1)

Accents and operators

Symbol	Meaning	Reference
$\hat{\square}$	Transformed quantity (hat)	Eq. (1.35)
$\bar{\square}$	Filtered quantity (bar)	Eq. (1.67)
$\tilde{\square}$	Average over $V_{\tilde{\delta}}$ (tilde)	Eq. (3.39)
$\dot{\square}$	First derivative with respect to time (dot)	Eq. (1.37)
$\ddot{\square}$	Second derivative with respect to time (double dot)	Eq. (1.37)
$\vec{\square}$	Vector (arrow)	Eq. (1.67)
\square'	Alternative quantity (prime)	Eq. (1.67)
\square'	Fluctuating quantity (prime)	Eq. (1.59)
\square'	Subfilter-scale or fluctuating quantity (prime)	Eq. (1.71)
$\langle \square \rangle$	Reynolds average (angle brackets)	Eq. (1.55)
$\langle \square \rangle$	Average in time and/or over homogeneous spatial directions (angle brackets)	Eq. (10.6)
$[\square]$	Physical units of a quantity (square brackets)	Eq. (3.1)
$ \square $	Magnitude of a vector or Frobenius norm of a matrix (pipes)	Eq. (4.10)
$\square \cdot \square$	Inner or dot product of two vectors (dot)	Eq. (4.9)
$\square \times \square$	Outer or cross product of two vectors (cross)	Eq. (4.9)
$\det(\square)$	Determinant of a matrix	Eq. (3.56)
$\mathcal{O}(\square)$	Near-wall scaling order	Eq. (3.64)
$\text{tr}(\square)$	Trace of a matrix	Eq. (3.56)

List of publications

Peer-reviewed journal publications

3. Trias, F. X., Gorobets, A., Silvis, M. H., Verstappen, R. W. C. P., and Oliva, A. (2017). “A new subgrid characteristic length for turbulence simulations on anisotropic grids”. *Phys. Fluids* 29, 115109. DOI: [10.1063/1.5012546](https://doi.org/10.1063/1.5012546).
2. Silvis, M. H., Remmerswaal, R. A., and Verstappen, R. (2017). “Physical consistency of subgrid-scale models for large-eddy simulation of incompressible turbulent flows”. *Phys. Fluids* 29, 015105. DOI: [10.1063/1.4974093](https://doi.org/10.1063/1.4974093).
1. Bloemsmas, E. A., Silvis, M. H., Stradomska, A., and Knoester, J. (2016). “Vibronic effects and destruction of exciton coherence in optical spectra of J-aggregates: A variational polaron transformation approach”. *Chem. Phys.* 481, pp. 250–261. DOI: [10.1016/j.chemphys.2016.06.018](https://doi.org/10.1016/j.chemphys.2016.06.018).

Preprints

5. Silvis, M. H. and Verstappen, R. (n.d. b). “Creating physics-based subgrid-scale models for large-eddy simulation”. (in preparation).
4. Silvis, M. H. and Verstappen, R. (n.d. a). “Velocity-gradient-based representations for incompressible turbulent flows”. (in preparation).
3. Streher, L. B., Silvis, M. H., Cifani, P., and Verstappen, R. W. C. P. (2020). “Mixed modeling for large-eddy simulation: The single-layer and two-layer minimum-dissipation-Bardina models”. arXiv: [2006.08516 \[physics.flu-dyn\]](https://arxiv.org/abs/2006.08516).
2. Silvis, M. H., Bae, H. J., Trias, F. X., Abkar, M., and Verstappen, R. (2019). “A nonlinear subgrid-scale model for large-eddy simulations of rotating turbulent flows”. arXiv: [1904.12748 \[physics.flu-dyn\]](https://arxiv.org/abs/1904.12748).
1. Silvis, M. H. and Verstappen, R. (2015). “Physically consistent subgrid-scale models for large-eddy simulation of incompressible turbulent flows”. arXiv: [1510.07881 \[physics.flu-dyn\]](https://arxiv.org/abs/1510.07881).

Peer-reviewed conference proceedings

5. Streher, L. B., Silvis, M. H., and Verstappen, R. (2018). “Mixed modeling for large-eddy simulation: The minimum-dissipation-Bardina-model”. In: *Proceedings of the 7th European Conference on Computational Fluid*

- Dynamics*. Ed. by Owen, R., De Borst, R., Reese, J., and Pearce, C. International Center for Numerical Methods in Engineering, Barcelona, Spain, pp. 335–345.
4. Silvis, M. H. and Verstappen, R. (2019). “Nonlinear Subgrid-Scale Models for Large-Eddy Simulation of Rotating Turbulent Flows”. In: *Direct and Large-Eddy Simulation XI*. ed. by Salvetti, M. V., Armenio, V., Fröhlich, J., Geurts, B. J., and Kuerten, H. Springer International Publishing, pp. 129–134. DOI: [10.1007/978-3-030-04915-7_18](https://doi.org/10.1007/978-3-030-04915-7_18).
 3. Silvis, M. H. and Verstappen, R. (2018). “Constructing Physically Consistent Subgrid-Scale Models for Large-Eddy Simulation of Incompressible Turbulent Flows”. In: *Turbulence and Interactions: Proceedings of the TI 2015 Conference*. Ed. by Deville, M. O., Couaillier, V., Estivalezes, J.-L., Gleize, V., Lê, T.-H., Terracol, M., and Vincent, S. Springer International Publishing, pp. 241–247. DOI: [10.1007/978-3-319-60387-2_26](https://doi.org/10.1007/978-3-319-60387-2_26).
 2. Silvis, M. H., Remmerswaal, R. A., and Verstappen, R. (2017). “A Framework for the Assessment and Creation of Subgrid-Scale Models for Large-Eddy Simulation”. In: *Progress in Turbulence VII: Proceedings of the iTi Conference in Turbulence 2016*. Ed. by Örlü, R., Talamelli, A., Oberlack, M., and Peinke, J. Springer International Publishing, pp. 133–139. DOI: [10.1007/978-3-319-57934-4_19](https://doi.org/10.1007/978-3-319-57934-4_19).
 1. Silvis, M. H., Trias, F. X., Abkar, M., Bae, H. J., Lozano-Durán, A., and Verstappen, R. W. C. P. (2016). “Exploring nonlinear subgrid-scale models and new characteristic length scales for large-eddy simulation”. In: *Studying Turbulence Using Numerical Simulation Databases - XVI: Proceedings of the 2016 Summer Program*. Ed. by Moin, P. and Urzay, J. Center for Turbulence Research, Stanford University, pp. 265–274.

Popular science writing

1. Silvis, M. (2015). “Osborne Reynolds: On the phenomenon of turbulence”. *Periodiek. Magazine of the FMF, student association for Physics and Mathematics, University of Groningen* 3, pp. 14–17. URL: http://perio.fmf.nl/archief/perio_2015-3.pdf#page=14.

Reports

2. Silvis, M. H. (2012). “Signatures of exciton-phonon coupling in linear absorption spectra of molecular aggregates: A polaron transformation approach”. Master’s thesis. University of Groningen, The Netherlands.
1. Silvis, M. H. (2010). “A quaternion formulation of the Dirac equation”. Bachelor’s thesis. University of Groningen, The Netherlands.

List of presentations

International conference presentations

13. Streher, L. B., Silvis, M. H., and Verstappen, R. (2018). “Mixed modeling for large-eddy simulation: The minimum-dissipation-Bardina model”. *7th European Conference on Computational Fluid Dynamics*, Glasgow, United Kingdom, June 11–15, 2018.
12. Silvis, M. H. and Verstappen, R. (2018). “Symmetry constraints for the modeling and numerical simulation of turbulent flows”. *Symmetry and Computation*, Marseille, France, April 3–7, 2018.
11. Silvis, M. H. and Verstappen, R. (2017). “A new turbulence model for large-eddy simulations of rotating flows”. *International Workshop on Complex Turbulent Flows*, Tangier, Morocco, November 27–28, 2017.
10. Trias, F. X., Gorobets, A., Silvis, M. H., Verstappen, R. W. C. P., and Oliva, A. (2017). “A new subgrid characteristic length for large-eddy simulation”. *International Workshop on Complex Turbulent Flows*, Tangier, Morocco, November 27–28, 2017.
9. Silvis, M. H., Bae, H. J., Trias, F. X., Abkar, M., Moin, P., and Verstappen, R. (2017). “Subgrid-scale models for large-eddy simulation of rotating turbulent channel flows”. *70th Annual Meeting of the APS Division of Fluid Dynamics*, Denver, Colorado, United States of America, November 19–21, 2017.
8. Silvis, M. H., Trias, F. X., and Verstappen, R. (2017). “New subgrid-scale models and characteristic length scales for large-eddy simulation of rotating turbulent flows”. *16th European Turbulence Conference*, Stockholm, Sweden, August 21–24, 2017.
7. Silvis, M. H. and Verstappen, R. (2017). “Nonlinear subgrid-scale models for large-eddy simulation of rotating turbulent flows”. *Direct and Large-Eddy Simulation XI*, Pisa, Italy, May 29–31, 2017.
6. Silvis, M., Trias, X., Abkar, M., Bae, H. J., Lozano-Durán, A., and Verstappen, R. (2016). “Subgrid-scale models for large-eddy simulation of rotating turbulent flows”. *69th Annual Meeting of the APS Division of Fluid Dynamics*, Portland, Oregon, United States of America, November 20–22, 2016.
5. Silvis, M., Remmerswaal, R., and Verstappen, R. (2016). “A framework for the assessment and creation of subgrid-scale models for large-eddy

- simulation”. *7th Interdisciplinary Turbulence Initiative Conference on Turbulence*, Bertinoro, Italy, September 7–9, 2016.
4. Verstappen, R. and Silvis, M. (2015). “Scale-truncating relaxation models for large eddy simulations”. *68th Annual Meeting of the APS Division of Fluid Dynamics*, Boston, Massachusetts, United States of America, November 22–24, 2015.
 3. Silvis, M. and Verstappen, R. (2015). “Physically-consistent subgrid-scale models for large-eddy simulation of incompressible turbulent flows”. *4th International Conference on Turbulence and Interactions*, Cargèse, France, November 2–6, 2015.
 2. Silvis, M. and Verstappen, R. (2015). “Going beyond eddy viscosity: Finding a minimal representation of subgrid-scale stresses in large-eddy simulation”. *15th European Turbulence Conference*, Delft, The Netherlands, August 25–28, 2015.
 1. Silvis, M. H., Verstappen, R. W. C. P., and Veldman, A. E. P. (2014). “The higher-order gradient model for large-eddy simulation of turbulent flows”. *6th European Conference on Computational Fluid Dynamics*, Barcelona, Spain, July 20–25, 2014.

International workshop presentations

2. Silvis, M., Trias, F. X., Abkar, M., Bae, H. J., Lozano-Durán, A., and Verstappen, R. (2016). “Exploring nonlinear subgrid-scale models and new characteristic length scales for large-eddy simulation”. *CTR Summer Program 2016*, Center for Turbulence Research, Stanford University, Stanford, California, United States of America, June 26 – July 22, 2016.
1. Silvis, M., Verstappen, R., and Veldman, A. (2014). “The higher-order gradient model for large-eddy simulation of turbulent flows”. *Mathematics of Turbulence*, Institute for Pure and Applied Mathematics, University of California, Los Angeles, United States of America, September 8 – December 12, 2014.

Presentations during national meetings

3. Silvis, M. and Verstappen, R. (2017). “Subgrid-scale modeling for large-eddy simulation of rotating channel flows”. *Turbulence Contact Day*, J. M. Burgerscentrum, Delft, The Netherlands, October 27, 2017.
2. Silvis, M. and Verstappen, R. (2016). “Physically consistent turbulence models for large-eddy simulation”. *Burgers Symposium 2016*, Lunteren, The Netherlands, June 16–17, 2016.

1. Silvis, M., Verstappen, R., and Veldman, A. (2015). “Going beyond eddy viscosity: Finding a general representation of subgrid-scale stresses in large-eddy simulation”. *Turbulence Contact Day*, J. M. Burgerscentrum, Delft, The Netherlands, June 12, 2015.

Presentations during scientific visits

2. Silvis, M., Remmerswaal, R., and Verstappen, R. (2017). “Physical consistency of subgrid-scale models for large-eddy simulation”. Chair of Fluid Dynamics, Technical University of Darmstadt, Darmstadt, Germany, February 14, 2017.
1. Silvis, M. and Verstappen, R. (2016). “Physical consistency of subfilter-scale models for large-eddy simulation of incompressible turbulent flows”. Heat and Mass Transfer Technological Center, Technical University of Catalonia, Terrassa, Spain, January 25–29, 2016.

Poster presentations during international conferences

2. Silvis, M. H. and Verstappen, R. (2018). “Symmetries and conservation laws as constraints for the modeling and numerical simulation of turbulent flows”. *Symmetry and Computation*, Marseille, France, April 3–7, 2018.
1. Silvis, M. H., Bloemsma, E. A., Stradomska, A. U., and Knoester, J. (2012). “Spectral signatures of exciton-phonon coupling in molecular aggregates: A polaron transformation approach”. *10th International Conference on Excitonic Processes in Condensed Matter, Nanostructured and Molecular Materials*, Groningen, The Netherlands, July 2–6, 2012.

Poster presentations during international workshops

1. Silvis, M. H. and Verstappen, R. W. C. P. (2014). “How to model subgrid-scale effects on large-scale energy distribution in large-eddy simulation of turbulent flows?” *Mathematics of Turbulence*, Institute for Pure and Applied Mathematics, University of California, Los Angeles, United States of America, September 8 – December 12, 2014.

Poster presentations during national meetings

3. Silvis, M. H. and Verstappen, R. W. C. P. (2015). “Symmetry-preserving subgrid-scale models for large-eddy simulation of turbulent flows”. *40th Woudschoten Conference*, Zeist, The Netherlands, October 7–9, 2015.
2. Silvis, M. H. and Verstappen, R. W. C. P. (2015). “Going beyond eddy viscosity: Finding a minimal representation of subgrid-scale stresses in

large-eddy simulation”. *Burgers Day*, J. M. Burgerscentrum, Delft, The Netherlands, January 15, 2015.

1. Bloemsma, E. A., Silvis, M. H., Malyshev, V. A., and Knoester, J. (2012). “Exciton Dynamics in Coupled Molecular Aggregates”. *Physics @ FOM*, Veldhoven, The Netherlands, January 17–18, 2012.

Bibliography

- Alexakis, A. and Biferale, L. (2018). “Cascades and transitions in turbulent flows”. *Phys. Rep.* 767–769, pp. 1–101. DOI: [10.1016/j.physrep.2018.08.001](https://doi.org/10.1016/j.physrep.2018.08.001).
- Anco, S. C. and Cheviakov, A. F. (2020). “On the different types of global and local conservation laws for partial differential equations in three spatial dimensions: Review and recent developments”. *Int. J. Nonlin. Mech.* 126, 103569. DOI: [10.1016/j.ijnonlinmec.2020.103569](https://doi.org/10.1016/j.ijnonlinmec.2020.103569).
- Anco, S. C. and Webb, G. M. (2020). “Hierarchies of new invariants and conserved integrals in inviscid fluid flow”. *Phys. Fluids* 32, 086104. DOI: [10.1063/5.0011649](https://doi.org/10.1063/5.0011649).
- Bardina, J., Ferziger, J. H., and Reynolds, W. C. (1983). *Improved Turbulence Models Based on Large Eddy Simulation of Homogeneous, Incompressible, Turbulent Flows*. Technical Report TF-19. Stanford University.
- Bardina, J., Ferziger, J. H., and Rogallo, R. S. (1985). “Effect of rotation on isotropic turbulence: computation and modelling”. *J. Fluid Mech.* 154, pp. 321–336. DOI: [10.1017/S0022112085001550](https://doi.org/10.1017/S0022112085001550).
- Barré de Saint-Venant, A. J. C. (1843). “Note à joindre au mémoire sur la dynamique des fluides”. *Compt. Rend.* 17, pp. 1240–1244.
- Beddhu, M., Taylor, L. K., and Whitfield, D. L. (1996). “Strong Conservative Form of the Incompressible Navier–Stokes Equations in a Rotating Frame with a Solution Procedure”. *J. Comput. Phys.* 128, pp. 427–437. DOI: [10.1006/jcph.1996.0221](https://doi.org/10.1006/jcph.1996.0221).
- Berselli, L. C. and Iliescu, T. (2003). “A higher-order subfilter-scale model for large eddy simulation”. *J. Comput. Appl. Math.* 159, pp. 411–430. DOI: [10.1016/S0377-0427\(03\)00544-2](https://doi.org/10.1016/S0377-0427(03)00544-2).
- Berselli, L. C., Iliescu, T., and Layton, W. J. (2006). *Mathematics of Large Eddy Simulation of Turbulent Flows*. Springer, Berlin, Heidelberg. DOI: [10.1007/b137408](https://doi.org/10.1007/b137408).
- Bourouiba, L. and Bartello, P. (2007). “The intermediate Rossby number range and two-dimensional–three-dimensional transfers in rotating decaying homogeneous turbulence”. *J. Fluid Mech.* 587, pp. 139–161. DOI: [10.1017/S0022112007007124](https://doi.org/10.1017/S0022112007007124).
- Bourouiba, L., Straub, D. N., and Waite, M. L. (2012). “Non-local energy transfers in rotating turbulence at intermediate Rossby number”. *J. Fluid Mech.* 690, pp. 129–147. DOI: [10.1017/jfm.2011.387](https://doi.org/10.1017/jfm.2011.387).
- Boussinesq, J. (1877). “Essai sur la théorie des eaux courantes”. *Mémoires présentés par divers savants à l’Académie des Sciences* 23, pp. 1–680.
- Brethouwer, G. (2016). “Linear instabilities and recurring bursts of turbulence in rotating channel flow simulations”. *Phys. Rev. Fluids* 1, 054404. DOI: [10.1103/PhysRevFluids.1.054404](https://doi.org/10.1103/PhysRevFluids.1.054404).

- Brethouwer, G. (2017). “Statistics and structure of spanwise rotating turbulent channel flow at moderate Reynolds numbers”. *J. Fluid Mech.* 828, pp. 424–458. DOI: [10.1017/jfm.2017.526](https://doi.org/10.1017/jfm.2017.526).
- Brethouwer, G., Schlatter, P., Duguet, Y., Henningson, D. S., and Johansson, A. V. (2014). “Recurrent Bursts via Linear Processes in Turbulent Environments”. *Phys. Rev. Lett.* 112, 144502. DOI: [10.1103/PhysRevLett.112.144502](https://doi.org/10.1103/PhysRevLett.112.144502).
- Buzzicotti, M., Aluie, H., Biferale, L., and Linkmann, M. (2018). “Energy transfer in turbulence under rotation”. *Phys. Rev. Fluids* 3, 034802. DOI: [10.1103/PhysRevFluids.3.034802](https://doi.org/10.1103/PhysRevFluids.3.034802).
- Cambon, C., Mansour, N. N., and Godefert, F. S. (1997). “Energy transfer in rotating turbulence”. *J. Fluid Mech.* 337, pp. 303–332. DOI: [10.1017/S002211209700493X](https://doi.org/10.1017/S002211209700493X).
- Carati, D., Winckelmann, G. S., and Jeanmart, H. (2001). “On the modelling of the subgrid-scale and filtered-scale stress tensors in large-eddy simulation”. *J. Fluid Mech.* 441, pp. 119–138. DOI: [10.1017/S0022112001004773](https://doi.org/10.1017/S0022112001004773).
- Cayley, A. (1858). “A Memoir on the Theory of Matrices”. *Phil. Trans. R. Soc. Lond.* 148, pp. 17–37. URL: <http://www.jstor.org/stable/108649>.
- Chae, D. (2005). “On the Spectral Dynamics of the Deformation Tensor and New A Priori Estimates for the 3D Euler Equations”. *Commun. Math. Phys.* 263, pp. 789–801. DOI: [10.1007/s00220-005-1465-8](https://doi.org/10.1007/s00220-005-1465-8).
- Chapman, D. R. and Kuhn, G. D. (1986). “The limiting behaviour of turbulence near a wall”. *J. Fluid Mech.* 170, pp. 265–292. DOI: [10.1017/S0022112086000885](https://doi.org/10.1017/S0022112086000885).
- Chen, Q., Chen, S., Eyink, G. L., and Holm, D. D. (2005). “Resonant interactions in rotating homogeneous three-dimensional turbulence”. *J. Fluid Mech.* 542, pp. 139–164. DOI: [10.1017/S0022112005006324](https://doi.org/10.1017/S0022112005006324).
- Cheviakov, A. F. and Oberlack, M. (2014). “Generalized Ertel’s theorem and infinite hierarchies of conserved quantities for three-dimensional time-dependent Euler and Navier–Stokes equations”. *J. Fluid Mech.* 760, pp. 368–386. DOI: [10.1017/jfm.2014.611](https://doi.org/10.1017/jfm.2014.611).
- Choi, H. and Moin, P. (2012). “Grid-point requirements for large eddy simulation: Chapman’s estimates revisited”. *Phys. Fluids* 24, 011702. DOI: [10.1063/1.3676783](https://doi.org/10.1063/1.3676783).
- Clark, R. A., Ferziger, J. H., and Reynolds, W. C. (1979). “Evaluation of subgrid-scale models using an accurately simulated turbulent flow”. *J. Fluid Mech.* 91, pp. 1–16. DOI: [10.1017/S002211207900001X](https://doi.org/10.1017/S002211207900001X).
- Comte-Bellot, G. and Corrsin, S. (1971). “Simple Eulerian time correlation of full- and narrow-band velocity signals in grid-generated, ‘isotropic’ turbulence”. *J. Fluid Mech.* 48, pp. 273–337. DOI: [10.1017/S0022112071001599](https://doi.org/10.1017/S0022112071001599).
- Dai, Y.-J., Huang, W.-X., and Xu, C.-X. (2016). “Effects of Taylor–Görtler vortices on turbulent flows in a spanwise-rotating channel”. *Phys. Fluids* 28, 115104. DOI: [10.1063/1.4967702](https://doi.org/10.1063/1.4967702).
- Deardorff, J. W. (1970). “Numerical study of three-dimensional turbulent channel flow at large Reynolds numbers”. *J. Fluid Mech.* 41, pp. 453–480. DOI: [10.1017/S0022112070000691](https://doi.org/10.1017/S0022112070000691).

- Deville, M. O. and Gatski, T. B. (2012). *Mathematical Modeling for Complex Fluids and Flows*. Springer, Berlin, Heidelberg. DOI: [10.1007/978-3-642-25295-2](https://doi.org/10.1007/978-3-642-25295-2).
- Du Vachat, R. (1977). “Realizability inequalities in turbulent flows”. *Phys. Fluids* 20, pp. 551–556. DOI: [10.1063/1.861911](https://doi.org/10.1063/1.861911).
- Euler, L. (1757). “Principes généraux de l’état d’équilibre des fluides”. *Mém. Acad. Sci. Berlin* 11, pp. 217–273.
- Frewer, M. (2009). “More clarity on the concept of material frame-indifference in classical continuum mechanics”. *Acta. Mech.* 202, pp. 213–246. DOI: [10.1007/s00707-008-0028-4](https://doi.org/10.1007/s00707-008-0028-4).
- Frisch, U. (1995). *Turbulence: The Legacy of A. N. Kolmogorov*. Cambridge University Press, Cambridge. DOI: [10.1017/CB09781139170666](https://doi.org/10.1017/CB09781139170666).
- Fureby, C. and Tabor, G. (1997). “Mathematical and Physical Constraints on Large-Eddy Simulations”. *Theor. Comp. Fluid Dyn.* 9, pp. 85–102. DOI: [10.1007/s001620050034](https://doi.org/10.1007/s001620050034).
- Gatski, T. B. and Jongen, T. (2000). “Nonlinear eddy viscosity and algebraic stress models for solving complex turbulent flows”. *Prog. Aerosp. Sci.* 36, pp. 655–682. DOI: [10.1016/S0376-0421\(00\)00012-9](https://doi.org/10.1016/S0376-0421(00)00012-9).
- Georgiadis, N. J., Rizzetta, D. P., and Fureby, C. (2010). “Large-Eddy Simulation: Current Capabilities, Recommended Practices, and Future Research”. *AIAA J.* 48, pp. 1772–1784. DOI: [10.2514/1.J050232](https://doi.org/10.2514/1.J050232).
- Germano, M., Piomelli, U., Moin, P., and Cabot, W. H. (1991). “A dynamic subgrid-scale eddy viscosity model”. *Phys. Fluids A* 3, pp. 1760–1765. DOI: [10.1063/1.857955](https://doi.org/10.1063/1.857955).
- Ghosal, S. (1999). “Mathematical and Physical Constraints on Large-Eddy Simulation of Turbulence”. *AIAA J.* 37, pp. 425–433. DOI: [10.2514/2.752](https://doi.org/10.2514/2.752).
- Godefert, F. S. and Moisy, F. (2015). “Structure and Dynamics of Rotating Turbulence: A Review of Recent Experimental and Numerical Results”. *Appl. Mech. Rev.* 67, 030802. DOI: [10.1115/1.4029006](https://doi.org/10.1115/1.4029006).
- Grundestam, O., Wallin, S., and Johansson, A. V. (2008). “Direct numerical simulations of rotating turbulent channel flow”. *J. Fluid Mech.* 598, pp. 177–199. DOI: [10.1017/S0022112007000122](https://doi.org/10.1017/S0022112007000122).
- Hamilton, W. R. (1853). *Lectures on Quaternions*. Hodges and Smith, Dublin.
- Hodge P. G., J. (1961). “On isotropic Cartesian tensors”. *Am. Math. Mon.* 68, pp. 793–795. DOI: [10.1080/00029890.1961.11989766](https://doi.org/10.1080/00029890.1961.11989766).
- Hopfinger, E. J., Browand, F. K., and Gagne, Y. (1982). “Turbulence and waves in a rotating tank”. *J. Fluid Mech.* 125, pp. 505–534. DOI: [10.1017/S0022112082003462](https://doi.org/10.1017/S0022112082003462).
- Horiuti, K. (2003). “Roles of non-aligned eigenvectors of strain-rate and subgrid-scale stress tensors in turbulence generation”. *J. Fluid Mech.* 491, pp. 65–100. DOI: [10.1017/S0022112003005299](https://doi.org/10.1017/S0022112003005299).
- Huang, X., Liu, Z., Yang, W., Li, Y., and Yang, Z. (2017). “A Cubic Nonlinear Subgrid-Scale Model for Large Eddy Simulation”. *J. Fluid. Eng. - T. ASME* 139, 041101. DOI: [10.1115/1.4035217](https://doi.org/10.1115/1.4035217).

- Jacquin, L., Leuchter, O., Cambon, C., and Mathieu, J. (1990). “Homogeneous turbulence in the presence of rotation”. *J. Fluid Mech.* 220, pp. 1–52. DOI: [10.1017/S0022112090003172](https://doi.org/10.1017/S0022112090003172).
- Johnston, J. P., Halleen, R. M., and Lezius, D. K. (1972). “Effects of spanwise rotation on the structure of two-dimensional fully developed turbulent channel flow”. *J. Fluid Mech.* 56, pp. 533–557. DOI: [10.1017/S0022112072002502](https://doi.org/10.1017/S0022112072002502).
- Kang, H. S., Chester, S., and Meneveau, C. (2003). “Decaying turbulence in an active-grid-generated flow and comparisons with large-eddy simulation”. *J. Fluid Mech.* 480, pp. 129–160. DOI: [10.1017/S0022112002003579](https://doi.org/10.1017/S0022112002003579).
- Kim, J. and Moin, P. (1985). “Application of a fractional-step method to incompressible Navier–Stokes equations”. *J. Comput. Phys.* 59, pp. 308–323. DOI: [10.1016/0021-9991\(85\)90148-2](https://doi.org/10.1016/0021-9991(85)90148-2).
- Kolmogorov, A. N. (1941). “The local structure of turbulence in incompressible viscous fluid for very large Reynolds number”. *Dokl. Akad. Nauk SSSR* 30, pp. 299–303.
- Kosović, B. (1997). “Subgrid-scale modelling for the large-eddy simulation of high-Reynolds-number boundary layers”. *J. Fluid Mech.* 336, pp. 151–182. DOI: [10.1017/S0022112096004697](https://doi.org/10.1017/S0022112096004697).
- Kristoffersen, R. and Andersson, H. I. (1993). “Direct simulations of low-Reynolds-number turbulent flow in a rotating channel”. *J. Fluid Mech.* 256, pp. 163–197. DOI: [10.1017/S0022112093002757](https://doi.org/10.1017/S0022112093002757).
- Kwak, D., Reynolds, W. C., and Ferziger, J. H. (1975). *Three-Dimensional, Time Dependent Computation of Turbulent Flow*. Technical Report TF-5. Stanford University.
- Lamballais, E., Lesieur, M., and Métais, O. (1996). “Effects of spanwise rotation on the vorticity stretching in transitional and turbulent channel flow”. *Int. J. Heat Fluid Fl.* 17, pp. 324–332. DOI: [10.1016/0142-727X\(96\)00043-4](https://doi.org/10.1016/0142-727X(96)00043-4).
- Langford, J. A. and Moser, R. D. (1999). “Optimal LES formulations for isotropic turbulence”. *J. Fluid Mech.* 398, pp. 321–346. DOI: [10.1017/S0022112099006369](https://doi.org/10.1017/S0022112099006369).
- Leon, S. J. (2006). *Linear Algebra with Applications*. 7th ed. Pearson Prentice Hall.
- Leonard, A. (1975). “Energy Cascade in Large-Eddy Simulations of Turbulent Fluid Flows”. In: *Turbulent Diffusion in Environmental Pollution. Proceedings of a Symposium held at Charlottesville, Virginia, April 8-14, 1973*. Ed. by Frenkiel, F. N. and Munn, R. E. Vol. 18 A. Adv. Geophys. Elsevier, pp. 237–248. DOI: [10.1016/S0065-2687\(08\)60464-1](https://doi.org/10.1016/S0065-2687(08)60464-1).
- Lilly, D. K. (1992). “A proposed modification of the Germano subgrid-scale closure method”. *Phys. Fluids A* 4, pp. 633–635. DOI: [10.1063/1.858280](https://doi.org/10.1063/1.858280).
- Liu, N., Lu, X., and Zhuang, L. (2004). “An improved dynamic subgrid-scale model and its application to large eddy simulation of rotating channel flows”. *Sci. China Ser. G* 47, pp. 463–476. DOI: [10.1360/03yw0228](https://doi.org/10.1360/03yw0228).
- Liu, S., Meneveau, C., and Katz, J. (1994). “On the properties of similarity subgrid-scale models as deduced from measurements in a turbulent jet”. *J. Fluid Mech.* 275, pp. 83–119. DOI: [10.1017/S0022112094002296](https://doi.org/10.1017/S0022112094002296).

- Lumley, J. L. (1970). "Toward a turbulent constitutive relation". *J. Fluid Mech.* 41, pp. 413–434. DOI: [10.1017/S0022112070000678](https://doi.org/10.1017/S0022112070000678).
- Lumley, J. L. (1979). "Computational Modeling of Turbulent Flows". In: *Advances in Applied Mechanics*. Ed. by Yih, C.-S. Vol. 18. Elsevier, pp. 123–176. DOI: [10.1016/S0065-2156\(08\)70266-7](https://doi.org/10.1016/S0065-2156(08)70266-7).
- Lumley, J. L. and Newman, G. R. (1977). "The return to isotropy of homogeneous turbulence". *J. Fluid Mech.* 82, pp. 161–178. DOI: [10.1017/S0022112077000585](https://doi.org/10.1017/S0022112077000585).
- Lund, T. S. and Novikov, E. A. (1992). "Parameterization of subgrid-scale stress by the velocity gradient tensor". In: *Annual Research Briefs*. Center for Turbulence Research, Stanford University, pp. 27–43.
- Marstorp, L., Brethouwer, G., Grundestam, O., and Johansson, A. V. (2009). "Explicit algebraic subgrid stress models with application to rotating channel flow". *J. Fluid Mech.* 639, pp. 403–432. DOI: [10.1017/S0022112009991054](https://doi.org/10.1017/S0022112009991054).
- Meneveau, C. and Marusic, I. (2013). "Generalized logarithmic law for high-order moments in turbulent boundary layers". *J. Fluid Mech.* 719, R1. DOI: [10.1017/jfm.2013.61](https://doi.org/10.1017/jfm.2013.61).
- Mininni, P. D., Alexakis, A., and Pouquet, A. (2009). "Scale interactions and scaling laws in rotating flows at moderate Rossby numbers and large Reynolds numbers". *Phys. Fluids* 21, 015108. DOI: [10.1063/1.3064122](https://doi.org/10.1063/1.3064122).
- Moffatt, H. K. (1969). "The degree of knottedness of tangled vortex lines". *J. Fluid Mech.* 35, pp. 117–129. DOI: [10.1017/S0022112069000991](https://doi.org/10.1017/S0022112069000991).
- Montecchia, M., Brethouwer, G., Johansson, A. V., and Wallin, S. (2017). "Taking large-eddy simulation of wall-bounded flows to higher Reynolds numbers by use of anisotropy-resolving subgrid models". *Phys. Rev. Fluids* 2, 034601. DOI: [10.1103/PhysRevFluids.2.034601](https://doi.org/10.1103/PhysRevFluids.2.034601).
- Moreau, J. J. (1961). "Constantes d'un îlot tourbillonnaire en fluide parfait barotrope". *C. R. Hebd. Acad. Sc.* 252, pp. 2810–2812.
- Morize, C., Moisy, F., and Rabaud, M. (2005). "Decaying grid-generated turbulence in a rotating tank". *Phys. Fluids* 17, 095105. DOI: [10.1063/1.2046710](https://doi.org/10.1063/1.2046710).
- Nakabayashi, K. and Kitoh, O. (2005). "Turbulence characteristics of two-dimensional channel flow with system rotation". *J. Fluid Mech.* 528, pp. 355–377. DOI: [10.1017/S0022112004002939](https://doi.org/10.1017/S0022112004002939).
- Navier, C. L. M. H. (1827). "Mémoire sur les lois du mouvement des fluides". *Mém. Acad. Sci. Inst. France* 6, pp. 389–440.
- Nicoud, F., Baya Toda, H., Cabrit, O., Bose, S., and Lee, J. (2011). "Using singular values to build a subgrid-scale model for large eddy simulations". *Phys. Fluids* 23, 085106. DOI: [10.1063/1.3623274](https://doi.org/10.1063/1.3623274).
- Nicoud, F. and Ducros, F. (1999). "Subgrid-Scale Stress Modelling Based on the Square of the Velocity Gradient Tensor". *Flow Turbul. Combust.* 62, pp. 183–200. DOI: [10.1023/A:1009995426001](https://doi.org/10.1023/A:1009995426001).
- Oberlack, M. (1997). "Invariant modeling in large-eddy simulation of turbulence". In: *Annual Research Briefs*. Center for Turbulence Research, Stanford University, pp. 3–22.

- Oberlack, M. (2001). “A unified approach for symmetries in plane parallel turbulent shear flows”. *J. Fluid Mech.* 427, pp. 299–328. DOI: [10.1017/S0022112000002408](https://doi.org/10.1017/S0022112000002408).
- Oberlack, M. (2002). “Symmetries and Invariant Solutions of Turbulent Flows and their Implications for Turbulence Modelling”. In: *Theories of Turbulence*. Ed. by Oberlack, M. and Busse, F. H. Vol. 442. International Centre for Mechanical Sciences. Springer Vienna, pp. 301–366. DOI: [10.1007/978-3-7091-2564-9_6](https://doi.org/10.1007/978-3-7091-2564-9_6).
- Obukhov, A. M. (1941a). “Spectral energy distribution in a turbulent flow”. *Izv. Akad. Nauk SSSR Ser. Geogr. Geofiz.* 5, pp. 453–466.
- Obukhov, A. M. (1941b). “Spectral energy distribution in a turbulent flow”. *Dokl. Akad. Nauk SSSR* 32, pp. 22–24.
- Piomelli, U., Rouhi, A., and Geurts, B. J. (2015). “A grid-independent length scale for large-eddy simulations”. *J. Fluid Mech.* 766, pp. 499–527. DOI: [10.1017/jfm.2015.29](https://doi.org/10.1017/jfm.2015.29).
- Poisson, S. D. (1831). “Mémoire sur les équations générales de l’équilibre et du mouvement des corps élastiques et des fluides”. *J. École Polytech.* 13, pp. 1–174.
- Pope, S. B. (1975). “A more general effective-viscosity hypothesis”. *J. Fluid Mech.* 72, pp. 331–340. DOI: [10.1017/S0022112075003382](https://doi.org/10.1017/S0022112075003382).
- Pope, S. B. (2011). *Turbulent Flows*. Cambridge University Press, Cambridge. DOI: [10.1017/CB09780511840531](https://doi.org/10.1017/CB09780511840531).
- Rasam, A., Brethouwer, G., Schlatter, P., Li, Q., and Johansson, A. V. (2011). “Effects of modelling, resolution and anisotropy of subgrid-scales on large eddy simulations of channel flow”. *J. Turbul.* 12, N10. DOI: [10.1080/14685248.2010.541920](https://doi.org/10.1080/14685248.2010.541920).
- Razafindralandy, D., Hamdouni, A., and Oberlack, M. (2007). “Analysis and development of subgrid turbulence models preserving the symmetry properties of the Navier–Stokes equations”. *Eur. J. Mech. B-Fluid.* 26, pp. 531–550. DOI: [10.1016/j.euromechflu.2006.10.003](https://doi.org/10.1016/j.euromechflu.2006.10.003).
- Rebholz, L. G. (2007). “Conservation laws of turbulence models”. *J. Math. Anal. Appl.* 326, pp. 33–45. DOI: [10.1016/j.jmaa.2006.02.026](https://doi.org/10.1016/j.jmaa.2006.02.026).
- Remmerswaal, R. A. (2016). “A Family of Orthogonalised Nonlinear LES Models Based on the Velocity Gradient: Discretisation and Analysis”. Master’s thesis. University of Groningen, The Netherlands.
- Reynolds, O. (1883). “An Experimental Investigation of the Circumstances Which Determine Whether the Motion of Water Shall Be Direct or Sinuous, and of the Law of Resistance in Parallel Channels”. *Phil. Trans. R. Soc. Lond.* 174, pp. 935–982. DOI: [10.1098/rstl.1883.0029](https://doi.org/10.1098/rstl.1883.0029).
- Reynolds, O. (1895). “On the Dynamical Theory of Incompressible Viscous Fluids and the Determination of the Criterion”. *Phil. Trans. R. Soc. Lond.* 186, pp. 123–164. DOI: [10.1098/rsta.1895.0004](https://doi.org/10.1098/rsta.1895.0004).
- Reynolds, O. (1903). *Papers on Mechanical and Physical Subjects*. Vol. 3. Cambridge University Press, Cambridge.

- Rivlin, R. S. (1955). “Further Remarks on the Stress-Deformation Relations for Isotropic Materials”. *J. Ration. Mech. Anal.* 4, pp. 681–702. URL: <http://www.jstor.org/stable/24900379>.
- Rivlin, R. S. and Ericksen, J. L. (1955). “Stress-Deformation Relations for Isotropic Materials”. *J. Ration. Mech. Anal.* 4, pp. 323–425. URL: <http://www.jstor.org/stable/24900365>.
- Rouhi, A., Piomelli, U., and Geurts, B. J. (2016). “Dynamic subfilter-scale stress model for large-eddy simulations”. *Phys. Rev. Fluids* 1, 044401. DOI: [10.1103/PhysRevFluids.1.044401](https://doi.org/10.1103/PhysRevFluids.1.044401).
- Rozema, W., Bae, H. J., Moin, P., and Verstappen, R. (2015). “Minimum-dissipation models for large-eddy simulation”. *Phys. Fluids* 27, 085107. DOI: [10.1063/1.4928700](https://doi.org/10.1063/1.4928700).
- Sagaut, P. (2006). *Large Eddy Simulation for Incompressible Flows. An Introduction*. 3rd ed. Springer, Berlin, Heidelberg. DOI: [10.1007/b137536](https://doi.org/10.1007/b137536).
- Sagaut, P. and Cambon, C. (2018). *Homogeneous Turbulence Dynamics*. Springer, Cham. DOI: [10.1007/978-3-319-73162-9](https://doi.org/10.1007/978-3-319-73162-9).
- Schumann, U. (1977). “Realizability of Reynolds-stress turbulence models”. *Phys. Fluids* 20, pp. 721–725. DOI: [10.1063/1.861942](https://doi.org/10.1063/1.861942).
- Sen, A., Mininni, P. D., Rosenberg, D., and Pouquet, A. (2012). “Anisotropy and nonuniversality in scaling laws of the large-scale energy spectrum in rotating turbulence”. *Phys. Rev. E* 86, 036319. DOI: [10.1103/PhysRevE.86.036319](https://doi.org/10.1103/PhysRevE.86.036319).
- Silvis, M. (2015). “Osborne Reynolds: On the phenomenon of turbulence”. *Periodiek. Magazine of the FMF, student association for Physics and Mathematics, University of Groningen* 3, pp. 14–17. URL: http://perio.fmf.nl/archief/perio_2015-3.pdf#page=14.
- Silvis, M. H., Bae, H. J., Trias, F. X., Abkar, M., and Verstappen, R. (2019). “A nonlinear subgrid-scale model for large-eddy simulations of rotating turbulent flows”. arXiv: [1904.12748](https://arxiv.org/abs/1904.12748) [[physics.flu-dyn](https://arxiv.org/abs/1904.12748)].
- Silvis, M. H., Remmerswaal, R. A., and Verstappen, R. (2017a). “A Framework for the Assessment and Creation of Subgrid-Scale Models for Large-Eddy Simulation”. In: *Progress in Turbulence VII: Proceedings of the iTi Conference in Turbulence 2016*. Ed. by Örlü, R., Talamelli, A., Oberlack, M., and Peinke, J. Springer International Publishing, pp. 133–139. DOI: [10.1007/978-3-319-57934-4_19](https://doi.org/10.1007/978-3-319-57934-4_19).
- Silvis, M. H., Remmerswaal, R. A., and Verstappen, R. (2017b). “Physical consistency of subgrid-scale models for large-eddy simulation of incompressible turbulent flows”. *Phys. Fluids* 29, 015105. DOI: [10.1063/1.4974093](https://doi.org/10.1063/1.4974093).
- Silvis, M. H., Trias, F. X., Abkar, M., Bae, H. J., Lozano-Durán, A., and Verstappen, R. W. C. P. (2016). “Exploring nonlinear subgrid-scale models and new characteristic length scales for large-eddy simulation”. In: *Studying Turbulence Using Numerical Simulation Databases - XVI: Proceedings of the 2016 Summer Program*. Ed. by Moin, P. and Urzay, J. Center for Turbulence Research, Stanford University, pp. 265–274.
- Silvis, M. H. and Verstappen, R. (2015). “Physically consistent subgrid-scale models for large-eddy simulation of incompressible turbulent flows”. arXiv: [1510.07881](https://arxiv.org/abs/1510.07881) [[physics.flu-dyn](https://arxiv.org/abs/1510.07881)].

- Silvis, M. H. and Verstappen, R. (2018). “Constructing Physically Consistent Subgrid-Scale Models for Large-Eddy Simulation of Incompressible Turbulent Flows”. In: *Turbulence and Interactions: Proceedings of the TI 2015 Conference*. Ed. by Deville, M. O., Couaillier, V., Estivaleres, J.-L., Gleize, V., Lê, T.-H., Terracol, M., and Vincent, S. Springer International Publishing, pp. 241–247. DOI: [10.1007/978-3-319-60387-2_26](https://doi.org/10.1007/978-3-319-60387-2_26).
- Silvis, M. H. and Verstappen, R. (2019). “Nonlinear Subgrid-Scale Models for Large-Eddy Simulation of Rotating Turbulent Flows”. In: *Direct and Large-Eddy Simulation XI*. Ed. by Salvetti, M. V., Armenio, V., Fröhlich, J., Geurts, B. J., and Kuerten, H. Springer International Publishing, pp. 129–134. DOI: [10.1007/978-3-030-04915-7_18](https://doi.org/10.1007/978-3-030-04915-7_18).
- Silvis, M. H. and Verstappen, R. (n.d. b). “Creating physics-based subgrid-scale models for large-eddy simulation”. (in preparation).
- Silvis, M. H. and Verstappen, R. (n.d. a). “Velocity-gradient-based representations for incompressible turbulent flows”. (in preparation).
- Smagorinsky, J. (1963). “General Circulation Experiments with the Primitive Equations”. *Mon. Weather Rev.* 91, pp. 99–164. DOI: [10.1175/1520-0493\(1963\)091<0099:GCEWTP>2.3.CO;2](https://doi.org/10.1175/1520-0493(1963)091<0099:GCEWTP>2.3.CO;2).
- Smith, L. M. and Waleffe, F. (1999). “Transfer of energy to two-dimensional large scales in forced, rotating three-dimensional turbulence”. *Phys. Fluids* 11, pp. 1608–1622. DOI: [10.1063/1.870022](https://doi.org/10.1063/1.870022).
- Spencer, A. J. M. and Rivlin, R. S. (1958). “The Theory of Matrix Polynomials and its Application to the Mechanics of Isotropic Continua”. *Arch. Ration. Mech. An.* 2, pp. 309–336. DOI: [10.1007/BF00277933](https://doi.org/10.1007/BF00277933).
- Spencer, A. J. M. and Rivlin, R. S. (1962). “Isotropic Integrity Bases for Vectors and Second-Order Tensors. Part I.” *Arch. Ration. Mech. An.* 9, pp. 45–63. DOI: [10.1007/BF00253332](https://doi.org/10.1007/BF00253332).
- Speziale, C. G. (1985a). “Galilean invariance of subgrid-scale stress models in the large-eddy simulation of turbulence”. *J. Fluid Mech.* 156, pp. 55–62. DOI: [10.1017/S0022112085001987](https://doi.org/10.1017/S0022112085001987).
- Speziale, C. G. (1985b). “Subgrid Scale Stress Models for the Large-Eddy Simulation of Rotating Turbulent Flows”. *Geophys. Astro. Fluid* 33, pp. 199–222. DOI: [10.1080/03091928508245430](https://doi.org/10.1080/03091928508245430).
- Speziale, C. G. (1998). “A review of material frame-indifference in mechanics”. *Appl. Mech. Rev.* 51, pp. 489–504. DOI: [10.1115/1.3099017](https://doi.org/10.1115/1.3099017).
- Staplehurst, P. J., Davidson, P. A., and Dalziel, S. B. (2008). “Structure formation in homogeneous freely decaying rotating turbulence”. *J. Fluid Mech.* 598, pp. 81–105. DOI: [10.1017/S0022112007000067](https://doi.org/10.1017/S0022112007000067).
- Stevens, R. J. A. M., Wilczek, M., and Meneveau, C. (2014). “Large-eddy simulation study of the logarithmic law for second- and higher-order moments in turbulent wall-bounded flow”. *J. Fluid Mech.* 757, pp. 888–907. DOI: [10.1017/jfm.2014.510](https://doi.org/10.1017/jfm.2014.510).
- Stokes, G. G. (1845). “On the Theories of the Internal Friction of Fluids in Motion, and of the Equilibrium and Motion of Elastic Solids”. *Trans. Cambridge Philos. Soc.* 8, pp. 287–305.

- Streher, L. B., Silvis, M. H., Cifani, P., and Verstappen, R. W. C. P. (2020). “Mixed modeling for large-eddy simulation: The single-layer and two-layer minimum-dissipation-Bardina models”. arXiv: [2006.08516](https://arxiv.org/abs/2006.08516) [[physics.flu-dyn](https://arxiv.org/abs/2006.08516)].
- Streher, L. B., Silvis, M. H., and Verstappen, R. (2018). “Mixed modeling for large-eddy simulation: The minimum-dissipation-Bardina-model”. In: *Proceedings of the 7th European Conference on Computational Fluid Dynamics*. Ed. by Owen, R., De Borst, R., Reese, J., and Pearce, C. International Center for Numerical Methods in Engineering, Barcelona, Spain, pp. 335–345.
- Tafti, D. K. and Vanka, S. P. (1991). “A numerical study of the effects of spanwise rotation on turbulent channel flow”. *Phys. Fluids A* 3, pp. 642–656. DOI: [10.1063/1.858215](https://doi.org/10.1063/1.858215).
- Tao, B., Katz, J., and Meneveau, C. (2002). “Statistical geometry of subgrid-scale stresses determined from holographic particle image velocimetry measurements”. *J. Fluid Mech.* 457, pp. 35–78. DOI: [10.1017/S0022112001007443](https://doi.org/10.1017/S0022112001007443).
- Thiele, M. and Müller, W.-C. (2009). “Structure and decay of rotating homogeneous turbulence”. *J. Fluid Mech.* 637, pp. 425–442. DOI: [10.1017/S002211200999067X](https://doi.org/10.1017/S002211200999067X).
- Tietjens, O. G., Prandtl, L., and Rosenhead, L. (1934). *Fundamentals of Hydro- and Aeromechanics*. McGraw-Hill Book Company, Inc., New York and London.
- Trias, F. X., Folch, D., Gorobets, A., and Oliva, A. (2015). “Building proper invariants for eddy-viscosity subgrid-scale models”. *Phys. Fluids* 27, 065103. DOI: [10.1063/1.4921817](https://doi.org/10.1063/1.4921817).
- Trias, F. X., Gorobets, A., Silvis, M. H., Verstappen, R. W. C. P., and Oliva, A. (2017). “A new subgrid characteristic length for turbulence simulations on anisotropic grids”. *Phys. Fluids* 29, 115109. DOI: [10.1063/1.5012546](https://doi.org/10.1063/1.5012546).
- Verstappen, R. (2011). “When Does Eddy Viscosity Damp Subfilter Scales Sufficiently?” *J. Sci. Comput.* 49, pp. 94–110. DOI: [10.1007/s10915-011-9504-4](https://doi.org/10.1007/s10915-011-9504-4).
- Verstappen, R. (2018). “How much eddy dissipation is needed to counterbalance the nonlinear production of small, unresolved scales in a large-eddy simulation of turbulence?” *Comput. Fluids* 176, pp. 276–284. DOI: [10.1016/j.compfluid.2016.12.016](https://doi.org/10.1016/j.compfluid.2016.12.016).
- Verstappen, R. W. C. P., Bose, S. T., Lee, J., Choi, H., and Moin, P. (2010). “A dynamic eddy-viscosity model based on the invariants of the rate-of-strain”. In: *Proceedings of the Summer Program*. Center for Turbulence Research, Stanford University, pp. 183–192.
- Verstappen, R. W. C. P., Rozema, W., and Bae, H. J. (2014). “Numerical scale separation in large-eddy simulation”. In: *Proceedings of the Summer Program*. Center for Turbulence Research, Stanford University, pp. 417–426.
- Verstappen, R. W. C. P. and Veldman, A. E. P. (2003). “Symmetry-preserving discretization of turbulent flow”. *J. Comput. Phys.* 187, pp. 343–368. DOI: [10.1016/S0021-9991\(03\)00126-8](https://doi.org/10.1016/S0021-9991(03)00126-8).

- Vreman, A. W. (2004). “An eddy-viscosity subgrid-scale model for turbulent shear flow: Algebraic theory and applications”. *Phys. Fluids* 16, pp. 3670–3681. DOI: [10.1063/1.1785131](https://doi.org/10.1063/1.1785131).
- Vreman, B., Geurts, B., and Kuerten, H. (1994a). “On the formulation of the dynamic mixed subgrid-scale model”. *Phys. Fluids* 6, pp. 4057–4059. DOI: [10.1063/1.868333](https://doi.org/10.1063/1.868333).
- Vreman, B., Geurts, B., and Kuerten, H. (1994b). “Realizability conditions for the turbulent stress tensor in large-eddy simulation”. *J. Fluid Mech.* 278, pp. 351–362. DOI: [10.1017/S0022112094003745](https://doi.org/10.1017/S0022112094003745).
- Vreman, B., Geurts, B., and Kuerten, H. (1996). “Large-eddy simulation of the temporal mixing layer using the Clark model”. *Theor. Comp. Fluid Dyn.* 8, pp. 309–324. DOI: [10.1007/BF00639698](https://doi.org/10.1007/BF00639698).
- Vreman, B., Geurts, B., and Kuerten, H. (1997). “Large-eddy simulation of the turbulent mixing layer”. *J. Fluid Mech.* 339, pp. 357–390. DOI: [10.1017/S0022112097005429](https://doi.org/10.1017/S0022112097005429).
- Wang, B.-C. and Bergstrom, D. J. (2005). “A dynamic nonlinear subgrid-scale stress model”. *Phys. Fluids* 17, 035109. DOI: [10.1063/1.1858511](https://doi.org/10.1063/1.1858511).
- Ward, D. (2016). “Assessing turbulence models for large-eddy simulation using exact solutions to the Navier–Stokes equations”. Bachelor’s thesis. University of Groningen, The Netherlands.
- Weis, J. and Hutter, K. (2003). “On Euclidean invariance of algebraic Reynolds stress models in turbulence”. *J. Fluid Mech.* 476, pp. 63–68. DOI: [10.1017/S0022112002003105](https://doi.org/10.1017/S0022112002003105).
- Wendling, I. and Oberlack, M. (2007). “On the Investigation of a Dynamic Non-linear Subgrid-Scale Model”. In: *Complex Effects in Large Eddy Simulations*. Ed. by Kassinos, S. C., Langer, C. A., Iaccarino, G., and Moin, P. Springer Berlin Heidelberg, pp. 89–97. DOI: [10.1007/978-3-540-34234-2_7](https://doi.org/10.1007/978-3-540-34234-2_7).
- Winckelmans, G. S., Jeanmart, H., and Carati, D. (2002). “On the comparison of turbulence intensities from large-eddy simulation with those from experiment or direct numerical simulation”. *Phys. Fluids* 14, pp. 1809–1811. DOI: [10.1063/1.1466824](https://doi.org/10.1063/1.1466824).
- Winckelmans, G. S., Wray, A. A., Vasilyev, O. V., and Jeanmart, H. (2001). “Explicit-filtering large-eddy simulation using the tensor-diffusivity model supplemented by a dynamic Smagorinsky term”. *Phys. Fluids* 13, pp. 1385–1403. DOI: [10.1063/1.1360192](https://doi.org/10.1063/1.1360192).
- Wu, H. and Kasagi, N. (2004). “Effects of arbitrary directional system rotation on turbulent channel flow”. *Phys. Fluids* 16, pp. 979–990. DOI: [10.1063/1.1649337](https://doi.org/10.1063/1.1649337).
- Xia, Z., Shi, Y., and Chen, S. (2016). “Direct numerical simulation of turbulent channel flow with spanwise rotation”. *J. Fluid Mech.* 788, pp. 42–56. DOI: [10.1017/jfm.2015.717](https://doi.org/10.1017/jfm.2015.717).
- Yang, Y.-T. and Wu, J.-Z. (2012). “Channel turbulence with spanwise rotation studied using helical wave decomposition”. *J. Fluid Mech.* 692, pp. 137–152. DOI: [10.1017/jfm.2011.500](https://doi.org/10.1017/jfm.2011.500).
- Yang, Z. X., Cui, G. X., Zhang, Z. S., and Xu, C. X. (2012a). “A modified nonlinear sub-grid scale model for large eddy simulation with application to

- rotating turbulent channel flows”. *Phys. Fluids* 24, 075113. DOI: [10.1063/1.4739063](https://doi.org/10.1063/1.4739063).
- Yang, Z., Cui, G., Xu, C., and Zhang, Z. (2012b). “Large eddy simulation of rotating turbulent channel flow with a new dynamic global-coefficient nonlinear subgrid stress model”. *J. Turbul.* 13, N48. DOI: [10.1080/14685248.2012.726996](https://doi.org/10.1080/14685248.2012.726996).
- Yeung, P. K. and Zhou, Y. (1998). “Numerical study of rotating turbulence with external forcing”. *Phys. Fluids* 10, pp. 2895–2909. DOI: [10.1063/1.869810](https://doi.org/10.1063/1.869810).
- Zang, Y., Street, R. L., and Koseff, J. R. (1993). “A dynamic mixed subgrid-scale model and its application to turbulent recirculating flows”. *Phys. Fluids A* 5, pp. 3186–3196. DOI: [10.1063/1.858675](https://doi.org/10.1063/1.858675).

Summary*

Physics-based turbulence models for large-eddy simulation

Theory and application to rotating turbulent flows

Fluid flows are everywhere. Consider, for example, rivers, the flow of air in the atmosphere and the blood that is flowing through our veins. Most fluid flows are very chaotic, or turbulent, and the prediction of their behavior is essential for many applications, including the design of cars, boats and airplanes. However, accurately predicting turbulent flows is very challenging because computers do not have enough memory to store all flow details.

In this thesis, we, therefore, apply a method called large-eddy simulation. With this method, the large eddies, or vortices, in flows are directly computed, whereas small eddies have to be described using turbulence models. The question we consider is: how to create physics-based turbulence models, which respect the physical and mathematical properties of flows?

To answer this question, we follow a systematic approach. We thereby obtain a framework of constraints for the construction of physics-based turbulence models. Using this framework, we show that existing turbulence models do not respect all properties of flows. We also illustrate how new physics-based turbulence models with desired properties can be created systematically.

We then apply the framework of constraints to develop a new turbulence model for rotating flows. We show that this model respects many properties of flows and provides outstanding predictions of rotating flows. We also demonstrate that these predictions are as good as, or much better than, predictions from existing turbulence models. Our work can, thus, aid in improving predictions of both rotating and nonrotating turbulent flows.

* A Dutch version of this summary can be found on page [229](#) of this thesis.

Inleiding

Stel je voor dat je langs een klein beekje loopt. Je hoort het zachte geruis van het water, dat je uitnodigt om dichterbij te komen. Op het oppervlak van het beekje zie je ingewikkelde patronen van rimpelingen en golven; en waar het water langs stenen stroomt, ontstaan wervels. Je merkt ook hoe kalm het beekje op sommige plekken is, om zich vervolgens in een stroomversnelling te storten. Terwijl je de stroming bestudeert, begin je je af te vragen wat er onder het oppervlak gebeurt. Welke verschijnselen treden er op in het heldere water? Hoe kunnen we deze beschrijven? In dit proefschrift bestuderen we deze vragen. We richten ons in het bijzonder op het beschrijven en voorspellen van turbulentie in vloeistofstromingen.

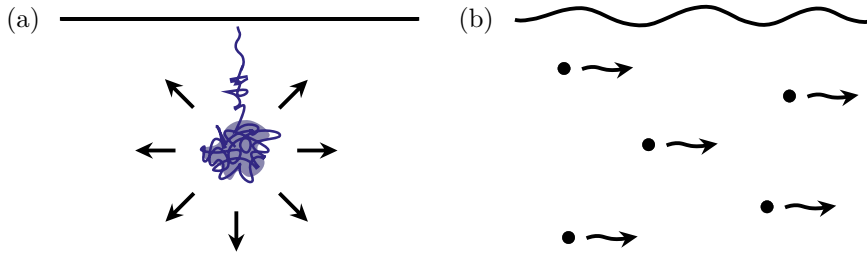
Turbulentie in vloeistofstromingen

Stromingsleer

Vloeistofstromingen zijn overal. Denk naast beekjes bijvoorbeeld aan rivieren, oceaanstromingen en aan het bloed dat door onze aderen stroomt. Door de term *vloeistof* voor zowel vloeistoffen als gassen te gebruiken, kunnen we daarnaast denken aan luchtstromingen in de atmosfeer en aan de lucht die zich door onze longen beweegt wanneer we in- en uitademen. Technische voorbeelden zijn het stromen van water door leidingen, het stromen van lucht rond een vliegtuig en het mengen van brandstof en zuurstof in de motor van een auto.

Zoals deze voorbeelden laten zien, is er een grote verscheidenheid aan vloeistofstromingen. We kunnen bijvoorbeeld stromingen waarnemen van één enkele vloeistof die zich in de vloeibare of gasfase bevindt, maar er bestaan ook stromingen van meerdere vloeistoffen in verschillende fases. Daarnaast kunnen we verschillende soorten vloeistoffen tegenkomen. Sommige vloeistoffen, waaronder lucht, zijn samendrukbaar of *compressibel*. Dat wil zeggen dat hun volume verandert door toepassing van druk. Andere vloeistoffen, zoals water, zijn (praktisch) *incompressibel*. Vloeistoffen verschillen ook in hun stroperigheid of *viscositeit*. Sommige vloeistoffen zijn zeer *viskeus*, zoals honing, terwijl andere vloeistoffen bijna niet viskeus zijn, zoals supervloeibare helium. We kunnen daarnaast zien dat vloeistofstromingen een wisselwerking aangaan met verschillende objecten, van bloedcellen tot vliegtuigen.

Het gedrag van stromingen heeft daardoor veel verschillende aspecten. We kunnen bijvoorbeeld golven waarnemen waar twee verschillende vloeistoffen zoals water en lucht samenkomen, zoals op het oppervlak van een beekje. Verschillende vloeistoffen kunnen ook mengen. Daarnaast kunnen vloeistofstromingen kleine deeltjes zoals sediment, zout, bloedcellen, voedingsstoffen en verontreinigingen transporteren. Stromingen kunnen ook warmte vervoeren,



Figuur 1: Schematische weergave van twee transportprocessen die plaatsvinden in vloeistofstromingen, namelijk (a) diffusie en (b) convectie.

zoals duidelijk is wanneer warme lucht in een ruimte circuleert. Wanneer een vloeistof langs een vast lichaam stroomt, zoals lucht om een vliegtuig, kan wrijving een belangrijke rol spelen. We kunnen daarnaast gladde van zeer chaotische stromingen onderscheiden. Dit onderscheid, waar we spoedig op terugkomen, speelt een belangrijke rol in dit proefschrift.

Bovenstaande laat zien dat vloeistofstromingen in allerlei verschillende situaties voorkomen en zeer divers gedrag vertonen. De studie van stromingen is daarom, zowel vanuit fundamenteel oogpunt als vanuit het perspectief van industriële en bouwkundige toepassingen, zeer interessant. De studie van vloeistofstromingen heet *stromingsleer* of *vloeistofmechanica* en heeft als doel om het gedrag van vloeistoffen en alle aan stromingen gerelateerde verschijnselen te begrijpen, beschrijven en voorspellen.

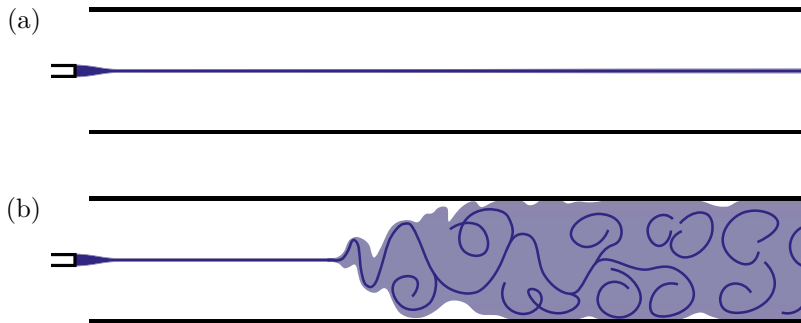
Transport

De studie van vloeistofstromingen heeft twee fundamenteel verschillende transportprocessen blootgelegd. Aan de ene kant is er *diffusie*. Diffusie verspreidt deeltjes die in een vloeistof ondergedompeld zijn door concentratieverschillen te verkleinen. Een bekend voorbeeld van dit proces is het verspreiden van een kleurstof in kalm water, schematisch weergegeven in Fig. 1(a).

Aan de andere kant is er *convectie*. Convectie, ook *advectie* genaamd, is het proces dat deeltjes met een stroming meevoert. Dit soort transport kan men bijvoorbeeld waarnemen in de bloedsomloop, die bloedcellen en voedingsstoffen verspreidt. Zie Fig. 1(b) voor een schematische weergave van convectie.

Naast het beïnvloeden van deeltjes in stromingen, hebben diffusie en convectie een effect op stromingen zelf. In het bijzonder transporteren zij natuurkundige grootheden zoals de *impuls* en *kinetische energie* van stromingen. De impuls is een maat voor de snelheid van een stroming, gegeven door het product van de massa en de snelheid van de vloeistof. De kinetische energie is de energie van de beweging van de vloeistof.

Diffusie heeft de volgende effecten op stromingen. Door diffusie van de impuls verspreiden delen van een stroming waar een vloeistof snel beweegt zich naar delen waar de vloeistof langzamer beweegt. Op dezelfde wijze diffundeert



Figuur 2: Schematische weergave van de experimentele waarnemingen van Reynolds van een kleurstof in (a) een regelmatige, gladde of *laminaire* stroming en in (b) een onregelmatige, chaotische of *turbulente* stroming.

langzaam bewegende vloeistof naar gebieden waar de vloeistof sneller beweegt. Hierdoor worden snel bewegende delen van de stroming afgeremd, terwijl langzaam bewegende vloeistof versnelt. Diffusie nivelleert ook de kinetische energie van stromingen. Bovendien leidt diffusie tot wrijving, die de kinetische energie van stromingen *dissipeert*, dat wil zeggen, in warmte omzet.

Convectie veroorzaakt totaal andere effecten. Zowel de convectie als de impuls hangen van de snelheid van een stroming af. De convectie van impuls is daardoor een *niet-lineair* proces, waarbij een stroming in wisselwerking treedt met zichzelf. Hierdoor kunnen stromingspatronen zoals wervels, die in het Engels ook wel *eddies* genoemd worden, zich samenvoegen of splitsen, waarbij wervels van een andere grootte ontstaan. Op vergelijkbare wijze kunnen verschillende wervels kinetische energie met elkaar uitwisselen. Waar diffusie stromingen gladder maakt, creëert convectie dus ingewikkeldere stromingspatronen. Met andere woorden, diffusie en convectie zijn concurrerende processen.

Competitie

Osborne Reynolds (1842–1912) heeft aangetoond dat de competitie tussen diffusie en convectie een belangrijke rol speelt in het bepalen van het gedrag van stromingen. In zijn baanbrekende artikel uit 1883¹ beschreef hij een reeks experimenten, waarin hij een kleurstof injecteerde in water dat door een glazen buis stroomde. Reynolds nam een aantal verschillende stromingstoestanden waar, die twee duidelijke extremen hadden.

Aan de ene kant zag hij dat de kleurstof uitgesmeerd werd tot een lange dunne streep (zie Fig. 2(a)). Aan de andere kant kon de vloeistof zich plotseling mengen met het water, om zich vervolgens over de hele buis te verspreiden (zie Fig. 2(b)). In het eerste geval concludeerde Reynolds dat de vloeistof zich

¹ Zie de verwijzing naar het artikel van Reynolds (1883) in de bibliografie die op pagina 207 van dit proefschrift begint.

zeer regelmatig en rustig bewoog. In het tweede geval liet de kleurstof een zeer onregelmatige, chaotische stroming zien.

Reynolds veronderstelde het bestaan van een *kritische stroomsnelheid*, die de overgang tussen beide stromingstoestanden markeert. Met behulp van dimensieanalyse beargumenteerde hij bovendien dat deze kritische snelheid af zou hangen van de diameter van de glazen buis en de viscositeit van de vloeistof. Reynolds bevestigde zijn hypothese door middel van experimenten waarin hij zorgvuldig probeerde verstoringen bij de ingang van de buis te reduceren.

Reynolds toonde zo aan dat hij de stromingstoestanden die hij waarnam, kon kenmerken met behulp van één getal, gebaseerd op de stroomsnelheid, de diameter van de buis en de viscositeit van de vloeistof. Zolang de waarde van dit getal, dat we nu het *Reynoldsgetal* noemen, onder een kritische waarde viel, nam Reynolds een gladde stroming waar. Met een Reynoldsgetal boven de kritische waarde was de stroming onregelmatig en chaotisch. Het Reynoldsgetal vormt een maat voor de relatieve sterkte van de convectie ten opzichte van de diffusie. Reynolds toonde dus aan dat de competitie tussen deze processen een belangrijke rol speelt in stromingen.²

Turbulentie

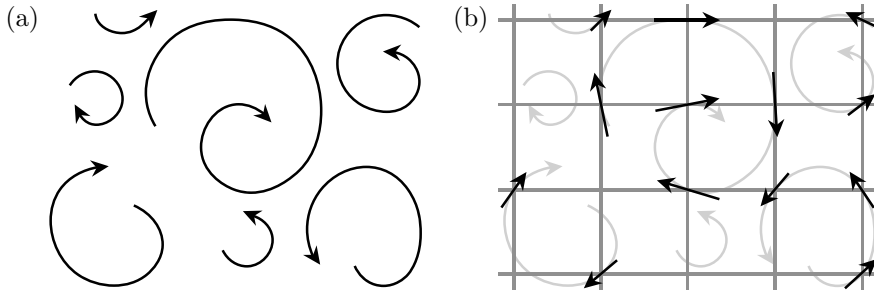
We noemen gladde, regelmatige stromingen *laminair* of gelaagd, terwijl chaotische, onregelmatige stromingen *turbulent* worden genoemd. In laminaire stromingen domineert diffusie de convectie en varieert de stroomsnelheid weinig. Turbulente stromingen worden daarentegen door convectie gedomineerd en laten grote fluctuaties in stroomsnelheid zien.

Door de overheersende rol van convectie bevatten turbulente stromingen wervels van veel verschillende groottes (zie bijvoorbeeld Fig. 3(a)), die voortdurend impuls en kinetische energie uitwisselen. Hierdoor mengen turbulente stromingen meer dan laminaire stromingen. Uitwisseling van kinetische energie leidt tot energieoverdracht van grote naar kleine wervels en omgekeerd. Deze processen heten respectievelijk de *directe* en *omgekeerde cascade* van energie. De kinetische energie van de kleinste wervels wordt gedissipeerd door de diffusie. Deze dissipatie is groter in turbulente dan in laminaire stromingen. Turbulente stromingen ondervinden hierdoor meer wrijving dan laminaire stromingen.

Een andere belangrijke eigenschap van turbulente stromingen is dat ze zeer instabiel zijn. Om preciezer te zijn, zijn ze zeer gevoelig voor variaties in de begintoestand van de stroming, voor oneffenheden in het stromingsdomein en voor veranderingen in de eigenschappen van de vloeistof. Hierdoor is het praktisch onmogelijk om dezelfde turbulente stroming tweemaal te produceren. In de stromingsleer wordt het gedrag van turbulente stromingen aangeduid met de term *turbulentie*.

Turbulente stromingen zijn niet alleen vanuit fundamenteel oogpunt interessant. Aangezien de meeste stromingen turbulent zijn, zijn hun eigenschappen ook relevant voor veel toepassingen. Het mengen van turbulente stromingen

² Zie voor meer informatie over deze en andere ontdekkingen van Reynolds bijvoorbeeld het populair-wetenschappelijke artikel van Silvis (2015).



Figuur 3: Schematische weergave van (a) een stroming met wervels van verschillende groottes en (b) de numerieke representatie van de snelheid van deze wervels op een grof rooster. Merk op dat de kleinste wervels niet gerepresenteerd kunnen worden.

kan bijvoorbeeld gebruikt worden om verbrandingsprocessen te optimaliseren. Het verminderen van de wrijving die turbulente stromingen ondervinden, is belangrijk voor het ontwerpen van auto's, boten en vliegtuigen. In dit werk richten we ons daarom op het beschrijven en voorspellen van het gedrag van turbulente stromingen.

Numerieke stromingsleer

Het gedrag van veel vloeistofstromingen, laminair dan wel turbulent, kan worden beschreven door de *Navier–Stokesvergelijkingen*. Deze vergelijkingen zijn genoemd naar de Franse ingenieur en natuurkundige Claude-Louis Navier (1785–1836) en de Ierse wis- en natuurkundige George Stokes (1819–1903), die beiden in de eerste helft van de negentiende eeuw hebben bijgedragen aan de wiskundige beschrijving van vloeistoffen (Navier 1827; Stokes 1845).

De Navier–Stokesvergelijkingen beschrijven diffusie en convectie van impuls, evenals de effecten van druk op stromingen. De term die de convectie van impuls beschrijft is niet-lineair in de stroomsnelheid. De diffusie van impuls wordt daarentegen door een lineaire term beschreven. De Navier–Stokesvergelijkingen zijn daardoor geldig voor *Newtonse vloeistoffen*. Newtonse vloeistoffen zijn vloeistoffen waarin de diffusie een lineaire functie is van de snelheid waarmee de vloeistof vervormt. Ondanks het feit dat vloeistoffen zeer uiteenlopende eigenschappen hebben, kunnen veel vloeistoffen als Newtons behandeld worden. Bovendien is aangetoond dat de Navier–Stokesvergelijkingen zeer nauwkeurige voorspellingen van het gedrag van zulke vloeistoffen geven.

Door de niet-lineaire convectieve term zijn er echter weinig exacte oplossingen van de Navier–Stokesvergelijkingen bekend. Daarnaast vertegenwoordigen de meeste ontdekte oplossingen eenvoudige, laminaire stromingen. Studies van stromingen zijn daarom vaak gebaseerd op numerieke berekeningen die door computers worden uitgevoerd. De numerieke studie van vloeistofstromingen heet *numerieke stromingsleer*. Berekeningen waarin de Navier–Stokesvergelijkingen numeriek worden opgelost, heten *directe numerieke simulaties*.

Modelleren van turbulentie

De meeste turbulente stromingen bevatten zowel zeer grote als kleine wervels (zie bijvoorbeeld Fig. 3(a)). Deze wervels spelen verschillende, maar belangrijke rollen. De grote wervels bevatten het grootste deel van de kinetische energie van een stroming, terwijl de energie van de kleine wervels door diffusie gedissipeerd wordt.

Wegens grenzen aan de beschikbare hoeveelheid computergeheugen kunnen de kleinste wervels meestal echter niet gerepresenteerd worden op de roosters die in numerieke simulaties gebruikt worden (zie Fig. 3(b)). Het gedrag van veel stromingen kan daardoor niet nauwkeurig voorspeld worden door de Navier–Stokesvergelijkingen numeriek op te lossen. Daarom zijn er alternatieve beschrijvingen van turbulente stromingen ontwikkeld.

Een bekende aanpak, die gebaseerd is op het werk van Reynolds (1895), probeert het gemiddelde gedrag van turbulente stromingen te voorspellen. Deze aanpak maakt gebruik van een variant van de Navier–Stokesvergelijkingen die de *Reynoldsgemiddelde Navier–Stokesvergelijkingen* worden genoemd. Door de niet-lineaire convectieve term hebben deze vergelijkingen echter geen gesloten vorm en kunnen zij niet opgelost worden zonder aanvullende informatie. We hebben dus te maken met een *sluitingsprobleem*.

Dit sluitingsprobleem wordt aangepakt door het voorschrijven of *modelleren* van de afwijkingen die de stroomsnelheid ten opzichte van de gemiddelde waarde heeft. Er zijn verschillende *sluitings-* of *turbulentiemodellen* voorgesteld om het gemiddelde gedrag van verschillende stromingen te voorspellen. De op een Reynoldsgemiddelde gebaseerde aanpak geeft echter weinig informatie over het tijdsverloop van stromingen.

Een andere populaire aanpak, die *large-eddy-simulatie* wordt genoemd, richt zich daarom op het voorspellen van de tijdsevolutie van de grote wervels (*eddies*) in stromingen. Zoals bij de Reynoldsgemiddelde Navier–Stokesvergelijkingen het geval is, hebben de vergelijkingen die de grote wervels beschrijven geen gesloten vorm. Het gedrag van kleine wervels en hun effect op de grote wervels moet daarom gemodelleerd worden.

De wervels die niet gerepresenteerd kunnen worden op de roosters die in numerieke simulaties gebruikt worden (zie Fig. 3(b)), worden over het algemeen als kleine wervels bestempeld. Modellen voor de kleine wervels worden daarom vaak *subgrid-scale-modellen* genoemd. Net als sluitingsmodellen voor de Reynoldsgemiddelde Navier–Stokesvergelijkingen worden *subgrid-scale-modellen* ook *turbulentiemodellen* genoemd. Het doel van *subgrid-scale-modellen* is om het aantal berekeningen dat nodig is om de Navier–Stokesvergelijkingen op te lossen, te reduceren en tegelijkertijd te zorgen voor betrouwbare en nauwkeurige oplossingen van het gedrag van de grote wervels in stromingen.

Overzicht van dit proefschrift

Vloeistofstromingen zijn overal. Denk bijvoorbeeld aan rivieren, luchtstromingen in de atmosfeer en het bloed dat door onze aderen stroomt. De meeste

stromingen zijn turbulent en het voorspellen van hun gedrag is cruciaal voor veel toepassingen, waaronder het ontwerpen van auto's, boten en vliegtuigen. Echter, het nauwkeurig voorspellen van turbulente stromingen is zeer uitdagend, omdat computers niet genoeg geheugen hebben om alle stromingsdetails op te slaan.

Met het doel om de numerieke voorspelling van incompressibele turbulente stromingen te verbeteren, passen we daarom *large-eddy*-simulatie toe. Bij *large-eddy*-simulatie worden alleen de grote wervels (*eddies*) in stromingen direct berekend, terwijl de kleine wervels beschreven moeten worden door middel van turbulentiemodellen. De vraag is echter: hoe maak je zulke modellen? Deze vraag kan op verschillende manieren worden beantwoord. Je kunt bijvoorbeeld kiezen uit de vele turbulentiemodellen die sinds de opkomst van de numerieke stromingsleer zijn ontwikkeld. De vraag blijft echter: wanneer is een turbulentiemodel goed ontworpen?

In dit proefschrift richten we ons daarom op het ontwikkelen van *op natuurkunde gebaseerde turbulentiemodellen*, dat wil zeggen, turbulentiemodellen die de wis- en natuurkundige eigenschappen van stromingen respecteren. De voornaamste vraag die wij beschouwen is:

Hoe maak je op natuurkunde gebaseerde turbulentiemodellen voor *large-eddy*-simulaties van incompressibele turbulente stromingen?

In de Engelstalige inleiding van dit proefschrift, te vinden in Hoofdstuk 1, bespreken we de wiskundige achtergrond die nodig is om deze vraag te beantwoorden. In het bijzonder leiden we eerst de Navier–Stokesvergelijkingen voor incompressibele turbulente stromingen af. Vervolgens bediscussiëren we de Reynoldsgemiddelde Navier–Stokesvergelijkingen. Ten slotte introduceren we de vergelijkingen van *large-eddy*-simulatie.

In Deel I van dit proefschrift streven we ernaar bovenstaande vraag te beantwoorden door een systematische aanpak te volgen. In het bijzonder bespreken we eerst in detail een aantal fundamentele wis- en natuurkundige eigenschappen van stromingen. Vervolgens zetten we bestaande voorwaarden op een rij en stellen we nieuwe voorwaarden op waaraan turbulentiemodellen moeten voldoen om deze eigenschappen te behouden. Op deze manier verkrijgen we een stelsel van eisen voor het maken van op natuurkunde gebaseerde turbulentiemodellen. We gebruiken dit stelsel om de eigenschappen van verscheidene bestaande turbulentiemodellen te analyseren. We illustreren ook hoe nieuwe op natuurkunde gebaseerde turbulentiemodellen op systematische wijze gemaakt kunnen worden en we geven voorbeelden van zulke modellen.

In Deel II passen we het stelsel van modeleisen toe om de numerieke voorspelling van roterende turbulente stromingen te verbeteren. In het bijzonder stellen we eerst een nieuw op natuurkunde gebaseerd turbulentiemodel voor *large-eddy*-simulaties van zulke stromingen voor. Vervolgens bestuderen en valideren we dit model met behulp van gedetailleerde berekeningen van roterende stromingen. Ten slotte bepalen we hoe het voorgestelde model presteert in vergelijking met een aantal bestaande turbulentiemodellen.

Zoals we zullen zien, stelt het stelsel van modeleisen ons in staat om systematisch op natuurkunde gebaseerde turbulentiemodellen te creëren die de meeste eigenschappen van stromingen respecteren. Deze modellen kunnen in willekeurige stromingsdomeinen gebruikt worden, zonder dat er zogenaamde dempingsfuncties of dynamische procedures nodig zijn. Bovendien zijn ze geschikt voor simulaties van laminaire en turbulente stromingen, en van stromingen die zich in de transitie tussen deze toestanden bevinden. We bestuderen één dergelijk op natuurkunde gebaseerd turbulentiemodel in detail en we laten zien dat dit model uitstekende voorspellingen van roterende stromingen geeft. We tonen ook aan dat deze voorspellingen zo goed zijn als, of veel beter dan voorspellingen van bestaande turbulentiemodellen. Ons werk kan dus helpen bij het verbeteren van voorspellingen van zowel roterende als niet-roterende turbulente stromingen.

In Deel I en Deel II van dit proefschrift bespreken we onze resultaten en conclusies uitvoerig. Beide delen bevatten een eigen wetenschappelijke samenvatting, inleiding en conclusiehoofdstuk. Een overkoepelende samenvatting van dit werk is te vinden op pagina 229. Een overzicht van de publicaties en presentaties die tot dit proefschrift hebben geleid, begint op pagina 201.

Samenvatting

Op natuurkunde gebaseerde turbulentie modellen voor large-eddy-simulatie

Theorie en toepassing op roterende turbulente stromingen

Vloeistofstromingen zijn overal. Denk bijvoorbeeld aan rivieren, luchtstromingen in de atmosfeer en het bloed dat door onze aderen stroomt. De meeste vloeistofstromingen zijn zeer chaotisch, of turbulent, en het voorspellen van hun gedrag is cruciaal voor veel toepassingen, waaronder het ontwerpen van auto's, boten en vliegtuigen. Echter, het nauwkeurig voorspellen van turbulente stromingen is zeer uitdagend, omdat computers niet genoeg geheugen hebben om alle stromingsdetails op te slaan.

In dit proefschrift passen we daarom een methode toe die *large-eddy*-simulatie heet. Bij deze methode worden de grote wervels (*eddies*) in stromingen direct berekend, terwijl kleine wervels beschreven moeten worden met turbulentie modellen. De vraag die wij beschouwen is: hoe maak je op natuurkunde gebaseerde turbulentie modellen, die de wis- en natuurkundige eigenschappen van stromingen respecteren?

Om deze vraag te beantwoorden volgen we een systematische aanpak. We verkrijgen zo een stelsel van eisen voor het maken van op natuurkunde gebaseerde turbulentie modellen. Met behulp van deze eisen laten we zien dat bestaande turbulentie modellen niet alle eigenschappen van stromingen respecteren. We illustreren ook hoe nieuwe op natuurkunde gebaseerde turbulentie modellen met gewenste eigenschappen systematisch gecreëerd kunnen worden.

Vervolgens passen we het stelsel van eisen toe om een nieuw turbulentie model voor roterende stromingen te ontwikkelen. We laten zien dat dit model veel eigenschappen van stromingen respecteert en uitstekende voorspellingen van roterende stromingen geeft. We tonen ook aan dat deze voorspellingen zo goed zijn als, of veel beter dan, voorspellingen van bestaande turbulentie modellen. Ons werk kan dus helpen bij het verbeteren van voorspellingen van roterende en niet-roterende turbulente stromingen.

Acknowledgments

This thesis is the result of around six and a half years of scientific research on turbulent fluid flows. This period of research started as I moved back to Groningen, The Netherlands, to start working on a PhD project, and came after I finished my studies in Physics in that same city and after I took a gap year. Over the course of the project, I had the opportunity to meet and learn from many people. In addition, I could attend scientific conferences and meetings in countries as diverse as The Netherlands, France, Italy, Spain, Sweden, Morocco and the United States of America. Eventually, I would have the experience of moving to a different country, to see if I could continue working as an academic researcher there. Therefore, I am grateful to have had the opportunity to pursue a PhD and I would like to express my gratitude to all people and institutions that directly or indirectly contributed to my work.

Research

First of all, I would like to thank my supervisors, *Roel Verstappen* and *Arthur Veldman*, for their guidance and advice. Roel, I really enjoyed our discussions and the fact that we turned out to have a similar way of thinking that often led us to have similar ideas. I also wish to thank you for leaving me free to plot out my own research course, and for motivating and enabling me to visit many conferences. Arthur, thank you for always seeking to keep the connection with applied computational fluid dynamics and for providing me with thoughtful comments on earlier versions of this thesis.

I would also like to extend my sincere thanks to my co-authors and collaborators, *Xavier Trias*, *Jane Bae*, *Mahdi Abkar*, *Adrián Lozano Durán* and *Larissa Streher*. Xavi, thank you for being both a mentor and a friend. Your experience in and knowledge of our field of research have helped me tremendously. I am also grateful for the times we shared during numerous conferences and visits. I especially have fond memories of together taking part in the Summer Program of the Center for Turbulence Research (CTR) at Stanford University during the summer of 2016. Jane, Mahdi, Adrián, thank you for the pleasant collaboration during and after the CTR Summer Program. Jane, many thanks for providing detailed reference data, with which I could compare my simulation results. Larissa, it was my pleasure to work with you as you were in the beginning stages of your PhD project and I was in the final stages of mine.

Likewise, I am grateful to the two students, *Ronald Remmerswaal* and *Daniel Ward*, whom I had the joy to guide during their research projects. Ronald, the code you wrote has been invaluable in obtaining the results presented in this thesis. Daniel, thank you for taking up a project that I wished I had the time to work on.

I kindly acknowledge *Martin Oberlack* for stimulating discussions during several stages of this work. I would also like to thank *Michel Deville* for sharing his insights relating to nonlinear turbulence models and realizability. *Geert Brethouwer*, thank you for your assistance in identifying turbulent bursts in numerical simulations of spanwise-rotating plane-channel flow.

In addition, I gratefully acknowledge the members of the committee that assessed this thesis, namely, *Kanat Camlibel*, *Bert Vreman* and *Bernard Geurts*, for reading and providing thoughtful comments on this work, and for their interesting questions.

Special thanks go to *Theodore Drivas*, *Perry Johnson* and *Michael Wilczek* for their interest in and their valuable comments on my work. Theo, I would also like to thank you for staying in touch after we met during the Mathematics of Turbulence program at the Institute for Pure and Applied Mathematics (IPAM) of the University of California, Los Angeles (UCLA) in the fall of 2014. Perry, thank you for sharing your perspective on life as an academic researcher. Michael, many thanks for providing a view into the career and life of a scientist.

Colleagues

Next, I would like to thank my colleagues from the University of Groningen and beyond. I am grateful to the (former) staff, students and visitors of the research group *Computational Mechanics and Numerical Mathematics* (CMNM) of the University of Groningen. *Aleix*, *Arthur*, *Bruno*, *Cristóbal*, *David*, *Donglin*, *Erik*, *Fred*, *Gerk*, *Harmen*, *Henk*, *Henri*, *Henry B.*, *Jassy*, *Jeremías*, *Jia*, *Jigar*, *Jing*, *Joseph*, *Larissa*, *Mark*, *Nico*, *Paolo*, *Peter*, *Roel C.*, *Roel L.*, *Roel V.*, *Ronald*, *Sourabh*, *Sven*, *Weiyang*, *Wybe*, *Xian-Ming*, *Yiming* and *Zhaoli*, thank you for your company and humor, and for our dinners, Christmas parties and summer barbecues. Aleix, thanks for staying in touch. Nico, thank you for the fun time we shared during your stay in Groningen. Thanks go to the (former) group members *Gerk*, *Hande*, *Henk*, *Henri*, *Henry B.*, *Joop*, *Peter* and *Roel L.* for our evenings of playing pool.

I am also grateful to the greater group of colleagues of the *Bernoulli Institute for Mathematics, Computer Science and Artificial Intelligence* of the University of Groningen. In particular, I would like to thank *Alev Sterk* for providing a view into the career of a scientist and *Konstantinos Efsthathiou* for showing me what excellent teaching is.

Furthermore, I would like to thank *Ingrid Molema* and *Heidi Disler* for the enthusiasm with which they led their inspiring grant writing courses. *Lemke Kraan*, *René Franssen* and *Aniek Ivens*, thank you for introducing me to popular science writing and communication. Thanks go to *Petra Rudolf* for her mentoring; to *Marco Koopman* for his organizational work at the graduate school and his interest in my progress; and to *Frank Brokken* for his passionate teaching of C++. Thanks also go to my C++ course buddies *Eelco*, *Jan* and *Yori*.

I wish to thank *Ayaboe* for staying in touch after we met during the Mathematics of Turbulence program at the Institute for Pure and Applied Mathematics

(IPAM) of the University of California, Los Angeles (UCLA) in the autumn of 2014.

Funding and facilities

The PhD research project that led to the current thesis could be carried out thanks to funding and facilities provided by different institutions. First of all, this work is part of the research programme Free Competition in the Physical Sciences with project number 613.001.212, which is (partly) financed by the *Dutch Research Council* (NWO). I am very grateful to NWO for giving me the opportunity to pursue a PhD.

I thankfully acknowledge support from the *Institute for Pure and Applied Mathematics* (IPAM) of the University of California, Los Angeles (UCLA) for enabling me to visit the Mathematics of Turbulence program during the fall of 2014. I also thank the *Center for Turbulence Research* (CTR) at Stanford University for its hospitality and financial support during the Summer Program of 2016. Moreover, I wish to thank the organizing committees of the *International Workshop on Complex Turbulent Flows*, which was held in Tangier, Morocco, in November 2017, and the conference on *Symmetry and Computation*, held in Marseille, France, in April 2018, for their financial support.

I would like to thank the *Center for Information Technology* (CIT) of the University of Groningen for their support and for providing access to the Peregrine high-performance computing cluster. I also acknowledge use of computational resources from the Certainty cluster awarded by the National Science Foundation to the *Center for Turbulence Research* (CTR) and from the MareNostrum supercomputer at the *Barcelona Supercomputing Center* (BSC).

The Netherlands

I wish to thank everyone who made life in Groningen so pleasant. Thanks go to my fellow (PhD) students *Bart, Froukje, Gerjan, Harm Jan, Jelle, Rieza* and *Willem* for the experiences we shared. *Roel T.*, thanks for being such an inspiring example of a young, great scientist. *Ivan* and *Faris*, thank you for introducing me to salsa and for our philosophical conversations.

Thanks also go to my roommates at the Mauritsstraat in Groningen. *Jantine* and *Erwin*, thank you for creating such a friendly and open atmosphere, and for always inviting me when family or friends were coming over. *Charlotte*, thank you for your warmth, the dinners and the great cakes. *Sebastiaan van L.* and *Harrit*, thanks for joining me, for the parties we threw and for the times we shared.

Nathalie, thank you for over fifteen years of friendship. Your mere presence makes me feel accepted and your easygoing approach to life often helped me to put things in perspective. *Henry O.*, thank you for our friendship, for your cooking skills, for always being down for something new, for the trips we made together and for showing me how one can both be laid-back and accomplish

many things at the same time. *Lukas* and *Bauke*, I am grateful that our friendships have only deepened in the course of the years. *Pieter*, thanks for the many fun times we shared.

Many thanks go to *Aron*, *Femke*, *Imre*, *Jonatan*, *Sebastiaan H.*, *Solveig*, *Stephanie* for our friendship, and our weekends of reflection and fun. *John*, *Kim*, *Lilian*, thank you for your support and the personal insights that helped me along the way. *Nathan*, I am grateful we stayed in touch after we met on the Camino de Santiago in Spain in 2012.

Thanks go to *Joel*, *Marijn*, *Luciano* and the others at *The Urban Dance Center* who introduced me to breakdance. I would also like to thank *Feline*, *Juan Carlos*, *Paul* and all others at *Salsa Juan Carlos* for the fun times we shared. I am grateful to the tenors and the other people at *Bragi* for our singing together, the many concerts we gave and the tours we made.

Germany

I also wish to thank everyone who started playing a prominent role in my life, as Josien and I moved to Germany. First of all, many thanks go to our neighbors, *Jonas*, *Anne W.* and *Albrecht* for welcoming us so warmly and for patiently introducing us to German customs. I would also like to thank the *Ono's* for accepting us so kindly in their choir and *Urs* for his warmth and practical support.

My gratitude goes to *Alpa*, *Anna-Lena*, *Anne K.*, *Benjamin*, *Dario*, *Dominik D.*, *Dominik P.*, *Florian*, *Jens*, *Juan*, *Julian*, *Lauritz*, *Markus*, *Martin O.*, *Martin S.*, *Ruth*, *Stefanie*, *Tim*, *Yi* and *Yongqi* for welcoming and accepting me so warmly at the *Chair of Fluid Dynamics (FDY)*, the fluid dynamics research group at the Technical University of Darmstadt, Germany. The monthly dinners and group activities mean a lot to me.

Special thanks go to *Martin Oberlack* for our interesting discussions about scientific research; for enabling me to attend the Summer School on Symmetry, similarity and conservation laws in solid and fluid mechanics, held in Cargèse, France, in April 2018; for helping Josien enroll at a German university; and for receiving me as a guest researcher. You and your research group have managed to build up a very welcoming and friendly work environment to which I hope to contribute, even if only in part time.

Family

Finally, I would like to express my gratitude to my family. *Frank* and *Margreet*, thank you for your unconditional support. I am happy that you have left me free to go my own way, while always offering me a listening ear or advice when I needed it. *Wouter*, my brother and dear friend, thank you for our contact and your warmth. Thanks also go to *Rosanne* and you for always offering me a place to stay in Groningen.

Sophie, Johan, Elin and *Sem*, thank you for your interest in me, even if our ways are different. *Wim*, you may live on the other side of the globe now, but I am thinking of you and your family. *Harm* and *Lenie*, thank you for your hospitality and care.

Finally, *Josien*, I am very happy to have you by my side. You are making my life so much more enjoyable and I am grateful for sharing with you a love for singing, playing the piano, philosophical and political topics, good hikes and vegetarian food. Thank you for bearing with me during the final stages of my PhD and for being willing to undertake the adventure of moving to a different country. It is a joy to be with you.

Maurits Silvis
Darmstadt, April 2020

Biography

Maurits Silvis was born in Zwolle, The Netherlands, on February 8, 1989. From 2007 to 2012, he studied Physics at the University of Groningen, The Netherlands. In 2008, he received the Young Talent Incentive Award of the Holland Society for the best first-year study results in Physics in the Netherlands. Later, he obtained both his bachelor's and master's degrees in Physics with honor.

From 2013 to 2020, Maurits was a PhD student in Computational Fluid Dynamics at the University of Groningen. He attended an educational program at the Institute for Pure and Applied Mathematics (IPAM) at the University of California, Los Angeles (UCLA) as well as a research program at the Center for Turbulence Research (CTR) at Stanford University. With his research, he contributed to the development of physics-based turbulence models, which can improve numerical predictions of turbulent fluid flows.

Maurits published his work in several scientific papers in peer-reviewed international journals and conference proceedings. He also presented his research during more than fifteen international meetings. In 2017, he received the Young Scientist Award for the best oral presentation at the International Workshop on Complex Turbulent Flows.

